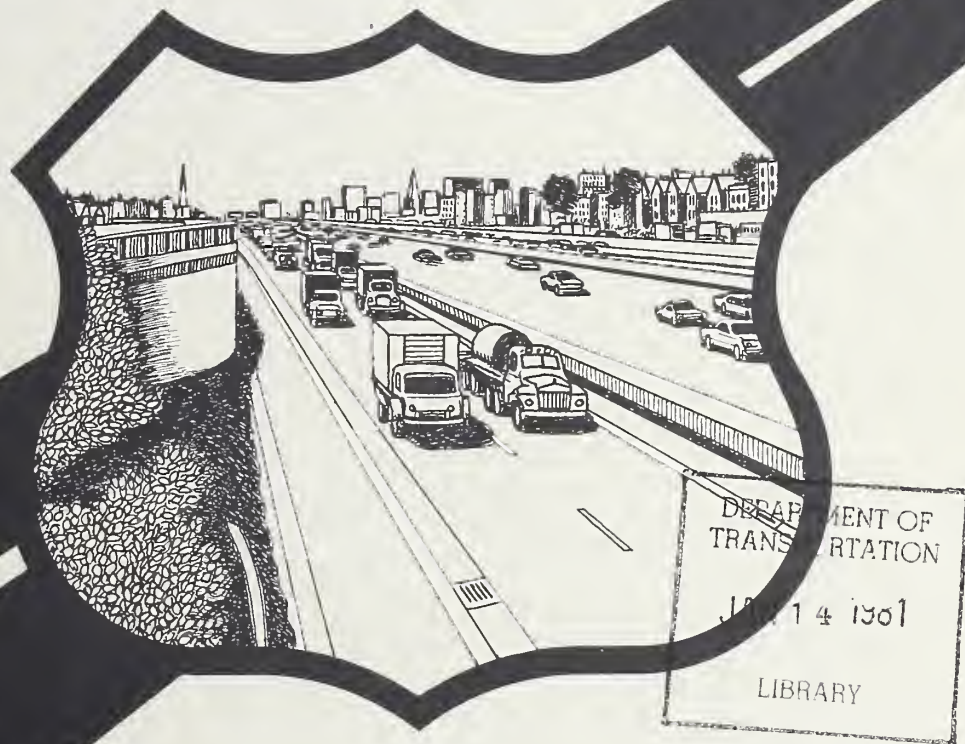


TE
662
.A3
no.
FHWA-
RD-
80-026

Report No. FHWA/RD-80/026

NEW STRUCTURAL SYSTEMS FOR ZERO-MAINTENANCE PAVEMENTS

Vol. I Analytical and Experimental Studies of an Anchored
Pavement: A Candidate Zero-Maintenance Pavement
May 1980
Final Report



Document is available to the public through
the National Technical Information Service,
Springfield, Virginia 22161



Prepared for
FEDERAL HIGHWAY ADMINISTRATION
Offices of Research & Development
Structures & Applied Mechanics Division
Washington, D.C. 20590

FOREWORD

This report describes an analytical and experimental study of three pavement configurations: anchored, elevated anchored, and conventional (rectangular slab). The purpose of the analytical study was to present thermal, mechanical, and thermo-mechanical properties of materials in a form suitable for computer programming, and to describe environmental and mechanical properties of the anchored and the conventional pavement configurations. Three types of analysis were conducted: heat transfer, thermal stress, and mechanical stress. The mechanical stress was evaluated by two methods: finite elements and beam theory. These analytical results are compared with experimental results. The heat transfer analysis was used to evaluate temperature distributions within the pavement and the soil to refine the mechanical stress analysis.

This report is one of several resulting from a research contract, "New Structural Systems for Zero-Maintenance Pavements," issued to Dames & Moore by the Office of Research and Development of the Federal Highway Administration. The objective of this research study is to identify and assess the potential of new and innovative structural concepts and systems to serve as "Zero-Maintenance" pavements. An interim report, "Unique Concepts and Systems for Zero Maintenance Pavements," Report No. FHWA-RD-77-76, provides an updated state-of-the-art and comprehensive review of each of the three major structural components of a pavement system: the subgrade, the base and subbase, and the pavement surface. Three additional manuals are being prepared to complete the study: a user manual for the computer program, a construction specifications manual, and an analysis manual. These manuals are tentatively scheduled for release and publication by the FHWA in early 1980.

Copies of the report are being distributed by transmittal memorandum primarily to research and development audiences.


Charles F. Schefley
Director, Office of Research
Federal Highway Administration

NOTICE

This document is disseminated under the sponsorship of the Department of Transportation in the interest of information exchange. The United States Government assumes no liability for its contents or use thereof.

The contents of this report reflect the views of the Dames & Moore organization and the Illinois Institute of Technology which are responsible for the facts and the accuracy of the data presented herein. The contents do not necessarily reflect the official views or policy of the Department of Transportation.

This report does not constitute a standard, specification, or regulation.

The United States Government does not endorse products or manufacturers. Trademarks or manufacturer's names appear herein only because they are considered essential to the object of this document.

662
A3
no.
FHWA-RD-
80-026

Technical Report Documentation Page

1. Report No. FHWA/RD-80/026	2. Government Accession No.	3. Recipient's Catalog No.	
4. Title and Subtitle NEW STRUCTURAL SYSTEMS FOR ZERO-MAINTENANCE PAVEMENTS Volume 1 Analytical and Experimental Studies of an Anchored Pavement: A Candidate Zero- Maintenance Pavement		5. Report Date May 1980	
6. Performing Organization Code		7. Author(s) S.K. Saxena, W.J. Rosenkranz, and S.G. Militsopoulos	
8. Performing Organization Report No.		9. Performing Organization Name and Address Dames & Moore Illinois Institute of 7101 Wisconsin Avenue Technology Washington, D.C. 20014 Civil Engineering Department and Chicago, Illinois 60616	
10. Work Unit No. (TRAIS) FCP 35E2-042		11. Contract or Grant No. DOT-FH-11-9114	
12. Sponsoring Agency Name and Address Office of Research and Development Federal Highway Administration U.S. Department of Transportation Washington, D.C. 20590		13. Type of Report and Period Covered Final Report July 1976-December 1979	
14. Sponsoring Agency Code DEPARTMENT OF TRANSPORTATION		15. Supplementary Notes FHWA contract manager: Dr. Floyd J. Stanek (HRS-14) Dames & Moore project manager: Dr. Mysore S. Nataraja JAN 14 1981	
16. Abstract New Structural Systems for Zero-Maintenance Pavements. The purpose of this study is to investigate the feasibility of designing and constructing cost-effective "Zero-Maintenance" highways. LIBRARY			
Volume 1: Analytical and Experimental Studies of an Anchored Pavement. This report documents an investigation of the design feasibility and construction cost-effectiveness of an anchored pavement concept for Zero-Maintenance highways. An analytical model is designed to verify computer program results and to investigate construction methods for a full-scale highway section. The purpose of the analytical study is (1) to present thermal, mechanical, and thermomechanical properties of typical materials in a form easily adaptable to computer programs, and (2) to describe environmental and mechanical properties of a conventional slab and an anchored pavement in both continuous and jointed configurations. The two pavements were subjected to heat transfer, thermal stress, and mechanical stress analyses. The anchored pavement offers two distinct advantages over a conventional pavement - deflections are lower and more uniform, and stresses in the soil are lower and distributed more widely by the rigid anchors. Subgrade-related failure is less likely to occur if loads are transmitted deeper within the subgrade. Three-dimensional finite element analysis is considered to be the most efficient technique for examining the significance of environmentally induced stress. The use of the finite element method is anticipated as more advanced analytic techniques are developed.			
This volume is the first in a series. The others in the series are: Volume 2: Analysis of Anchored Pavements Using ANSYS and Volume 3: Anchored Pavement System Designed for Edens Expressway. Abstracts of these volumes are included on page ii of this volume.			
17. Key Words Pavement systems Anchored pavement FEMESH and ANSYS	18. Distribution Statement No restrictions. This document is available to the public through the National Technical Information Service, Springfield, Virginia 22161.		
19. Security Classif. (of this report) Unclassified	20. Security Classif. (of this page) Unclassified	21. No. of Pages 238	22. Price

Abstracts of Related Documents

Volume 2: Analysis of Anchored Pavements Using ANSYS

This report is a manual which provides a set of procedures to evaluate the response of an anchored pavement subjected to vehicle static loads, moisture variation in the subgrade, and/or temperature variation through the surface of the pavement. These procedures include two computer programs known as FEMESH and ANSYS. The FEMESH program generates rectangular meshes in either a two or three dimensional coordinate system for any prespecified number and spacing of nodes. The ANSYS program evaluates the stresses, strains, and deflections at all elements in each material included in the analytical model. The program can be used for any number of different materials in any direction. In the analysis of heat transfer, the program provides the distribution of temperature as a function of time at predesignated points. The program is versatile and capable of solving complex geometrical structures supported on a geologically complex earth mass. The behavior of an anchored pavement section is evaluated with sets of computer programmed mechanistic models. The manual was written to minimize reference to other publications.

Volume 3: Anchored Pavement System Designed for Edens Expressway

This report provides an analysis example of an actual pavement and the cost estimate using the anchored system. The actual pavement is the Edens Expressway in Chicago. The report provides the response of the Edens Expressway subjected to mechanical and environmental loads using the anchored pavement concept. The mechanical and thermal properties of materials that could be encountered in future reconstruction of Edens Expressway are presented in a consistent form for computer programming. These properties are viewed as typical design values during investigation of pavement response. The behavior of the anchored pavement under induced temperature loads and weakening of subgrade (by thawing action) is clearly demonstrated. This report will enable application of the anchored pavement concept by any road with heavy traffic. The example problem provides the input parameters of materials and loads for the analysis, the generation of finite element mesh, and the results of the analysis. The computer program ANSYS was used for this study (the manual for the use of the program is presented in Vol. 2 of this series of reports).

TABLE OF CONTENTS

CHAPTER I	INTRODUCTION	1
1.1	SCOPE OF STUDY	1
1.2	RELATED DOCUMENTS	4
CHAPTER II	EXPERIMENTAL INVESTIGATION	5
2.1	GENERAL	5
2.2	MODEL DESCRIPTION AND INSTRUMENTATION	5
2.2.1	Slabs	5
2.2.2	Subgrade	7
2.2.3	Container	7
2.2.4	Loading and Measuring Equipment	7
2.3	TEST DETAILS	11
2.3.1	Anchored Slab on Soil Subgrade - AS62	11
2.3.2	Conventional Slab on Subgrade - S62	21
2.3.3	Elevated Anchored Slab - ASE62	39
2.4	RESULTS	39
CHAPTER III	VERIFICATION OF COMPUTER PROGRAM	55
3.1	INTRODUCTION	55
3.2	VERIFICATION FOR HEAT TRANSFER	55
3.3	VERIFICATION FOR MECHANICAL LOADS	57
3.3.1	Results of Analysis	62
CHAPTER IV	ANALYSIS OF THE PAVEMENT SYSTEMS	80
4.1	INTRODUCTION	80
4.2	MATERIAL CHARACTERIZATION	80
4.2.1	General Behavior of Pavement Systems	80
4.2.2	Material Properties	84
4.2.2.1	Thermal	84
4.2.2.2	Mechanical	91
4.3	ENVIRONMENTAL LOADS	103
4.3.1	General	103
4.3.2	Characterization of Loads	103

	Page
4.3.3 Description of Models	114
4.3.4 Heat Transfer Analysis	121
4.3.5 Thermal Stress Analysis	121
4.3.6 Moisture	135
4.4 ANALYSIS OF MECHANICAL LOADS	138
4.4.1 General	138
4.4.2 Description of Models	138
4.4.3 Results	141
4.5 SUPERPOSITION OF ENVIRONMENTAL AND MECHANICAL LOADS	157
4.5.1 General	157
4.5.2 Results	157
4.6 ANALYSIS OF JOINTS	160
4.6.1 General	160
4.6.2 Description of Joint and Mathematical Model	160
4.6.3 Results	162
CHAPTER V CONCLUSIONS AND RECOMMENDATIONS	164
5.1 CONCLUSIONS	164
5.2 RECOMMENDATIONS	165
BIBLIOGRAPHY	173
APPENDIXES	
A. TABLES OF SURFACE STRAINS	179
B. GEOTECHNICAL PROPERTIES OF SUBGRADE	188
C. FINITE ELEMENT FORMULATION	218

FIGURES

Figure	Page
1. Configuration of Conventional and Anchored Pavements Studied	2
2. Aluminum Plates	6
3. Views of a 62-in. (157.5cm) Long Anchored Slab	8
4. Plan View of Testing Tank with Sampling Tank	9
5. Plan View and Cross Section of Loading Platform	10
6. Cross Section of AS62 on Subgrade	12
7. Plan View of AS62 on Subgrade	13
8. Various Positions of Load, Dial Gages, and Surface Deflections	14
9. Position of Foil Strain Gages on Anchored Slab	15
10. Preloading by a Line Load	17
11. Load Versus Deflection Curve for Line Preloading at Center of AS62	18
12. Load Versus Deflection Curve for Line Preloading at Left Edge of AS62	19
13. Load Versus Deflection Curve for Line Preloading at Right Edge of AS62	20
14. Load at Center -- Traffic Lane	22
15. Load at Center -- Shoulder Lane	23
16. Load at Edge -- Traffic Lane	24
17. Position of Foil Gages on Conventional Slab	25
18. Load Versus Deflection Curve for Line Preloading at Center of S62	26
19. Longitudinal Surface Deflection Along Line L1-N1, Load Position 1, S62 - AS62	27
20. Longitudinal Surface Deflection Along Line L2-N2, Load Position 1, S62 - AS62	28
21. Longitudinal Surface Deflection Along Line L3-N3, Load Position 1, S62 - AS62	29

FIGURES (cont'd)

Figure	Page
22. Transverse Surface Deflection Along Line T1-R1, Load Position 1, S62 - AS62	30
23. Transverse Surface Deflection Along Line T2-R2, Load Position 1, S62 - AS62	31
24. Transverse Surface Deflection Along Line T3-R3, Load Position 1, S62 - AS62	32
25. Longitudinal Surface Deflection Along Line L1-N1, Load Position 3, S62 - AS62	33
26. Longitudinal Surface Deflection Along Line L2-N2, Load Position 3, S62 - AS62	34
27. Longitudinal Surface Deflection Along Line L3-N3, Load Position 3, S62 - AS62	35
28. Transverse Surface Deflection Along Line T1-R1, Load Position 3, S62 - AS62	36
29. Transverse Surface Deflection Along Line T2-R2, Load Position 3, S62 - AS62	37
30. Transverse Surface Deflection Along Line T3-R3, Load Position 3, S62 - AS62	38
31. Cross Section of ASE62 on Subgrade	41
32. View of Elevated Pavement	42
33. Longitudinal Surface Deflection Along Line L1-N1, Load Position 1, ASE62 - AS62	43
34. Longitudinal Surface Deflection Along Line L2-N2, Load Position 1, ASE62 - AS62	44
35. Longitudinal Surface Deflection Along Line L3-N3, Load Position 1, ASE62 - AS62	45
36. Transverse Surface Deflection Along Line T1-R1, Load Position 1, ASE62 - AS62	46
37. Transverse Surface Deflection Along Line T2-R2, Load Position 1, ASE62 - AS62	47
38. Transverse Surface Deflection Along Line T3-R3, Load Position 1, ASE62 - AS62	48

FIGURES (cont'd)

Figure	Page
39. Longitudinal Surface Deflection Along Line L1-N1, Load Position 3, ASE62 - AS62	49
40. Longitudinal Surface Deflection Along Line L2-N2, Load Position 3, ASE62 - AS62	50
41. Longitudinal Surface Deflection Along Line L3-N3, Load Position 3, ASE62 - AS62	51
42. Transverse Surface Deflection Along Line T1-R1, Load Position 3, ASE62 - AS62	52
43. Transverse Surface Deflection Along Line T2-R2, Load Position 3, ASE62 - AS62	53
44. Transverse Surface Deflection Along Line T3-R3, Load Position 3, ASE62 - AS62	54
45. Model Used for Computer Program Heat Transfer Analysis Verification	56
46. Actual Recorded Tautochrones at Sta. 724 + 7.5 of the Vormsund Test Road, April 26, 1963	58
47. Measured and Input Surface Temperature for the Vormsund Test Road, April 26, 1963	59
48. Tautochrones Generated by the Finite Element Model . . .	61
49. Finite Element Models of SAS62 and SS62 for Stress Analysis Verification	64
50. Longitudinal Deflections at Center for Comparison of Experimental Models, Finite Element Models, and Models Using Beam Theory	65
51. Longitudinal Deflections at Center for Comparison of Finite Element Models of SS62 and SAS62	67
52. Finite Element Models of AS62 and S62 for Stress Analysis Verification	68
53. Finite Element Model of ASE62 for Stress Analysis Verification	69
54. Surface Deflection Contours for 750-lb. (340 kg) Load at Position 1 of S62	70

FIGURES (cont'd)

Figure	Page
55. Vertical Stress and Strain Contours for 750-lb. (340 kg) Load at Position 1 of S62	71
56. Surface Deflection for 750-lb. (340 kg) Load at Position 1 of AS62	72
57. Vertical Stress and Strain Contours for 750-lb. Load (340 kg) at Position 1 of AS62	73
58. Surface Deflection Contours for 200-lb. (91 kg) Load at Position 1 of ASE62	74
59. Vertical Stress and Strain Contours for 200-lb. (91 kg) Load at Position 1 of ASE62	75
60. Transverse Surface Deflections Along Line T1-R1, Load Position 1 of S62	77
61. Transverse and Longitudinal Surface Deflection Along Lines T1-R1 and L2-N2, Load Position 1 of AS62	78
62. Transverse and Longitudinal Surface Deflection Along Lines T1-R1 and L2-N2, Load Position 1 of ASE62	79
63. Geographic Delineation of Climates	81
64. Typical Variation of Surface Deflection in a Freeze/Thaw Seasonal Cycle	82
65. Comparison of Deflection Basins for Various Times of Year Under 1000-lb. (450 kg) Load of Dynaflect Test Apparatus	83
66. Seasonal Change in Moisture Content	85
67. Conceptual Dependence of Thermal Properties on Temperatures	87
68. Volumetric Heat Capacities of Various Soils Near Freezing Temperatures	88
69. Variation of Thermal Conductivities with Temperature	89
70. Variation in Thermal Conductivity of Soils with Moisture Content	92
71. General Correlation Between Modulus and Thermal Conductivity in Frozen Soils	93

FIGURES (cont'd)

Number	Page
72. Conceptual Diagram Illustrating the Freezing of Soil Moisture	95
73. Effect of Temperature on Modulus of Moist, Fine- drained Soil due to "Cementation" of Particles by Ice	96
74. Influence of Temperature on the Unfrozen Water Content of Soils	97
75. Effect of Moisture and Temperature on the Strength of a Clay in Compression	99
76. Effect of Temperature on the Stress-Strain Behavior of a Clay	100
77. Coefficient of Cubic Expansion of Water as a Function of Temperature	101
78. Strength Properties of Asphaltic Concrete (AC) as a Function of Temperature	102
79. Relative Strength of Portland Concrete Cement (PCC) as a Function of Temperature	104
80. Elastic Modulus of PCC as a Function of Temperature . .	105
81. Heat Balance at the Pavement Surface	107
82. Variation of Solar Radiation Intensity	109
83. Correlation Between Surface and Air Temperatures	111
84. Temperature Difference Between Pavement Surface and Air at Various Times of the Year	112
85. Typical Diurnal Variation of Temperature in Natural Soil	113
86. Surface Temperature Input for Mathematical Model (Summer Condition)	115
87. Surface Temperature Input for Mathematical Model (Winter Condition)	116
88. Model in Which Heat Content of System is Constant: Temperature Content is Controlled by Surface Temperature	117

FIGURES (cont'd)

Number	Page
89. Model in Which Heat Content of System is not Constant Because of Added Surface Convection and Radiation . . .	118
90. Two-dimensional Mesh Used in Heat Transfer and Thermal Stress Analysis	119
91. Thermal Modeling Details	120
92. Summer Tautochrones at Pavement Centerline	122
93. Winter Tautochrones at Pavement Centerline	123
94. Tautochrones in Natural Slope on a Summer Day	124
95. Mathematical Model Used to Simulate Slab/Soil Interface Behavior	125
96. Interface Behavior of Sand on Mortar for Various Contact Pressures	127
97. Variation of Interface Modulus with Confining Pressure	128
98. Surface Deflections due to Thermal Strains, Summer . . .	129
99. Surface Deflections Due to Thermal Strains, Winter . . .	130
100. Plan View of Three-dimensional Mesh Used for Thermal Stress Analysis	132
101. Perspective View of Three-dimensional Mesh Used for Thermal Stress Analysis	133
102. Deflection Contours for Three-dimensional Anchored Slab During Summer Day	134
103. Sources of Water and Directions of Flow in Pavement Systems	136
104. Effect of Traffic on Moisture Content of Subgrade Soils	137
105. Transverse Section of Three-dimensional Mesh Used for Thermal and Mechanical Stress Analysis	139
106. Three-dimensional Continuous Pavement Model, Anchored and Conventional	140
107. Pavement Configurations	142

FIGURES (cont'd)

Figure	Page
108. Difference Between Deflection Behavior with Load at a Joint in a Jointed Pavement and with Load on a Continuous Pavement	143
109. Transverse Surface Deflections at Load in 100-ft. (30-m) Models	144
110. Longitudinal Surface Deflections in Outer Wheel Path for 100-ft. (30-m) Models	145
111. Surface Deflection Contours for Continuous Anchored Pavement	147
112. Longitudinal Deflections in Outer Wheel Path for 100-ft. (30-m) Slab Models	148
113. Transverse Deflections at Load in 100-ft. (30-m) Models (Weak Subgrade)	150
114. Transverse Deflections 75 in. (2 m) from Load in 100-ft. (30 m) Models	151
115. Longitudinal Deflections in Outer Wheel Path for Single Slab Models	152
116. Longitudinal Deflections for 50-ft. (15-m) Slab in Weak Subgrade with Load at a 1-in. (2.5 cm) Joint	153
117. Transverse Deflections at Joint in 50-ft. (15-m) Jointed Pavements in Weak Soil	155
118. Transverse Deflections 75 in. (2 m) from Load (Joint) in 50-ft. (15 m) Jointed Pavements in Weak Soil	156
119. Results of Surface Deflection Load Superposition (Summer)	158
120. Results of Surface Deflection Load Superposition (Winter)	159
121. Joint Concept Proposed for Use in Anchored Pavement . .	161
122. Results of Joint Response to Slab Movement Analysis . .	163
123. Possible Technique for Analysis of the Effects of Isolated Ice Lenses in Two and Three Dimensions by the Finite Element Method	168
124. Deflections Resulting From Ice Lense Growth 24 in. (61 cm)Beneath a Conventional Slab at Joint	169

FIGURES (cont'd)

Figure	Page
125. Results of Ice Lense Growth 24 in. (61 cm) Beneath Pavement(Anchored Slab)	170
126. Scheme to Study Dynamic Loads in Pavement Systems Using Transient Dynamic Finite Element Analysis	171
127. Front Panel of Soil Strain Gage.	189
128. Rear Panel of Soil Strain Gage.	190
129. Calibration Fixture for Sensors.	191
130. Sensor Spacing Calibration of Amplitude Dial.	192
131. Applied Load Versus Average Surface Deflection for Rigid Footing.	194
132. Vertical Stress Versus % Average Strain at 1.63 in. Depth for Footing.	196
133. Vertical Stress Versus % Average Strain up to Failure at 1.63 in. Depth for Rigid Footing.	197
134. Secant Modulus of Subgrade Using the Slope of the Stress Versus Strain Curve.	198
135. Secant Modulus of Subgrade Versus Poisson's Ratio.	199
136. Applied Stress Versus Average % Strain for Unconfined Compression Test.	201
137. Secant Modulus Versus % Strain for Unconfined Compression Test.	202
138. Deviator Stress Versus % Strain at Different Confining Pressures for Triaxial Compression Test.	203
139. Mohr Circles for Triaxial Compression Test.	204
140. Modulus of Elasticity Confining Stress from Triaxial Compression Test.	205
141. Deviator Stress Versus % Strain at Different Confining Pressures for Triaxial Compression Test.	206
142. Mohr Circles for Triaxial Compression Test.	207
143. Secant Modulus Versus % Strain at Different Confining Pressures from Triaxial Compression Test.	208

FIGURES (cont'd)

Figures	Page
144. Secant Modulus at 0.1% Strain Versus Confining Pressure from Triaxial Compression Test.	209
145. Coefficient of Consolidation, Primary Compression Ratio, and Void Ratio at Different Pressures Using Logarithmic Fitting	211
146. Applied Pressure Versus % Strain.	212
147. Secant Modulus of Soil at Different % Strains	213
148. Grain Size Distribution	214
149. Flow Curve and Atterberg Limits	215
150. Dry Density Versus % Water Content.	216
151. K_0 Versus OCR for Soils of Varying Plasticity	217

TABLES

Table	Page
1. Material Properties Used in Thermal Verification Program	60
2. Material Properties Used in Stress Verification Program	63
3. Typical Heat Capacities of Road Materials (BTU/lb.-F ⁰).	90
4. Material Properties Used in Finite Element Model.	106
5. Surface Strains of AS62 for Load Position 1	179
6. Surface Strains of AS62 for Load Position 2	179
7. Surface Strains of AS62 for Load Position 3	180
8. Surface Strains of AS62 for Load Position 4	180
9. Surface Strains of AS62 for Load Position 5	181
10. Surface Strains of AS62 for Load Position 6	181

TABLES (cont'd)

Table	Page
11. Surface Strains of S62 for Load Position 1	182
12. Surface Strains of S62 for Load Position 2	182
13. Surface Strains of S62 for Load Position 3	183
14. Surface Strains of S62 for Load Position 4	183
15. Surface Strains of S62 for Load Position 5	184
16. Surface Strains of S62 for Load Position 6	184
17. Surface Strains of ASE2 for Load Position 1	185
18. Surface Strains of ASE2 for Load Position 2	185
19. Surface Strains of ASE2 for Load Position 3	186
20. Surface Strains of ASE2 for Load Position 4	186
21. Surface Strains of ASE2 for Load Position 5	187
22. Surface Strains of ASE2 for Load Position 6	187
23. Displacement Models for Finite Elements	221

CHAPTER I INTRODUCTION

Serious concern over the costs of highway systems has raised a question as to the feasibility of designing and constructing cost effective "zero maintenance" highways. For this project, the Federal Highway Administration (FHWA) has defined zero maintenance as that requiring no structural work for 20 years, then only minor work for the next 10 years.

As a result of research sponsored by FHWA, several structural concepts have been proposed (Saxena, Wang, Udwari, and Rosenkranz, 1977) for zero maintenance performance. These include pile support, edge stiffening, thick cellular systems, waffle-type systems, modified conventional systems, and a flexible, "floating," V-shaped pavement.

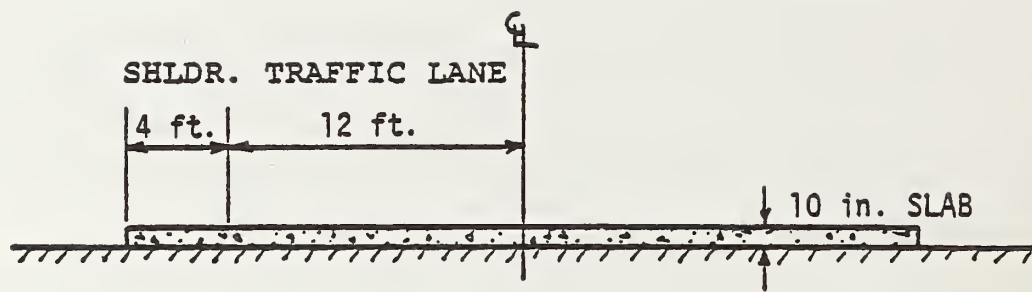
A limited study of various concepts showed an anchored pavement (Figure 1) to be promising because it uses a similar amount of structural material as present systems, does not pose great construction difficulties, and probably requires little subgrade preparation.

1.1 SCOPE OF STUDY

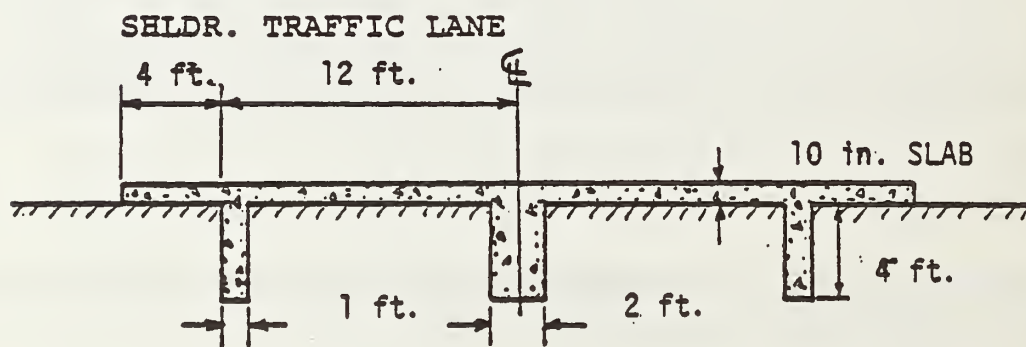
Investigation of the proposed anchored system was divided into two sections: Model Study and Analytical Study.

The scope of the model study was twofold: first and foremost, to verify the analytical model (computer program) results and second, to investigate construction methods and problems for a full-scale highway section. The model study should also help determine specifications for a full-scale test.

The analytical study had two intents: the first was to present thermal, mechanical, and thermomechanical properties of typical materials encountered in highway construction and pavement design in a consistent form, easily adaptable to computer programs. These properties were compiled after a comprehensive literature search to ascertain typical values and expected ranges. General trends as well as actual values are discussed in this report. The second was environmental and mechanical analyses of a conventional slab and an anchored pavement (Figure 1) in both continuous and jointed configurations.



a) Conventional.



1 in. = 2.54 cm

b) Anchored.

Figure 1. Configuration of conventional and anchored pavements studied.

In the heat transfer analysis, extreme temperatures were simulated to determine temperature distributions within the structural elements and supporting subgrade; results were compared with field test data reported in the literature. Thermal stress analysis, based on temperature distributions derived in the heat transfer analysis, was also conducted and results were compared with those reported in the literature. To complete the environmental analysis, the effects of moisture and its transport through the systems were studied.

Pavement response to mechanical loads imposed by vehicles was investigated for all configurations. The results from the mechanical stress analysis were superimposed on the results from the environmental stress analysis so that the relative magnitudes of stresses and displacements could be seen. The most detrimental load (worst case) in each system is presented so that the gross behavior of each system can be understood. Finally, the relative advantages and disadvantages of each system are discussed.

Two-dimensional finite elements were used for heat transfer and stress analysis, and three-dimensional finite elements for mechanical stress analysis. A computer program entitled Engineering Analysis System (ANSYS) developed by Swanson (1975) was used because of its versatility. With ANSYS, several types of analysis are possible including static, dynamic, and heat transfer of two- and three-dimensional structural systems. A large element library is also available, and material and geometric nonlinearities are possible.

The finite element method was chosen because it lends itself to analysis of complex nonlinear and transient field problems in several dimensions. Such analysis would be otherwise impossible without costly experimental investigations.

The investigation is reported in the following sequence:

Chapter II - Investigations. Presents experimental study of the anchored pavement 62 in. (157.5 cm) long. For comparison purposes, a conventional slab was tested under similar conditions. The results of a series of other experiments are also presented.

Chapter III - Verification of Computer Program. Presents the types of verification and the numerical values derived from experiments and actual field tests to form a comparison for the analytical solution.

Chapter IV - Analysis of Pavement Concepts. Presents material characterizations, analysis of environmental loads, analysis of mechanical loads, and superposition of mechanical and environmental effects.

Chapter V - Conclusions and Recommendations.

The report also has a bibliography and three appendices dealing with soil properties in experimental work and finite element formulations.

1.2 RELATED DOCUMENTS

This document is developed so that it can be used with a minimal reference to other materials. Two subsequent reports which include information on anchored pavement system concepts are Volume 2: Analysis of Anchored Pavements Using ANSYS and Volume 3: Anchored Pavement System Designed for Edens Expressway. See page ii of this volume for information on the limited availability of these subsequent volumes.

CHAPTER II EXPERIMENTAL INVESTIGATIONS

2.1 GENERAL

The response of subgrade to load applied on conventional pavement slabs has been previously investigated. Experimental investigations of the structural behavior of rigid pavements were made at Arlington Experimental Farm, Va. (Teller and Sutherland, 1935, 1936, 1943) and at Iowa State Engineering Experimental Station (Spangler, 1935, 1937). These experiments and the work by the U.S. Army Corps of Engineers resulted in modification of Westergaard's formulas (1927) for the most critical conditions when the slab corners are warped upwards.

Full-scale tests were performed at Schiphol Airport in Holland (Vander Veen, 1953) and on Interstate 80, near Ottawa, Illinois, as part of the AASHO Road Test Program. The latter generated many studies. Because the above mentioned were tests conducted in the field, it was difficult to separate moisture and temperature effects from load effects. Model tests were performed under controlled conditions to study the effect of stresses due to load alone by Vesic and Saxena (1970). In these tests, behaviors of slabs resting on an elastic subgrade of known properties were relatively close to those predicted in analytical studies.

2.2 MODEL DESCRIPTION AND INSTRUMENTATION

The model tests for this investigation were 1/20th scale and involved anchored and conventional aluminum slabs of similar lengths; a subgrade of known properties; a container tank for the soil and for conducting the experiment; and loading and measuring equipment.

2.2.1 Slabs

Both the anchored and conventional slabs were 62 in. (157.5 cm) long, 21.63 in. (55 cm) wide, and 0.5 in. (1.27 cm) deep (Figure 2). For the anchored slab, there was an anchor near each edge and a central anchor. The two edge anchors measured 1.88 in. (4.8 cm) deep and 0.625 in. (1.6 cm) wide. The central anchor was also 1.88 in. (4.8 cm) deep, but was 1.25 in. (3.2 cm) wide. The lengths of the anchors and the slab were obviously the same. The anchors were

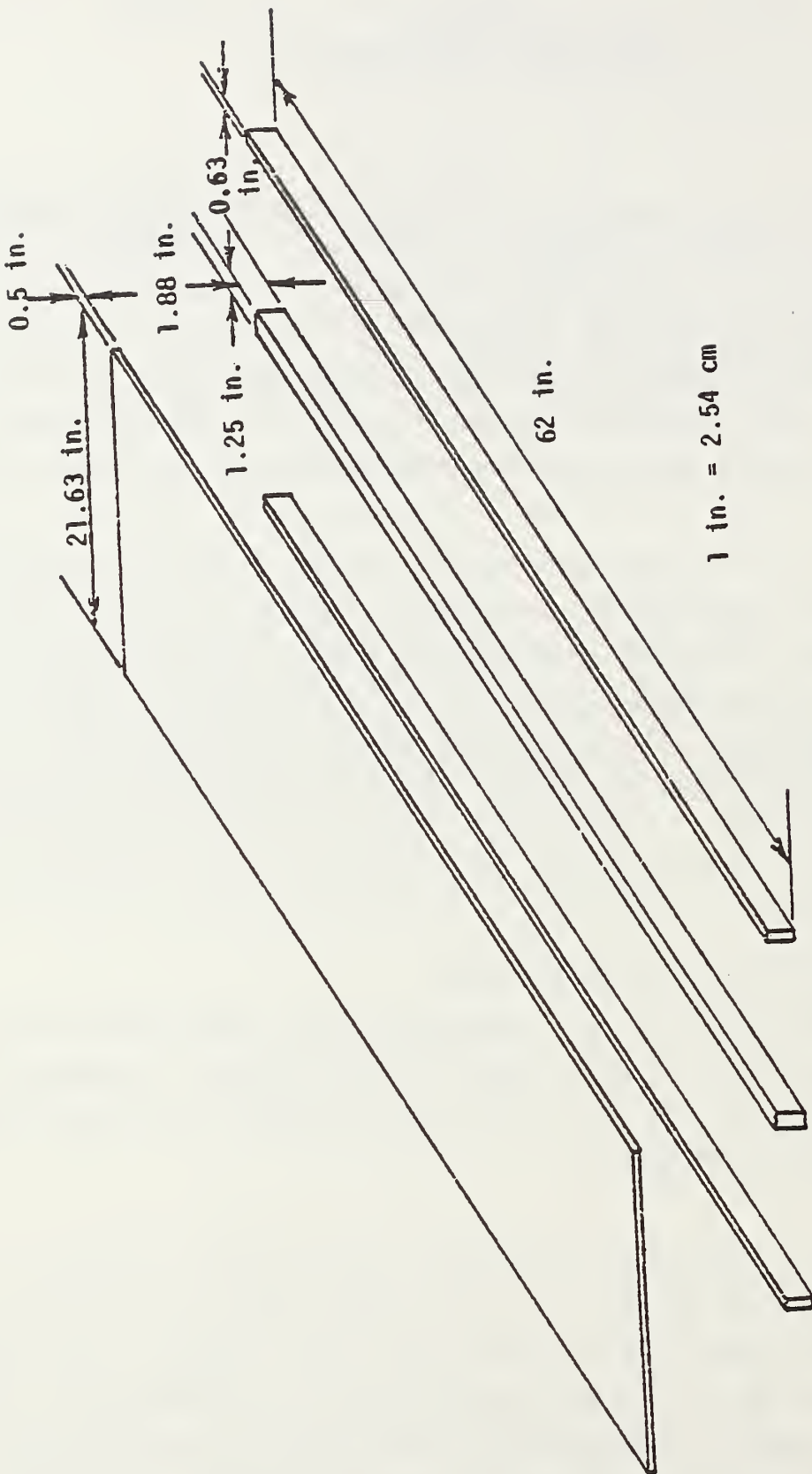


Figure 2. Aluminum plates.

attached to the slab by screws centered at 5 in. (12.7 cm). The top and bottom views of the slab are shown in Figure 3.

This series of tests were conducted to keep the slab 5 in. from the edges of the container in which the experiment was being performed (Figure 3). Tests on conventional slab were performed using the 62 in. (157.5 cm) slab without the anchors.

2.2.2 Subgrade

The subgrade used was 42% kaolinite clay, 42% silica sand, and 16% water (by weight). The subgrade was classified as a silty clay with a plasticity index of 16 and an optimum water content of about 8%. The soil was mixed with an over-the-optimum water content.

2.2.3 Container

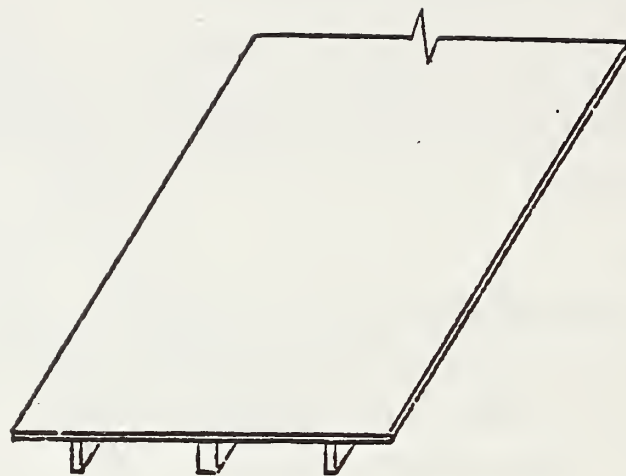
A steel tank was used for the tests. The tank was divided into two areas, testing and sampling (Figure 4). The testing area was 73 in. (185.4 cm) long, 36.25 in. (92.1 cm) wide, and 22.75 in. (57.8 cm) deep. The sampling area was 27.88 in. (70.8 cm) long, with other dimensions being the same.

A soil mixer and a compactor were used to prepare the subgrade. The silty clay subgrade was mixed in 100-lb. (45.36 kg) batches then deposited in the tank. The subgrade was compacted in 2-in. (5.08 cm) layers. For a uniform compaction, two passes of the compactor per layer were found to be sufficient. Before placing another layer, the top 0.5 in. (1.27 cm) of the previous layer was raked to ensure proper bond. Every effort was made to have uniform compaction in all layers. The leveling of the upper layer was done with precision to ensure proper contact between the slab and subgrade.

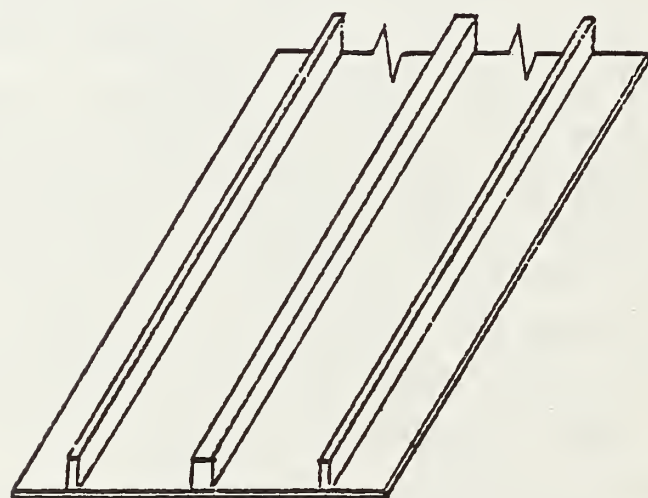
Anchors were placed before the leveling of the upper layer, then the slab was screwed to them. To avoid disturbing the soil, this method was considered better than welding the anchors to the plate. Crossbars were utilized to keep the anchors in position during compaction. The crossbars were later removed.

2.2.4 Loading and Measuring Equipment

The loading platform (Figure 5) was designed to represent a 1/20th scale model of two rear axle trucks with four tires per axle and a maximum capacity of 18,000 lb. (8165 kg) per axle. The 18,000-lb. axle load on a 1/20th



a) Top view.



b) Bottom view.

Figure 3. Views of a 62-in. (157.5-cm) long anchored slab.

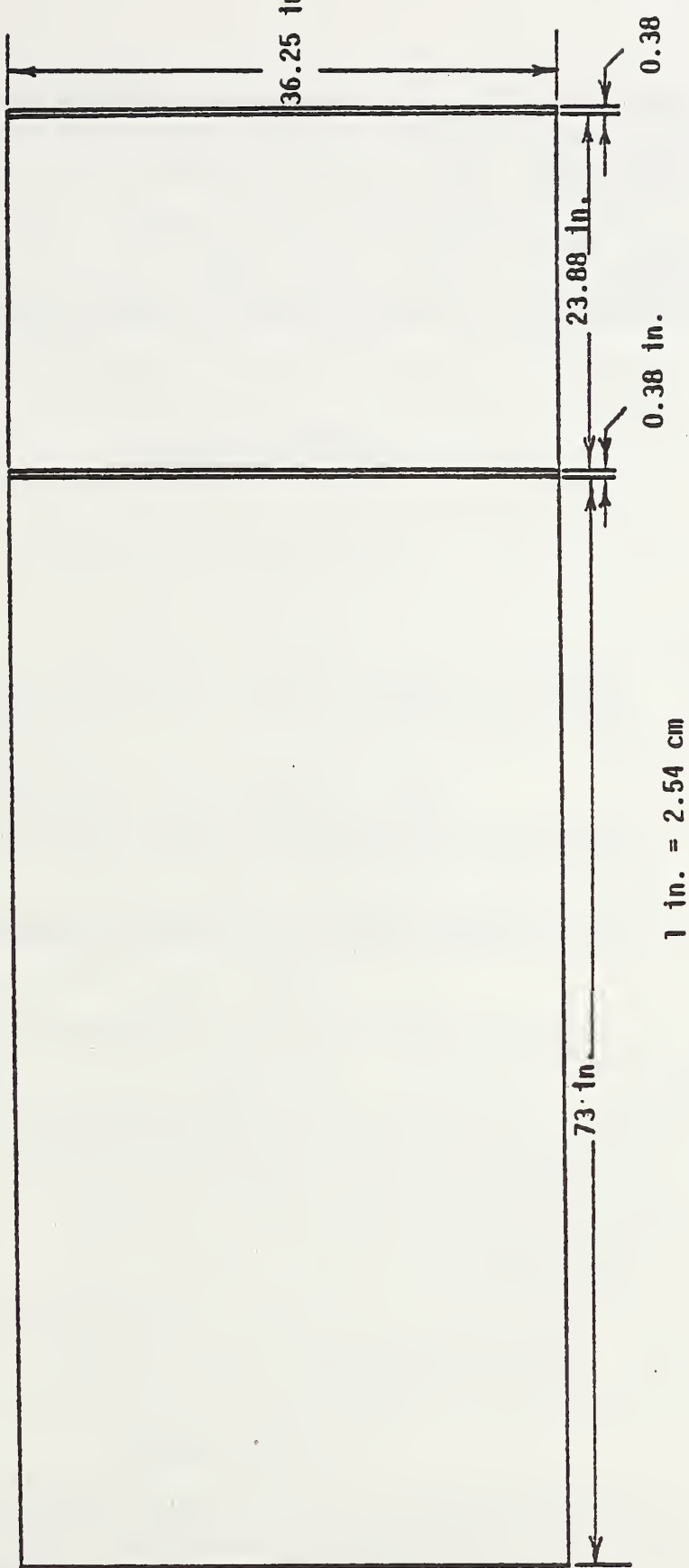
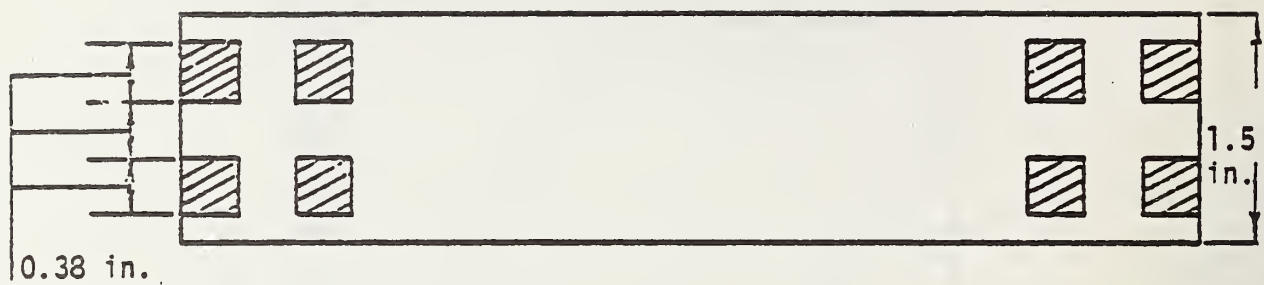
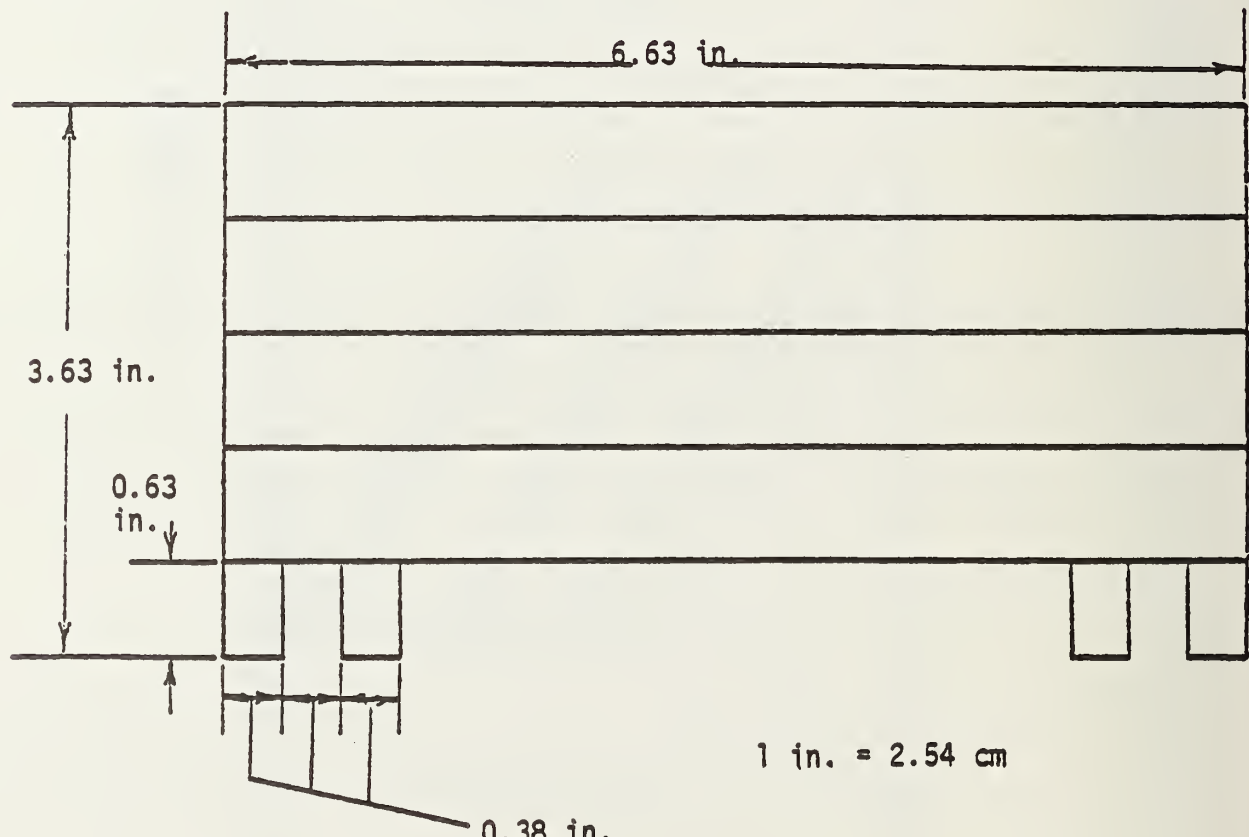


Figure 4. Plan view of testing tank with sampling tank.



a) Plan view.



b) Cross section.

Figure 5. Plan view and cross section of loading platform.

scale model was equal to a scale 45-lb. (20.4 kg) load; however, greater loads were used within the elastic range to investigate the response of the slab-subgrade system. For load application, a manual jack with an attached load cell was used. A strain indicator unit and balance unit were used to measure the strains of 10 foil strain gages fixed at various locations on the slab. The foil gages were used in a quarter bridge circuit with an internal 120 ohm dummy.

The following notations were used for the series:

1. Anchored slab, 62 in. (157.5 cm) long, on soil subgrade -- AS62
2. Conventional slab, 62 in. (157.5 cm) long on soil subgrade -- S62
3. Anchored slab, 62 in. (157.5 cm) long elevated by 0.5 in. (1.27 cm) from soil subgrade -- ASE62

2.3 TEST DETAILS

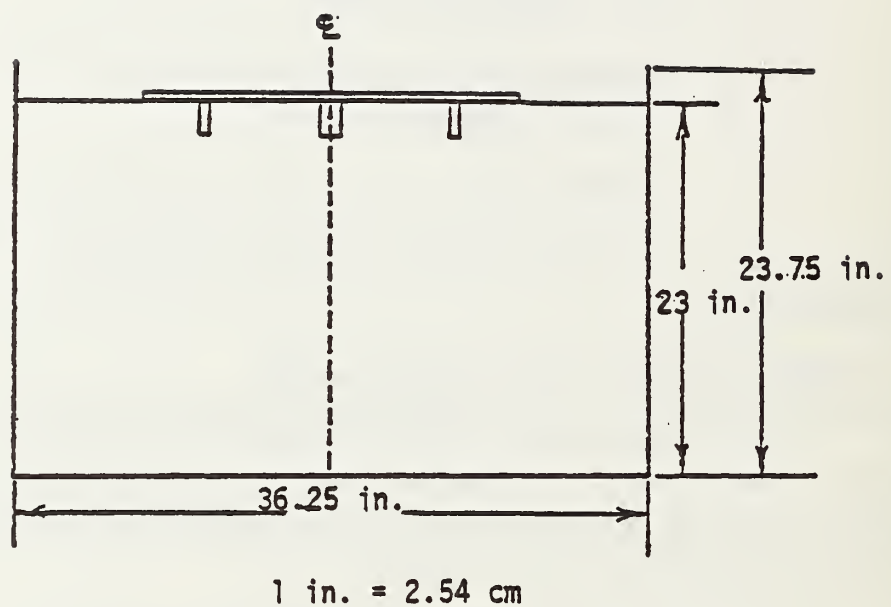
2.3.1 Anchored Slab on Soil Subgrade - AS62

The soil was placed using the technique described in Section 2.2. After the final layer was placed and leveled, a film of oil was spread over the area not covered by the slab, to prevent evaporation of moisture. This area was then covered with thin plastic sheets.

A cross section and a plan view of the slab on the subgrade soil are shown in Figures 6 and 7 respectively. The location of the dial gages for measuring surface deflections of the anchored slab are shown in Figure 8. The 16 numbered points where the deflection was measured were used to draw transverse and longitudinal deflections along sections T1-R1, T2-R2, and T3-R3, and along sections L1-N1, L2-N2, and L3-N3 respectively, also shown in Figure 8.

Ten foil gages were placed on the slab to measure strains and deduce the stresses and bending moments. Five foil gages were placed on top surface of the slab, two on the bottom surface, and the other three on the anchors (Figure 9).

The aluminum material in the experimental range were linear, isotropic, and elastic. Therefore, two independent elastic constants (E = modulus of elasticity and v = Poisson's ratio) were necessary.



AS62 represents 62 in. long
anchored slab on soil
subgrade

Figure 6. Cross section of AS62 on subgrade.

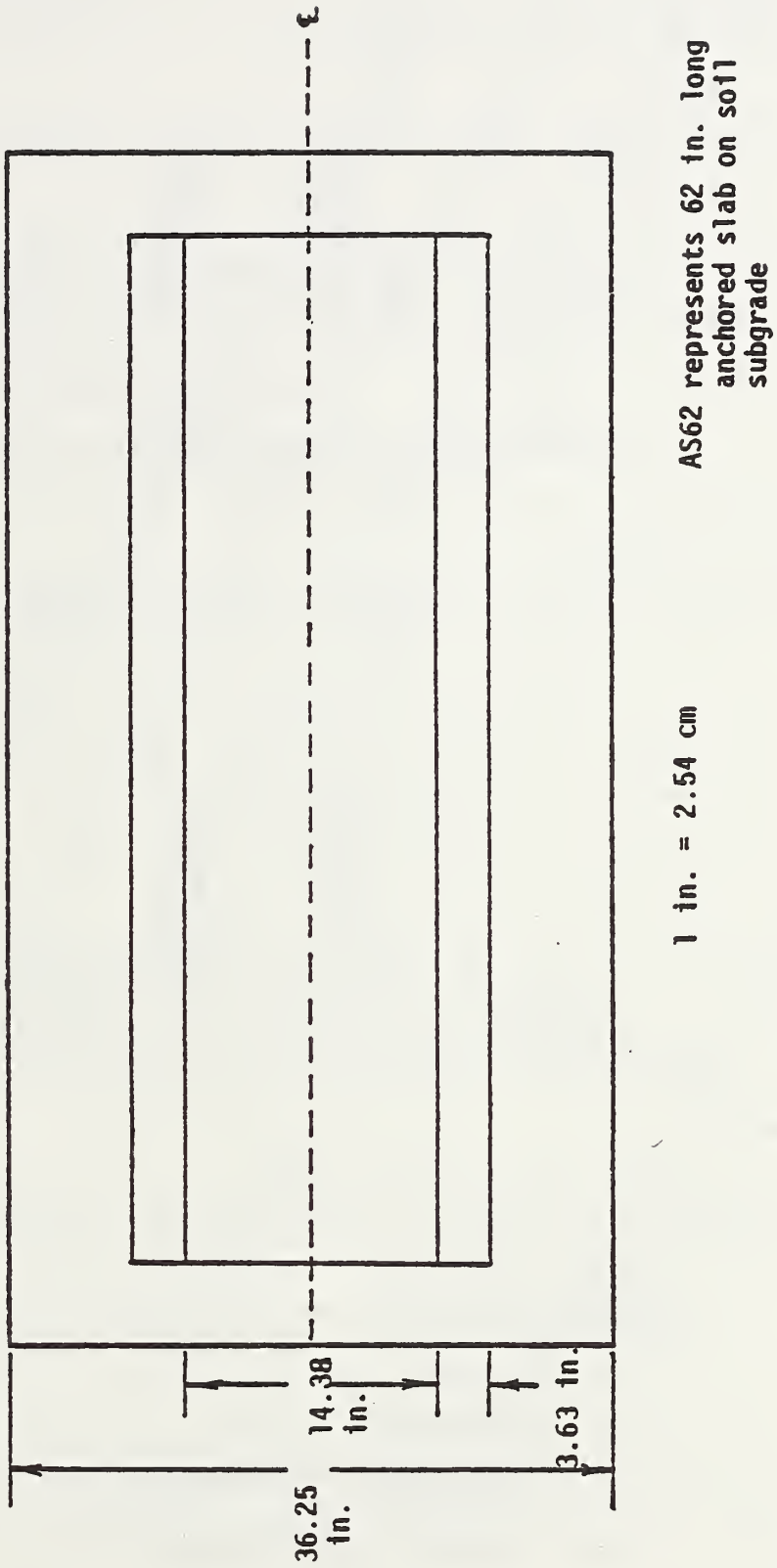
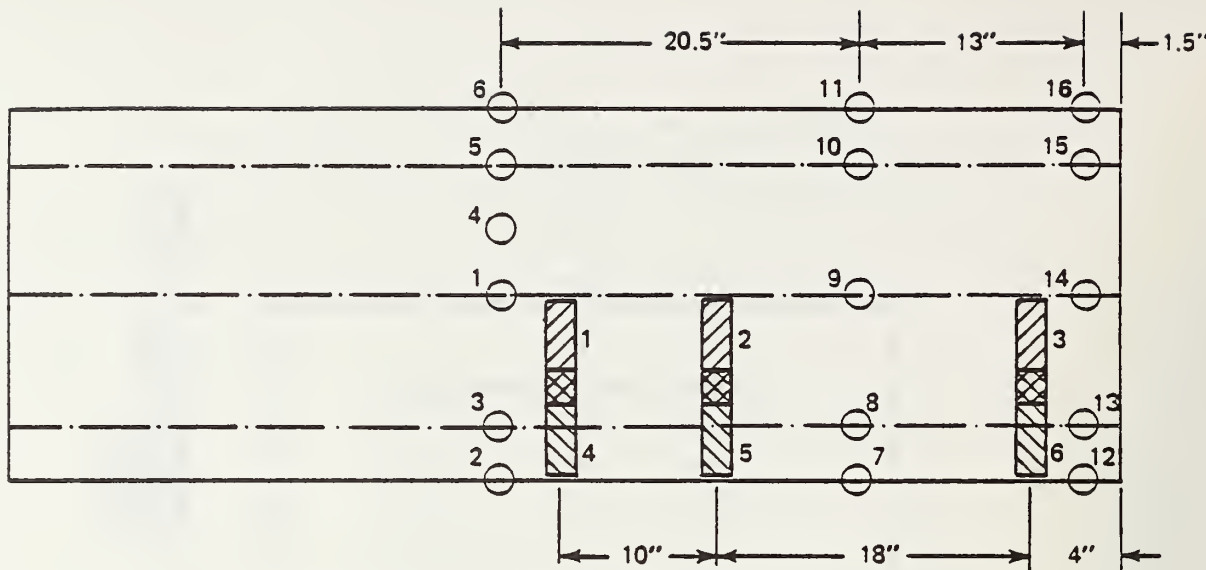
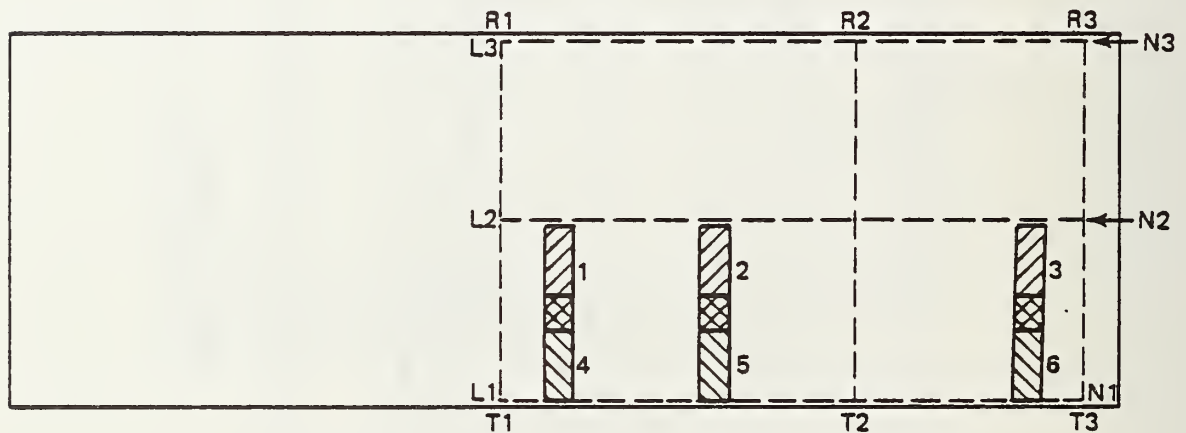


Figure 7. Plan view of AS62 on subgrade



VARIOUS POSITIONS OF LOAD WITH FIXED DIAL GAGES ON
S62, AS62, AND ASE62



VARIOUS POSITIONS OF LOAD AND LOCATION OF LINES
WHERE SURFACE DEFLECTION ARE PLOTTED FOR S62, AS62, AND ASE62

1"=2.54cm

KEY

- CENTERLINE OF ANCHORS
- LINES WHERE SURFACE DEFLECTION HAVE BEEN PLOTTED
- ▨ LOAD POSITION
- ▨▨ LOAD POSITIONS 1 AND 4 , CROSS HATCHED AREAS BEING COMMON
- DIAL GAGES
- S62 REPRESENTS 62" LONG SLAB ON SOIL SUBGRADE
- AS62 REPRESENTS 62" LONG ANCHORED SLAB ON SOIL SUBGRADE
- ASE62 REPRESENTS 62" LONG SLAB ANCHORED SLAB ELEVATED 0.5" ON SOIL SUBGRADE

Figure 8. VARIOUS POSITIONS OF LOAD, DIAL GAGES, AND SURFACE DEFLECTIONS

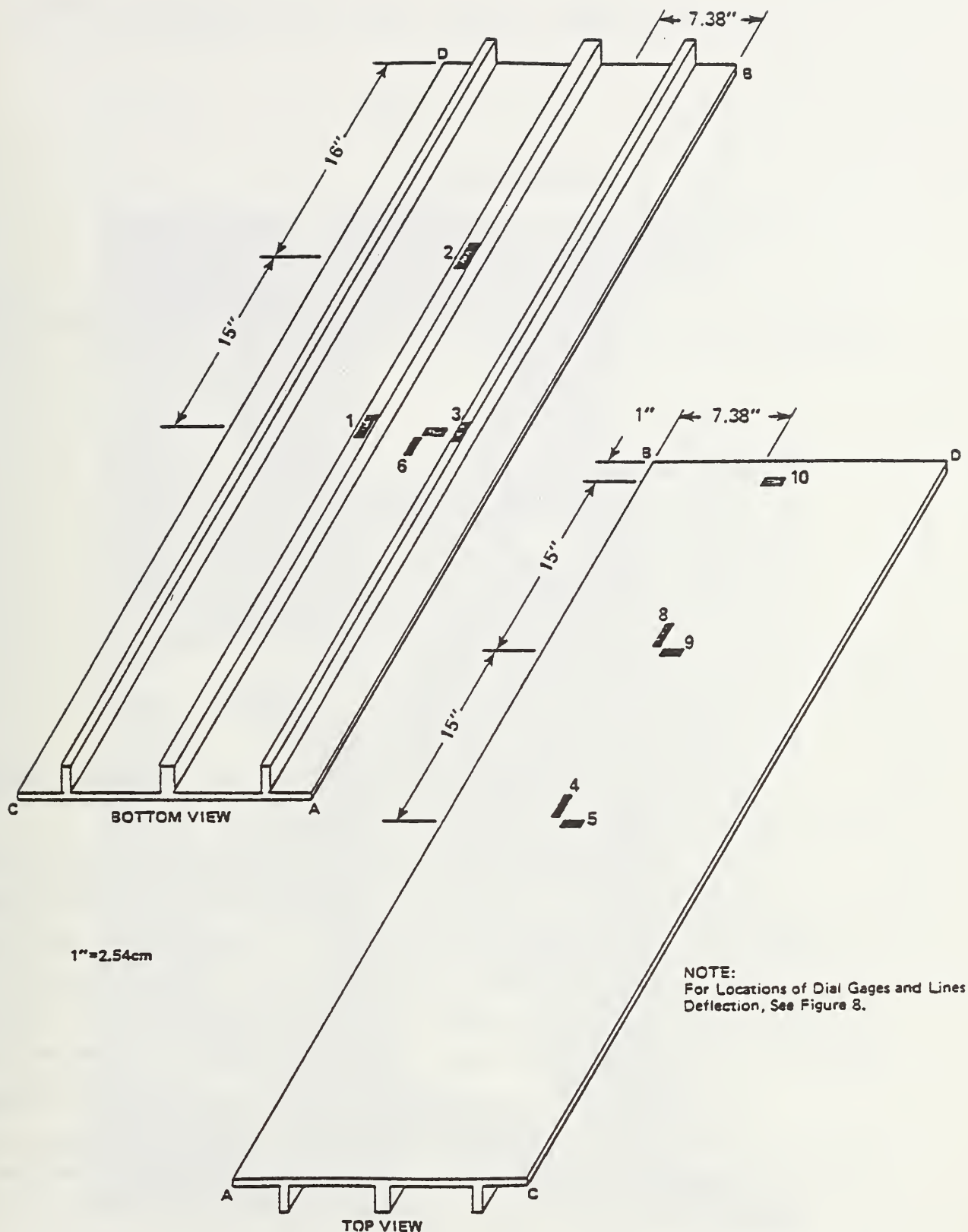


Figure 9 . POSITION OF FOIL GAGES ON ANCHORED SLAB

The stresses (Desai and Abel, 1972) can be computed as follows:

$$\begin{bmatrix} \sigma_x \\ \sigma_y \\ \sigma_z \end{bmatrix} = \frac{E}{(1+v)(1-2v)} \begin{bmatrix} 1-v & v & v \\ v & 1-v & v \\ v & v & 1-v \end{bmatrix} \begin{bmatrix} \epsilon_x \\ \epsilon_y \\ \epsilon_z \end{bmatrix} \quad 1$$

The bending moments (Popov, 1968) can be also computed from the stresses as:

$$\begin{bmatrix} M_x \\ M_y \\ M_z \end{bmatrix} = \frac{1}{c} \begin{bmatrix} \sigma_z & I_{xy} \\ \sigma_x & I_{yz} \\ \sigma_y & I_{zx} \end{bmatrix} \quad 2$$

where

c = distance of foil gages from the neutral axis.

The modulus of elasticity of the aluminum used was 10.5×10^6 psi (738.150 kg/cm²) and the Poisson's ratio was 0.33.

A "line preloading" was initially used at the center, quarter distances, and edges of the anchored slab. The preloading was considered necessary to prevent loss of contact between the anchored slab and the soil and to bring the soil within the elastic range. The preloading is shown in Figure 10. The hysteresis loops (load versus deflection) for loads at the center, and at the two edges of the anchored slab are shown in Figures 11, 12, and 13 respectively.

The deflection at the loading point was measured from dial gage No. 1. After preloading and ensuring that the soil was in the elastic range, the deflection measuring dial gages were placed. Dial gages Nos. 1 and 13 measured 0.0001 in. (0.003 mm) per division; Nos. 11 and 15 measured 0.0005 in. (0.013 mm) per division, and the others measured 0.001 in. (0.025 mm) per division.

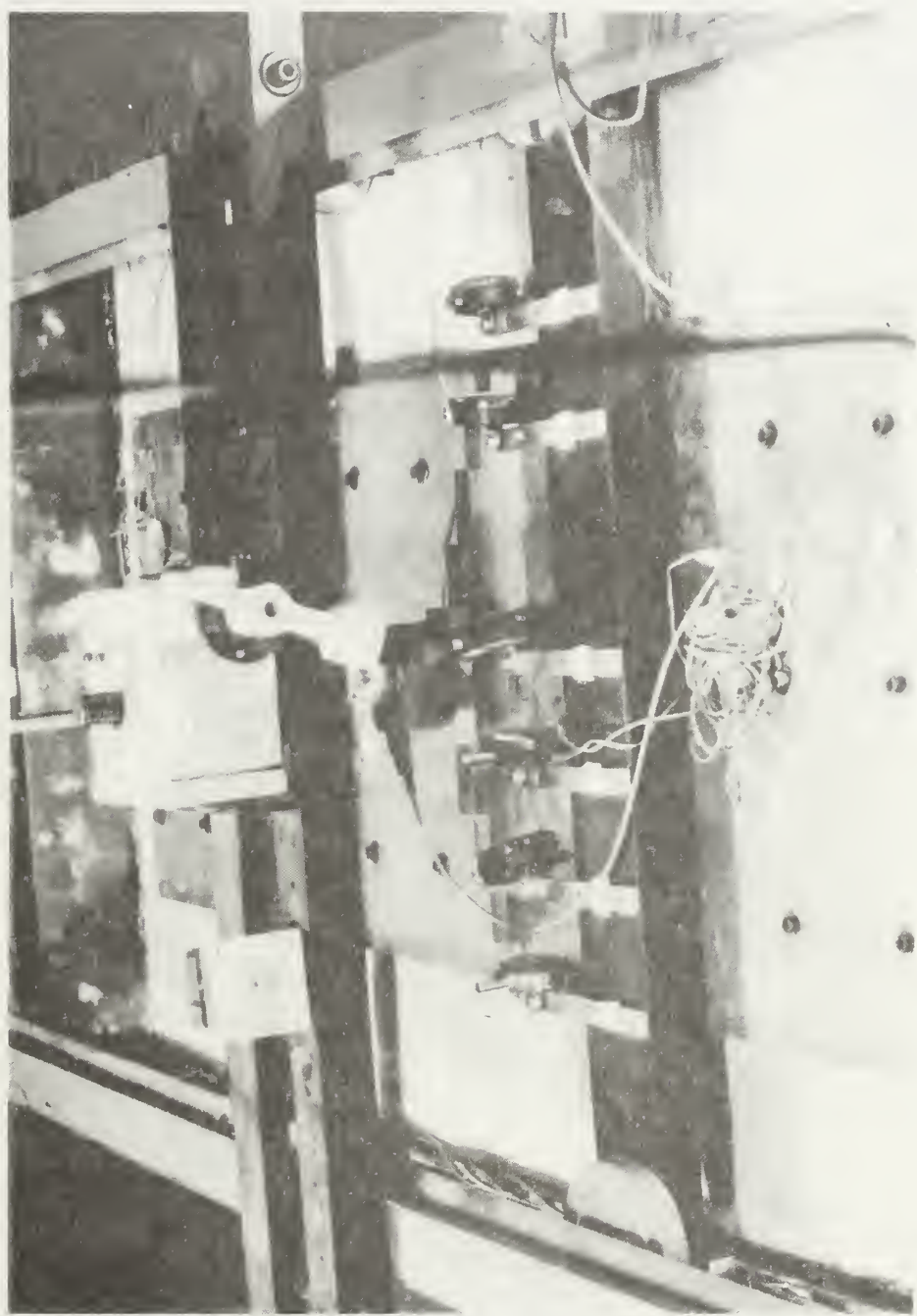


Figure 10. Preloading by a line load.

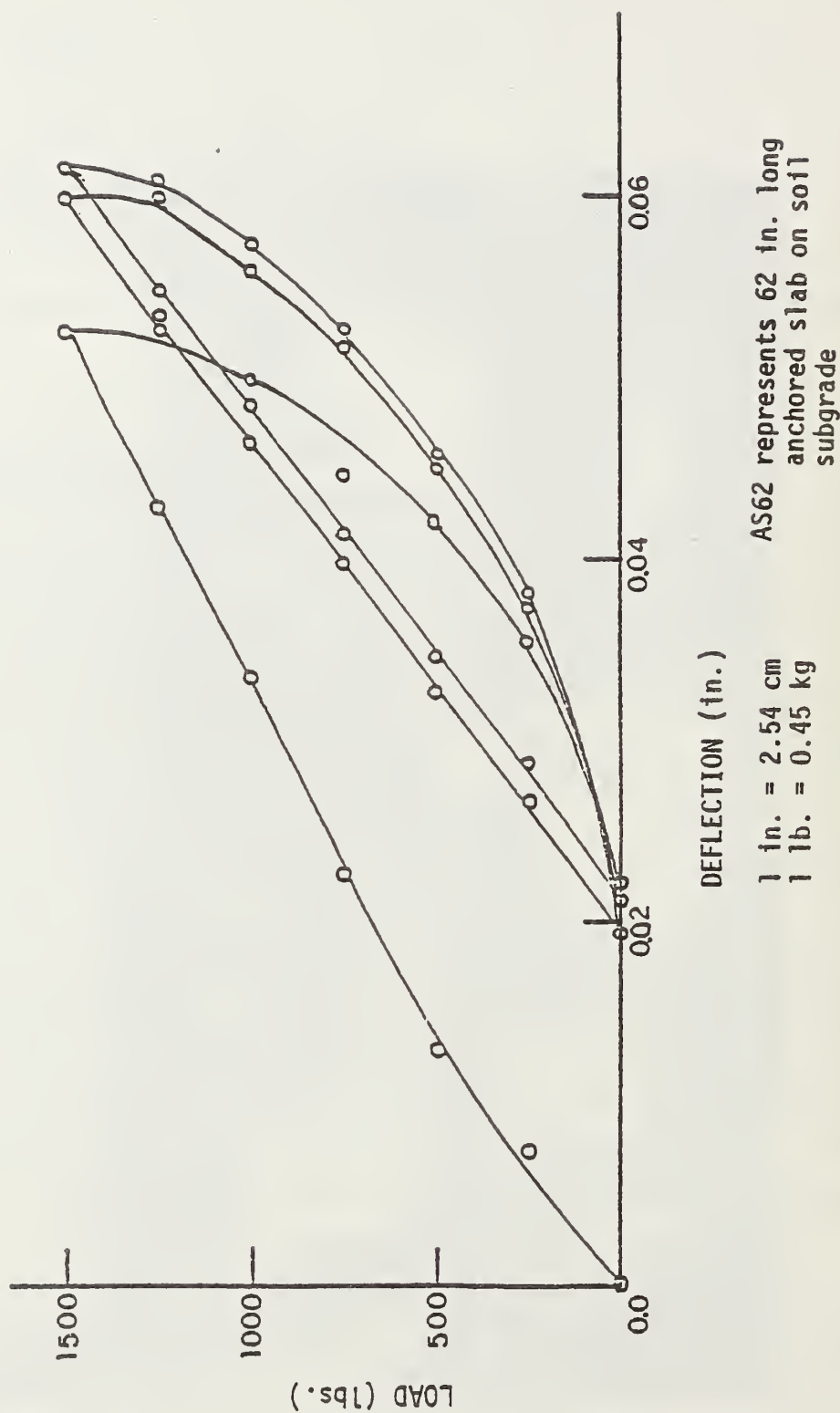


Figure 11. Load versus deflection curve for line preloading at center of AS62.

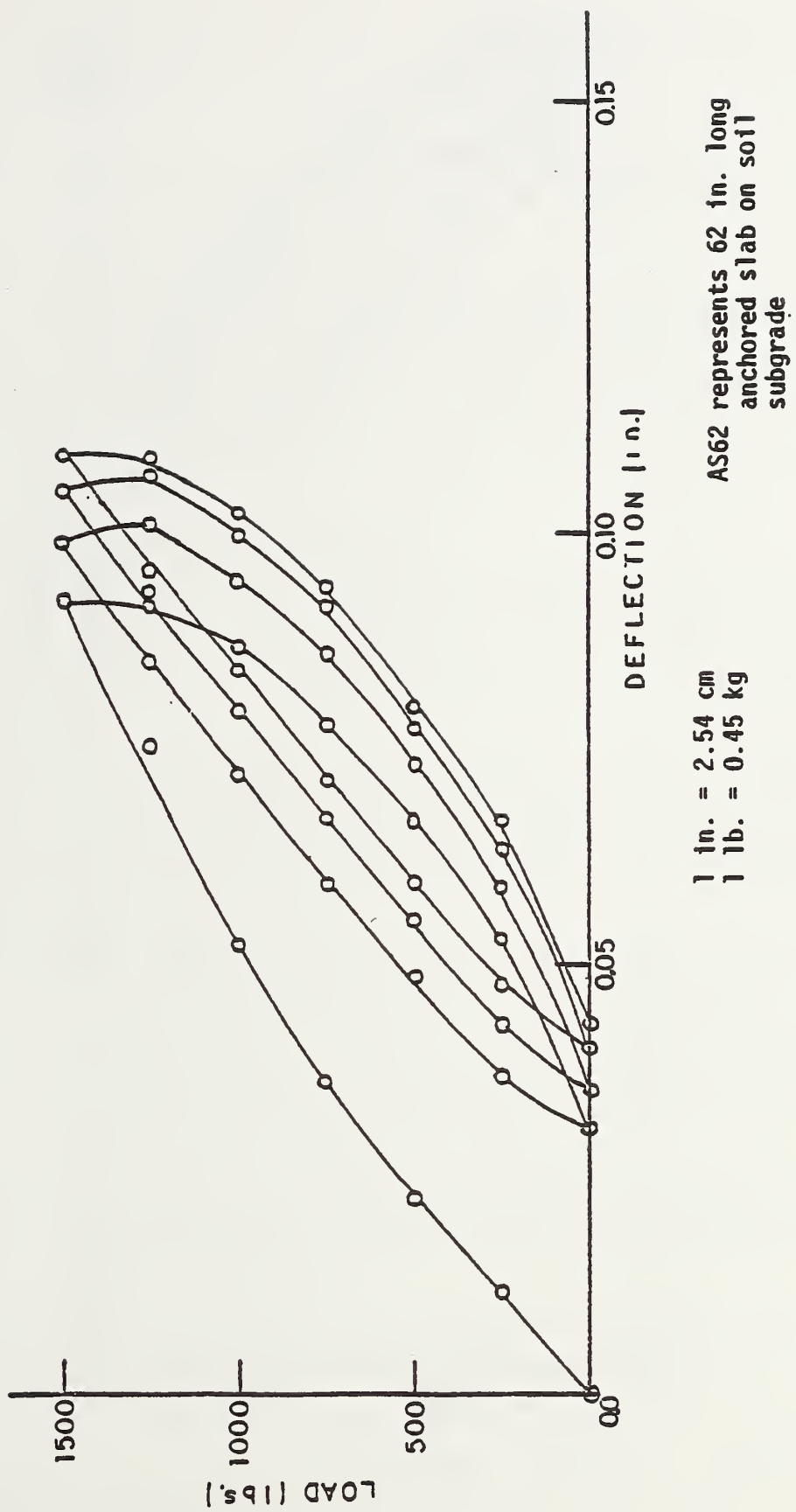


Figure 12. Load versus deflection curve for line preloading at left edge of AS62.

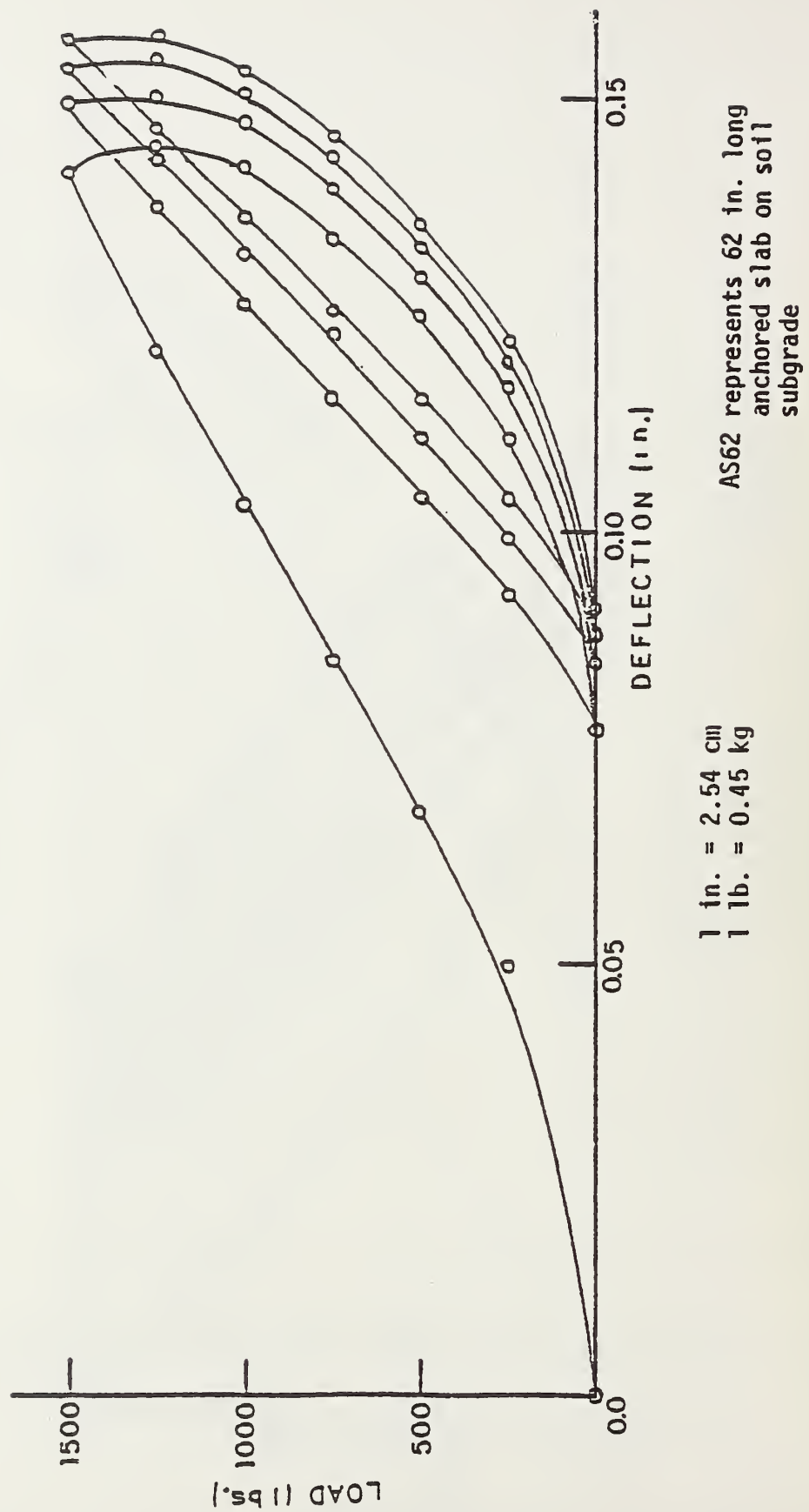


Figure 13. Load versus deflection curve for line preloading at right edge of AS62.

Six load positions were used to investigate the response of a "continuous pavement" and of pavement at a joint with zero transfer load (Figure 8). Figures 14, 15, and 16 show various loading configurations.

Longitudinal (L1-N1, L2-N2, L3-N3) and transverse (T1-R1, T2-R2, T3-R3) surface deflection lines for load at position 1 and position 3 were plotted in Figures 19 through 30.

The load increment was 250 lb. (113.4 kg) although the maximum load applied was 1500 lb. (680.4 kg). The resulting deflections are tabulated; the plots only show the deflection for 250-lb. (113.4 kg), 500-lb. (227 kg), and 750-lb. (340 kg) loads. The measured strains are shown in Appendix A, Tables 5 through 16.

2.3.2 Conventional Slab on Subgrade - S62

Soil placement and compaction procedures were similar to those for AS62. Great effort was made to level and surface the top layer. The slab was then placed, and the remaining soil surface was covered by oil and plastic sheets as previously described.

Deflections were measured at 16 locations, as shown in Figure 8. Load positions and the sections where deflections are plotted are shown in Figure 8. Six foil gages were attached on top of the slab, and four were attached on the bottom of the slab (Figure 17).

The preloading system was then mounted at the center of the slab. The dial gage No. 1 was placed to measure the surface deflection beneath the load. The maximum load applied was 750 lb. (340 kg) with increments (or decrements) of 250 lb. (113.4 kg). Figure 18 shows the load versus deflection relation for three cycles of loadings at the center of the slab.

Subsequent loading did not produce any appreciable change in the hysteresis loop. Similar hysteresis loops were derived for line preloading at the left and right edges of the slab.

The slab subgrade system was also preloaded at the left and right intermediate sections. After the preloading, the regular loading was applied. A maximum load of 750 lb. (340 kg) (load increment, 250 lb. = 113.4 kg) was used at six locations (Figure 8). Tables II through 16 (Appendix A) contain measured strains for the six load positions.

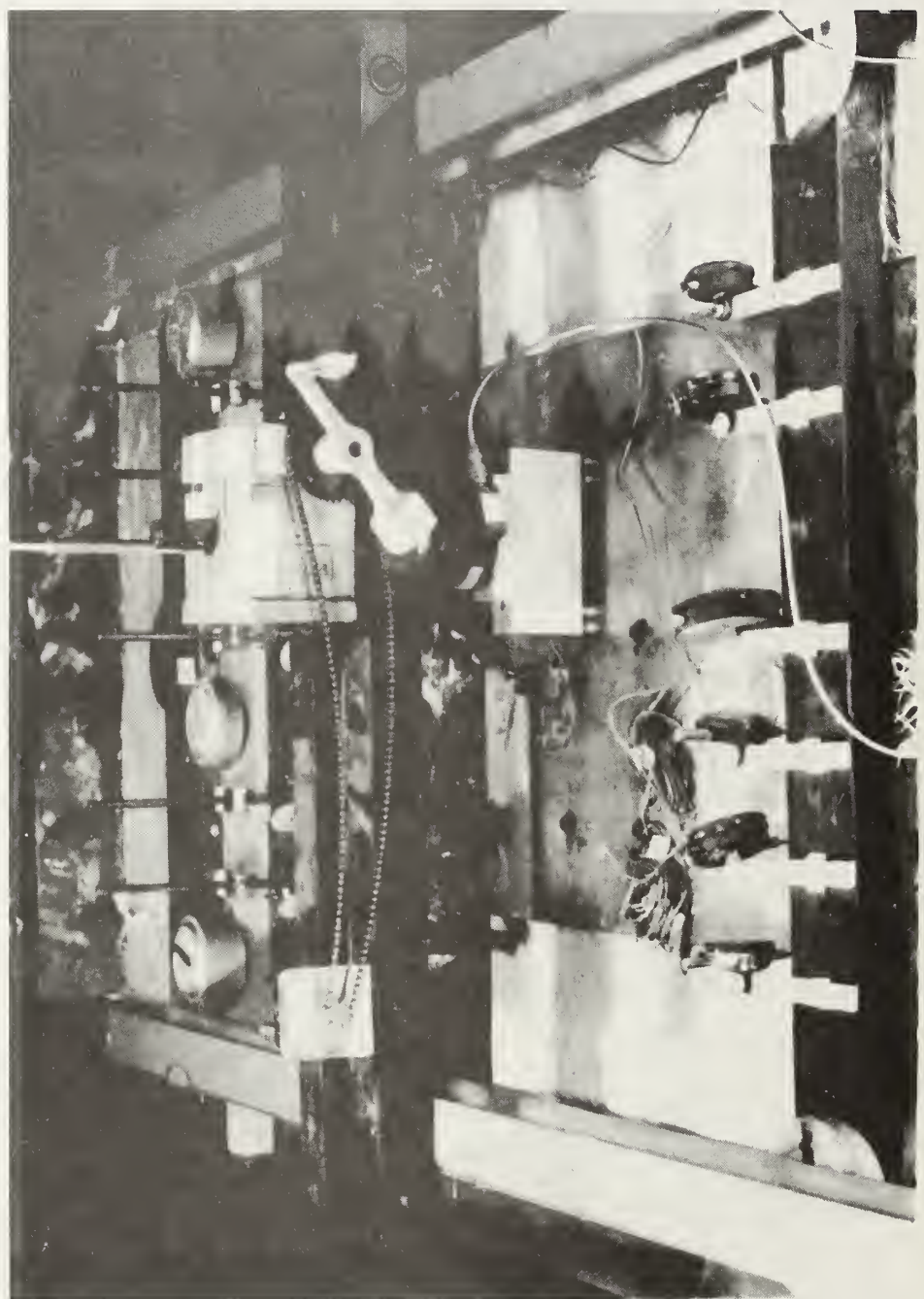
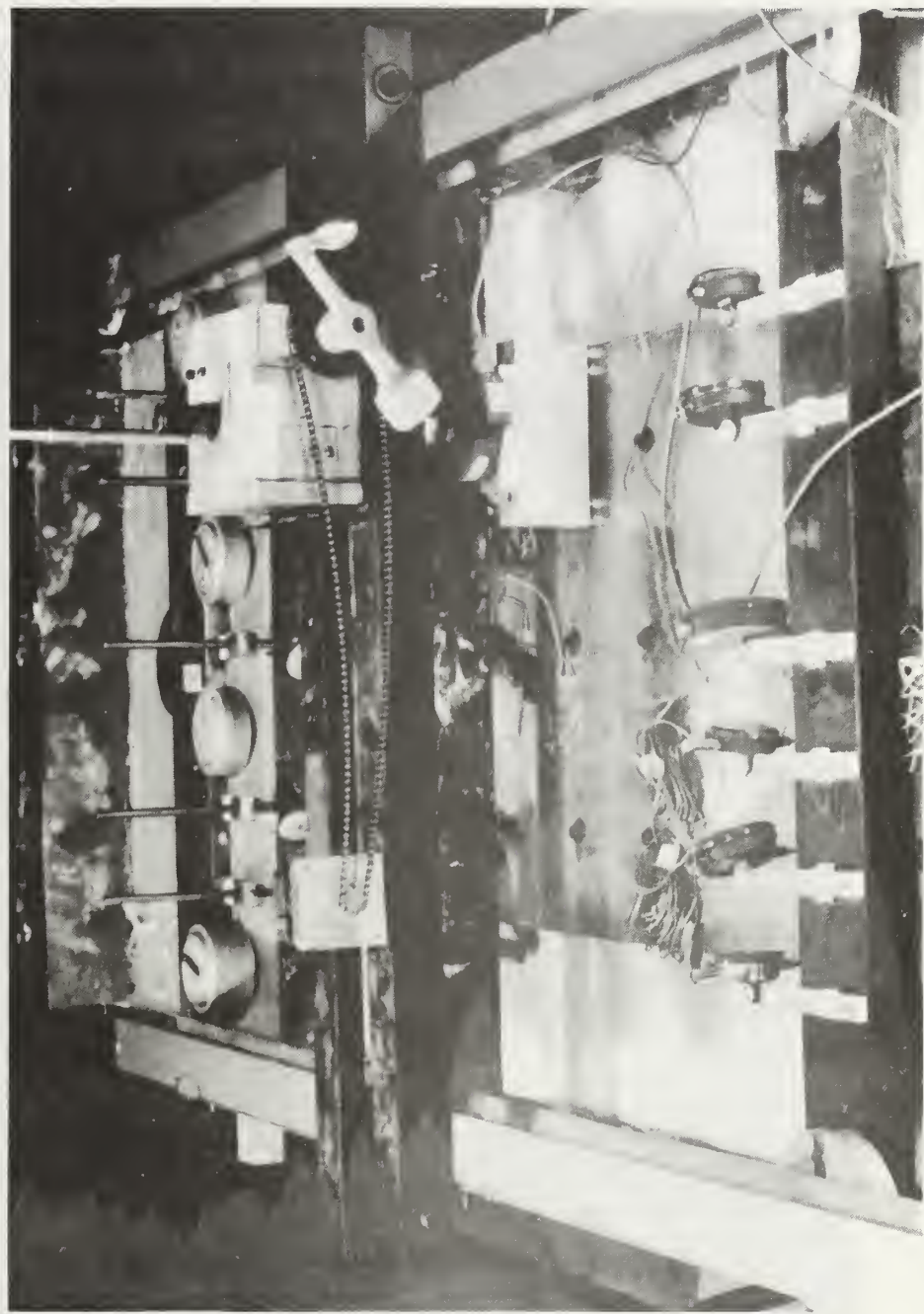


Figure 14. Load at center -- traffic lane.

Figure 15. Load at center -- shoulder lane.



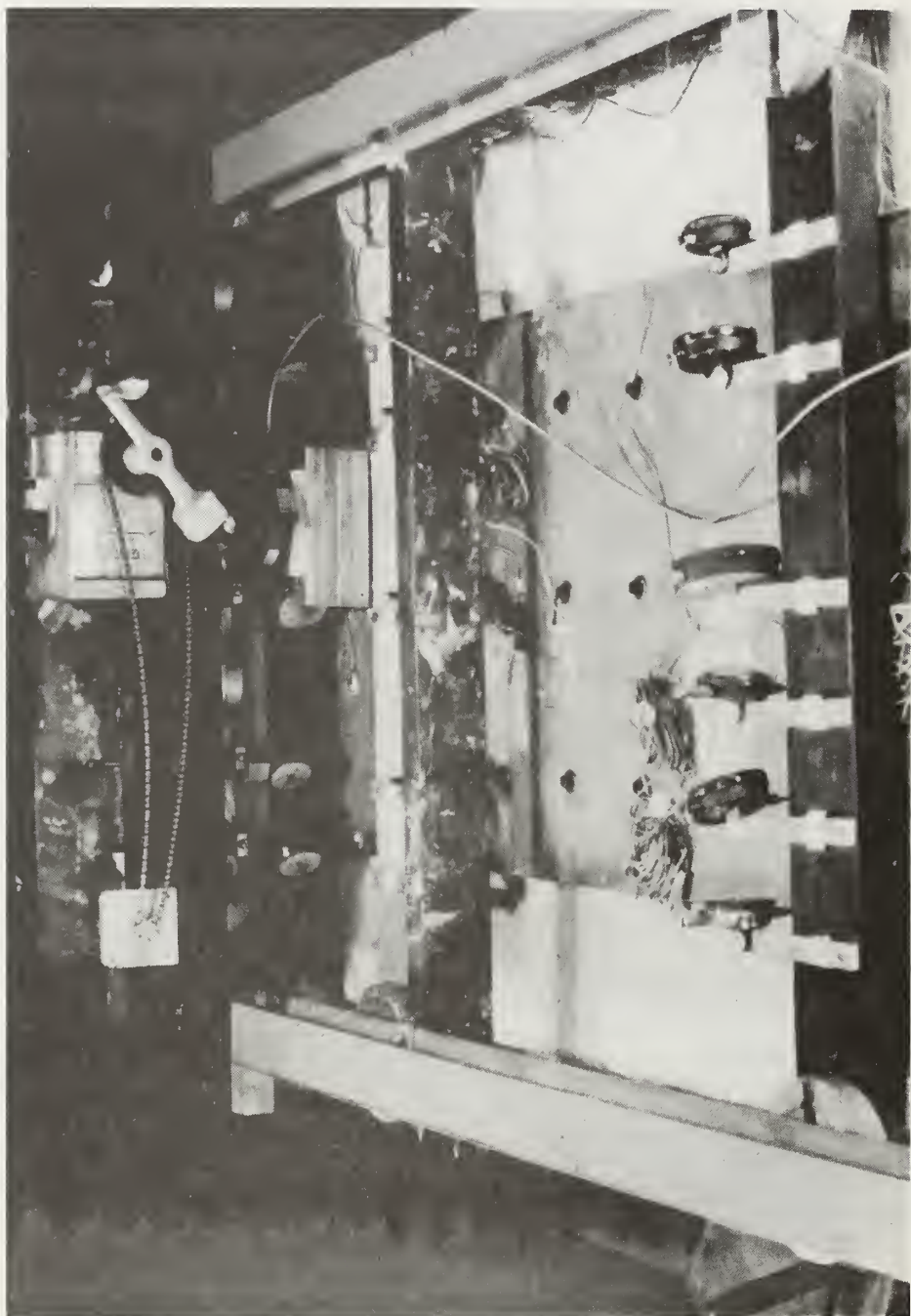


Figure 16. Load at edge -- traffic lane.

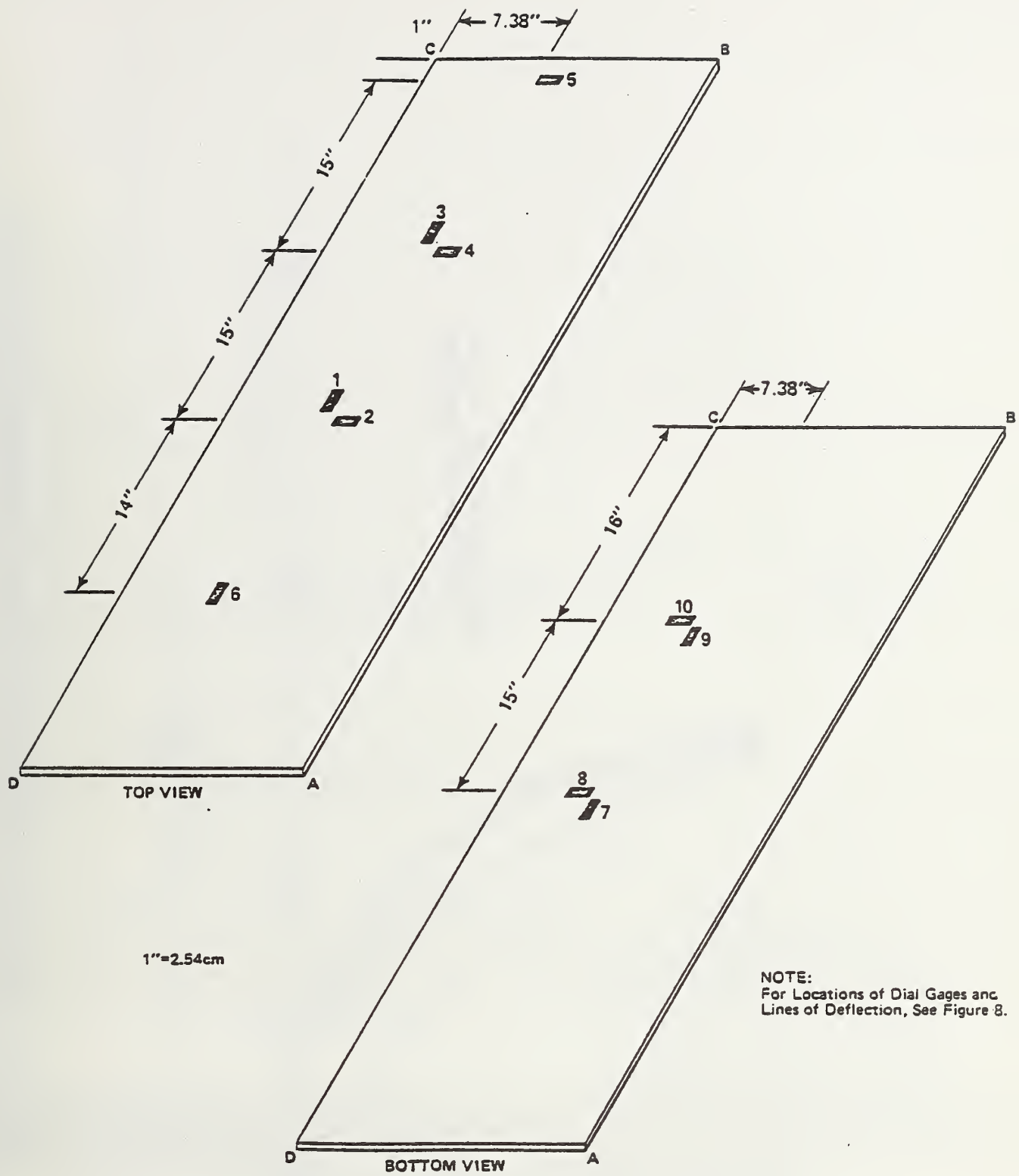


Figure 17. POSITION OF FOIL GAGES ON CONVENTIONAL SLAB

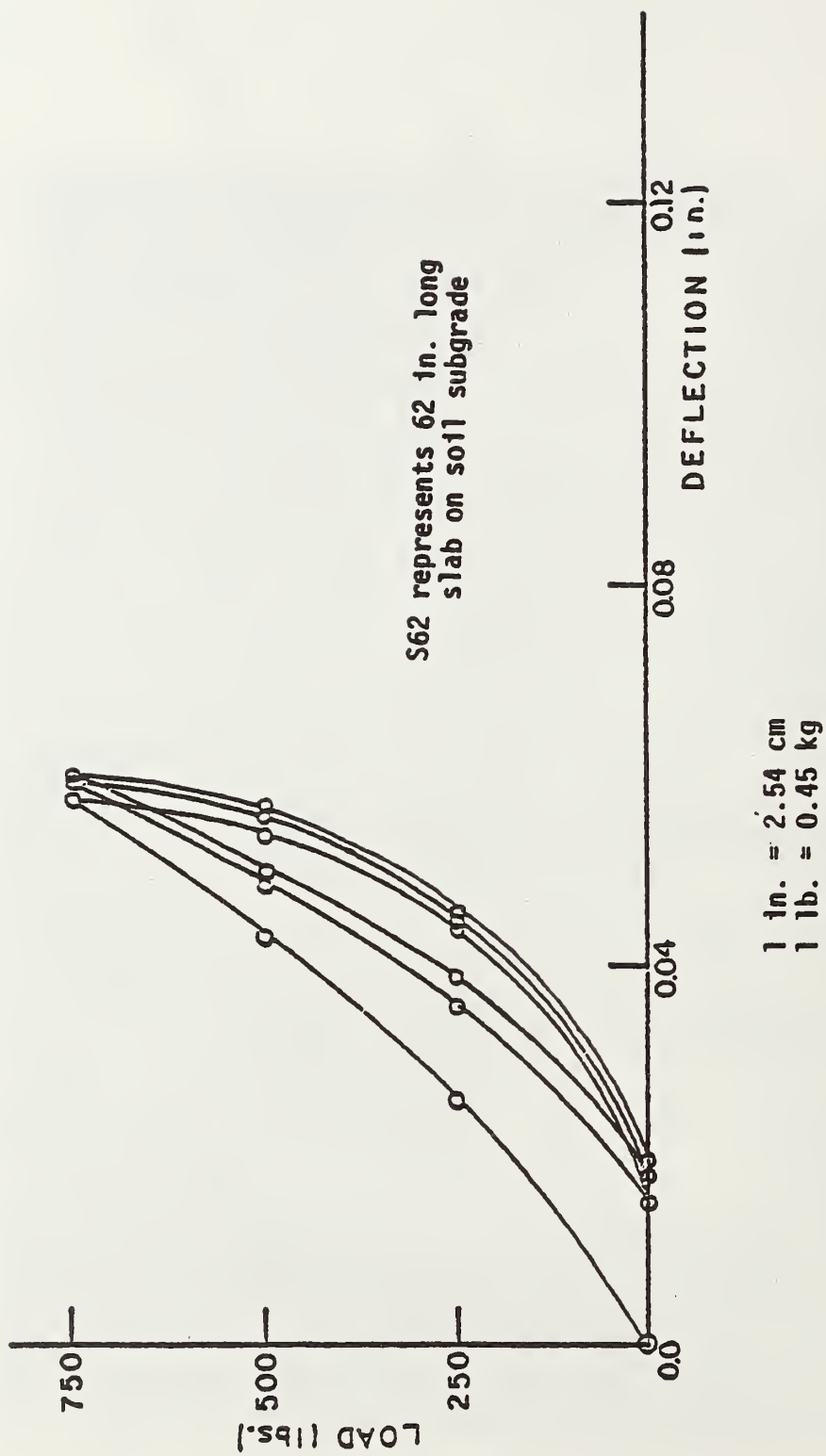


Figure 18. Load versus deflection curve for line preloading at center of S62.

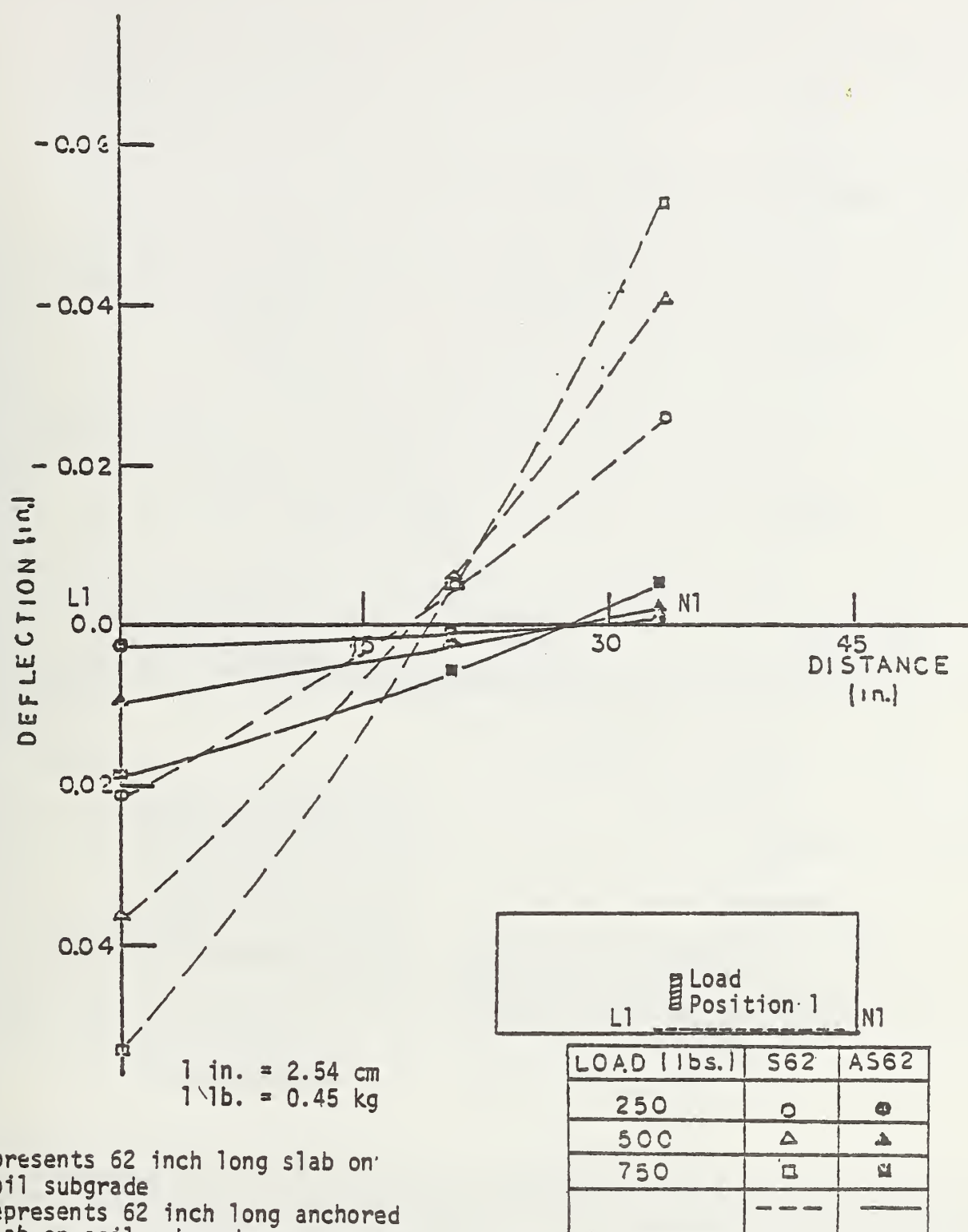
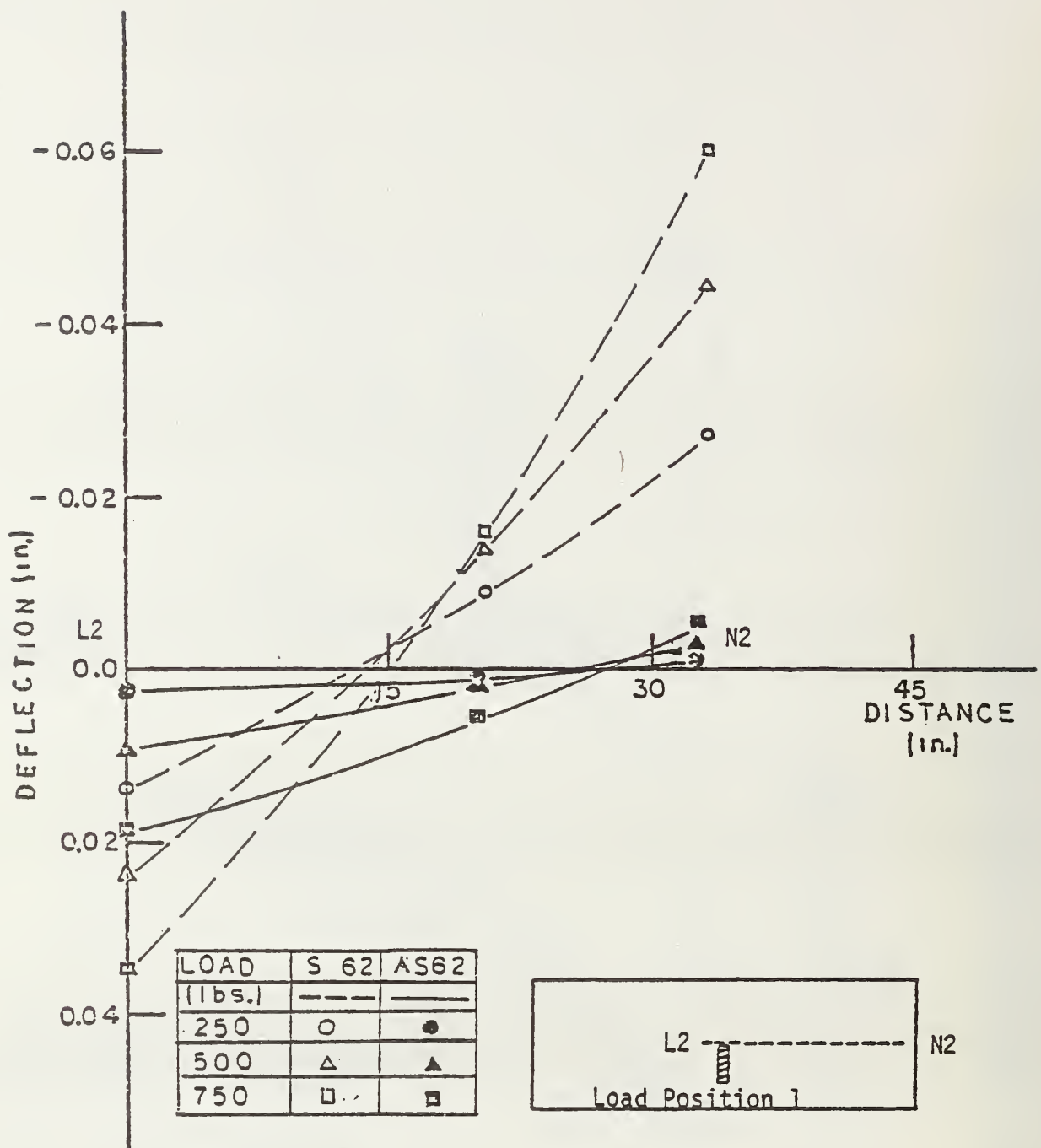


Figure 19. Longitudinal surface deflection along line L1-N1, load position 1, S62 - AS62.



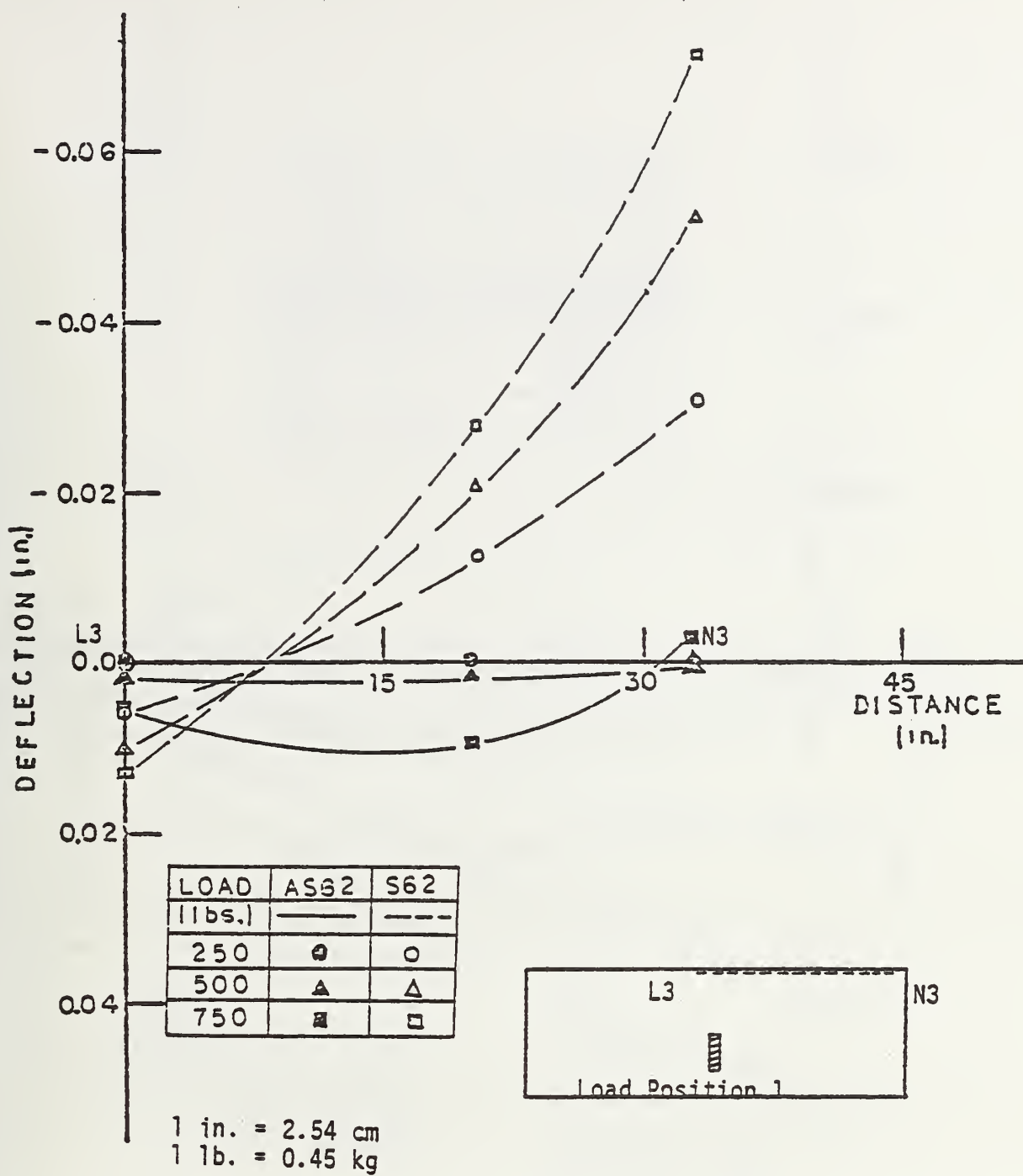
1 in. = 2.54 cm.

1 lb. = 0,45 kg

S62 represents 62 inch long slab on
soil subgrade

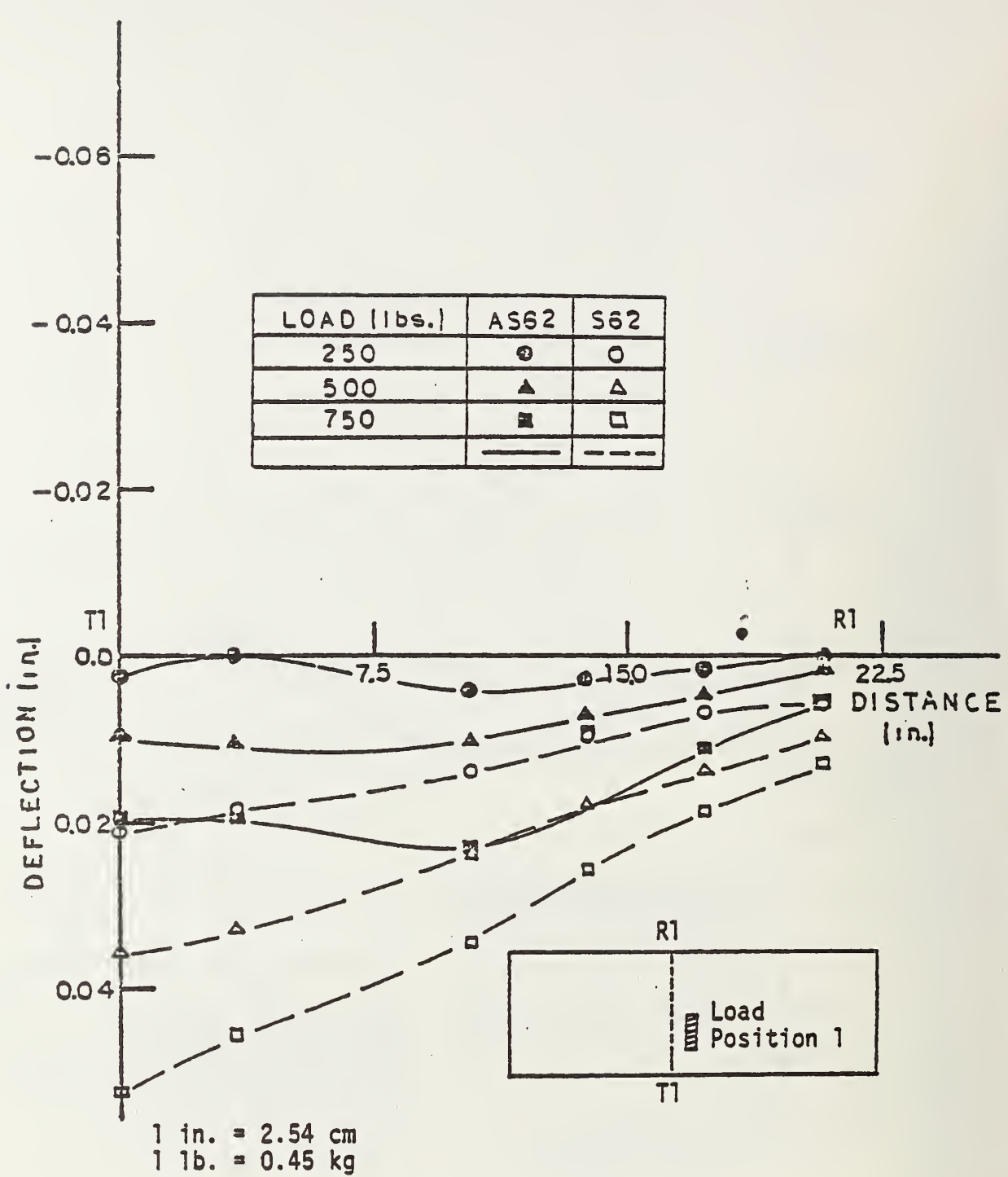
AS62 represents 62 inch long anchored slab on soil subgrade

Figure 20. Longitudinal surface deflection along line L2-N2,
load position 1, S62 - AS62.



S62 represents 62 inch long slab on
soil subgrade
AS62 represents 62 inch long anchored
slab on soil subgrade

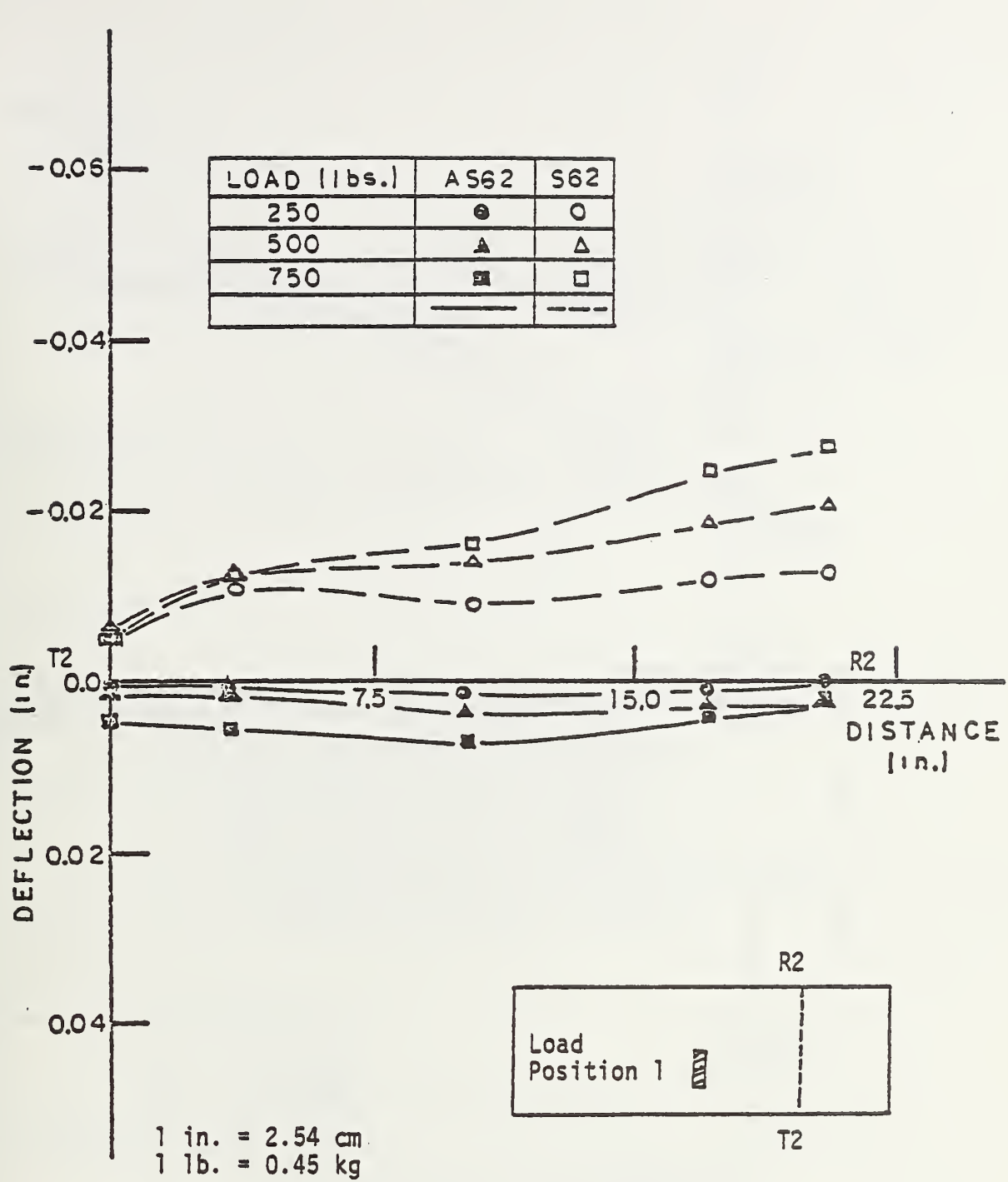
Figure 21. Longitudinal surface deflection along line L3-N3, load position 1, S62 - AS62.



S62 represents 62 inch long slab on soil subgrade

AS62 represents 62 inch long anchored slab on soil subgrade

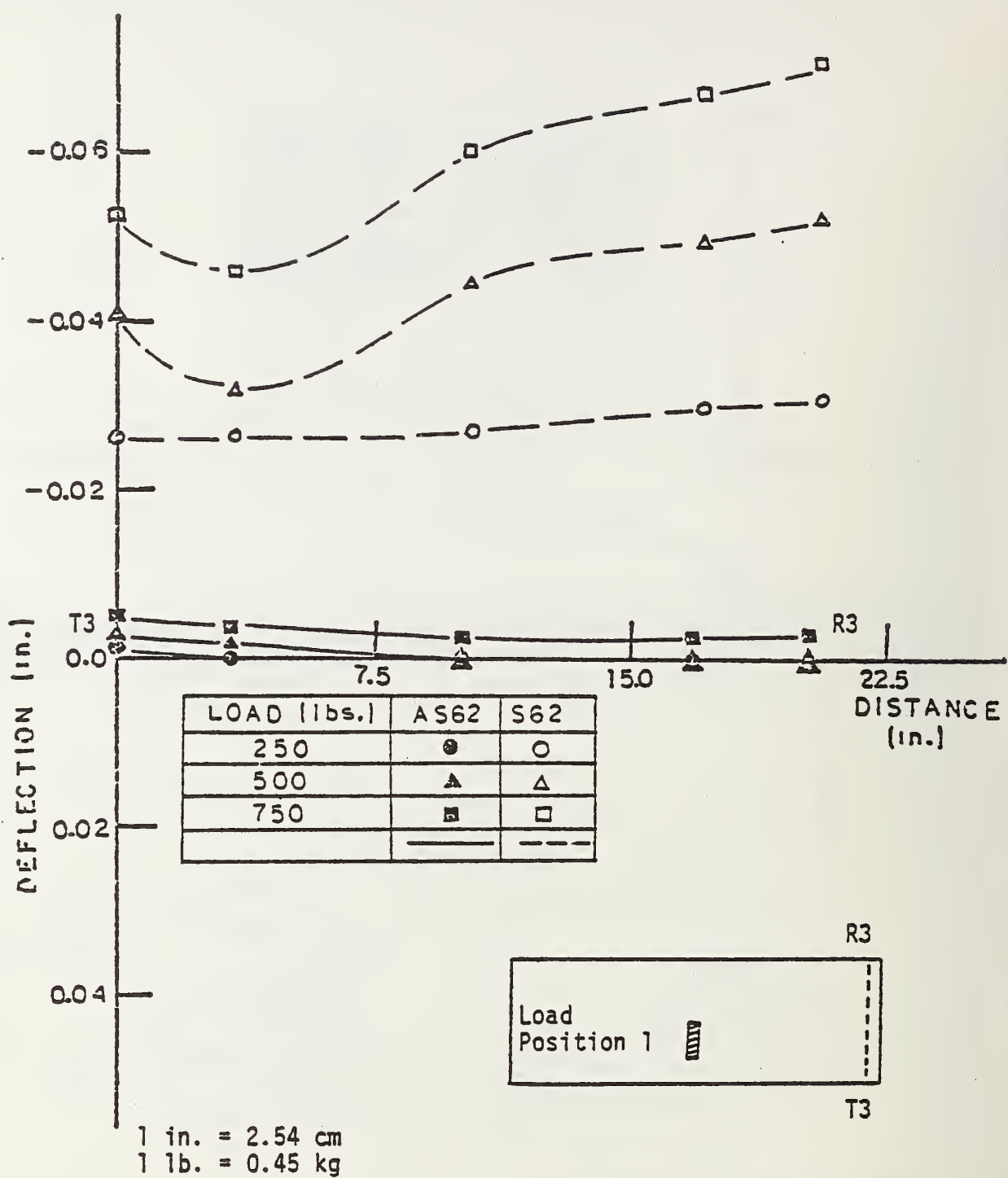
Figure 22. Transverse surface deflection along line T1-R1, load position 1, S62 - AS62.



S62 represents 62 inch long slab on soil subgrade

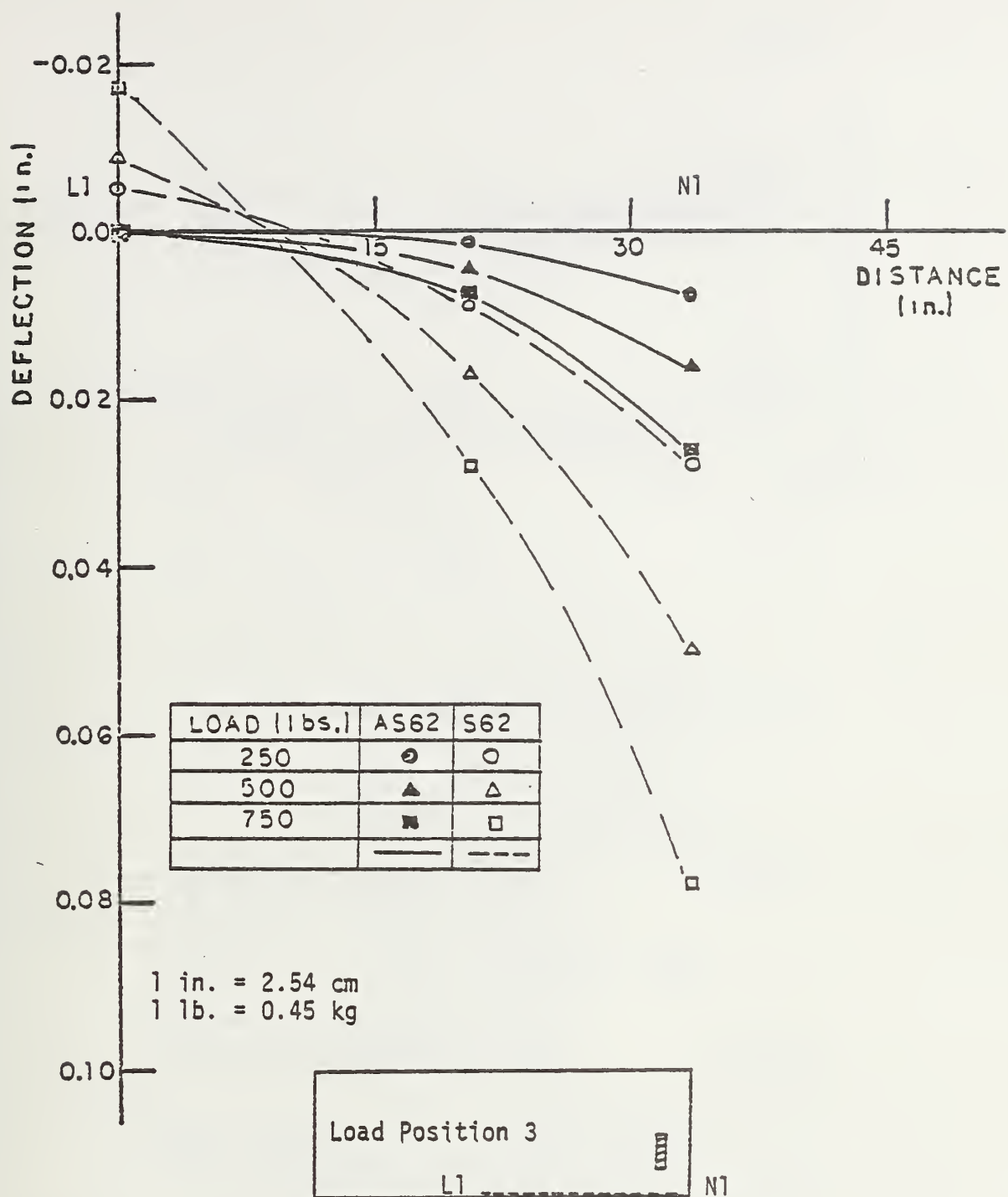
AS62 represents 62 inch long anchored slab on soil subgrade

Figure 23. Transverse surface deflection along line T2-R2, load position 1, S62 - AS62.



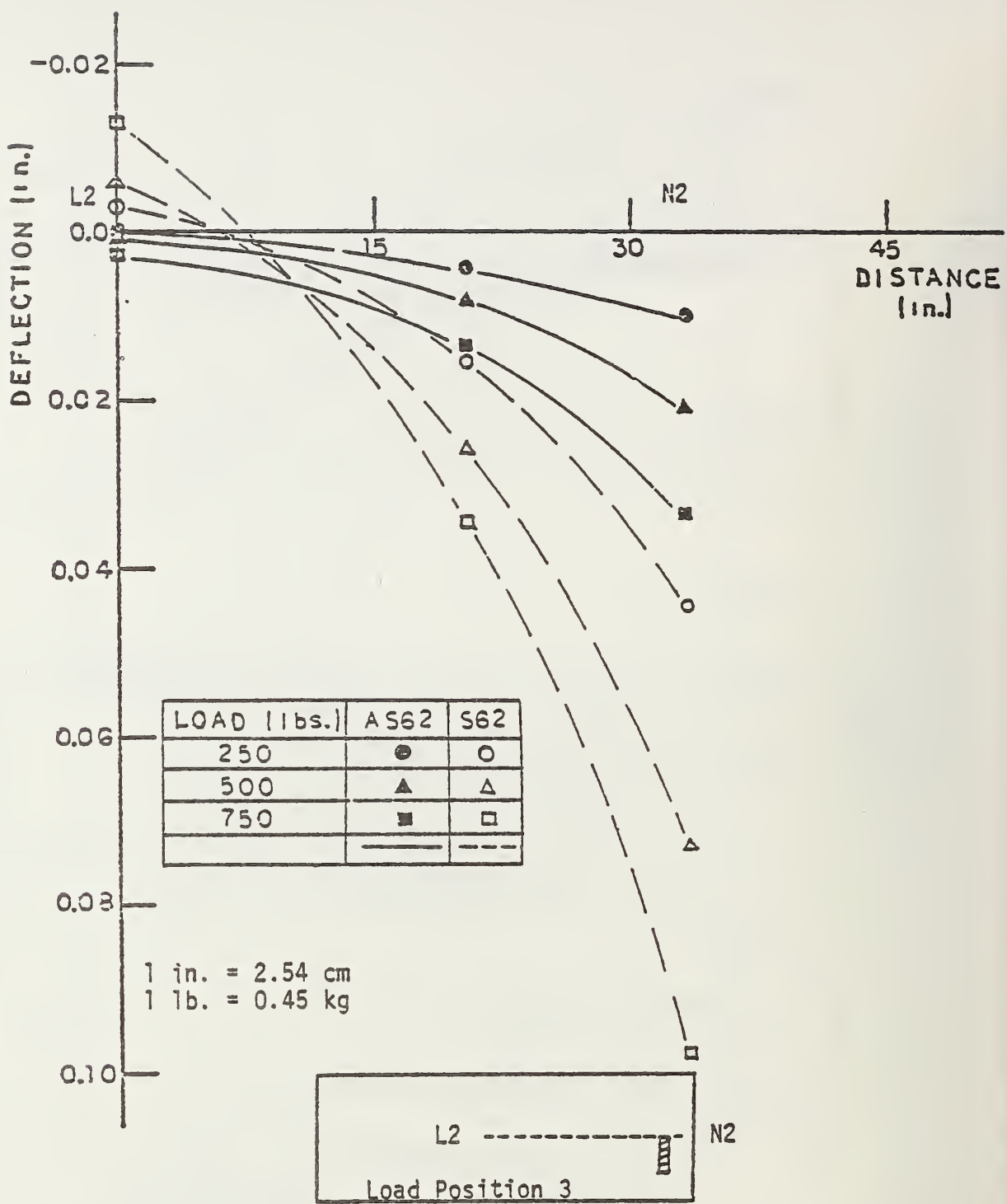
S62 represents 62 inch long slab on
soil subgrade
AS62 represents 62 inch long anchored
slab on soil subgrade

Figure 24. Transverse surface deflection along line T3-R3,
load position 1, S62 - AS62.



S62 represents 62 inch long slab on
soil subgrade
AS62 represents 62 inch long anchored
slab on soil subgrade

Figure 25. Longitudinal surface deflection along line L1-N1,
load position 3, S62 - AS62.



S62 represents 62 inch long slab on
soil subgrade
AS62 represents 62 inch long anchored
slab on soil subgrade

Figure 26. Longitudinal surface deflection along line L2-N2,
load position 3, S62 - AS62.

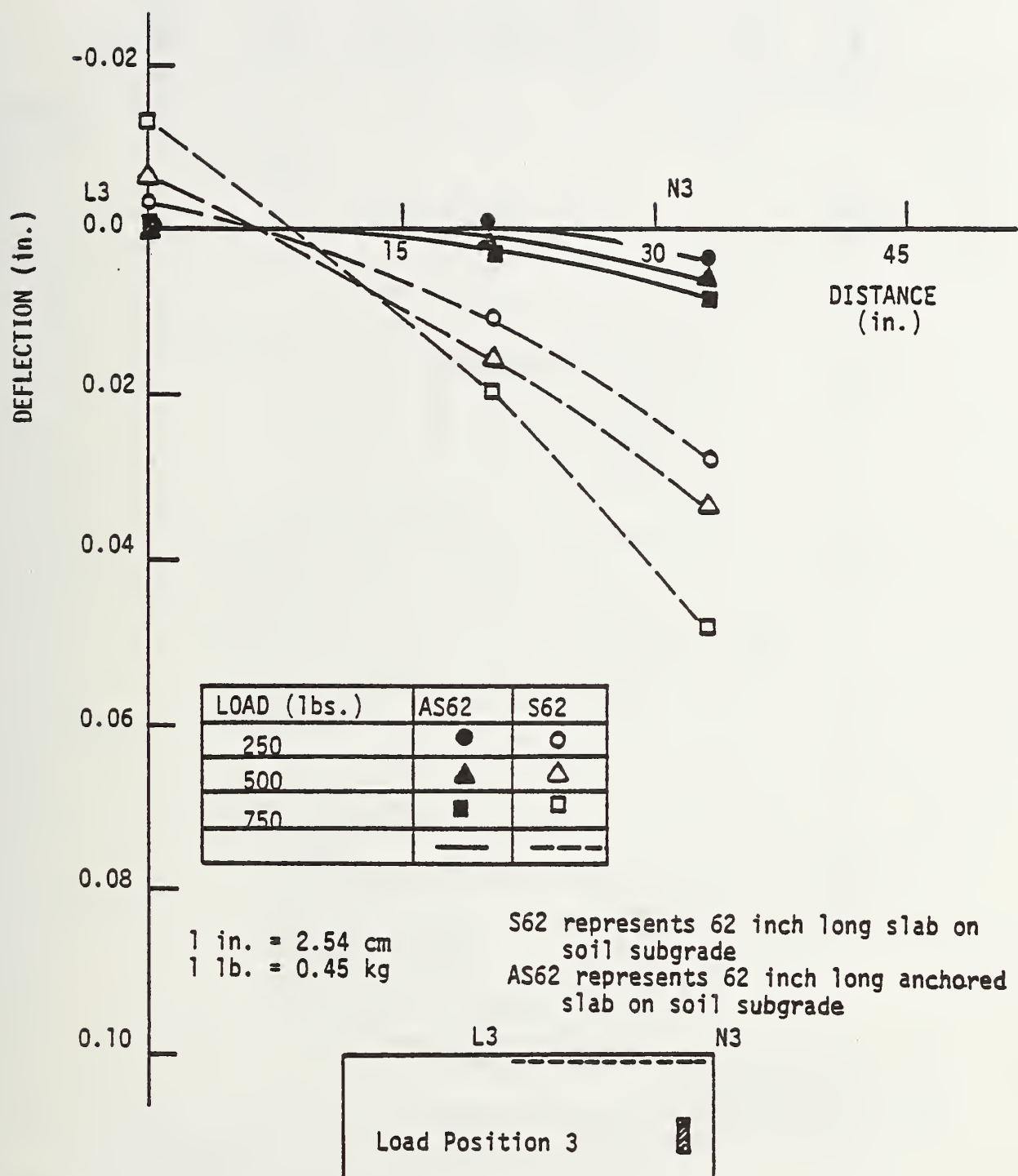
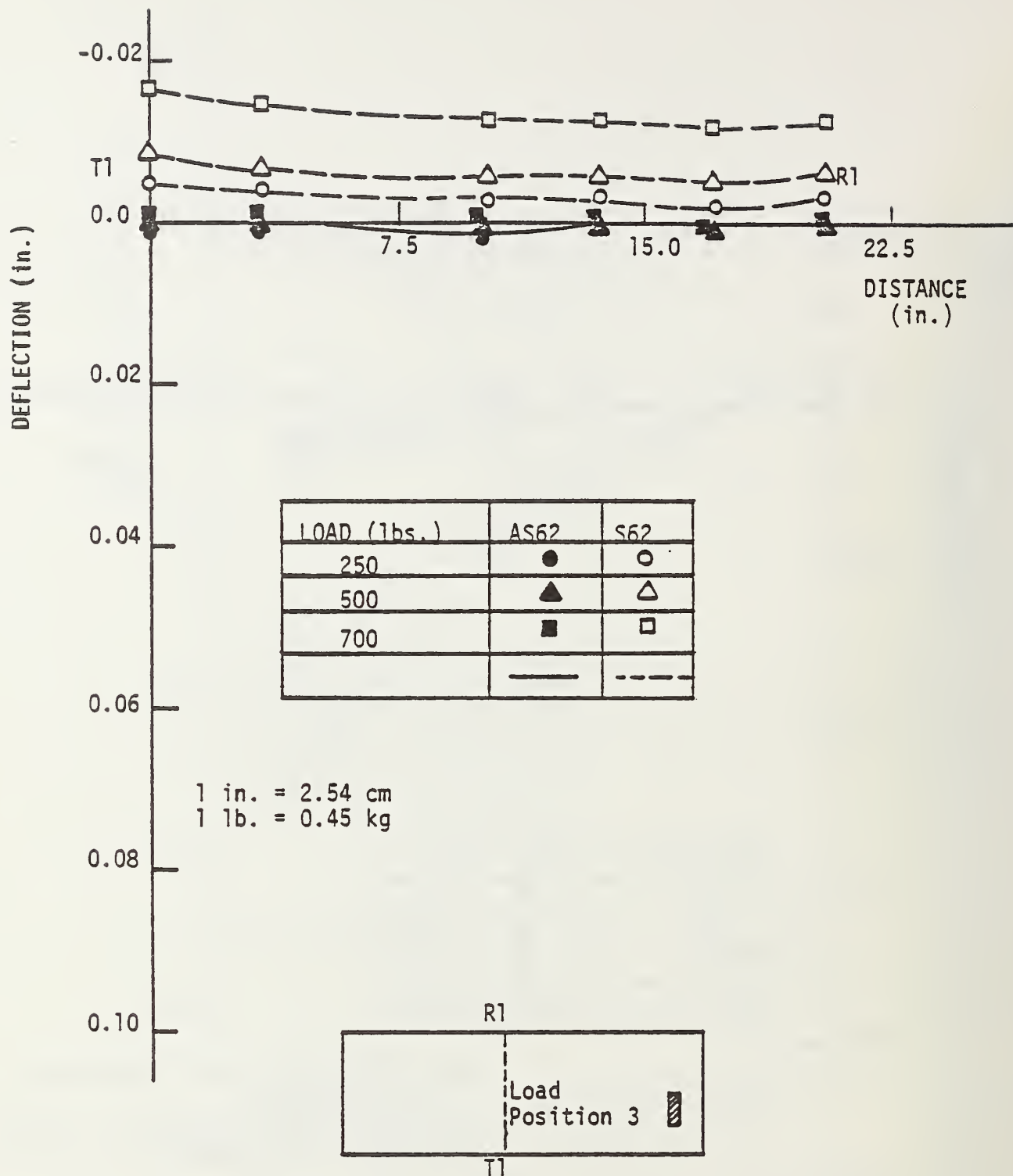


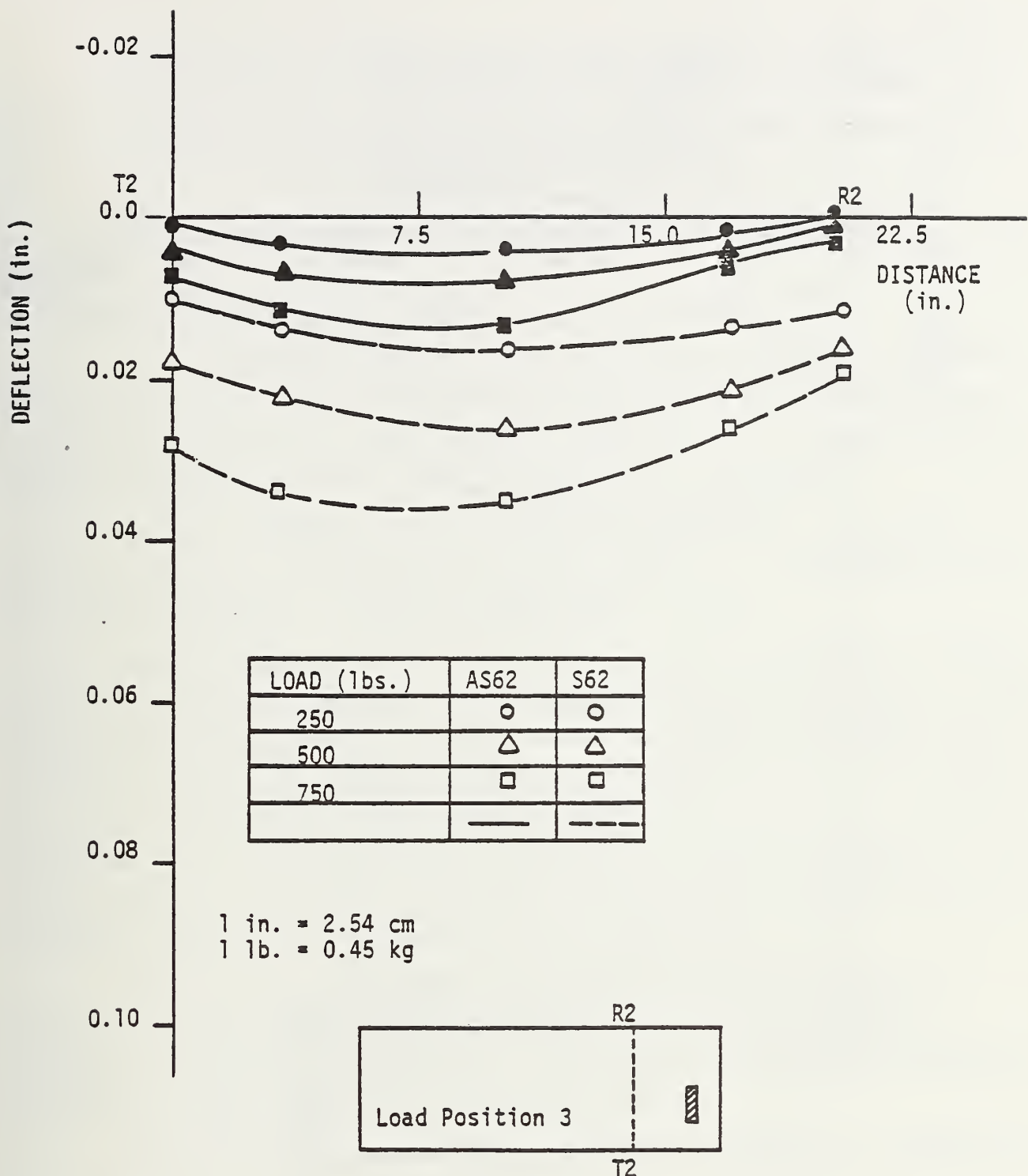
Figure 27. Longitudinal surface deflection along line L3-N3, load position 3, S62-AS62.



S62 represents 62 inch long slab on soil subgrade

AS62 represents 62 inch long anchored slab on soil subgrade

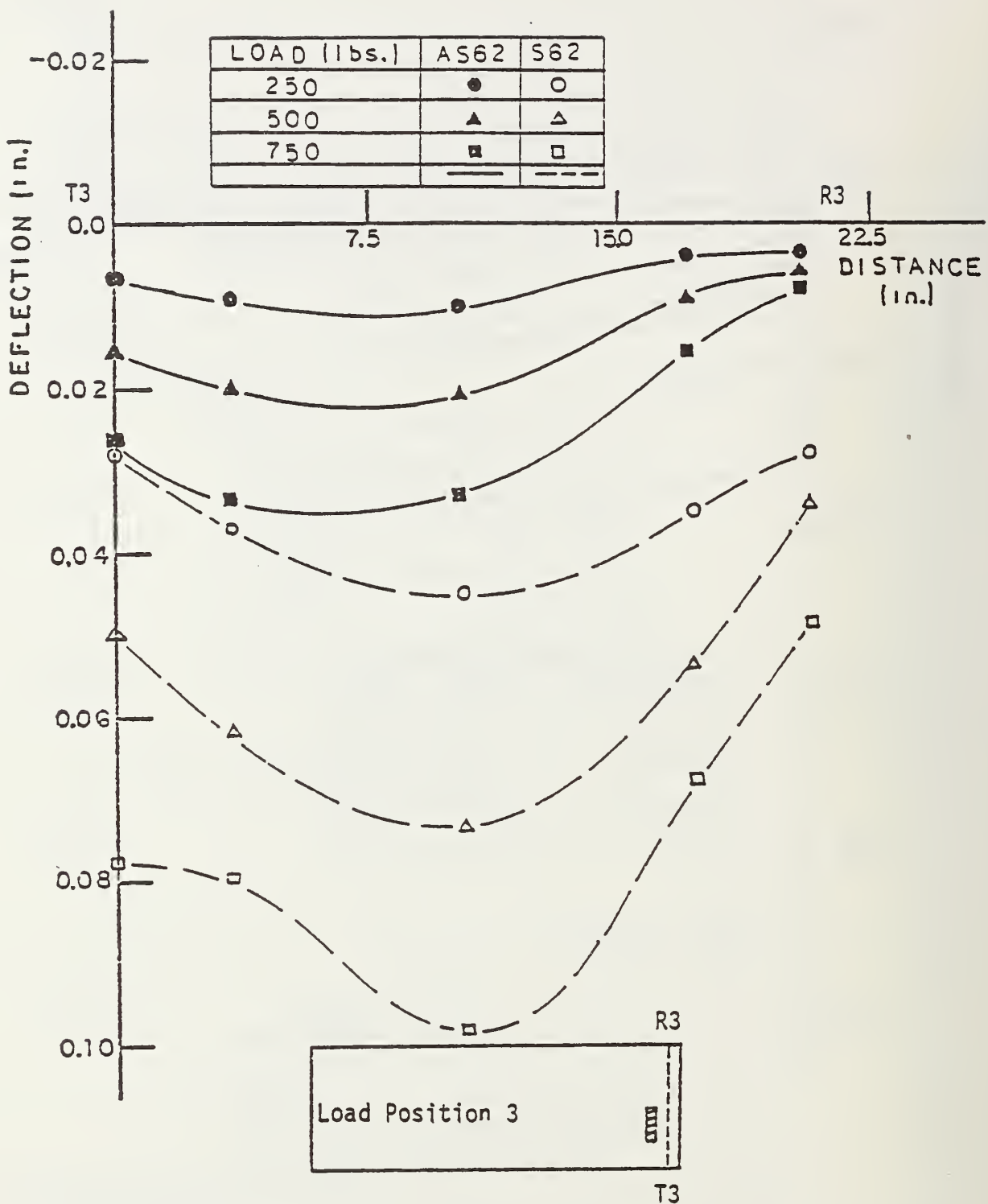
Figure 28. Transverse surface deflection along line T1-R1, load position 3, S62 - AS62.



S62 represents 62 inch long slab on
soil subgrade

AS62 represents 62 inch long anchored
slab on soil subgrade

Figure 29. Transverse surface deflection along line T2-R2,
load position 3, S62 - AS62.



S62 represents 62 inch long slab on
soil subgrade

AS62 represents 62 inch long anchored
slab on soil subgrade

1 in. = 2.54 cm
1 lb. = 0.45 kg

Figure 30. Transverse surface deflection along line T3-R3,
load position 3, S62 - AS62.

Figures 19, 20, and 21 are plots of the longitudinal surface deflections for loads at position 1. Figures 22, 23, and 24 represent plots of the transverse surface deflections for loads at position 1. Surface deflection for load at position 3 are shown in Figures 25 through 30.

The above plots, being most representative for a static load in a conventional pavement, are shown in this report.

2.3.3 Elevated Anchored Slab - ASE62

The procedure followed was similar to that for the AS62 and S62 experiments. Before the slab was screwed to the anchors, an 0.5 in. (1.27 cm) space was left between the slab and the subgrade. Figure 31 shows a cross section of the model, and Figure 32 shows a view of experimental set up.

Sixteen dial gages and six load positions were used to study the elastic response of the soil-structure system (Figure 8). Location of sections where surface deflection is plotted is also shown in Figure 8.

Ten foil gages as used in Section 2.3.1 were utilized in this investigation (Figure 9). Preloading of the soil was performed to keep the soil in the elastic range during experiment. The preloading was done at center, at quarter distance on the left, at quarter distance on the right, and near edge on left and right. The preloadings were done symmetrically to avoid any possible lifting of the anchored slab. After preloading, the loadings platform was replaced and the slab was loaded at six places, as described previously. The maximum load applied was 300 lb. (136 kg) with increments of 100 lb. (45.36 kg).

For position 1, longitudinal surface deflections are plotted in Figures 33, 34, and 35, and transverse surface deflections are plotted in Figures 36, 37, and 38. For position 3, longitudinal and transverse deflection are plotted in Figures 39 through 44.

Strain measurements are shown in Tables 17 through 22 Appendix A.

2.4 RESULTS

As shown in the next chapter, the trends of observed deflections of the model test agree well with the analytical results for the anchored slab. In the experimental work, the conventional slab was taken as a basis of comparison.

The surface deflections of the anchored slab in the longitudinal direction and the central transverse section for the central loading position

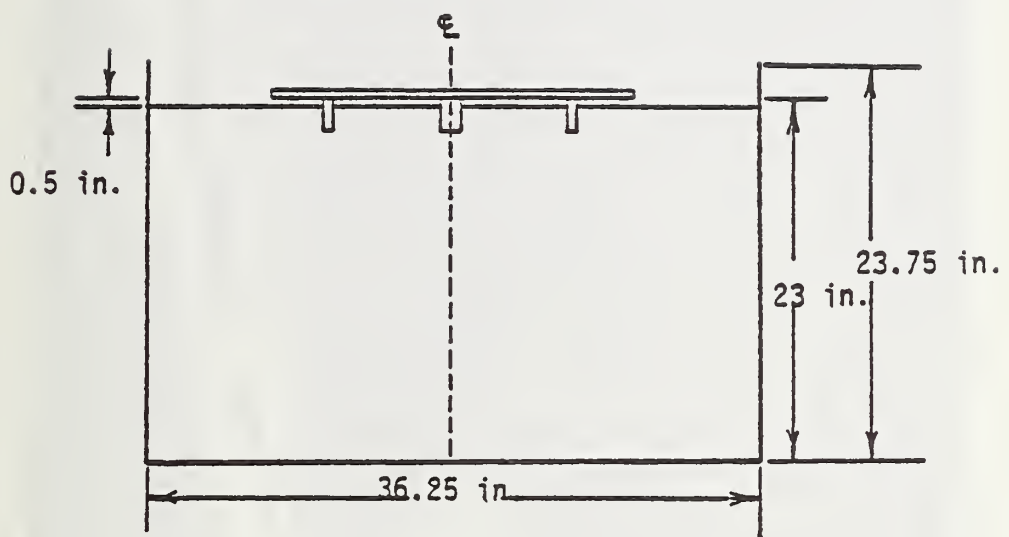
(position 1) are about one-third of those obtained for a conventional slab. At sections T2-R2 (quarter distance from edge) and T3-R3 (near edge). The conventional slab exhibited significant uplifting, whereas the anchored slab had almost no uplift or insignificant uplift only at the edge.

Similar trends, that is, differential magnitudes of the order of one-third, were observed for the edge loading (position 3) as shown in Figures 25, 26, 27, 29, and 30. The uplifting of the center was very pronounced for the conventional slab but insignificant for the anchored slab (Figure 28).

The anchored slab was also compared with the elevated slab system. The surface deflections beneath the load for position 1 of the anchored slab are about one-third to two-thirds of the deflections for the elevated slab (Figures 33 through 44). No significant uplifting was observed in the elevated slab.

Figures 39 through 44 indicate the following:

1. For a load of 250 lb., (113.4 kg) the deflections of the anchored slab in full contact (AS62) and the elevated anchored slab (ASE62) were found to be very similar. This indicates that much of the load was being carried by the anchors to the soil beneath.
2. Higher loads on the elevated slab would have caused punching failure and hence could not be used in the experiment; however, analytical investigation (though not performed in this report) could be of interest.



1 in. = 2.54 cm

ASE62 represents 62 in. long
anchored slab elevated
0.5 in. on soil subgrade

Figure 31. Cross section of ASE62 on subgrade.



Figure 32. View of elevated pavement.

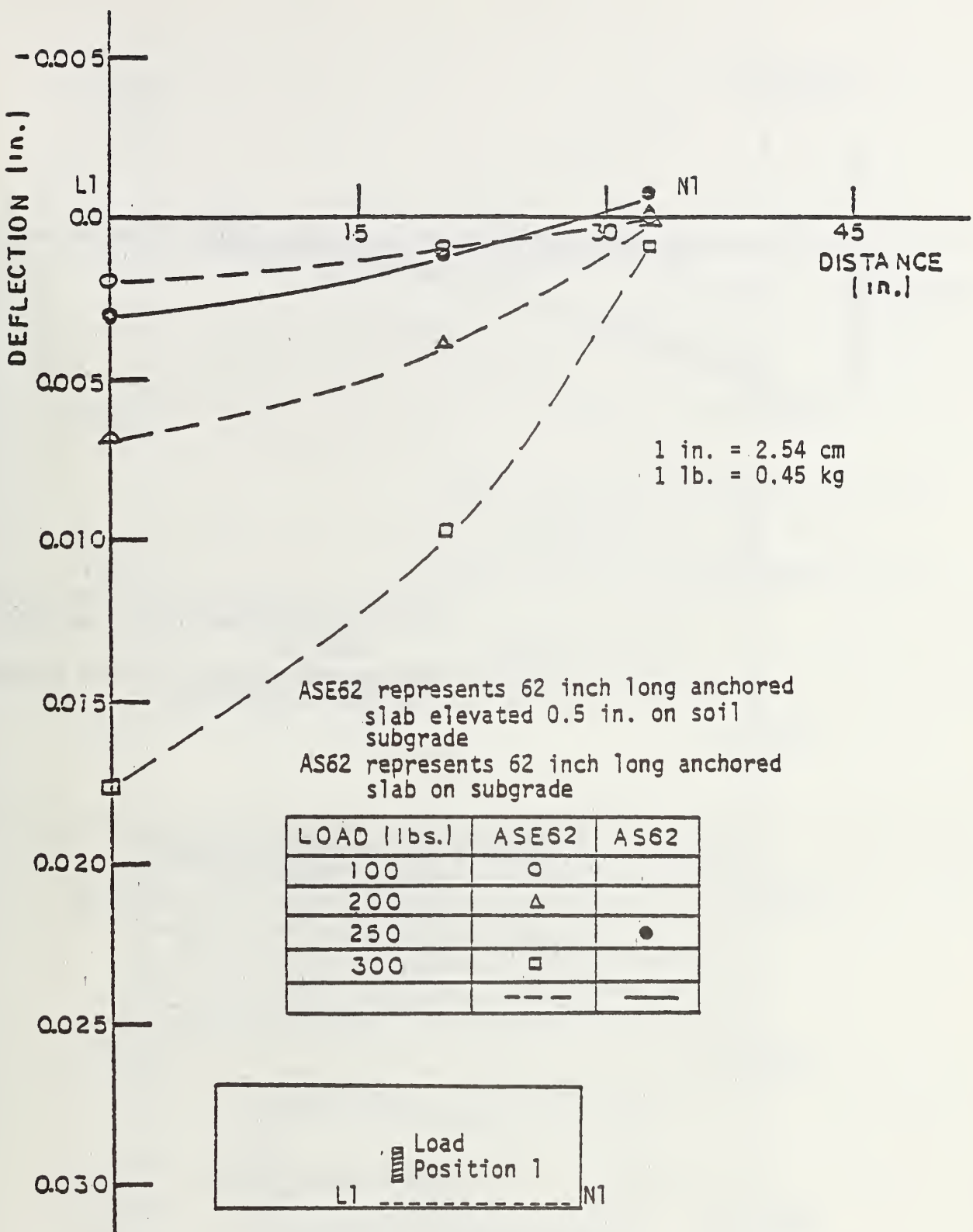


Figure 33. Longitudinal surface deflection along line L1-N1, load position 1, ASE62 - AS62.

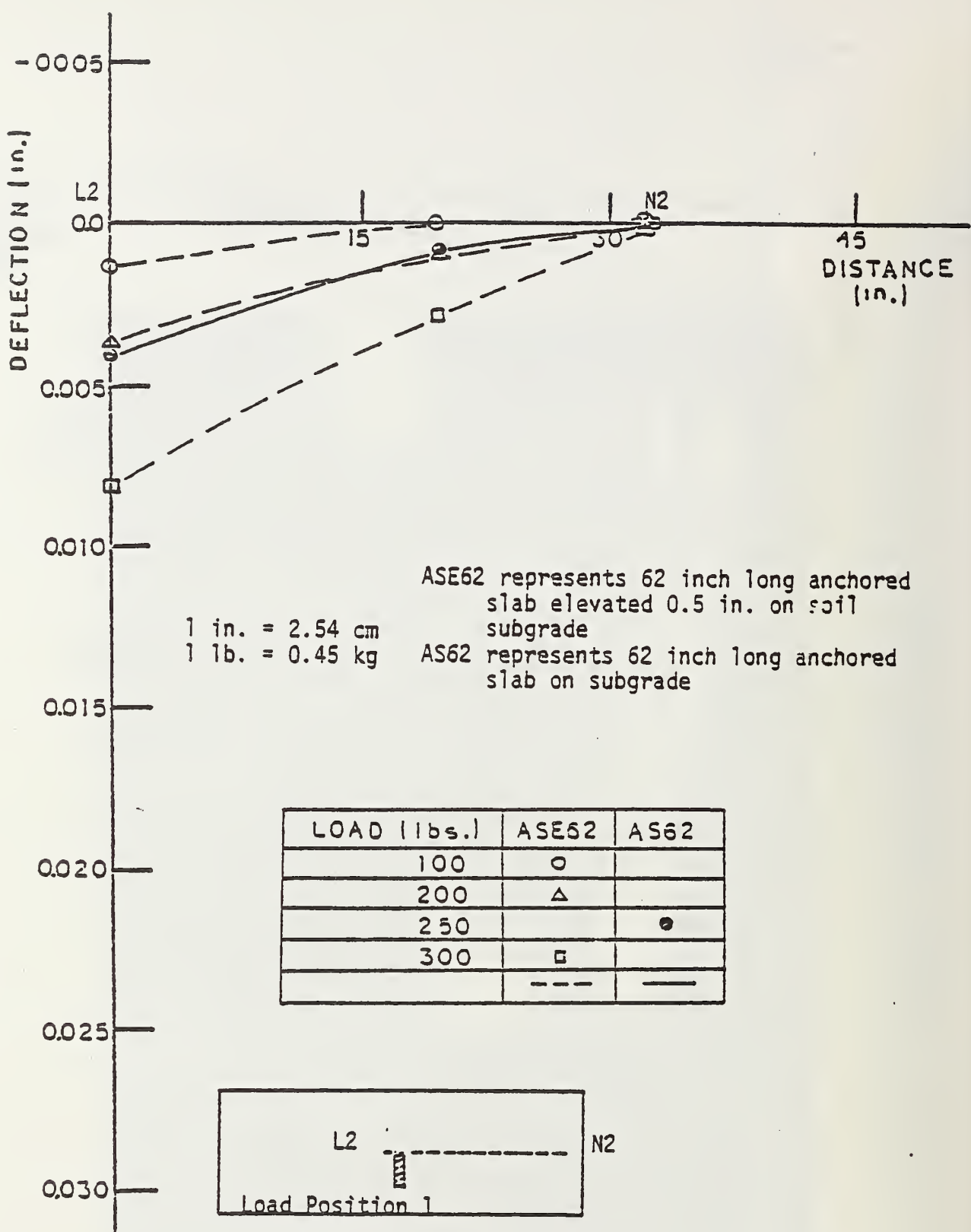


Figure 34. Longitudinal surface deflection along line L2-N2, load position 1, ASE62 - AS62.

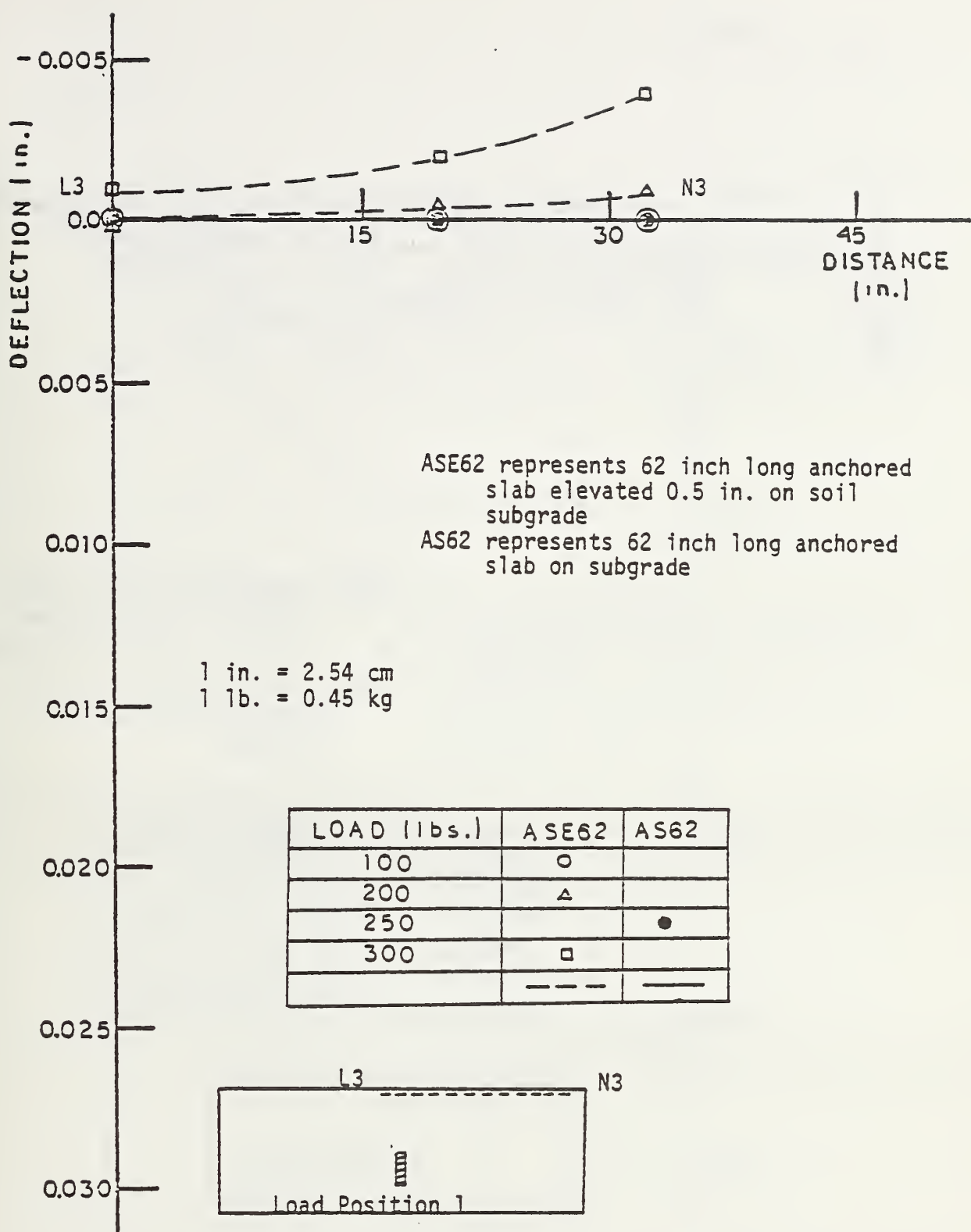


Figure 35. Longitudinal surface deflection along line L3-N3, load position 1, ASE62 - AS62.

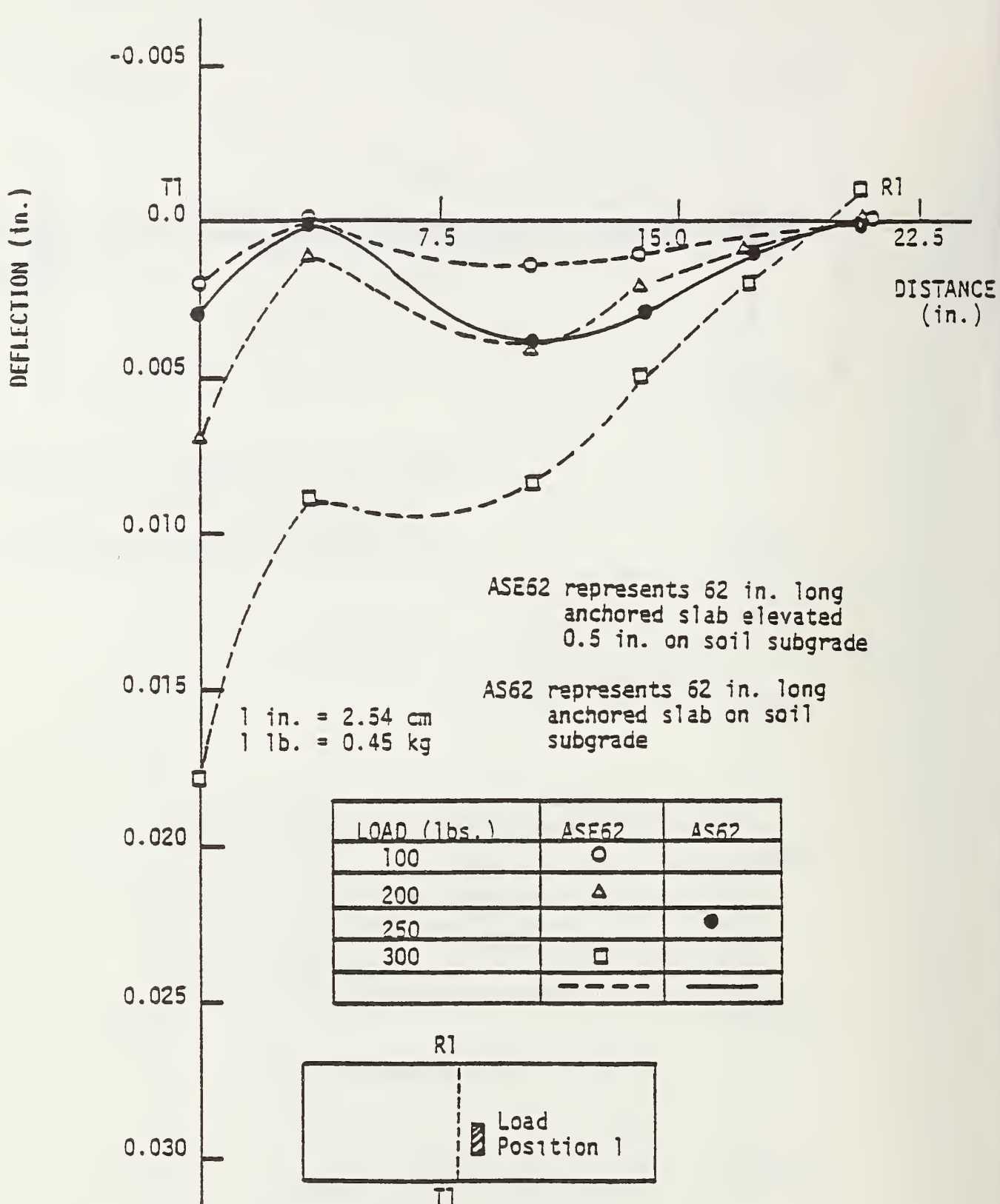


Figure 36. Transverse surface deflection along line T1-R1, load position 1, ASE62 - AS62.

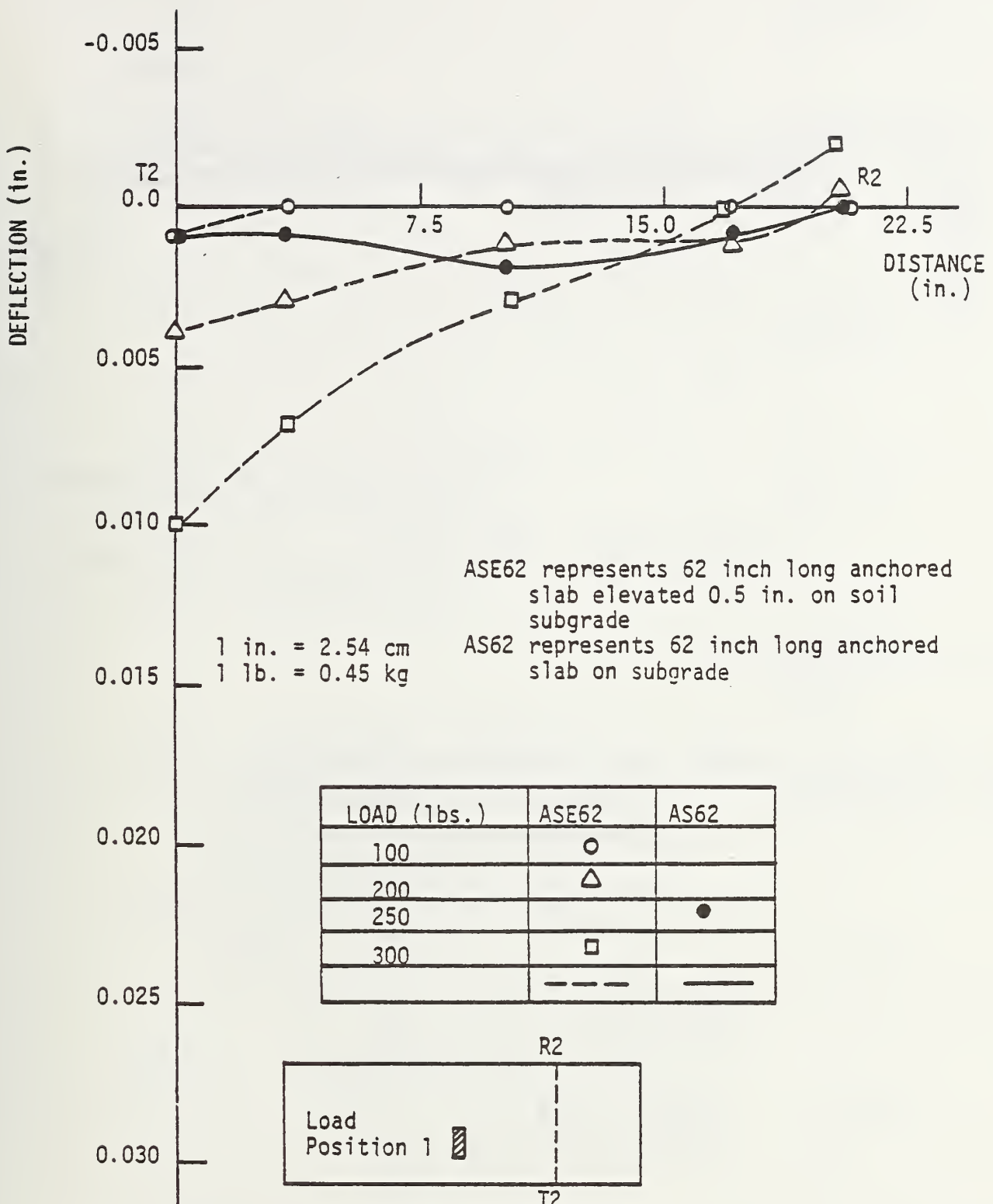


Figure 37. Transverse surface deflection along line T2-R2 load position 1, ASE62 - AS62.

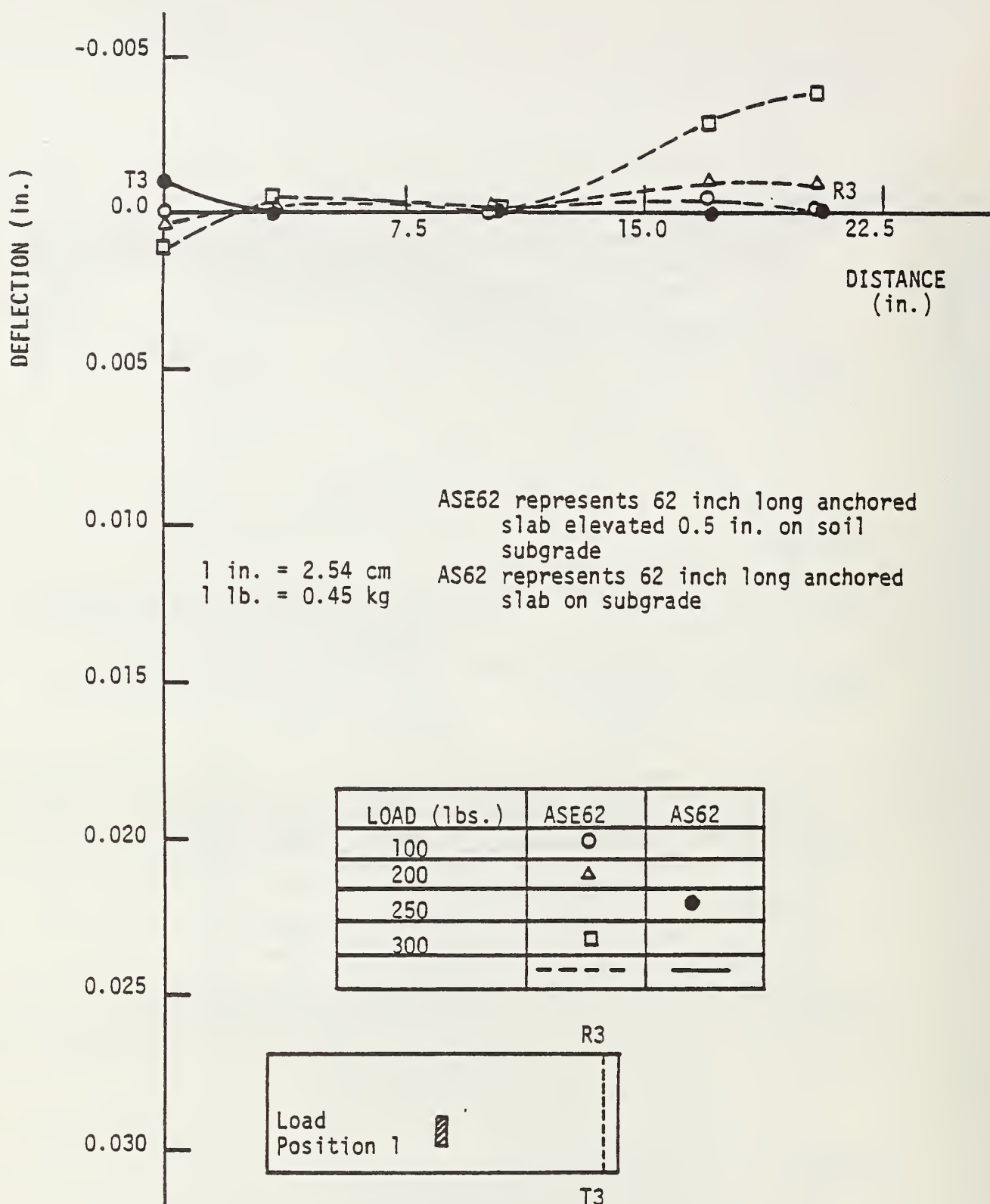


Figure 38. Transverse surface deflection along line T3-R3, load position 1, ASE62 - AS62.

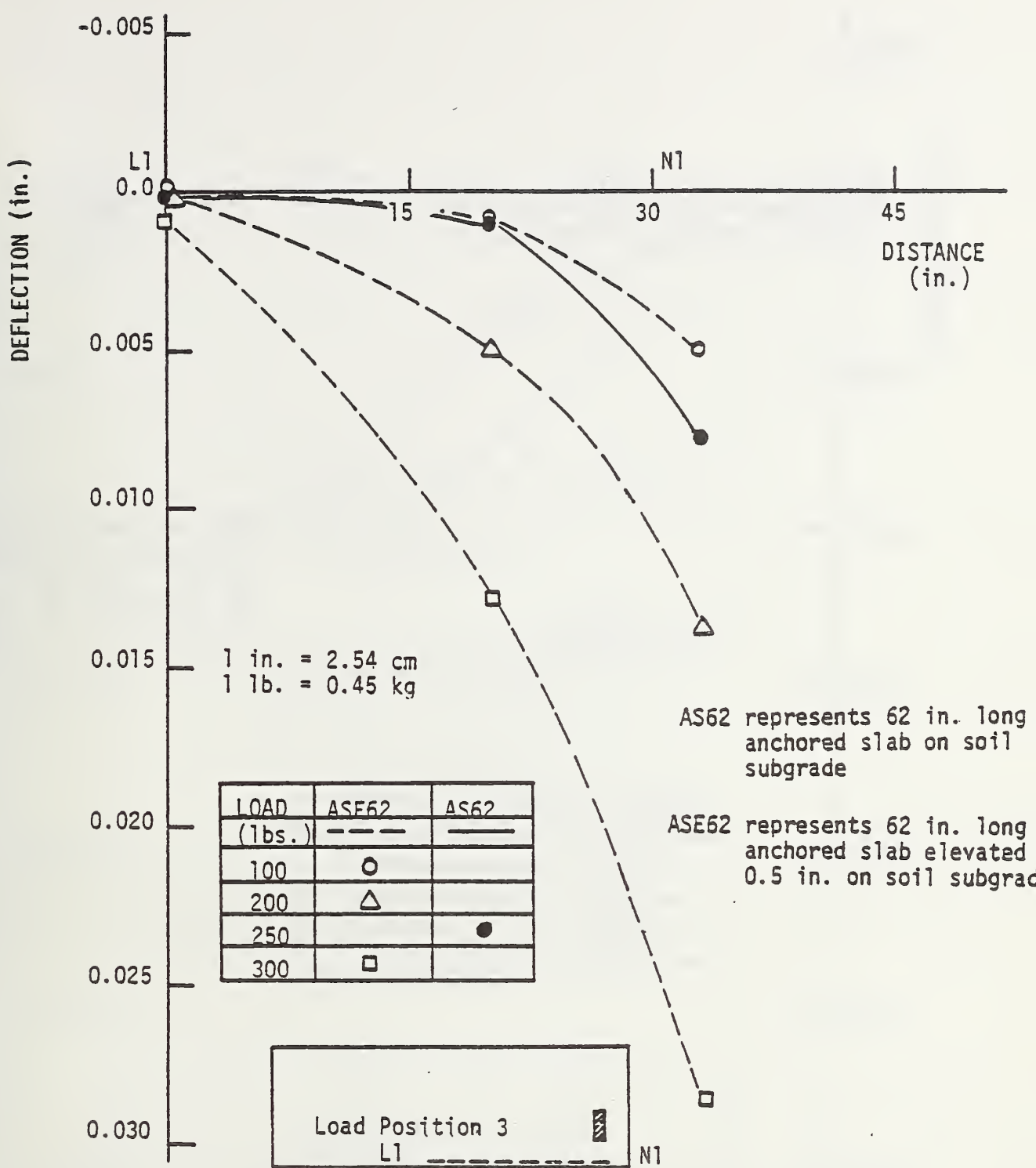


Figure 39. Longitudinal surface deflection along line L1-N1, load position 3, ASE62 - AS62.

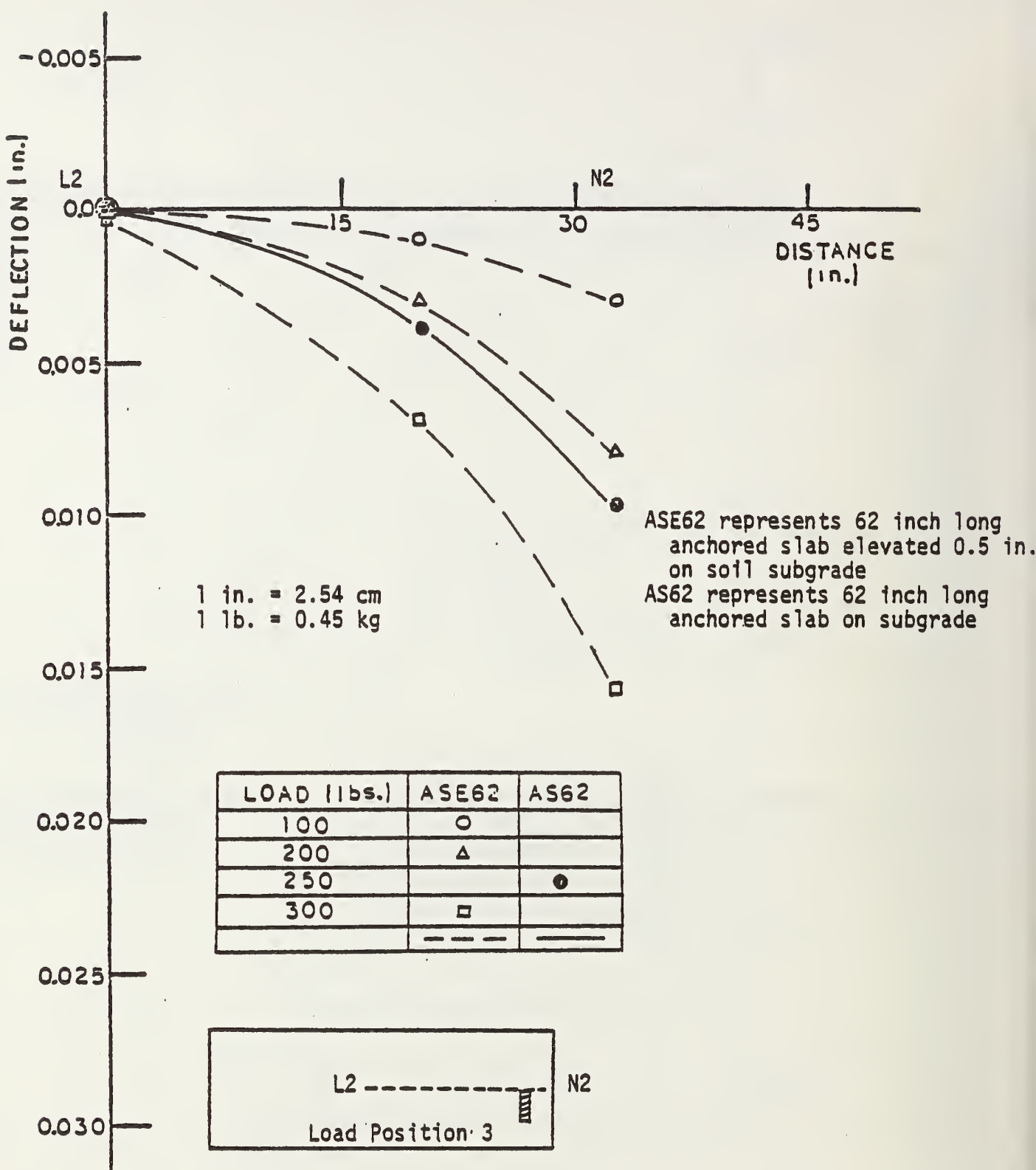


Figure 40. Longitudinal surface deflection along line L2-N2, load position 3, ASE62 - AS62.

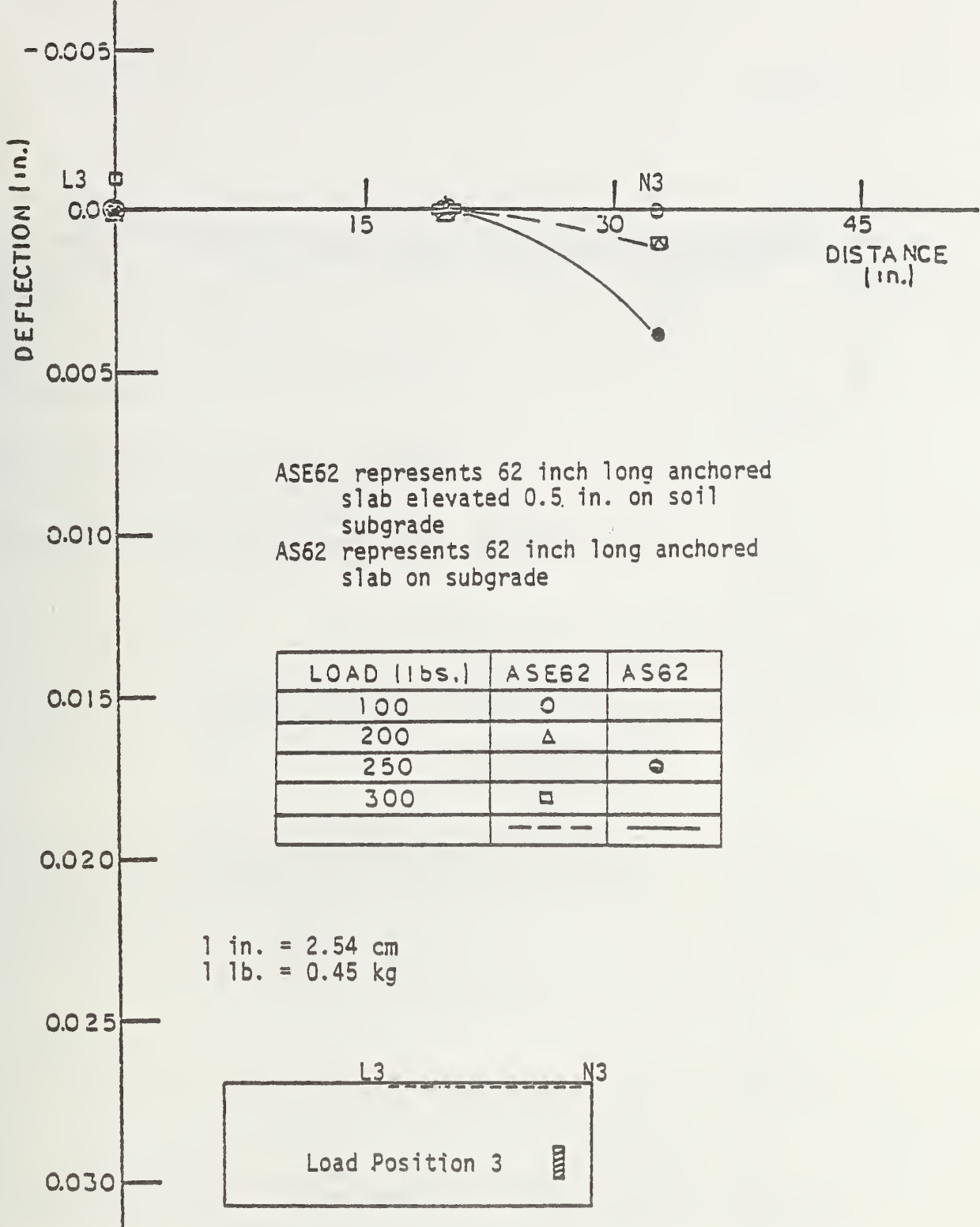


Figure 41. Longitudinal surface deflection along line L3-N3, load position 3, ASE62 - AS62.

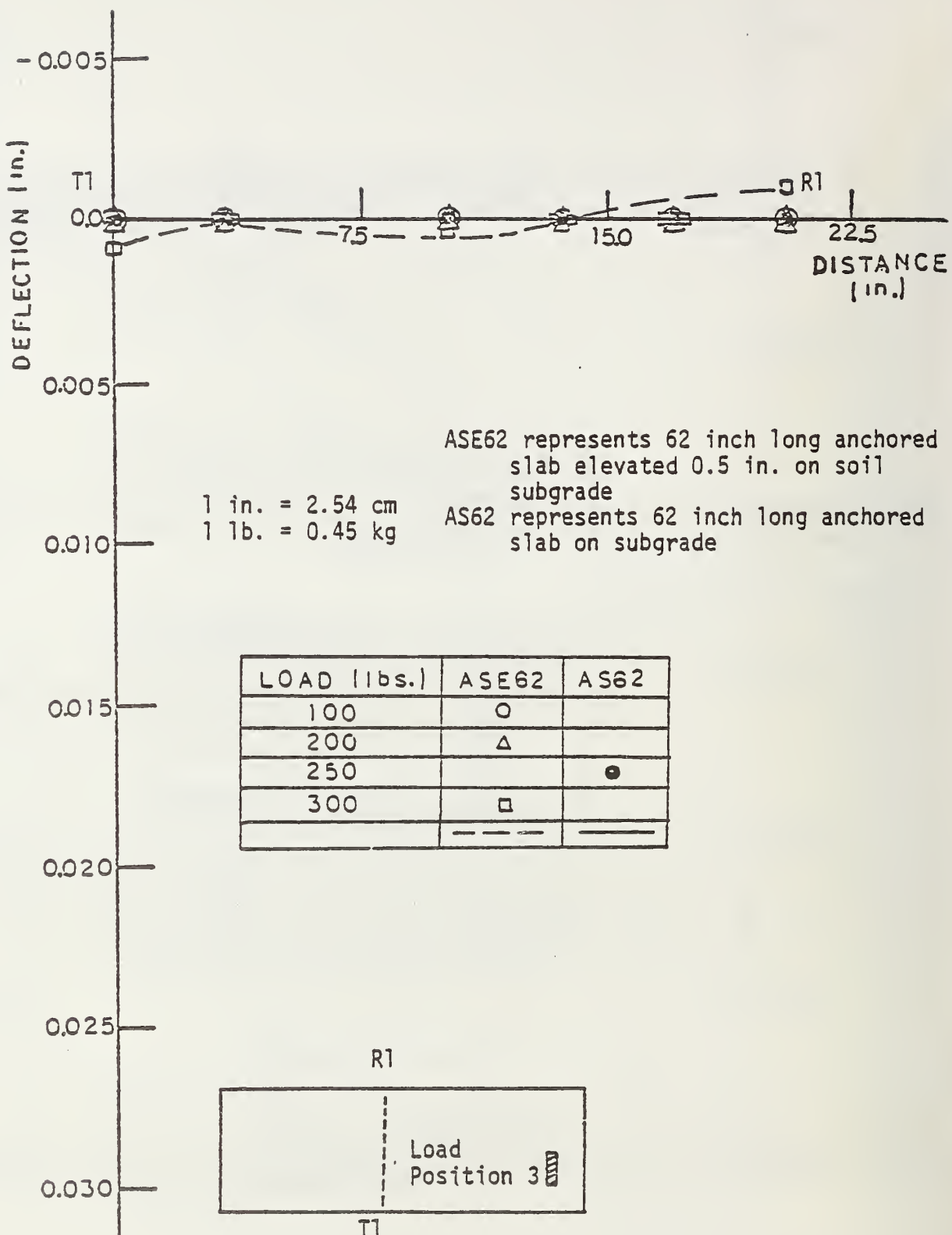


Figure 42. Transverse surface deflection along line T1-R1, load position 3, ASE62 - AS62.

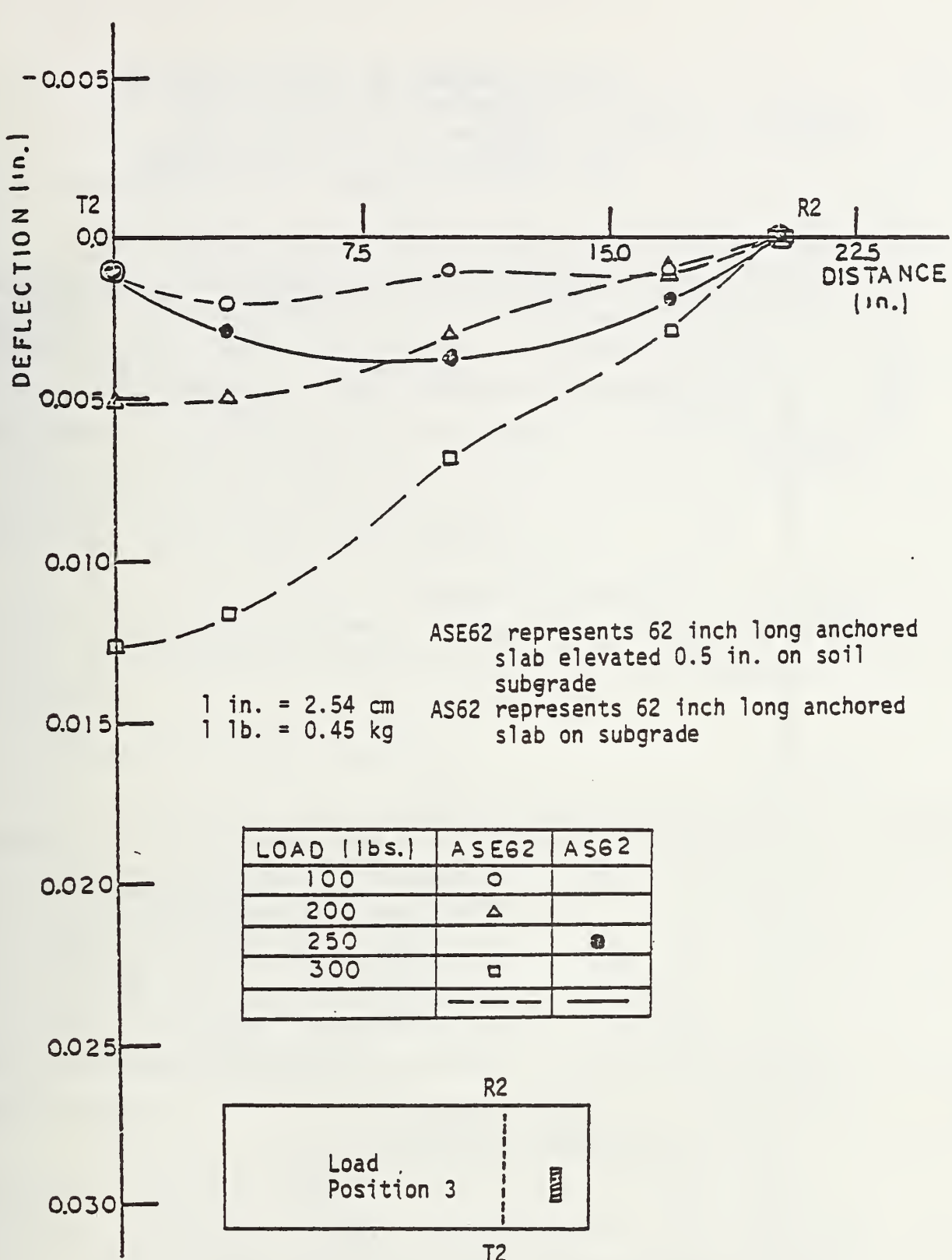


Figure 43. Transverse surface deflection along line T2-R2, load position 3, ASE62 - AS62.

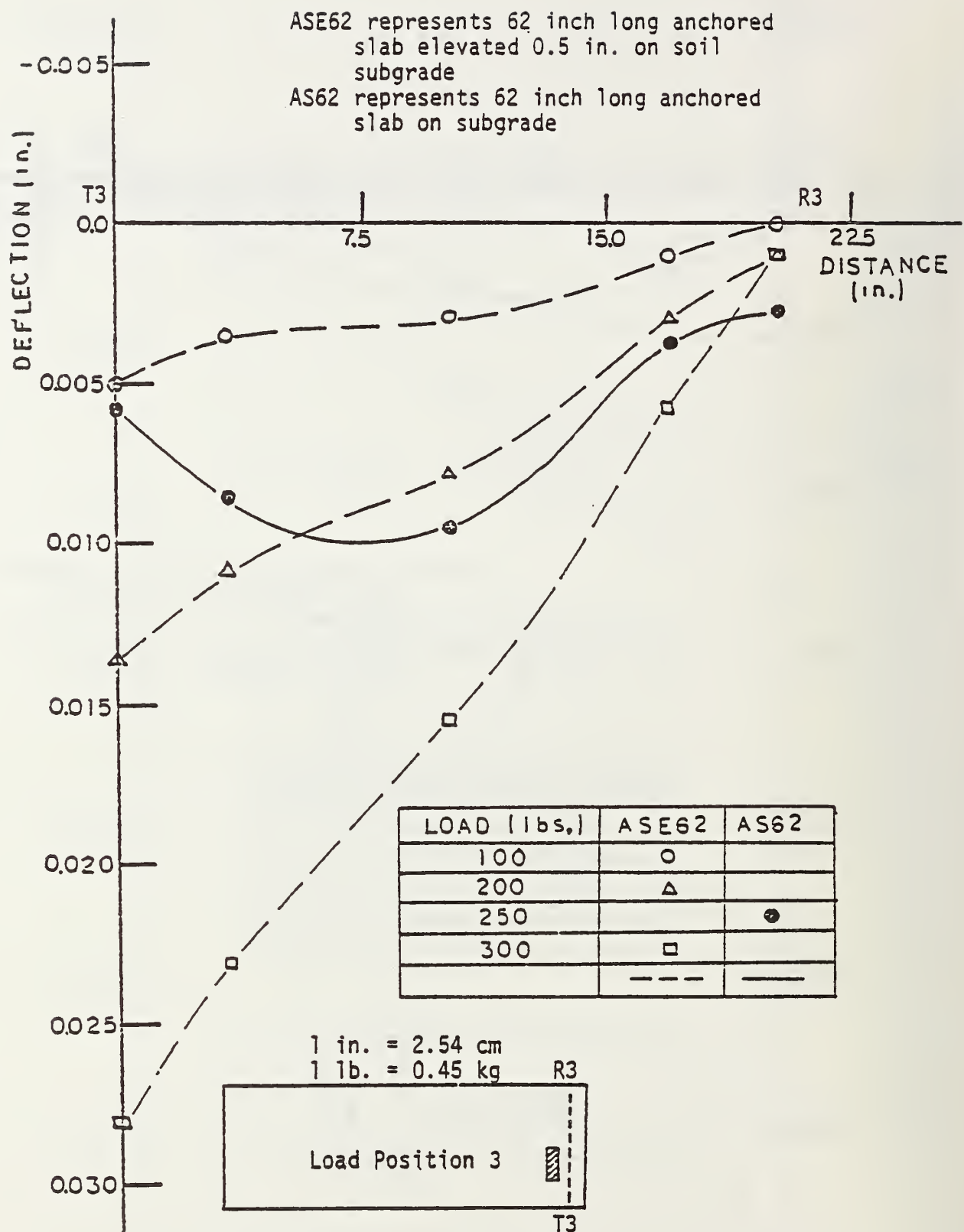


Figure 44. Transverse surface deflection along line T3-R3, load position 3, ASE62 - AS62.

CHAPTER III

VERIFICATION OF COMPUTER PROGRAM

3.1 INTRODUCTION

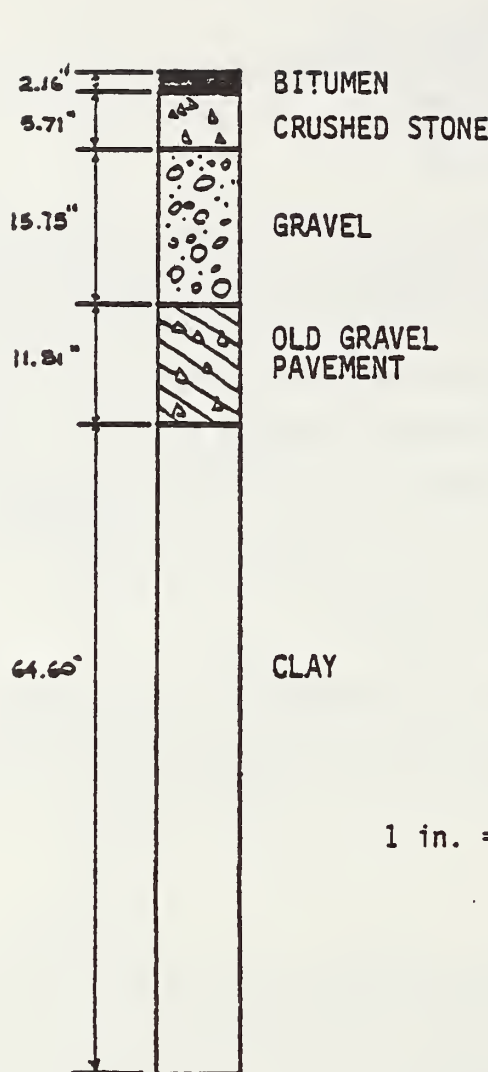
Before any numerical method is used to solve complex structural or field problems, it should be checked against similar (though often simpler) situations which either possess closed-form or otherwise known solutions. Equally acceptable checks can be made against experimentally observed results or actual field conditions provided care was taken to ensure accuracy in their measurement. This section presents the types of verification, mathematical modeling techniques, and numerical values derived from actual field conditions and experiments used to form a comparison for the solution and thereby forecast the relative degree of accuracy of further studies.

The verification study makes use of the heat transfer and mechanical (static) stress analysis options available in the computer program ANSYS. As a result, test programs were developed specifically to lend credence to these types of analysis.

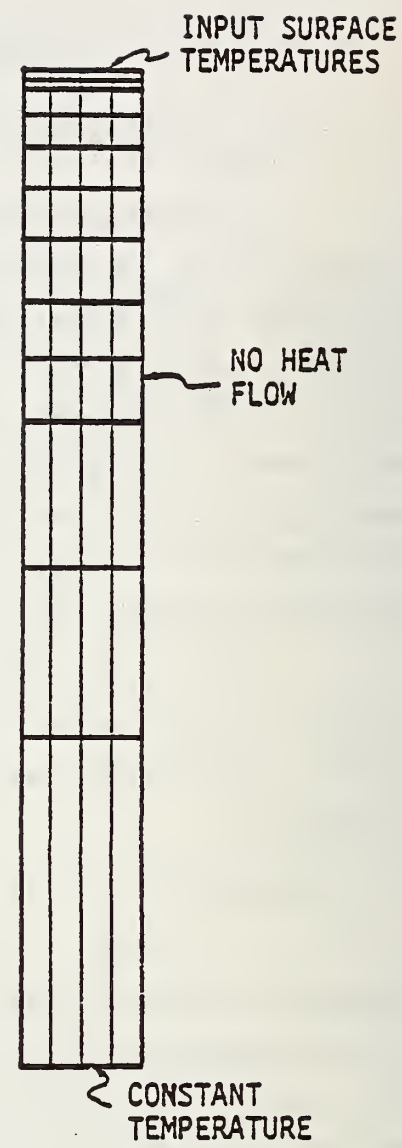
3.2 VERIFICATION FOR HEAT TRANSFER

A literature review of problems associated with thermal soil mechanics produced a series of papers describing a road test in Norway during the 1957-69 period (Noss, 1973; Nordal, 1973; Frivik et al., 1977). Atmospheric conditions were monitored and temperature profiles within the ground (tautochrones) at various hours of the day were obtained. Of critical importance to this investigation was the additional reporting of material properties - thermodynamic and mechanical (Frivik et al., 1977). With such a complete set of data, it was possible to construct a mathematical model to simulate the prototypical road test section behavior.

The site -- the Vormsund test road -- consists of several sections of pavements. The section modeled is at station 724 + 7.5; the profile is shown in Figure 45. The temperature profiles were taken along the pavement centerline, to assure a near one-dimensional system. Since, however, the mathematical model used for actual analysis would be two-dimensional, it was decided to model the test road by two-dimensional isoparametric finite elements, the same types used in the primary study. The mesh is shown in Figure 45. No heat flow was allowed on vertical boundaries; the lower boundary was kept at a constant temperature.



a) Pavement profile.



b) Finite element mesh.

Figure 45. Model used for computer program heat transfer analysis verification.

These boundary conditions simulate a soil mass of infinite extent. The lower boundary condition is consistent with observed values (Figure 46) and the modeled constant temperature at the 100 in. (254 cm) depth is sufficient.

The input surface temperature was approximated by piecewise linear segments of 3 to 6 hours (Figure 47). The analysis is nonlinear, as material properties can vary with temperature. The reported values of thermal conductivity and specific heat vary only slightly in the temperature ranges considered, and a nominal value for each was chosen. The input values are given in Table 1 and are considered typical. The analysis uses a time-stepping, tentative procedure that updates the stiffness (conductivity) and damping (specific heat) matrices after each iteration. The analysis assumed a uniform temperature throughout the system and then cycled through a 3-day period, changing surface temperatures with iterations. The constant temperature is a valid assumption since at the starting time, the temperature is nearly constant with depth.

The finite element analysis yielded the tautochrones shown in Figure 48 for the third day. The convergence is quite rapid as the second and third day tautochrones are nearly the same. By comparing the actual tautochrones (Figure 46) with the generated values (Figure 48), close agreement - within 3 or 4°F (1.8 to 2.2°C) - can be seen. The trends in the curves are accurately portrayed with thermal damping effects simulated well.

This verification has only considered temperatures above freezing. The program does not accurately account for the water phase changes associated with freezing and thawing. Provisions can be made, however, to deal with this complex problem.

3.3 VERIFICATION FOR MECHANICAL LOADS

The experimental pavement study was discussed in Chapter II. By determining the geometry, boundary conditions, and material properties of the physical model, a mathematical model can be generated and results compared. A comparison of anchored pavement with the conventional slab and with the elevated anchored slab (representing loss of contact below the slab) is presented. First, the input properties of different materials, used in analyses, are identified.

The properties of the materials utilized in the experimental study are presented in Appendix B. Soil properties (E and ν) were determined by several methods, including triaxial compression, constant stress consolidation, and plate load test.

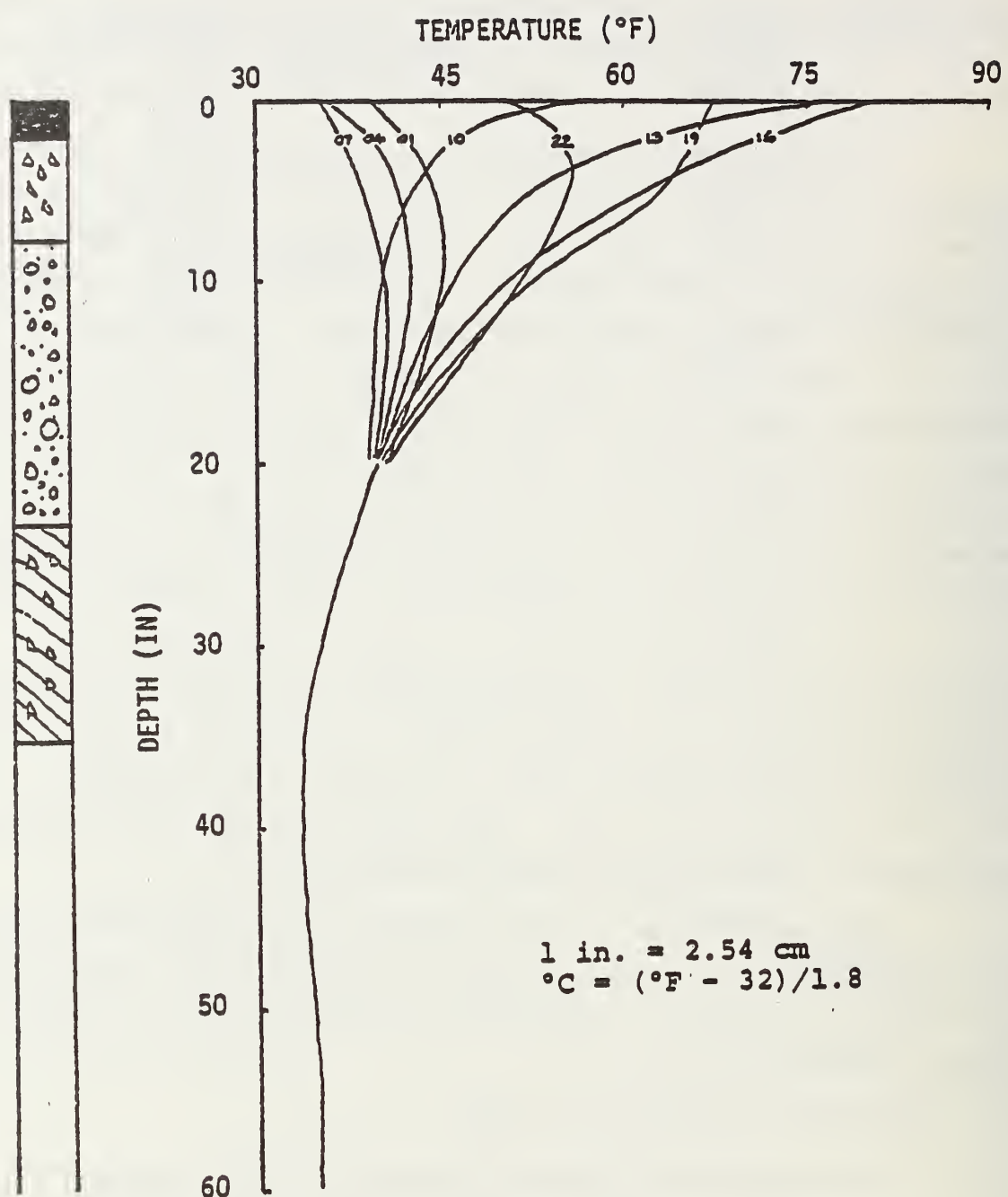


Figure 46. Actual recorded tautochrones at Sta. 724+7.5 of the Vormsund test road, April 26, 1963 (Nordal, 1973).

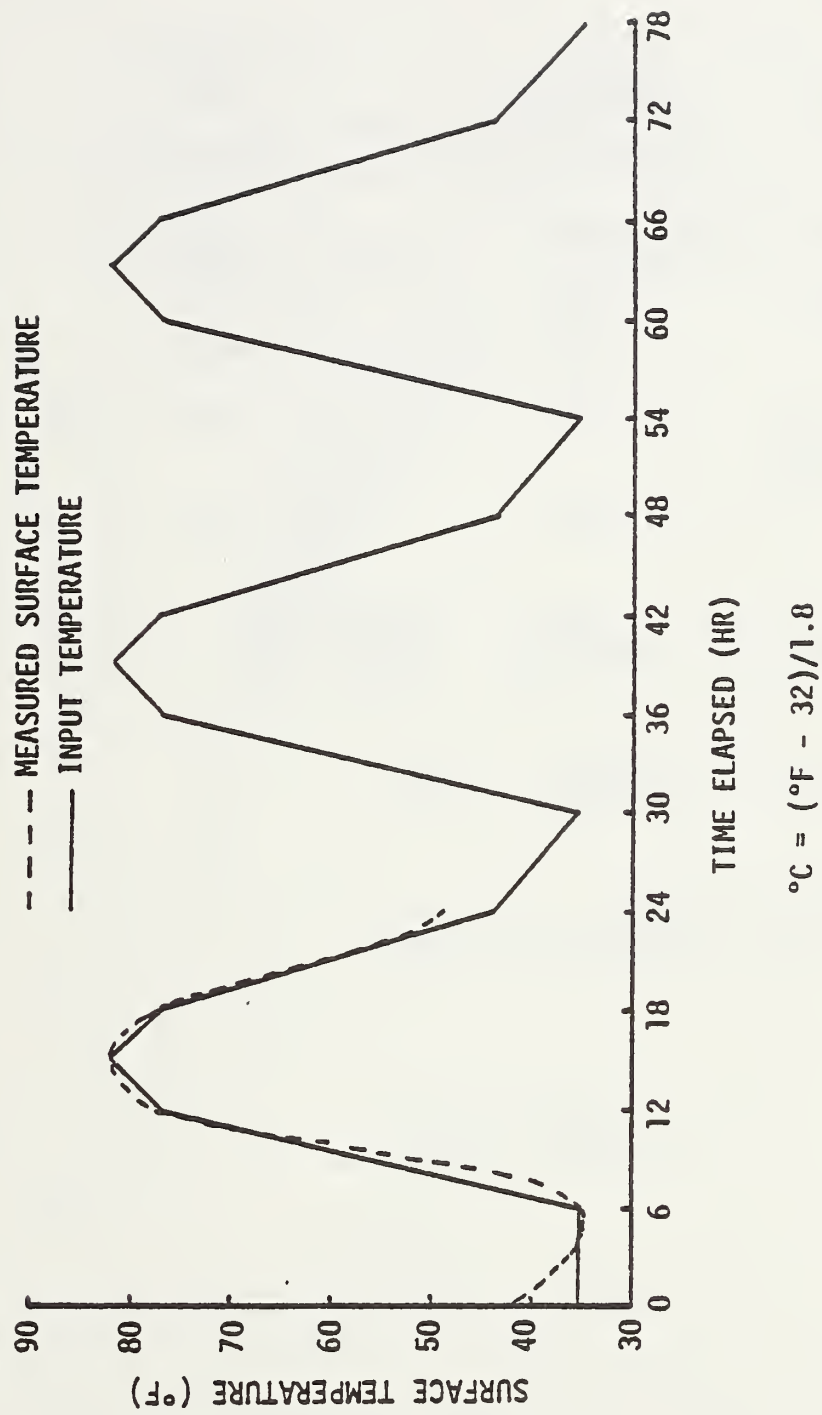


Figure 47. Measured and input surface temperature for the Vormsund test road on April 26, 1963.

Table 1. Material properties used in thermal verification program.

<u>MATERIAL</u>	<u>THERMAL</u>	<u>MASS SPECIFIC</u>	<u>DENSITY</u>
	<u>CONDUCTIVITY</u> (BTU/HR-IN- $^{\circ}$ F)	<u>HEAT</u> (BTU/LBM- $^{\circ}$ F)	<u>(LB/IN3)</u>
Bitumen	0.069	0.245	0.082
Cr. Stone	0.093	0.267	0.075
Gravel	0.082	0.226	0.075
Old Gravel Pavement	0.082	0.226	0.075
Clay	0.059	0.345	0.067

$$1 \text{ BTU/HR-IN-}^{\circ}\text{F} = \frac{0.099}{1.8^{\circ}\text{C} + 32} \quad \frac{\text{CAL-KG}}{\text{HR-CM-}^{\circ}\text{C}}$$

$$1 \text{ BTU/LBM-}^{\circ}\text{F} = \frac{0.554}{1.8^{\circ}\text{C} + 32} \quad \frac{\text{CAL}}{^{\circ}\text{C}}$$

$$1 \text{ LB/IN}^3 = 27.7 \frac{\text{GR}}{\text{CM}^3}$$

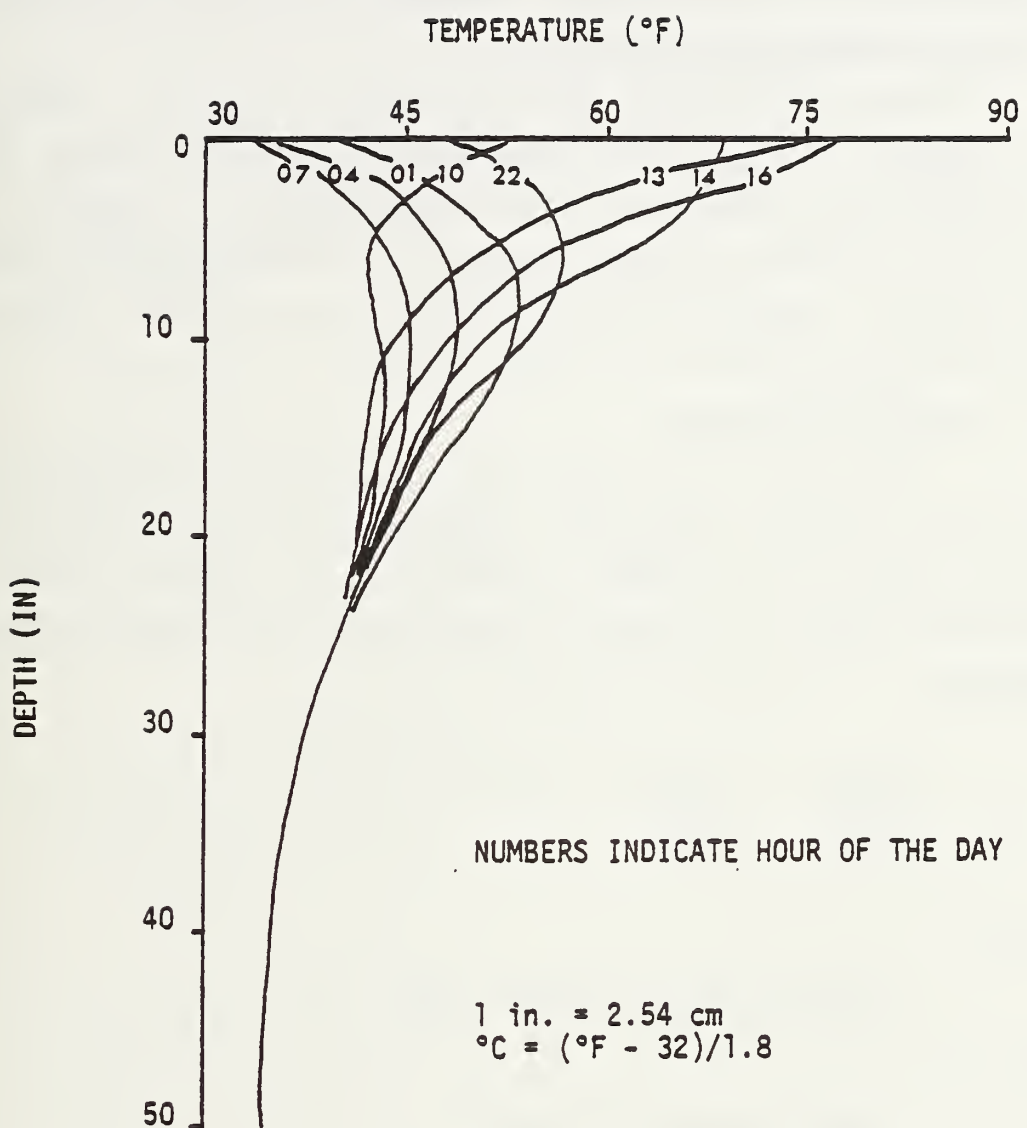


Figure 48. Tautochrones generated by the finite element model.

It is reasonable to assume that the plate load test will provide a better in-situ value of the modulus of elasticity. The plate load test was conducted in the sampling area. This area did not undergo many preloadings as the main experimental area. The preloadings will increase the modulus. The adopted modulus for the analytical comparison was 850 psi (60 kg/cm^2). The input values are summarized in Table 2.

Eight node brick elements were used in the finite element analysis (3-D analysis). In the case of AS62 and S62, interface elements of infinitesimal length were used between the slab and the subgrade soil. Thus the effect of the uplifting, when the slab loses contact with the subgrade soil, was taken into consideration. Modeling the steel container was considered necessary to avoid great errors, as found by preliminary analysis.

3.3.1 Results of Analysis

The finite element models of simply supported anchored slab (SAS62) and simply supported conventional slab (SS62) are shown in Figure 49. A line load of 2.95 psi (0.21 kg/cm^2) was applied 1 in. (2.54 cm) offset of the transverse centerline. From the "beam theory" the following relation can be computed:

$$\frac{\Delta_{SAS62}}{\Delta_{SS62}} = \frac{I_{SAS62}}{I_{SS62}} = 24$$

3

where

Δ denotes deflection under load

and

I denotes moment of inertia

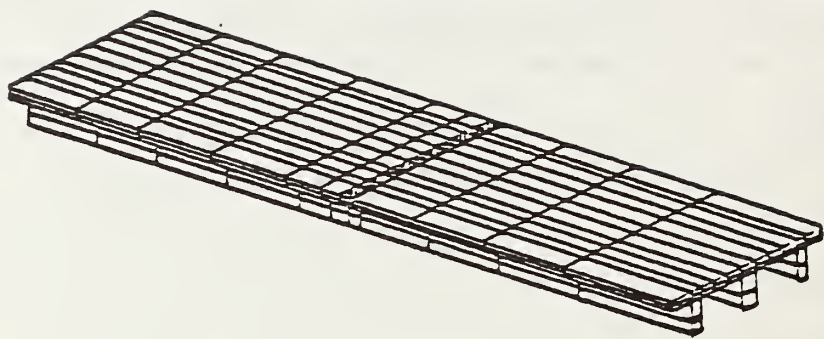
The equivalent moment of inertia for the anchored slab (SAS62) is 5.28 in.^4 (219.78 cm^4) and for the conventional slab (SS62) is 0.22 in.^4 (9.16 cm^4). The neutral axis of the cross section of the anchored slab is 0.647 in. (1.65 cm) below the top surface of the slab.

The longitudinal deflections at the centerline are plotted in Figure 50 showing the experimental deflection, the deflection obtained by finite

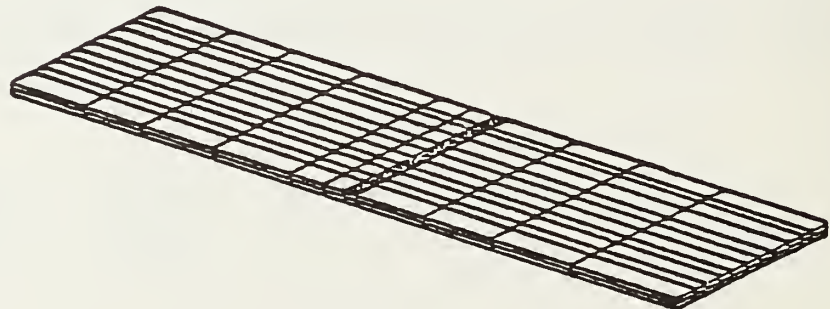
Table 2. Material properties used in stress verification program.

<u>MATERIAL</u>	<u>YOUNG'S MODULUS</u> (psi)	<u>POISSON'S RATIO</u>
Aluminum	10×10^6	0.35
Steel	30×10^6	0.33
Soil (Silty Clay)	850	0.40

$$1 \text{ psi} = 0.0703 \text{ kg/cm}^2$$

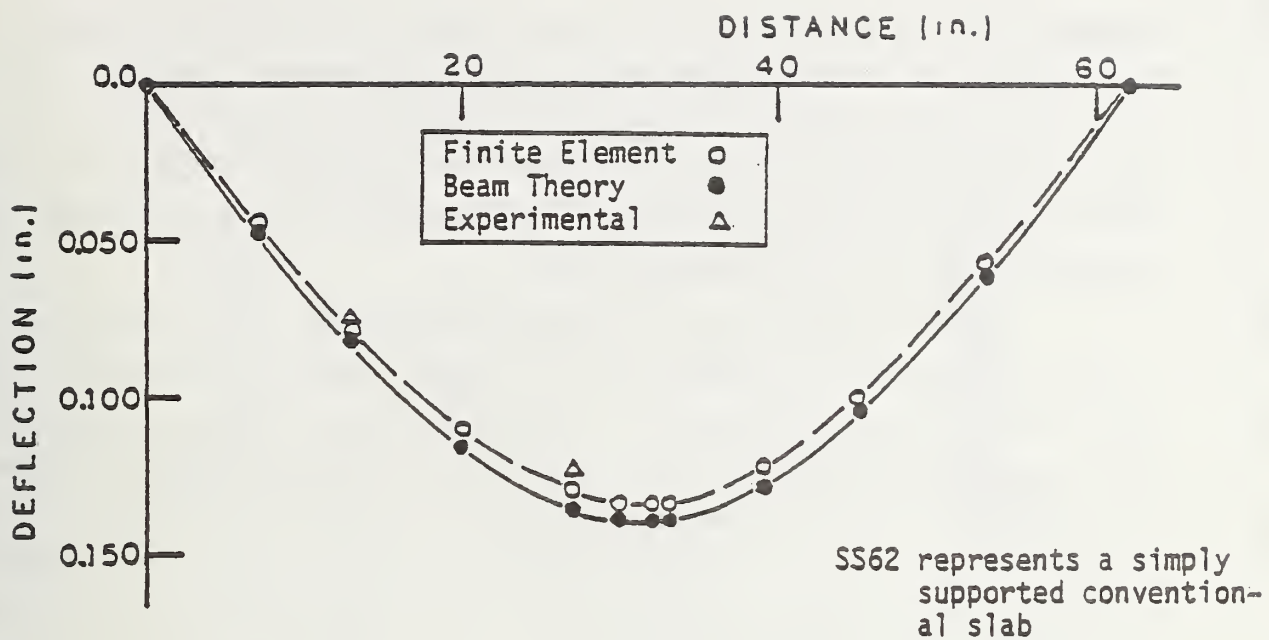


a) Finite element model of SAS62. SAS62 represents a simply supported anchored slab

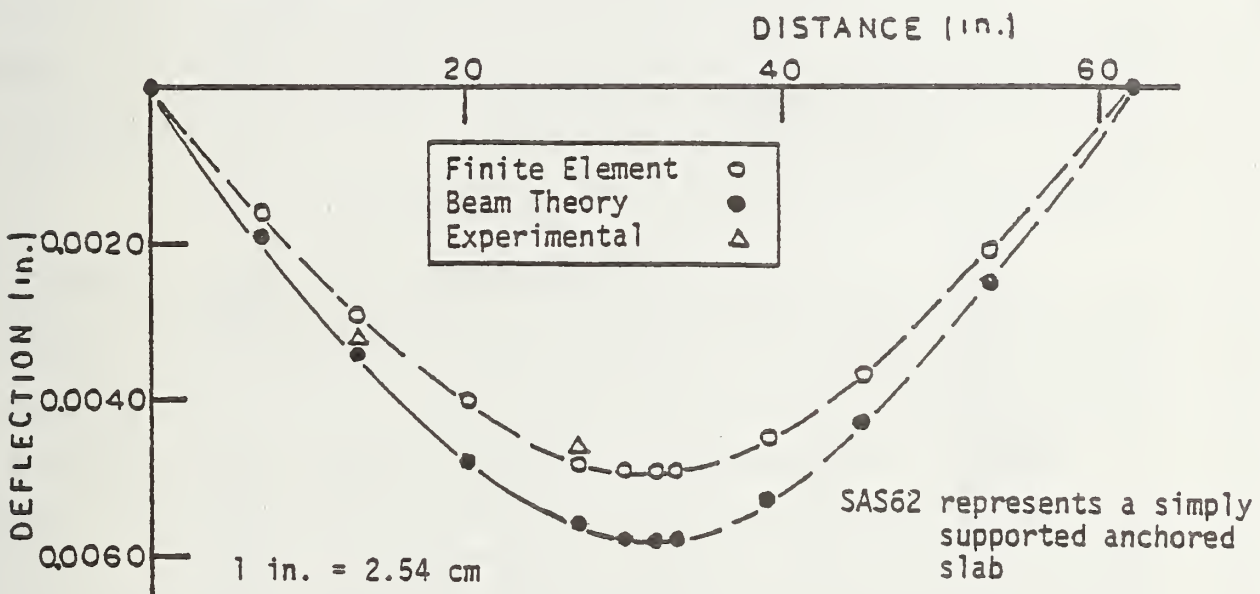


b) Finite element model of SS62. SS62 represents a simply supported conventional slab

Figure 49. Finite element models of SAS62 and SS62 for stress analysis verification.



a) Longitudinal deflections at center of SS62.



b) Longitudinal deflections at center of SAS62.

Figure 50. Longitudinal deflections at center for comparison of experimental models, finite element models, and models using the beam theory.

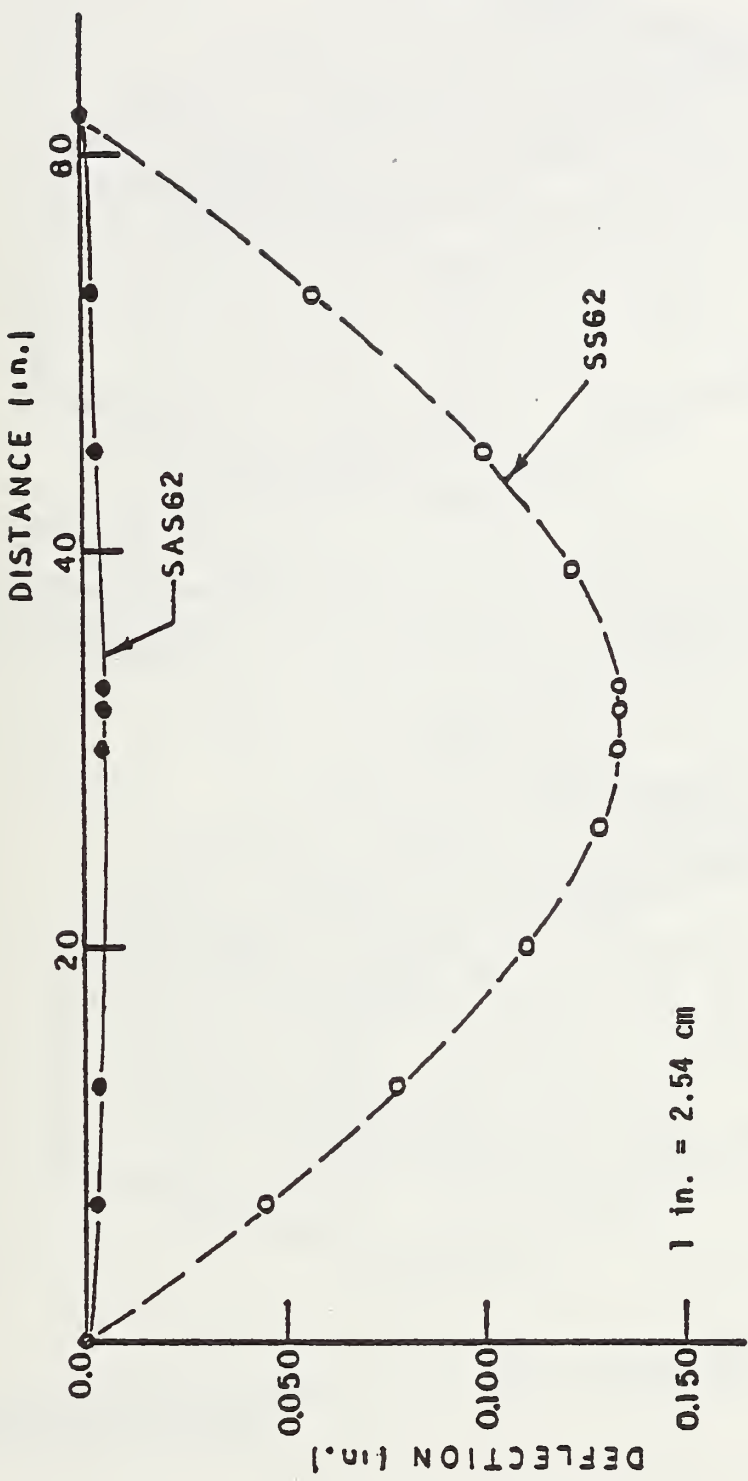
element method, and that obtained by beam theory. The difference between the results from finite element method and the experimental values is about 7% for the simply supported anchored slab (SAS62) and about 4.5% for the simply supported conventional slab (SS62). The difference between the beam theory approach and the experimental value is about 8% for the anchored slab and about 8.5% for the conventional slab.

Figure 51 shows the longitudinal deflections at the centerline of the simply supported anchored slab and simply supported conventional slab, using the finite element approach. The finite element models for anchored slab on subgrade (AS62) and conventional slab on subgrade (S62), are shown in Figure 52. The finite element model for an elevated slab (ASE62) is shown in Figure 53. A 750-lb. (340.2 kg) load was applied at position 1 (Figure 8) in the experiment sequence AS62 and S62; a 200-lb. (90.72 kg) load was applied at position 1 in the sequence ASE62.

Figure 54 shows the surface deflection contours for the sequence S62 with a maximum deflection of 0.1 in. (2.54 mm) under the load. More than half of the slab loses contact from the subgrade soil, with a maximum uplift of 0.012 in. (0.30 mm). The vertical stress and strain contours are given in Figure 55, with a maximum stress of 9 psi (0.63 kg/cm^2) and a maximum strain of 0.005 in./in. (cm/cm) underneath the load.

Figure 56 shows the surface deflection contours for the sequence AS62 with a maximum deflection of 0.031 in. (0.8 mm) in the right anchor (closest to the load). No serious uplift of the anchored slab is noted. Only the left and right edges are lifted, with a maximum uplift of 0.004 in. (0.1 mm). The vertical stress and strain contours in the subgrade are given in Figure 57 with a maximum stress of 2 psi (0.14 kg/cm^2) and a maximum strain of 0.002 (in./in. or cm/cm) underneath the right anchor. The stresses in the subgrade immediately under the slab are reduced considerably with a maximum stress of 1 psi (0.07 kg/cm^2), compared with 9 psi (0.63 kg/cm^2) in conventional slab.

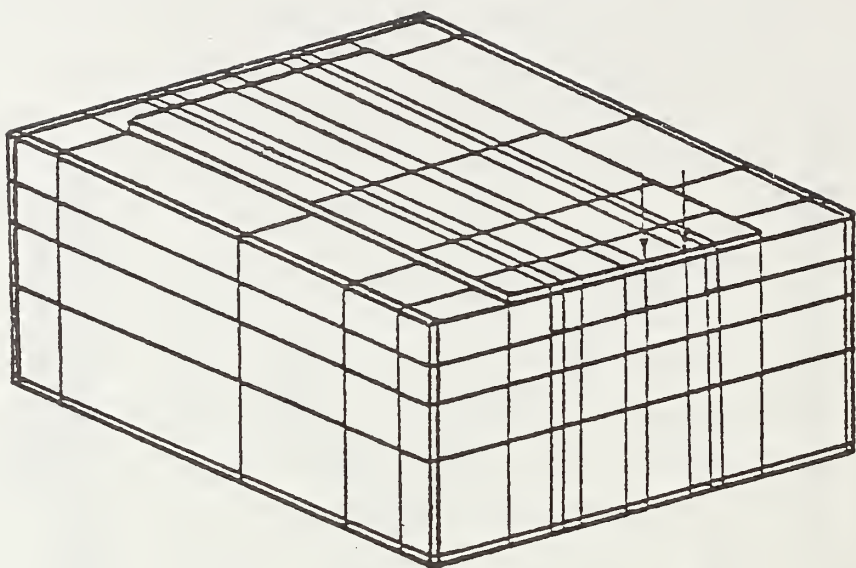
Figure 58 shows the surface deflection contours for the sequence ASE62 with a maximum deflection of 0.011 in. (0.28 mm) at the right edge of the centerline (near the load), with no serious uplift. Only the left far edge is lifted, with a maximum uplift of 0.001 in. (0.03 mm). The stress and strain contours are plotted in Figure 59, with a maximum stress of 1 psi (0.07 kg/cm^2) and a maximum strain of 0.0008 (in./in. or cm/cm) underneath



SS62 represents a simply supported convention-
al slab

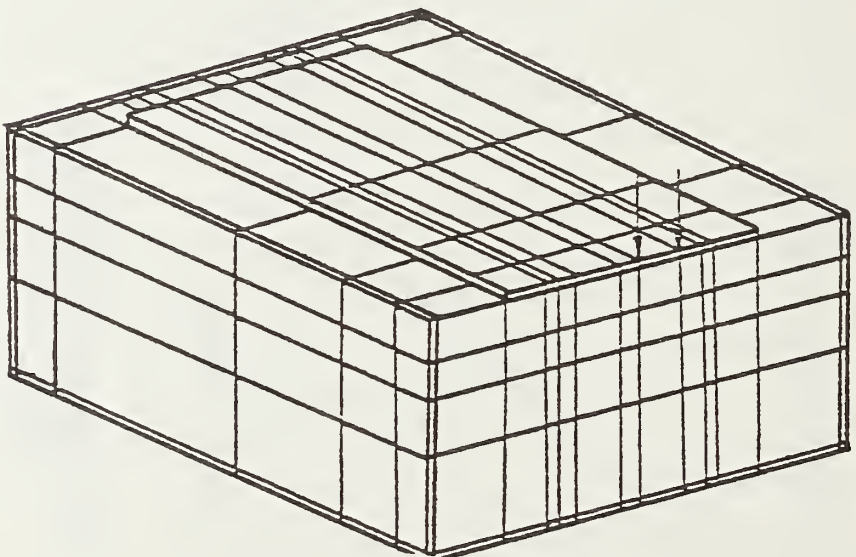
SAS62 represents a simply supported anchored
slab

Figure 51. Longitudinal deflections at center for comparison of finite element models of SS62 and SAS62.



a) Finite element model of AS62.

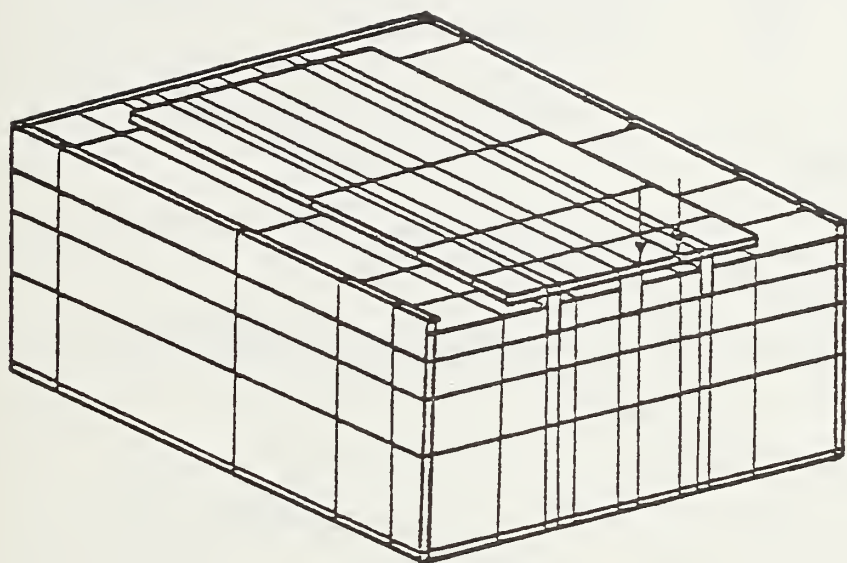
AS62 represents 62 in. long
anchored slab on soil
subgrade



b) Finite element model of S62.

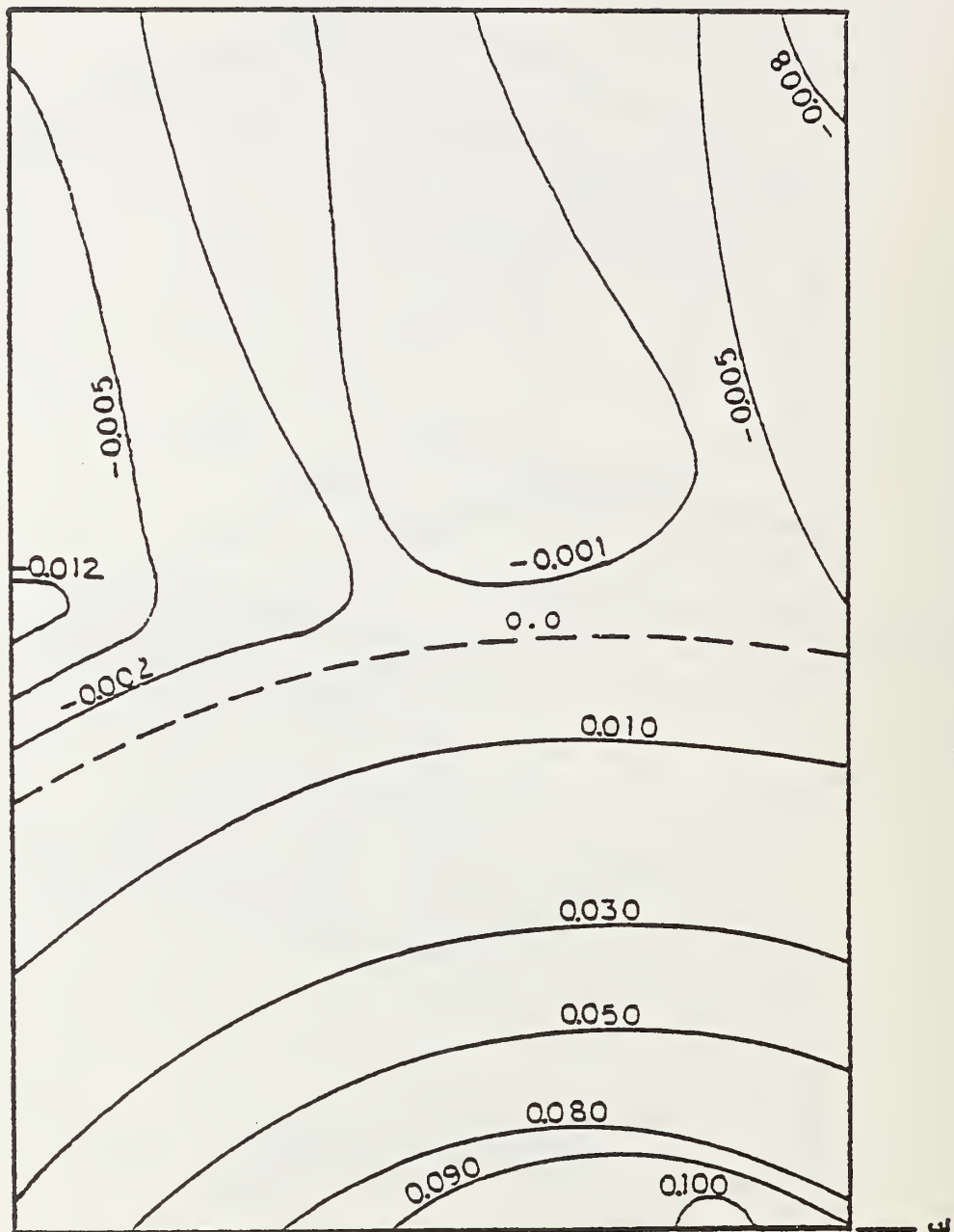
S62 represents 62 in. long
slab on soil subgrade

Figure 52. Finite element models of AS62 and S62 for stress analysis verification.



ASE62 represents 62 in. long
anchored slab elevated
0.5 in. on soil subgrade

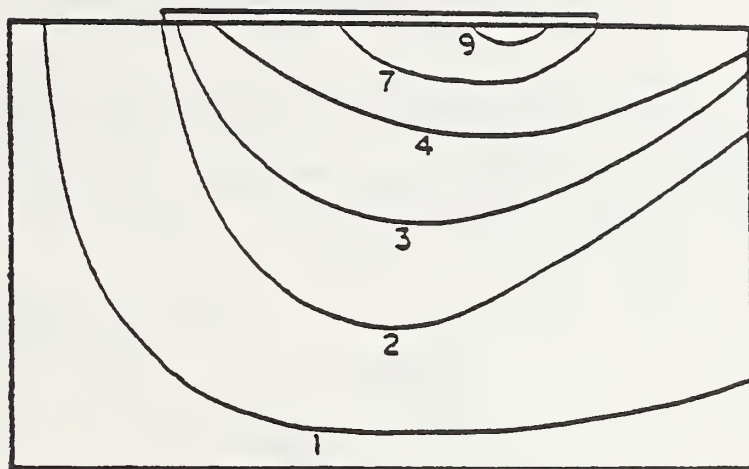
Figure 53. Finite element model of ASE62 for stress analysis verification.



1 in. = 2.54 cm

S62 represents 62 in. long
slab on soil subgrade

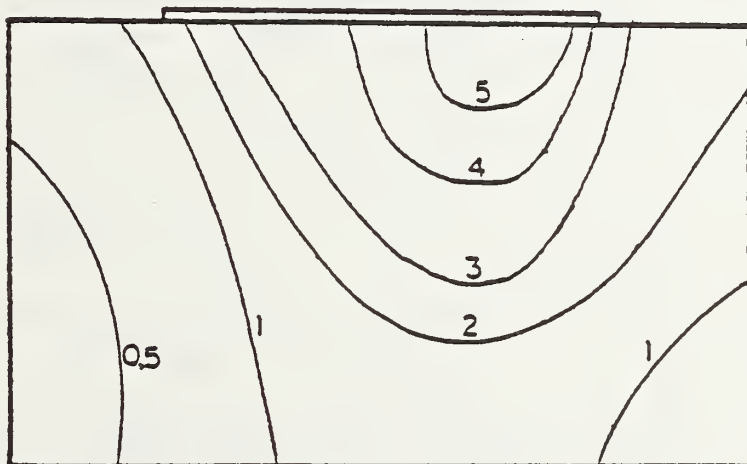
Figure 54. Surface deflection contours (in.) for 750-lb. (340kg) load at position 1 of S62.



$$1 \text{ psi} = 0.07 \text{ kg/cm}^2$$

a) Vertical stress (psi) contours.

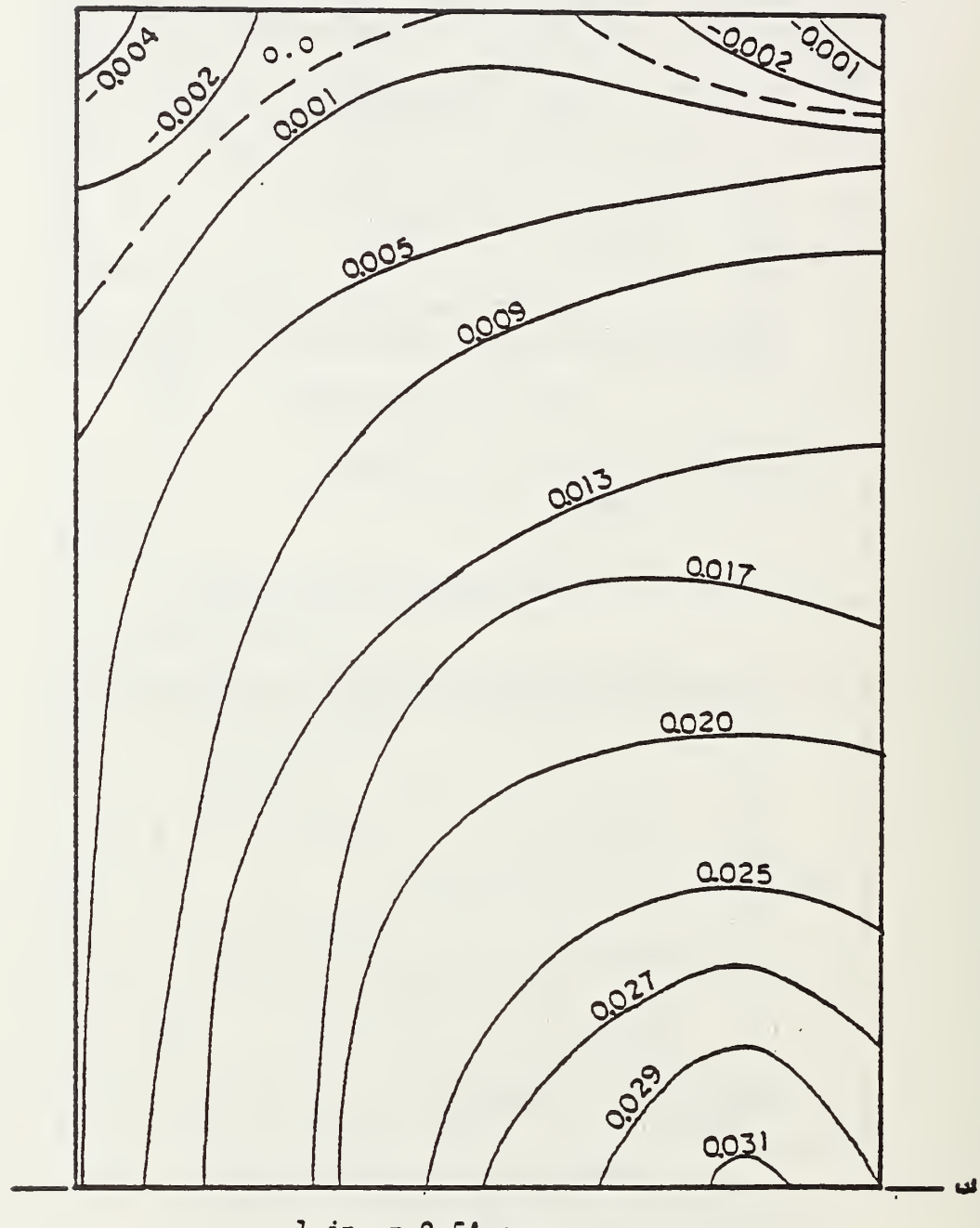
S62 represents 62 in. long
slab on soil subgrade



$$1 \text{ micro in./in.} = 0.001 \text{ cm/cm}$$

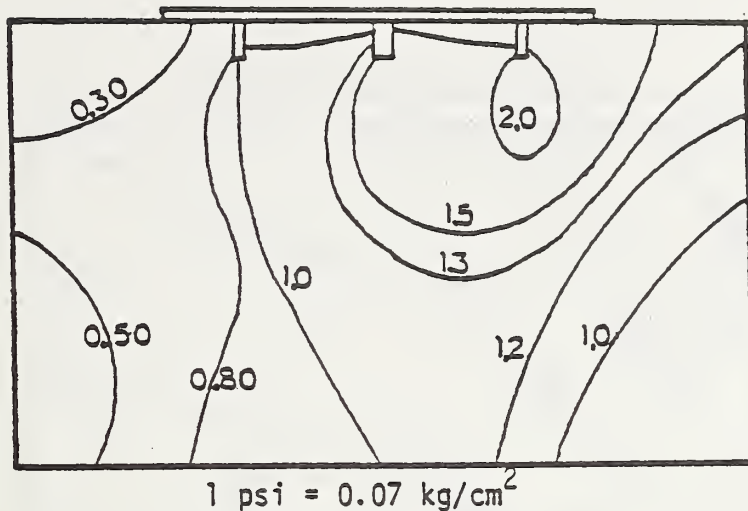
b) Vertical strain (microin./in.) contours.

Figure 55. Vertical stress and strain contours for 750-lb.
(340 kg) load at position 1 of S62.



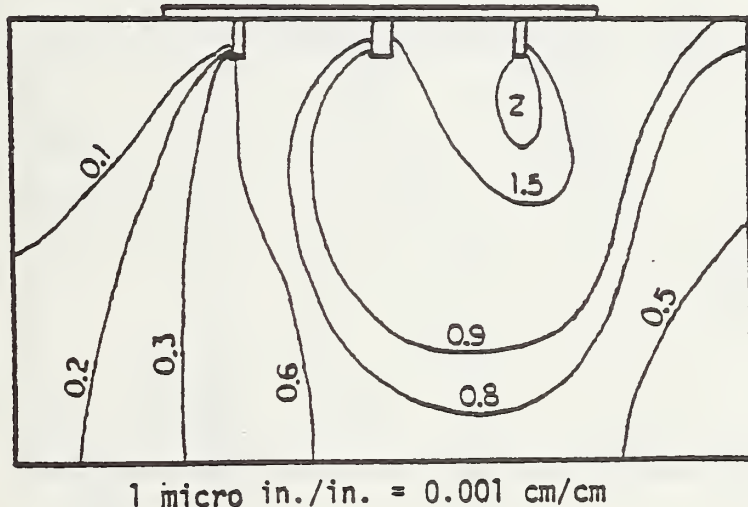
AS62 represents 62 in. long
anchored slab on soil
subgrade

Figure 56. Surface deflection contours (in.) for 750-lb.
(340 kg) load at position 1 of AS62.



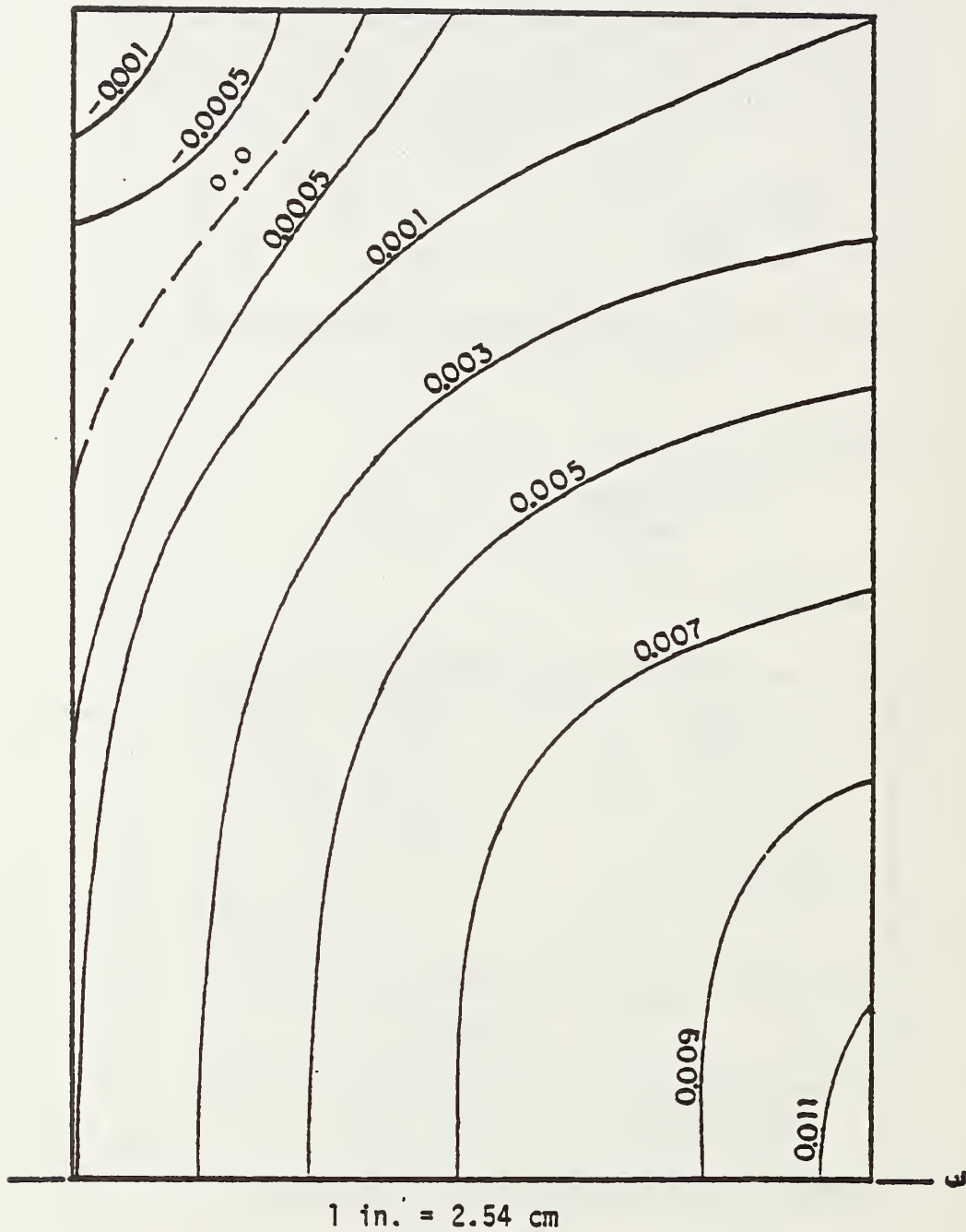
a) Vertical stress (psi) contours.

AS62 represents 62 in. long
anchored slab on soil
subgrade



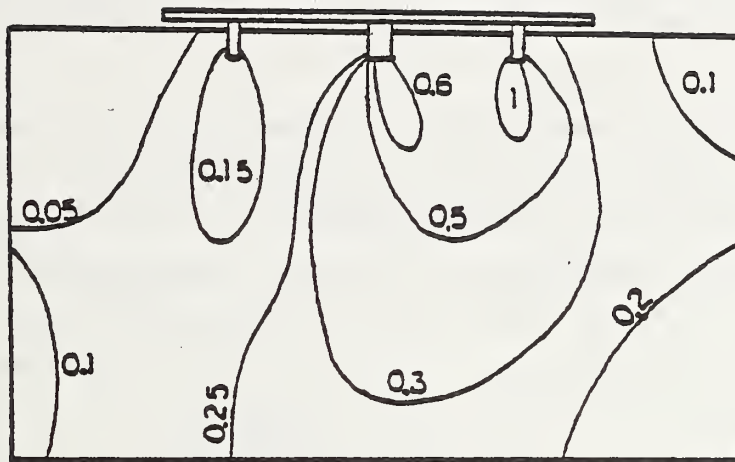
b) Vertical strain (micro in./in.) contours.

Figure 57. Vertical stress and strain contours for 750-lb.
(340 kg) load at position 1 of AS62.



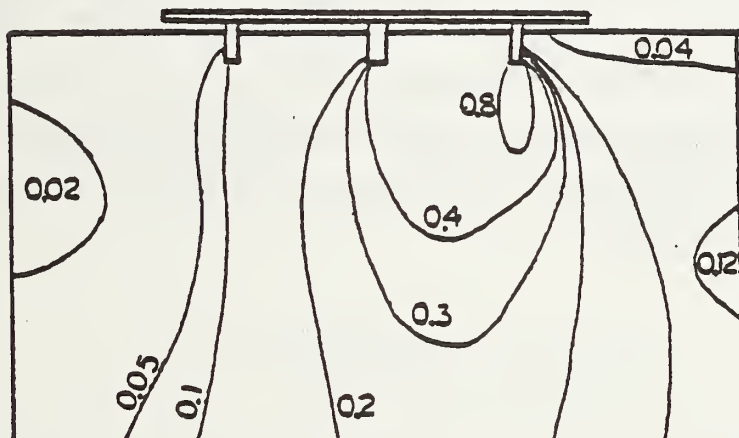
ASE62 represents 62 in. long
anchored slab elevated
0.5 in. on soil subgrade

Figure 58. Surface deflection contours (in.) for 200-lb.
(91 kg) load at position 1 of ASE62.



$$1 \text{ psi} = 0.07 \text{ kg/cm}^2$$

a) Vertical stress (psi) contours.



$$1 \text{ micro in./in.} = 0.001 \text{ cm/cm}$$

b) Vertical strain (micro in./in) contours.

ASE62 represents 62 in. long
anchored slab elevated
0.5 in. on soil subgrade

Figure 59. Vertical stress and strain contours for 200-lb (91 kg) load at position 1 of ASE62.

the right anchor (near the load). The central anchors carry 23% less than the right anchors, while the left anchor carries 49% less load than the right anchor.

The finite element results are compared with the experimental analysis. For sequence S62, the transverse surface deflections of the finite element model along the transverse center line T1-R1 for 750-1 lb. (342 kg) load at position 1, are plotted in Figure 60. The difference is about 20%. The conventional slab was loaded after the anchored and elevated anchored pavement loading was completed. It is apparent that many loadings and unloadings have strengthened the soil. This is probably one of the major factors contributing to this difference between experimental and analytical values. In Figure 61, the transverse and longitudinal centerline surface deflections of the finite element model of AS62 for 750-1 lb. (342 kg) load are plotted. The difference is about 11%. The longitudinal and the transverse surface deflections of the finite element model of ASE62 are shown in Figure 62 for a 300-lb. (157 kg) load at position 1. The difference of the transverse deflection (T1-R1) between the finite element and the experimental results of ASE62 is about 18%. In general, the trends of observed deflections of the model tests agree well with the analytical (finite element) results.

Although the results of only a few of the many experiments conducted are presented in this report, the inferences are based on a study of all the experimental results.

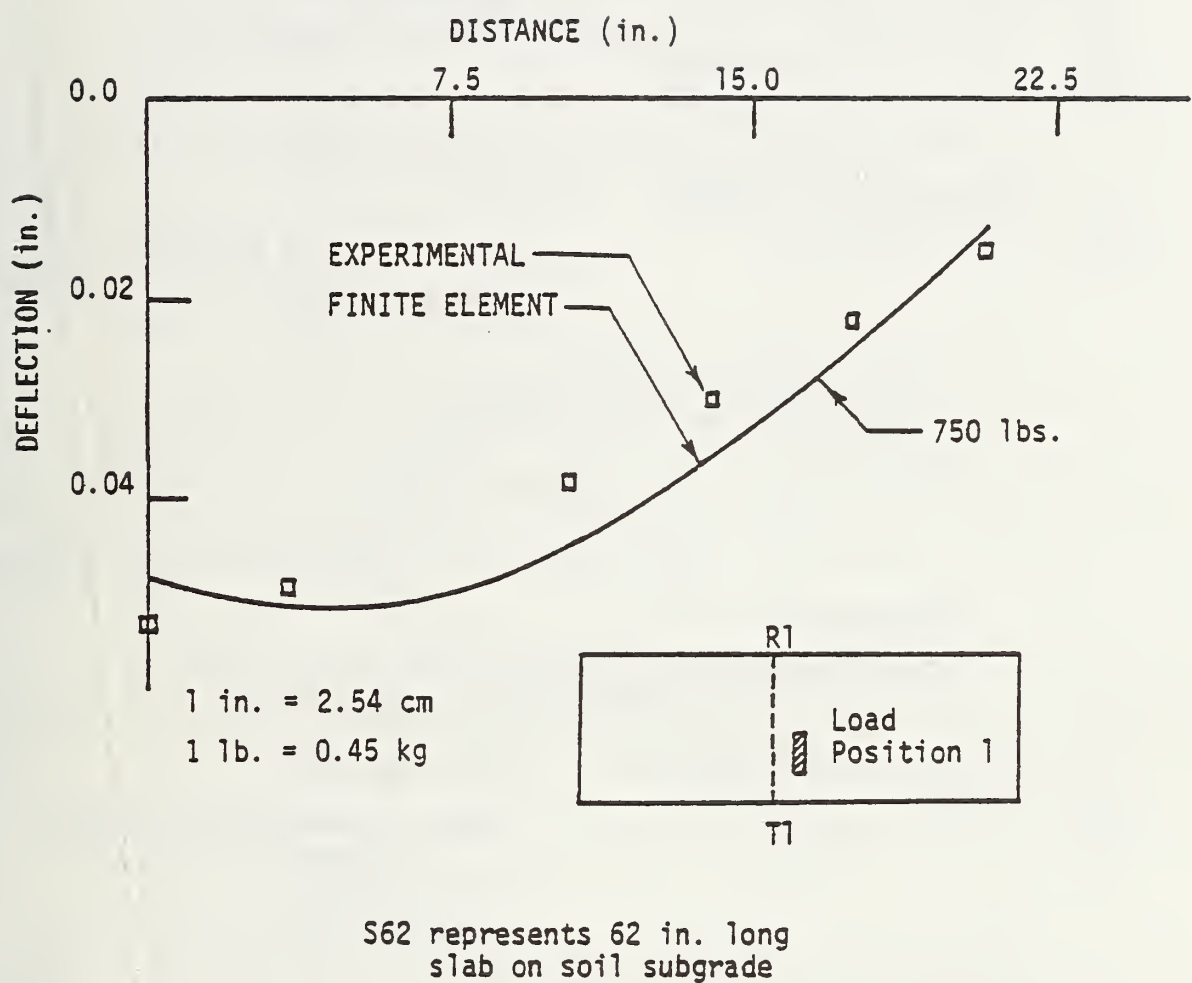
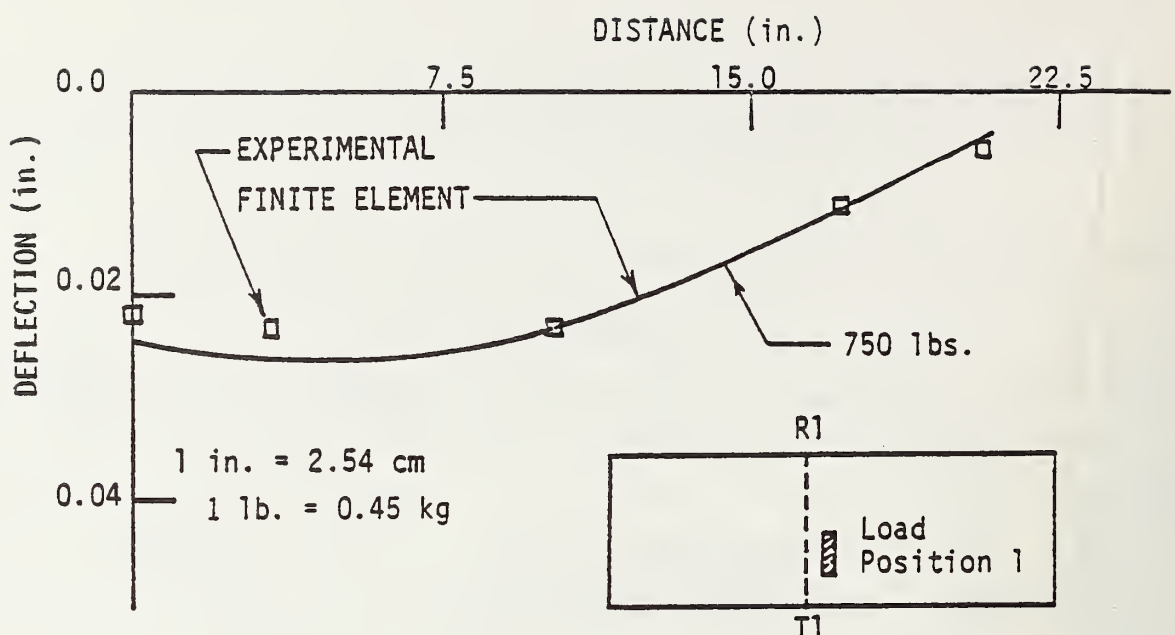
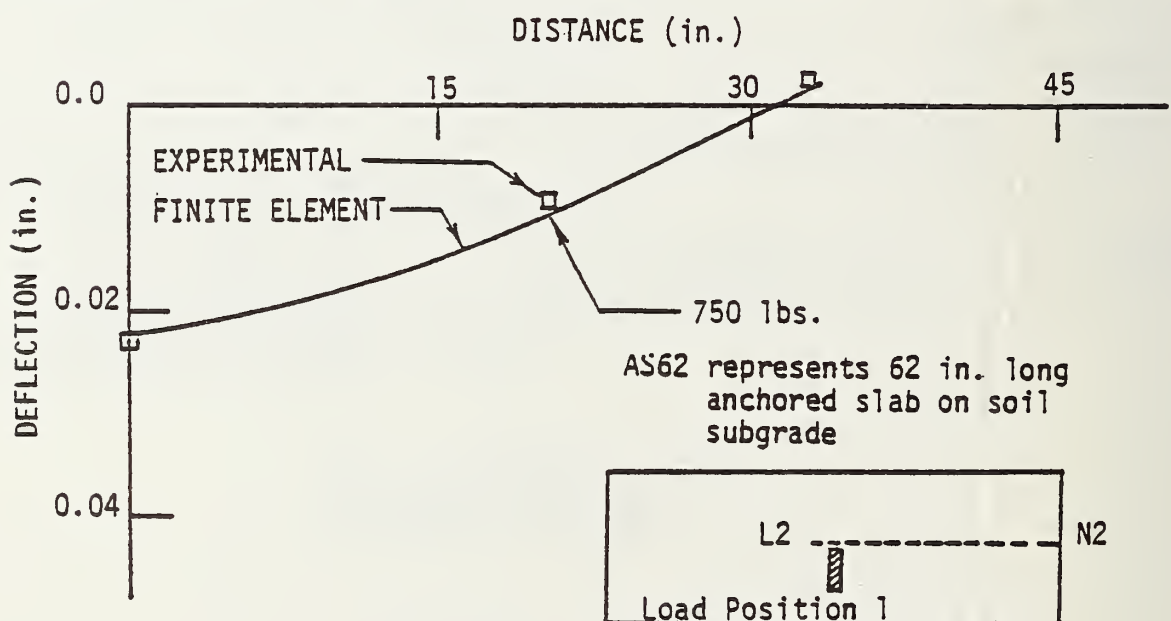


Figure 60. Transverse surface deflection along line T1-R1, load position 1 of S62.

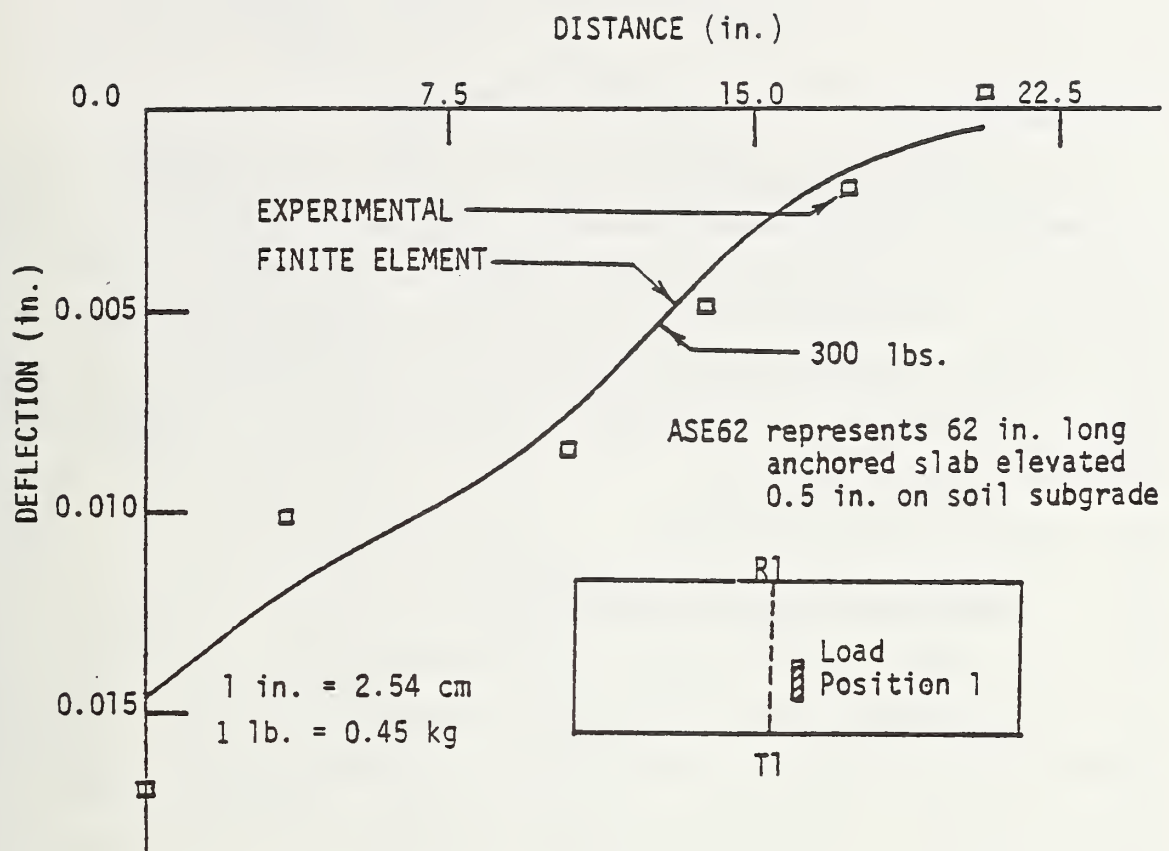


a) Transverse surface deflection along line T1-R1,
load position 1, AS62.

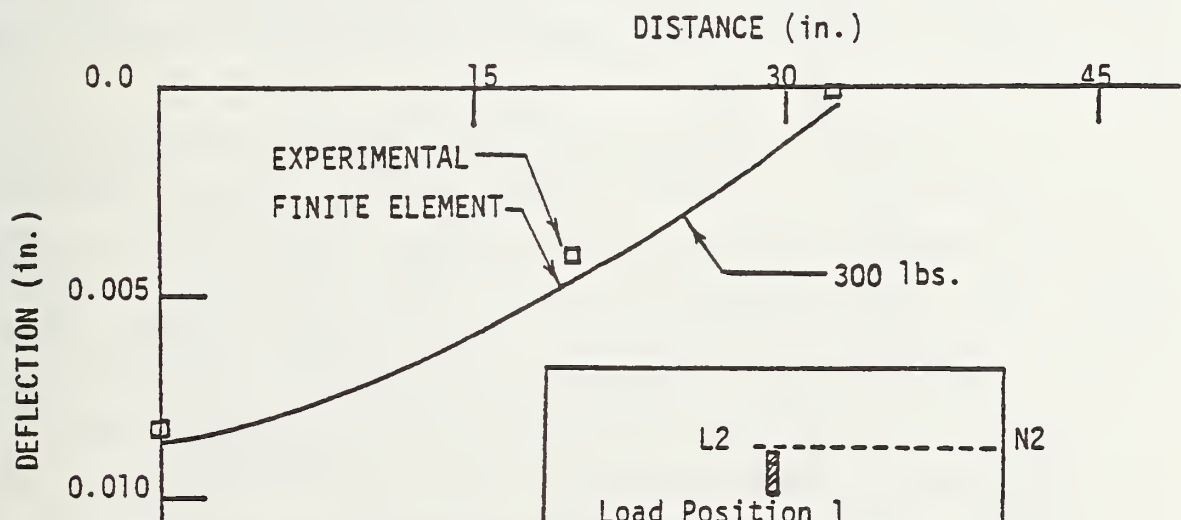


b) Longitudinal surface deflection along line L2-N2, load
load position 1, AS62.

Figure 61. Transverse and longitudinal surface deflection along
lines T1-R1 and L2-N2, load position 1, AS62.



a) Transverse surface deflection along line T1-R1,
load position 1, ASE62.



b) Longitudinal surface deflection along line L2-N2,
load position 1, ASE62.

Figure 62. Transverse and longitudinal surface deflection along lines T1-R1 and L2-N2, load position 1, ASE62.

CHAPTER IV

ANALYSIS OF THE PAVEMENT SYSTEMS

4.1 INTRODUCTION

The goal of the analysis was to compare the behavior of the proposed pavement system (the anchored pavement) with that of a conventional pavement. The physical configuration of each pavement has been shown in Chapter I (Figure 1). The results of the analysis are divided into two parts - environmental loading effects and mechanical loading effects. The results are later superimposed. A pavement joint is also analysed for suitability in the proposed anchored pavement.

4.2 MATERIAL CHARACTERIZATION

4.2.1 General Behavior of Pavement Systems

Pavement systems generally do not exhibit the same behavior throughout the year. In areas prone to freezing or freeze/thaw cycles, pavement behavior is often radically different under frozen and unfrozen conditions, especially in frost-susceptible soils such as clays and silts. Carpenter (1976) and others have attempted to isolate gross climatic conditions in the United States using descriptors such as Wet-Freeze/Thaw, Dry-No Freeze (Figure 63). By rationally determining the extreme conditions which occur with a high enough probability, it is possible to design a pavement system to withstand these extremes as well as more normal conditions.

As an example, consider the results reported by Moore *et al.* (1969) for surface deflections of a flexible pavement in a wet, seasonal freeze-thaw area. Figure 64 presents a trend in surface deflection characteristics throughout a typical year. Four primary periods exist in the yearly cycle: 1) period of deep frost characterized by low deflections due to increased rigidity of the pavement as well as increased bearing capacity and modulus of subgrade reaction of the soil; 2) period of rapid strength loss during the spring thaw, which gives rise to a corresponding rapid increase in surface deflections; 3) period of rapid recovery in late spring; and 4) period of gradual slow strength recovery leading back to the frost condition. There would probably be a rather rapid strength recovery after the first permanent frost preceding the period of low deflections, thus starting the cycle again. Shapes of deflection basins at certain key times can be seen in Figure 65. The almost uniform deflection in the frost period and

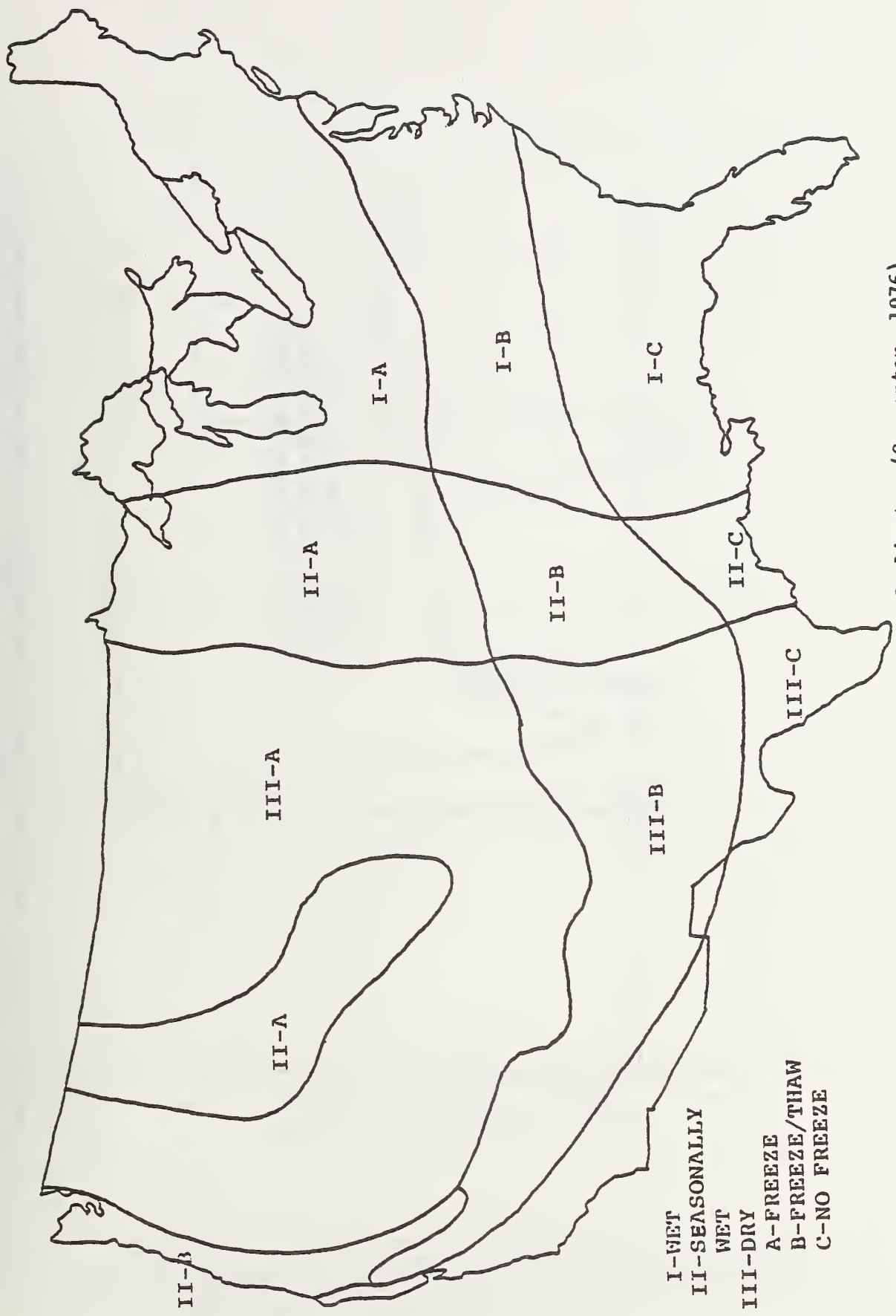


Figure 63. Geographic delineation of climates (Carpenter, 1976).

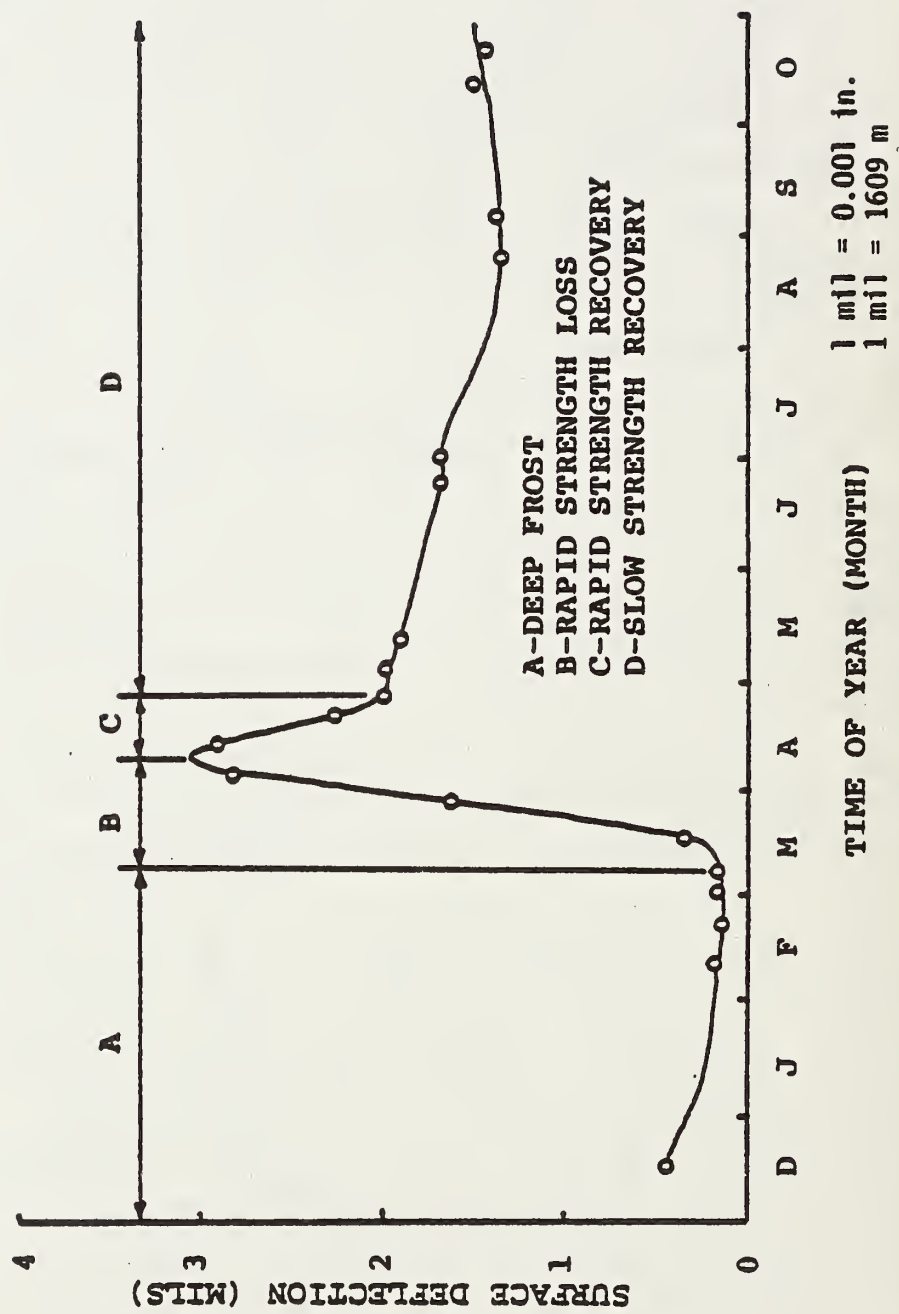


Figure 64. Typical variation of surface deflection in a freeze/thaw seasonal cycle (Moore et al., 1969).

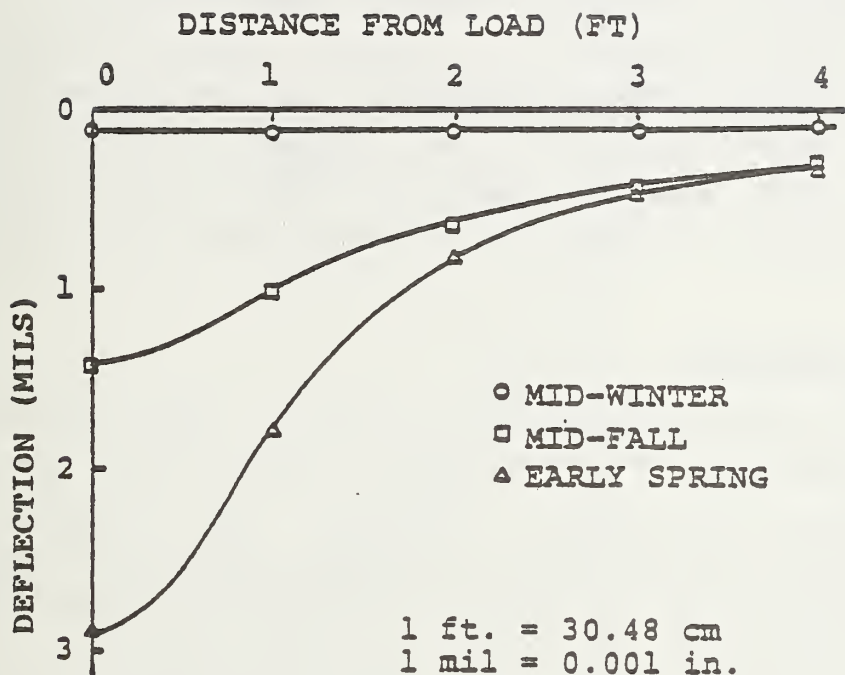


Figure 65. Comparison of deflection basins for various times of year under 1000 pound load (453.6 kg) of dynaflect test apparatus (Moore et al. 1969).

the more localized deformation during the period of subgrade weakening in early spring can be easily noted.

One obvious critical period in the structures' design life is the cyclic appearance of these periods of rapid strength loss. This problem is aggravated by the upward flow of moisture in both liquid and vapor form as soil freezes due to flow along thermal gradients and also due to subpressures at the freezing front. When the thaw period arrives, a greater than normal water content exists in the upper layer of the subgrade, and the soil is greatly weakened. Figure 66 shows the typical seasonal change in moisture content near the surface of various classes of soil. In general, the water content increases until the thaw period then decreases gradually. The finer grained soils (clays), because of lower permeability, exhibit smaller changes in moisture throughout the year. Also, during summer, as temperatures increase, evapo-transpiration tends to decrease moisture content until the freezing period when the cycle is reinitiated.

4.2.2 Material Properties

Two basic types of analysis were performed: heat transfer analysis and mechanical stress analysis. The finite element formulation used for analysis requires knowledge of certain material properties. ANSYS is capable of handling temperature-dependent, nonlinear material mechanical behavior and temperature-dependent thermal properties such as thermal conductivity and heat capacity.

Due to the extreme variability in soil properties from soil to soil and with variation in moisture, temperature, confining pressure, etc., it was decided to choose typical extreme values for properties to represent limiting (best or worst) cases rather than attempt a parametric study of pavement response under several types of material constituents.

4.2.2.1 Thermal. Heat transfer through soils is primarily a conduction phenomenon; however, convection and radiation do occur. Solar radiation and convection through air and liquids at the soil surface as well as convection of heat through vapor, soil, and liquid interfaces within the pore structure are possible. In the basic three-dimensional heat transfer equation for conduction,

$$c \frac{\partial T}{\partial t} = \frac{\partial}{\partial x} (k_x \frac{\partial T}{\partial x}) + \frac{\partial}{\partial y} (k_y \frac{\partial T}{\partial y}) + \frac{\partial}{\partial z} (k_z \frac{\partial T}{\partial z})$$

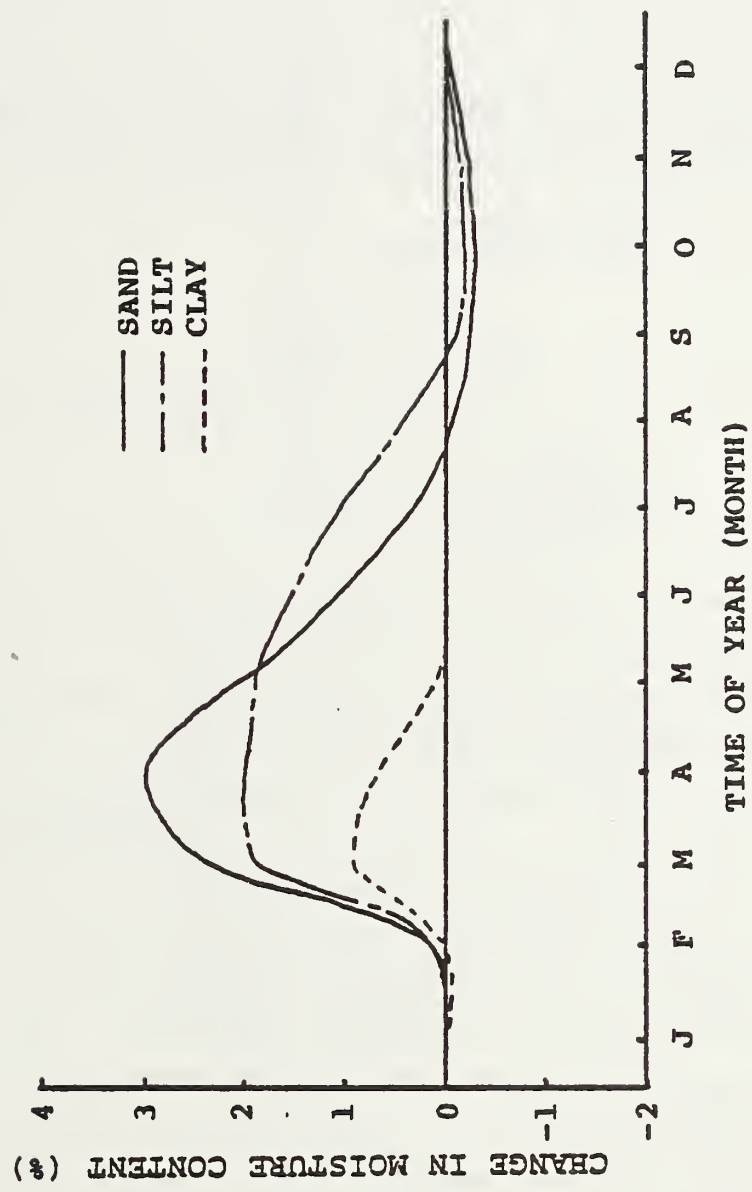


Figure 66. Seasonal change in moisture content (Cumberledge et al., 1973).

two material properties are required: heat capacity, c , and conductivity, k . Heat capacity is defined as the quantity of heat necessary to produce a unit change in temperature for a unit mass. Because of the multi-phase character of soil (vapor, liquid, minerals), the total heat capacity is usually a weighted sum of the components such that

$$c = \sum g_i c_i$$

5

where g_i is the mass of the i^{th} component and c_i is its heat capacity per unit mass. A specific relation can be made for frozen and unfrozen soils:

$$T > 0^{\circ}\text{C}: c_v = \gamma_d c_{ms} + \frac{w_T}{100} \gamma_d c_{mw}$$

6

$$T < 0^{\circ}\text{C}: c_v = \gamma_d c_{ms} + \frac{w_T}{100} \gamma_d c_{mw} + \frac{w_{IT}}{100} \gamma_d c_{mi}$$

7

$$+ \left(\frac{\Delta w/100}{\Delta T} \right) T \gamma_d L$$

where γ_d is soil dry density; c_v is volumetric heat capacity; L is latent heat of fusion of water; c_{ms} , c_{mw} , and c_{mi} are mass heat capacities of soil, water, and ice, respectively; w_T and w_{IT} are moisture contents of unfrozen and frozen water at temperature T , respectively; and the term in parenthesis is the gradient of unfrozen water content versus temperature at temperature T (Williams, 1973). The heat capacity of moist soil as it freezes is thus augmented by the latent heat of fusion of water, which produces a large spike in the c versus T relation, often 20 to 200 times as great as unfrozen or well-frozen soil heat capacities, depending upon water content. This spike generally appears over a small range of temperatures, usually less than 1°F (0.56°C) (Figure 67). Some typical volumetric heat capacities for soils are presented in Figure 68 showing variation in c_v with temperature as a soil freezes and as it thaws. Table 3 presents values for soils and structural materials that are used in the finite element models. Notice that asphaltic concrete and plain concrete can have peaks if some moisture is present in pores.

Conductivity is a measure of the ease with which heat can flow through a material. Some typical variations of thermal conductivity with temperature for soils and structural materials are shown in Figure 69. Kersten (1949) has made extensive laboratory tests to measure conductivity of soils and has developed

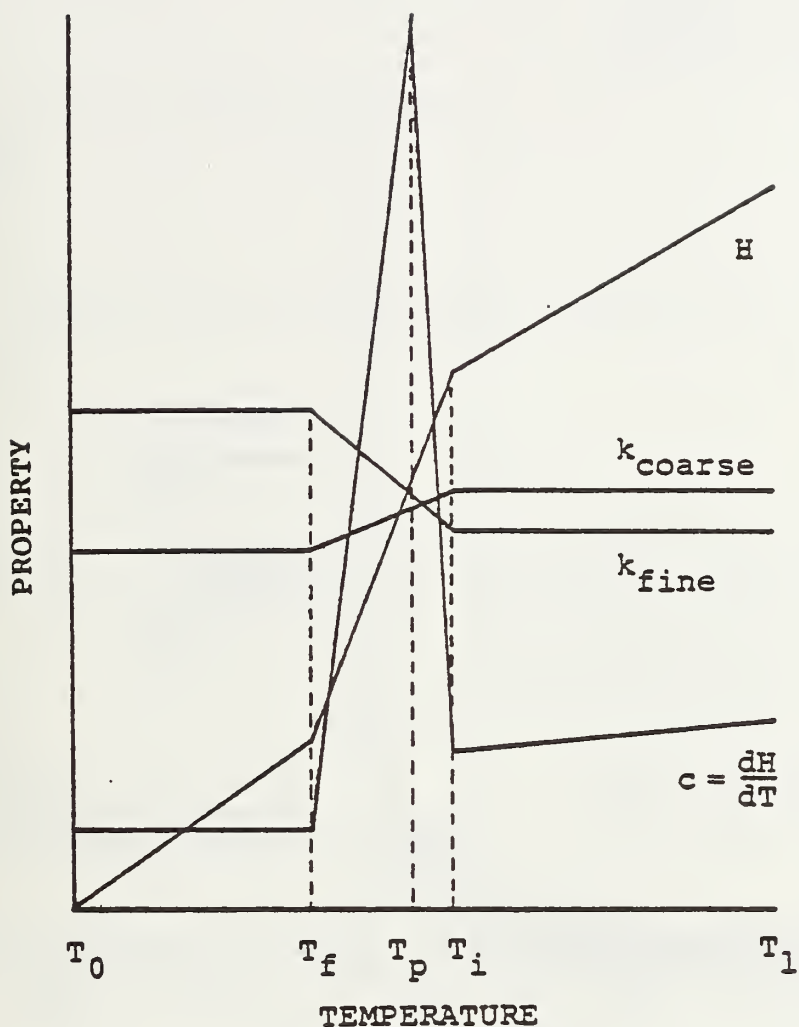


Figure 67. Conceptual dependence of thermal properties on temperatures (Frivik et al., 1977; Comini et al., 1974).

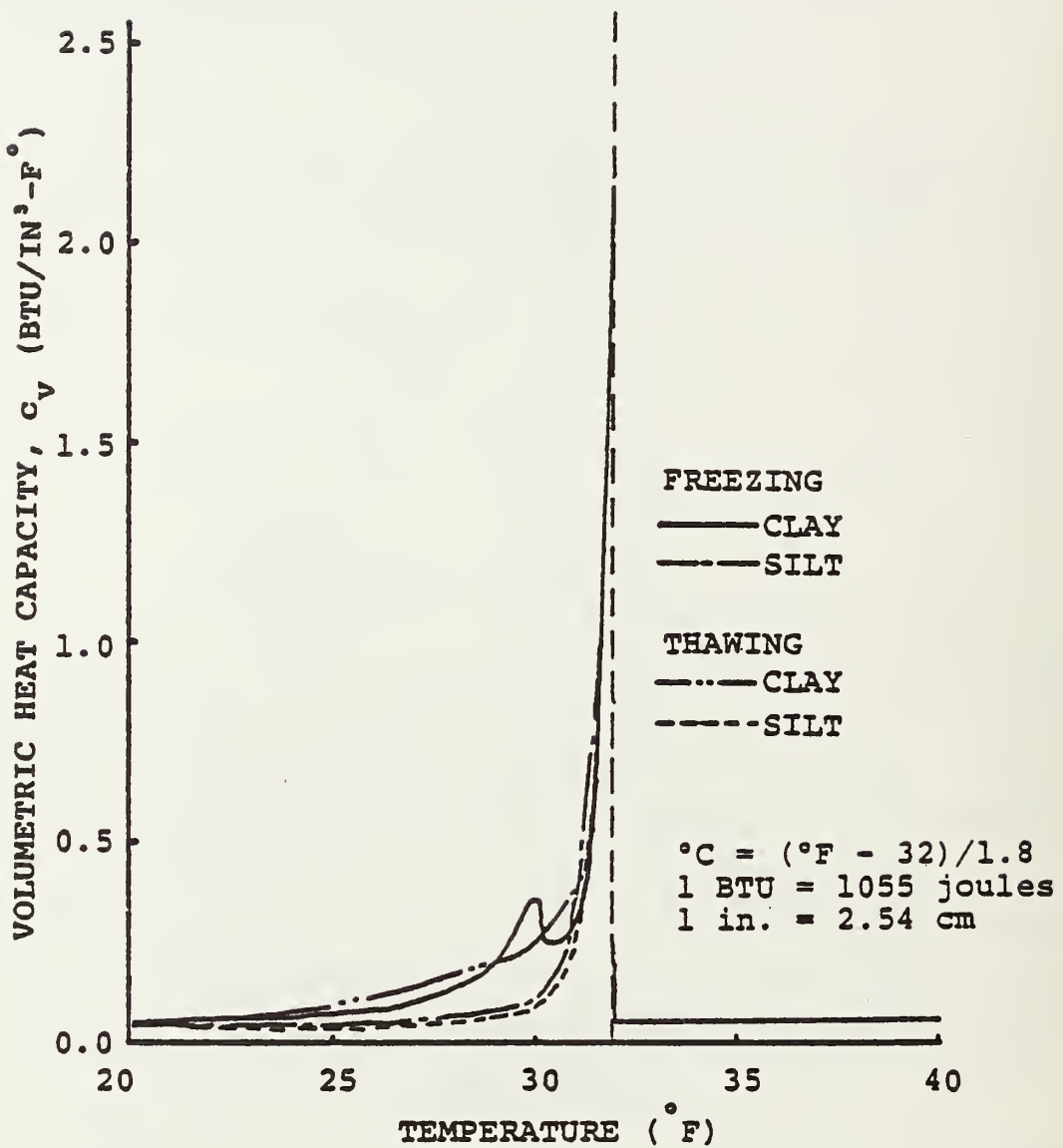


Figure 68. Volumetric heat capacities of various soils near freezing temperatures (Williams, 1973).

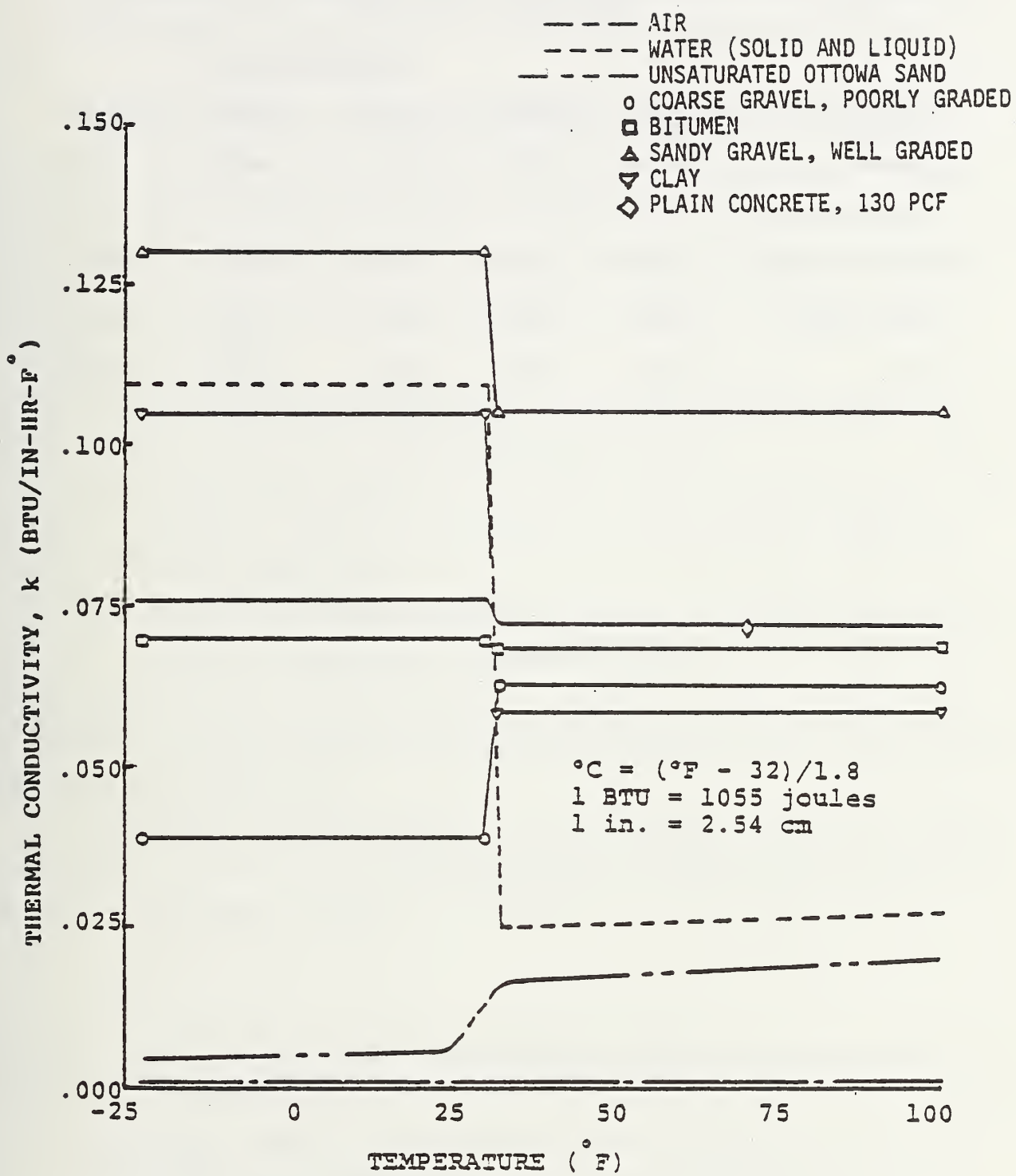


Figure 69. Variation of thermal conductivities with temperature (Frivik et al., 1977; Neville, 1963; Sucec, 1975; Hoekstra, 1969).

Table 3. Typical heat capacities of road materials (BTU/lb.-F⁰)
 (Frivick et. al., 1977).

MATERIAL	TEMPERATURE (°F)				
	-22.00	30.38	31.98	32.00	122.00
Bitumen	0.22	0.22	10.1	0.26	0.29
Plain Concrete					0.16
Coarse Gravel	0.18	0.18	5.06	0.19	0.22
Sandy Gravel	0.23	0.23	29.0	0.31	0.33
Clay	0.22	0.22	33.4	0.30	0.32

$$^{\circ}\text{C} = ({}^{\circ}\text{F} - 32)/1.8$$

empirical relations for thermal conductivity of frozen and unfrozen sands and clays based on water content (Figure 70). His general observations are as follows:

1. k of unfrozen soil increases slightly with temperature.
2. At optimum moisture content for compaction, the k below freezing averages about 17% greater than above freezing.
3. At a constant moisture content, as density increases, k increases.
4. At constant density, as moisture increases, k increases up to saturation.
5. For saturated unfrozen soils, k decreases as density decreases. For frozen soils, there is no clear relation.
6. k varies with texture. For a given density and water content, k is greater in coarser soils (gravel and sand) than in fine soils (silty loam, clay).
7. k varies with mineral content. Quartz has a high k , kaolin a low value, and feldspars an intermediate value.

Thermal conductivity has also been linked to strength, as shown in Figure 71. This relation is rather crude and is a composite of several curves for individual materials (clays, sands, etc.).

Convection at the surface has also been considered. Duffie and Beckman (1974) report a relation for the film coefficient of forced convection heat loss from flat plates exposed to wind:

$$h_w = 5.7 + 3.8v$$

8

where h_w is the film coefficient or heat transfer coefficient in $\text{W/m}^2 \cdot \text{C}^\circ$ and v is wind velocity in m/sec .

4.2.2.2. Mechanical. Mechanical strength properties of materials within pavement systems also vary with temperature. This temperature dependence is important during a thermal stress analysis and reflects material behavior of the system that may be greatly different over different temperature ranges. The temperature-dependent strength properties used in this investigation were elastic modulus (for a linear analysis), Poisson's ratio, and the coefficient of

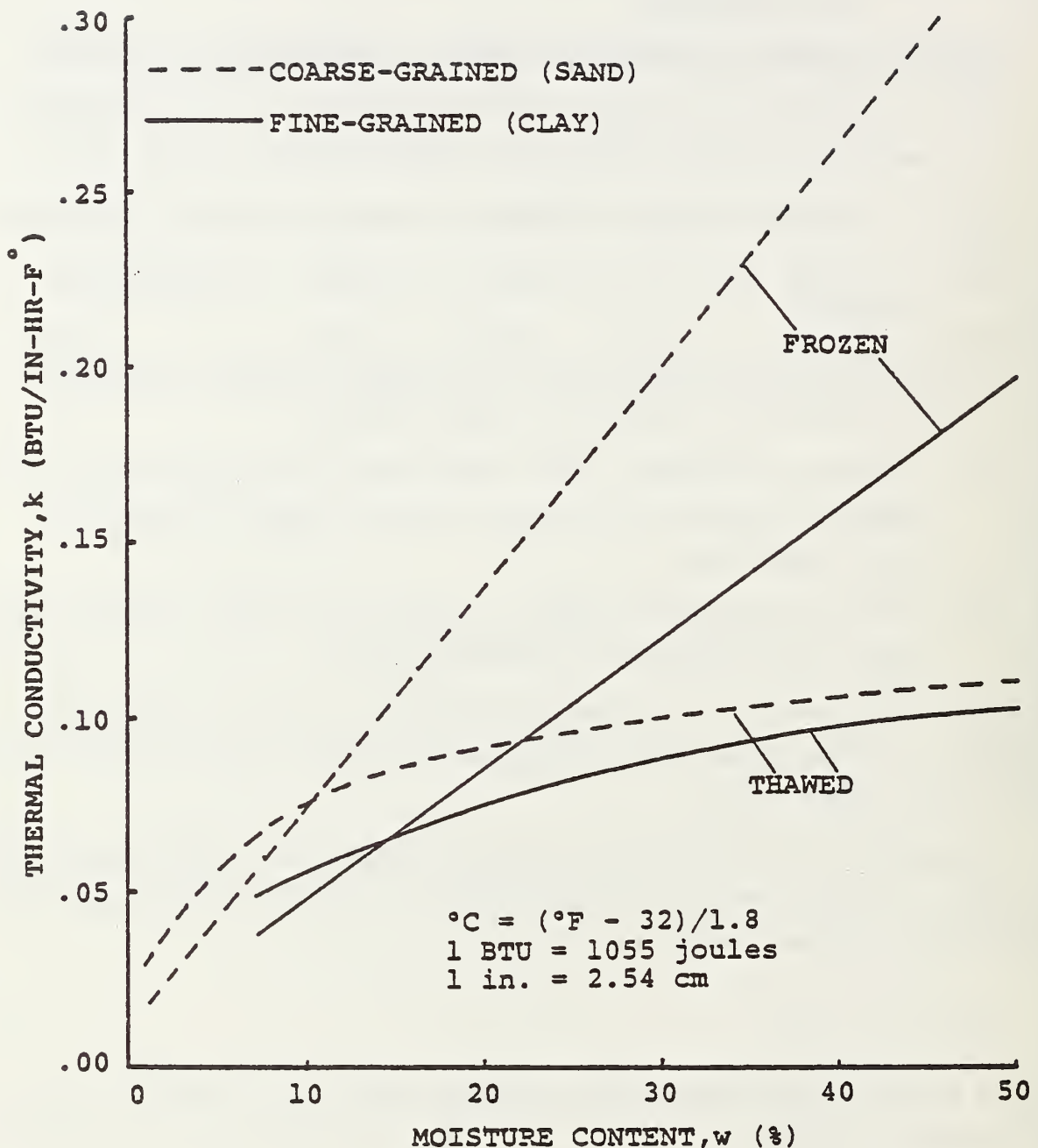


Figure 70. Variation in thermal conductivity of soils with moisture content. (for 100 PCF dry density)
(Kerston, 1949).

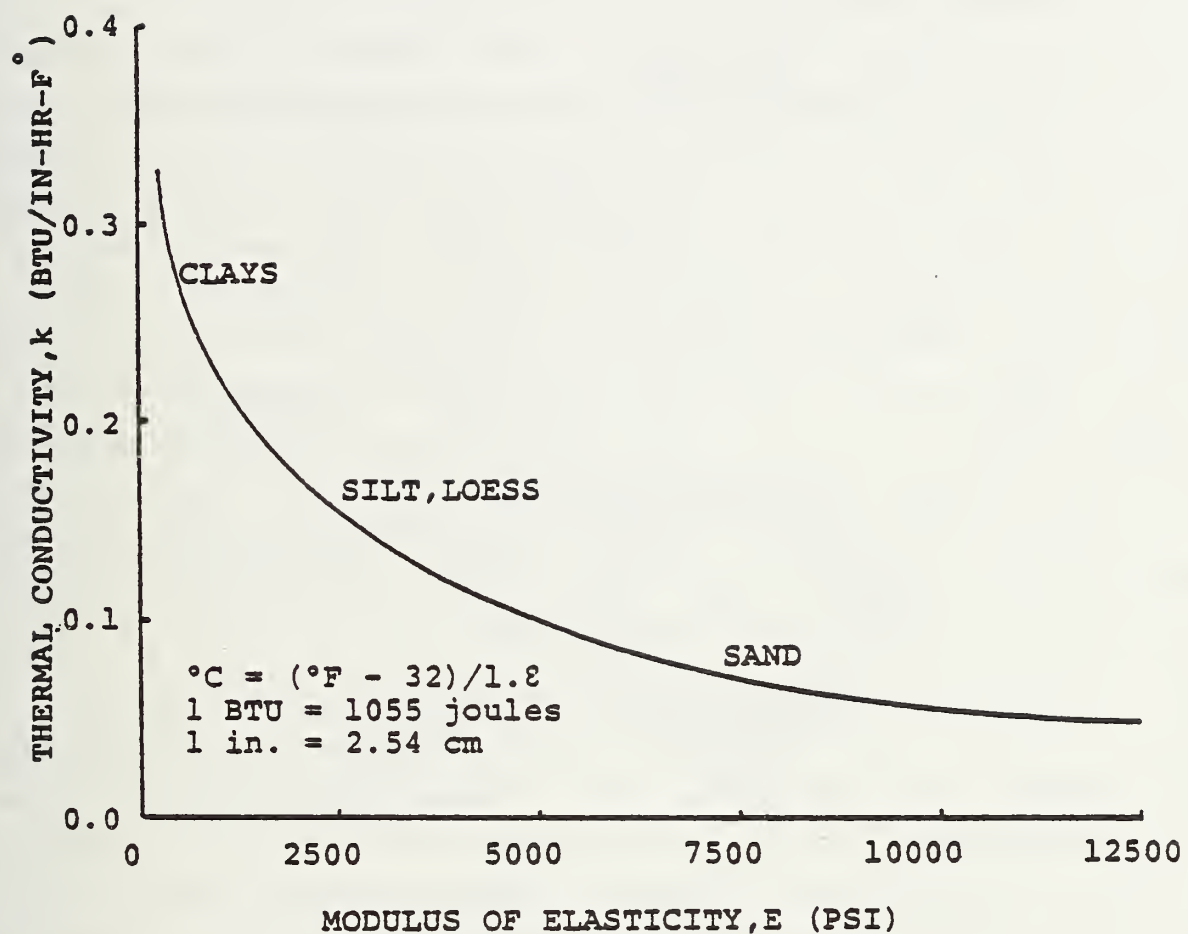


Figure 71. General correlation between modulus and thermal conductivity in frozen soils (Jumikis, 1966).

linear expansion of the material under a uniform temperature gradient. In a nonlinear inelastic analysis, strength is input as a series of piecewise linear stress-strain curves with some initial elastic modulus.

Because of the complex multi-material and multi-phase constituency of soil, it is difficult to characterize behavior over a complete temperature regime with only a modulus and Poisson's ratio. As moist soil freezes, all water within the soil system does not freeze at once. Jumikis (1966) has described the freezing process in soils by first considering the types of water within soil: free water, which exists in pores in bulk and is not bound to the soil particles; capillary water, which is held in sufficiently small pore structures by capillary action; film water surrounding particles in various layers; and hygroscopic moisture actually bound to the soil (film water and hygroscopic water are adsorbed water). These forms of moisture usually exist simultaneously and have different freezing points, resulting in quite complex microscopic behavior. Free water freezes first at 32°F (0°C). Capillary water freezes at about 29.5°F (-1.4°C) and freezing precedes through the less stressed film layers. Film water is stressed by the electrostatic attraction between the water dipoles and the charged surface at the soil particle, so film water close to the particle surface is more highly stressed and has a lower freezing point.

A simplified view of this action is depicted in Figure 72. An arbitrary division of the film into four layers illustrates the freezing process. Layer 1 freezes first, then layer 2, etc. As the stressed water freezes, the bonding forces between water molecules are broken, and they begin to leave the film water and join growing ice crystals. Because free water freezes first, film water tends to migrate to the freezing bulk water ice crystals at and behind the freezing front.

To simulate the mechanical behavior due to this gradual accumulation and growth of ice in the pore structure of moist soils, a modulus versus temperature relation was developed. Figure 73 depicts possible soil behavior as film water freezes, binding soil particles in a matrix of frozen water. The relation is conceptual and would vary greatly from soil to soil. Coarse-grained soil, in which a higher percentage of water is free water, would tend to have a more rapid strength increase as the temperature dropped below freezing due to a smaller unfrozen water content (Figure 74). Finer grained soils, such as clays, with

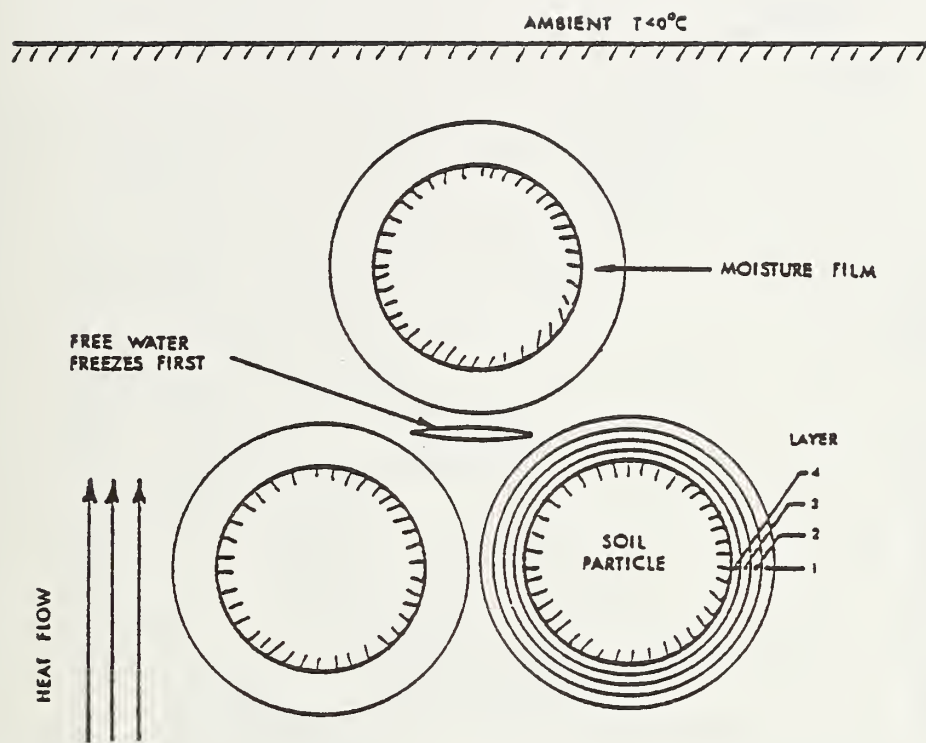


Figure 72. Conceptual diagram illustrating the freezing of soil moisture.

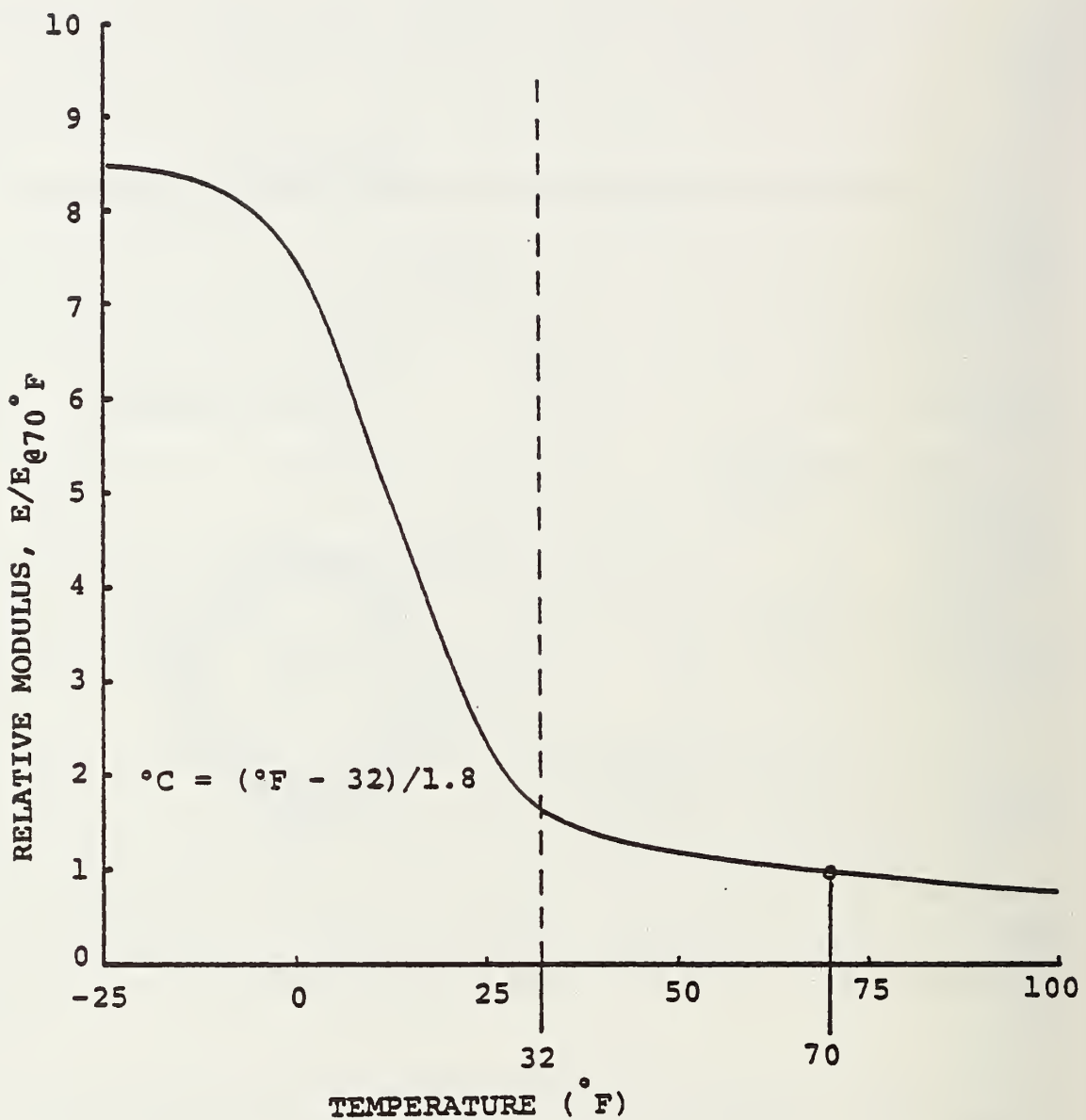


Figure 73. Effect of temperature on modulus of moist, fine-drained soil due to "cementation" of particles by ice (Tystovich, 1975).

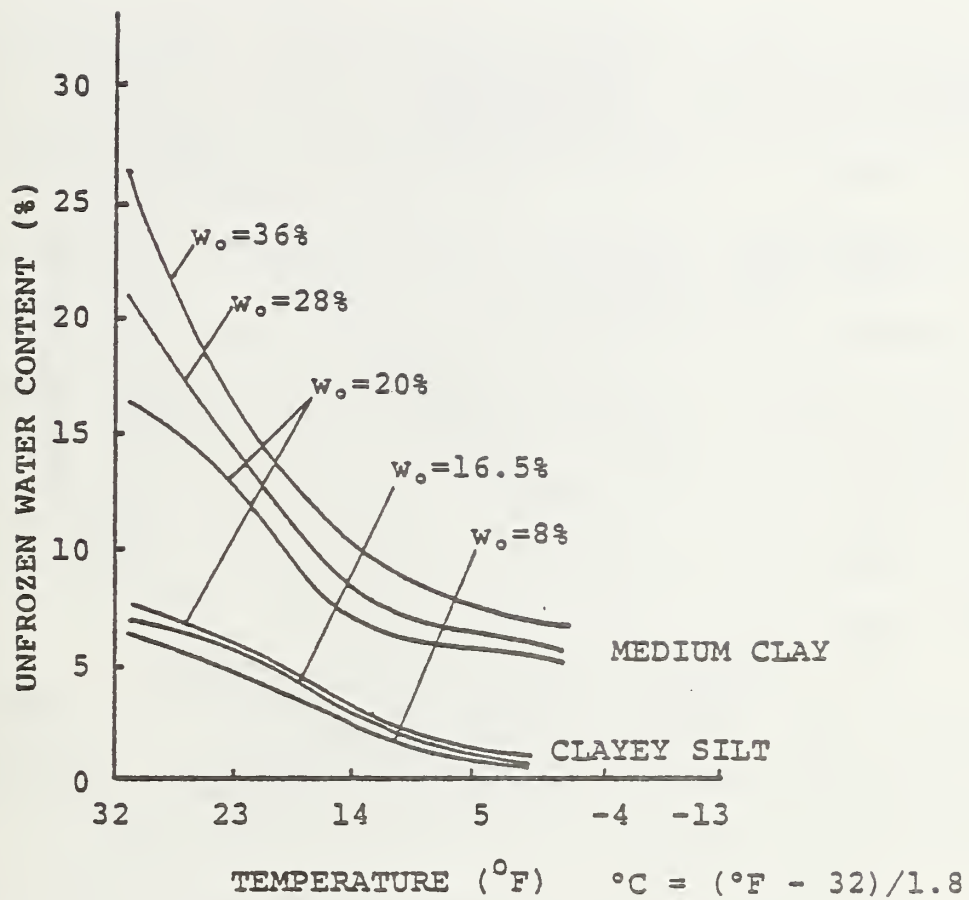


Figure 74. Influence of temperature on the unfrozen water content of soils (Yong, 1965).

high specific surface areas, would probably have the gradual strength increase shown in Figure 73 (Tsytovich, 1975).

The modulus of elasticity of ice varies with temperature and type of ice, but is generally in the range of 300,000 to 1,500,000 psi (21,000 to 105,000 kg/cm²). With this in mind, a crude relation between modulus and temperature may be drawn based upon a weight relation such that

$$E_T = (w_{TI}/100)E_I + (1-w_{TI})/100 E_s \quad 9$$

where E_T , E_I , and E_s are moduli of the total soil system, ice, and unfrozen soil, respectively, and w_{TI} is the percentage of ice in the system. This relation, however, does not consider the matrix-particle effect attributed to the alteration of the gross structure of the unfrozen soil/water system.

Static soil strength for temperatures above freezing is not so variable. Typical compressive strengths for clays at different temperatures and water contents are shown in Figure 75. For a given moisture content, clays decrease in strength with increasing temperature above 70°F (21°C), decreasing approximately 30% in strength for a change of 75°F (42°C). Modulus is however less variable (Figure 76). Poisson's ratio for ice is about 0.33 to 0.38; similar ranges exist in unfrozen soil. Thus, it was assumed that a near constant value of between 0.35 and 0.45 for Poisson's ratio could be used over an expected range of temperatures.

The coefficient of cubic expansion for water as a function of temperature is shown in Figure 77. Because it is a solid, ice shows relatively little volumetric expansion under temperature gradients. Water tends to rise linearly from the freezing point until near the vapor phase.

Structural materials, such as asphaltic concrete (AC), Portland cement concrete (PCC), and steel fiber reinforced concrete (SFRC), also have temperature-dependent material properties, although under different mechanisms. AC is a viscoelastic material that flows. As the temperature increases, its viscosity decreases and flow increases, leading to a structural weakening. Figure 78 depicts this phenomenon by a rapid decrease in modulus at temperatures above 50°F (10°C). Poisson's ratio for AC generally increases with temperature and is limited to a value of 0.5, that of an incompressible fluid.

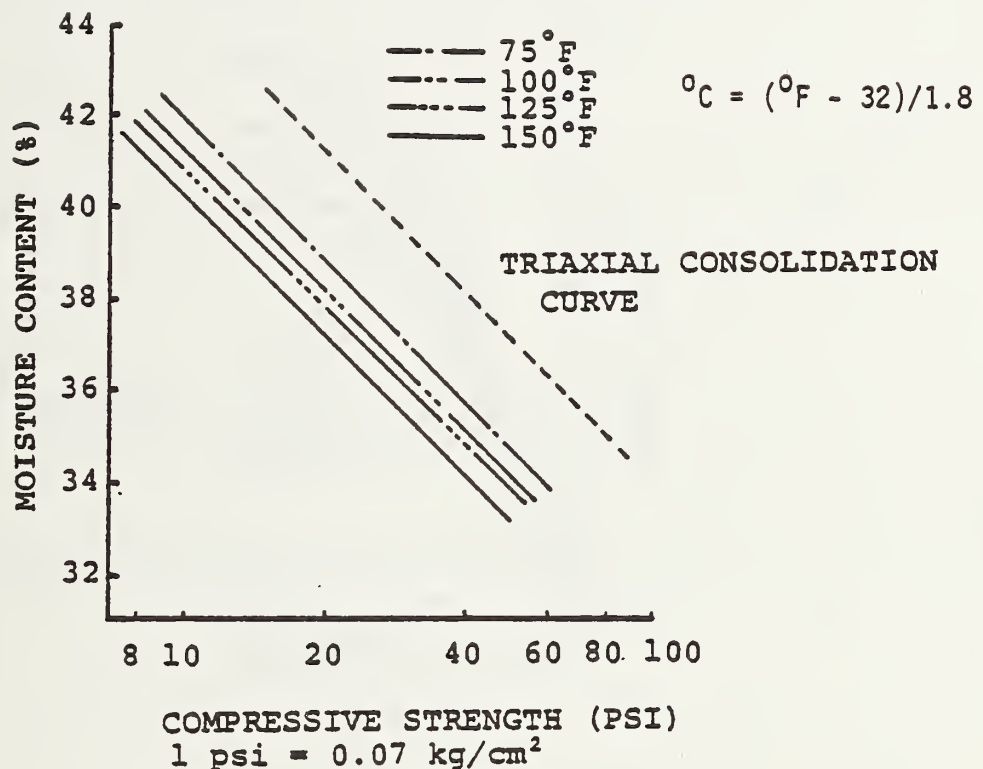


Figure 75. Effect of moisture and temperature on the strength of a clay in compression (Sherif and Burrous, 1969).

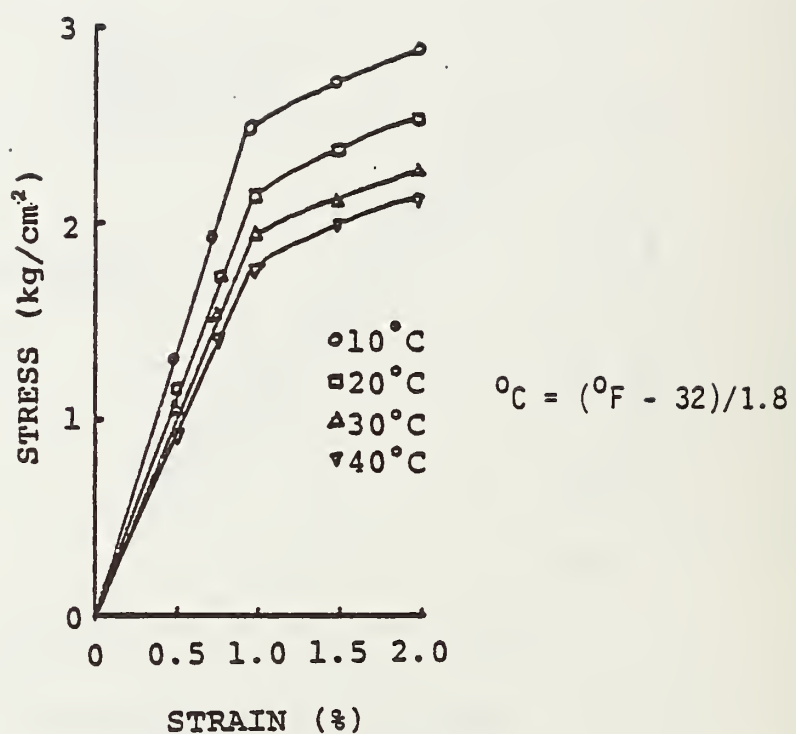


Figure 76. Effect of temperature on the stress-strain behavior of a clay (Murayama, 1969).

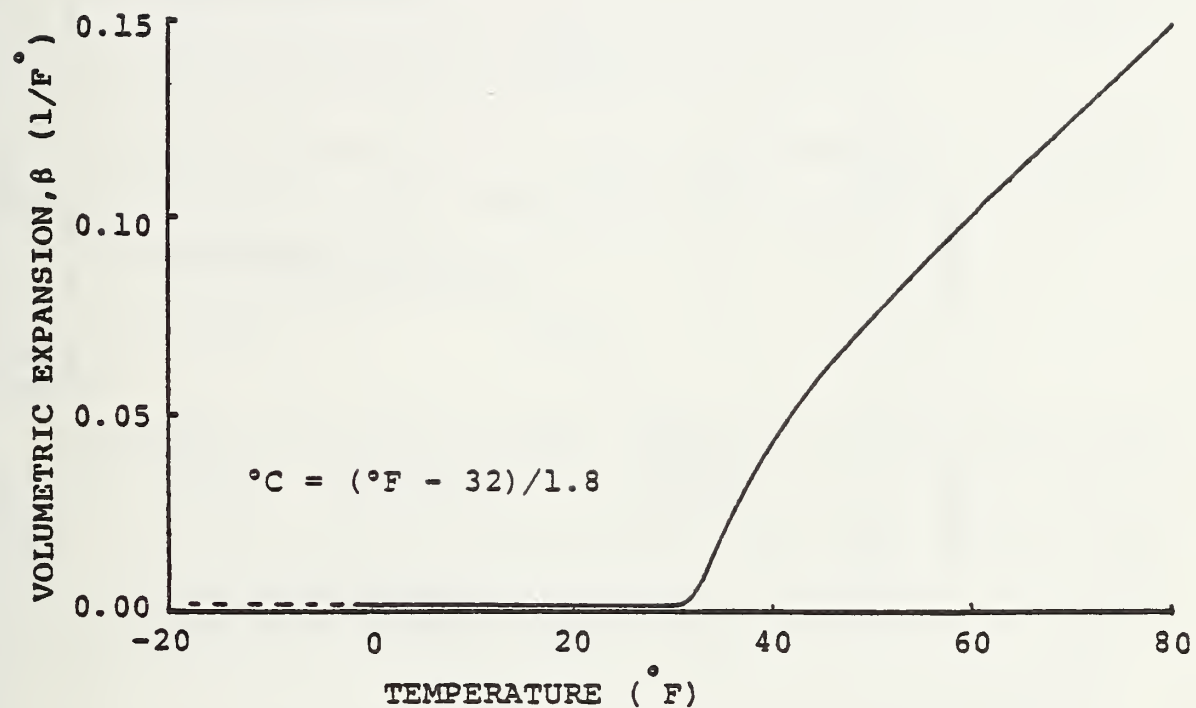


Figure 77. Coefficient of cubic expansion of water as a function of temperature.

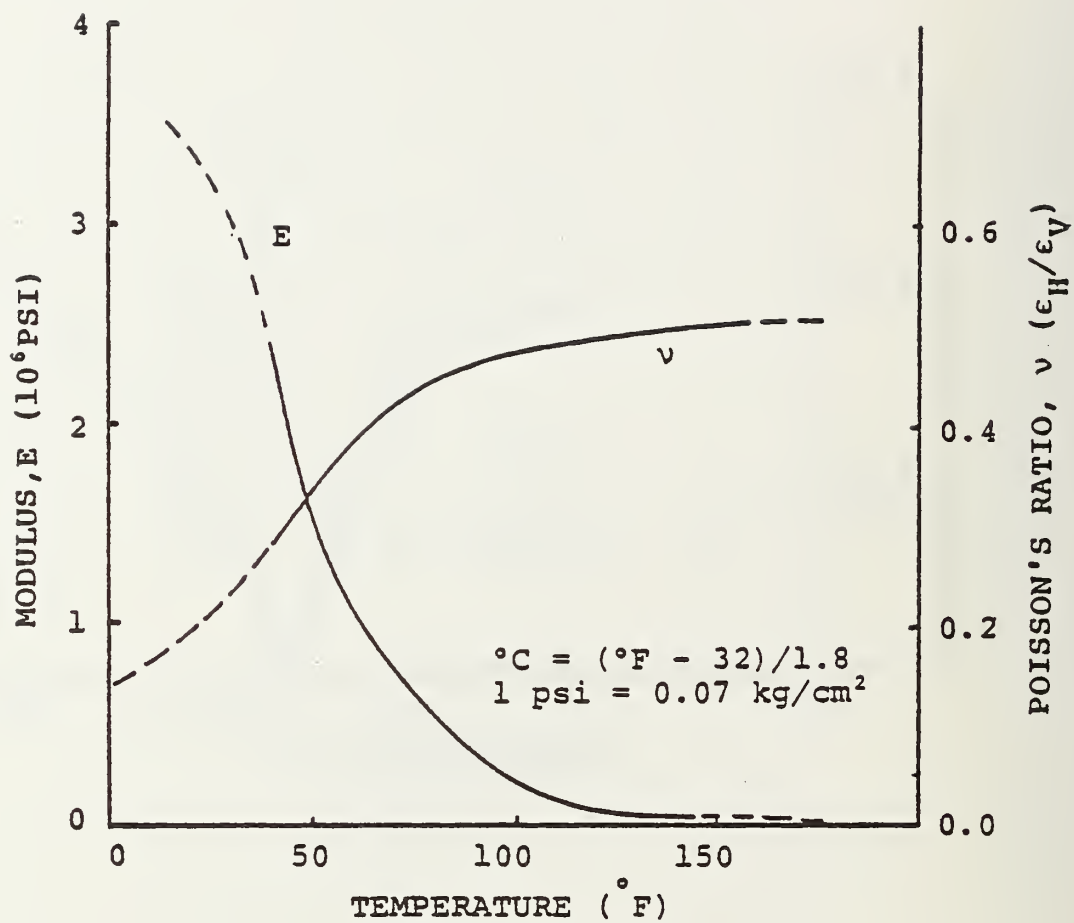


Figure 78. Strength properties of asphaltic concrete (AC) as a function of temperature (Nair and Chang, 1973).

Compressive strength of PCC does not vary greatly at ambient temperatures above about 50°F (10°C) (Figure 79), but does increase at freezing temperatures, probably through a mechanism of moisture freezing within pores in the concrete. Elastic modulus (E_c) for PCC has been extrapolated using the ACI formula:

$$E_c = 57,500 \sqrt{f'_c}$$

10

to provide the temperature-dependent relation shown in Figure 80. Properties of SFRC were then extrapolated using the same relative modulus curve and a 70°F (21°C) modulus value of 9 million psi (633,000 kg/cm²).

The material properties used in the finite element modeling procedure are summarized in Table 4. Linear interpolation and extrapolation for intermediate values are automatically used in the computer program.

4.3 ENVIRONMENTAL LOADS

4.3.1 General

Environmental loadings on pavement systems are defined in this study as consisting of thermal loads generated by radiation and convection of heat at the surface, freeze/thaw action, localized ice lens formations, moisture migration, salt intrusion, and factors that cannot be directly solved by the finite element method, such as the effects of vegetation and chemical attack. Heat transfer and moisture migration can be analyzed directly by finite element analysis. Forms of chemical attack, the effect of changes in moisture distribution, etc., can be analyzed indirectly by considering the effect of these actions on the properties of the system, then performing a stress or thermal analysis.

4.3.2 Characterization of Loads

The primary thrust of the investigation centers on the effects of thermal loads. To fully understand the nature of thermal inputs into a pavement system, a knowledge of the heat balance at the pavement (or soil) surface is required. For an infinitesimal thickness of surface it is possible to express the balance of heat flow, both into and out of the surface. Figure 81 depicts the balance at the surface, including heat generated within the soil and heat input at the surface as convection and radiation loads. External sources of heat are subdivided into four categories. First is radiation, perhaps the largest

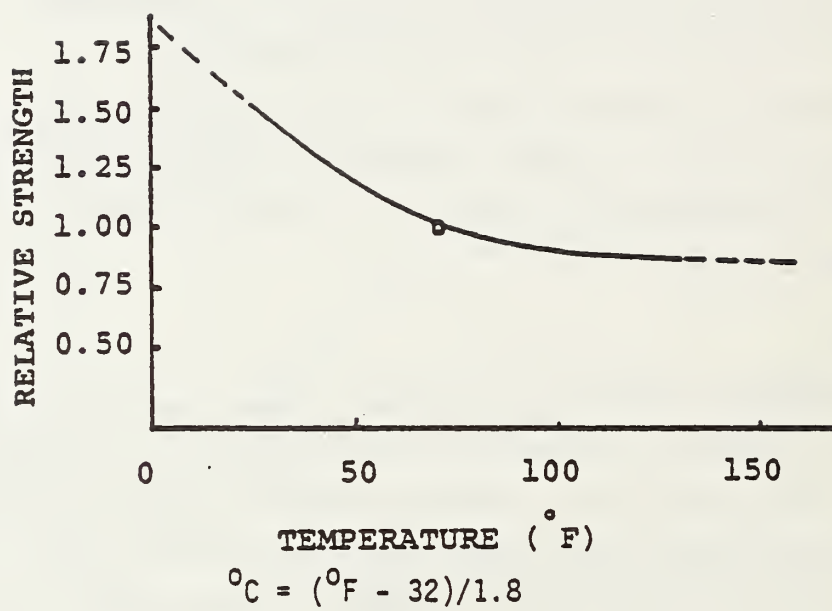


Figure 79. Relative strength of PCC as a function of temperature (Neville, 1963).

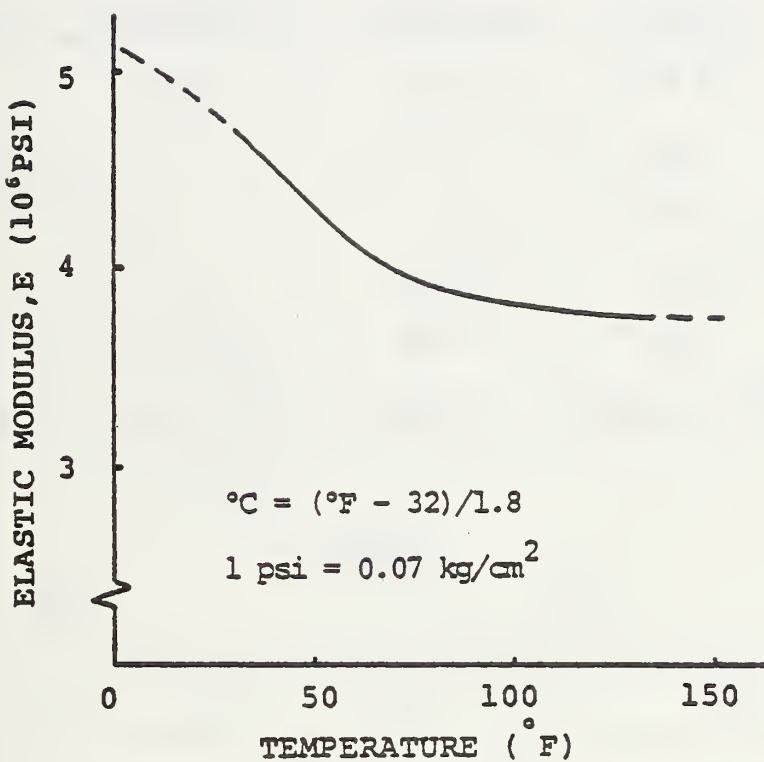


Figure 80. Elastic modulus of PCC as a function of temperature (based upon Figure 79).

Table 4. Material properties used in the finite element model.

TEMPERATURE °F	<u>SOIL</u>			<u>SFRC</u>	
	c_v BTU/LB-F°	k BTU/IN-HR-F°	c_v BTU/LB-F°	k BTU/IN-HR-F°	
-22.00	0.22	0.105	0.16	0.073	
30.4	0.22	0.105			
31.9	33.40				
32.0	0.30	0.058			
120.0	0.32	0.058	0.16	0.073	
1 BTU/HR-IN-°F = $\frac{0.099}{1.8°C + 32}$		$\frac{CAL-KG}{HR-CM-°C}$	1 BTU/LBM-°F = $\frac{0.554}{1.8°C + 32} \cdot \frac{CAL}{°C}$		

TEMPERATURE °F	<u>SOIL</u>			<u>SFRC</u>		
	E PSI	v	α 1/F°	E PSI	v	α 1/F°
-22	8500	0.35	0.000006	15 M	0.20	0.0000055
0	8000	0.38	0.000009			
32	1200	0.40				
70				9 M		
120	1000	0.45	0.000500	8.5M	0.20	0.0000055

$$°C = (°F - 32)/1.8$$

$$1 \text{ psi} = 0.0703 \frac{\text{KG}}{\text{CM}^2}$$

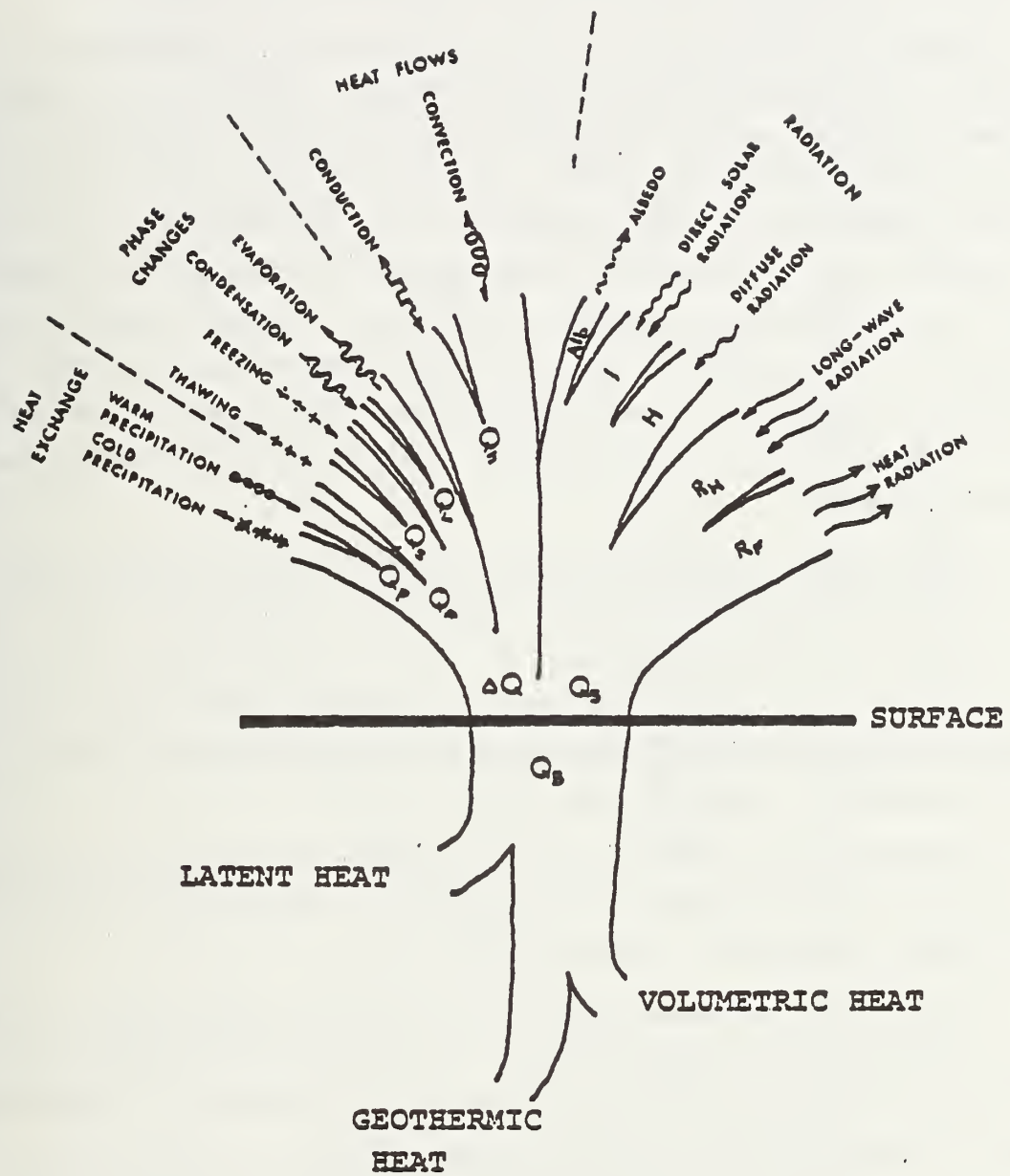


Figure 81. Heat balance at the pavement surface (Noss, 1973).

single heat source and most important factor in the heat balance at the surface. The short-wave radiation source, the sun, contributes direct and diffuse radiation (Figure 82). Long-wave radiation from clouds and water vapor and long-wave radiation directed outward from the surface complete the sources.

Secondly, direct heat flow due to convection and conduction at the surface both add and withdraw heat from the surface. Convection in pavement systems consists almost entirely of forced convection, heat transferred through a film of air moving across the surface. Equation 8 gives a simple relation to calculate the coefficient of heat transfer or film coefficient for a flat horizontal surface in wind. Convection can be modeled with convection elements available in the program that requires as input the film coefficient and contributing area. This convection link is a linear element with two nodes. One node receives the temperature input, and the other is connected to the surface. Conduction is also possible through contact with materials of different temperature at the surface.

Phase changes constitute another important source of heat at the surface. As water freezes, it releases a quantity of heat equal to the latent heat of fusion. This heat is dissipated at the surface as surface ice and snow freezes. Conversely, as surface ice thaws, it requires a heat equal to the latent heat of fusion to convert from solid to liquid. The latent heat of fusion of water at atmospheric pressure is 80 cal/gm.

Evaporation and condensation are also phase change processes, but from liquid to vapor. Here the important quantity is the latent heat of vaporization, which for water at atmospheric pressure is 540 cal/gm.

Finally, heat exchange on the surface between precipitation and the surface is possible. Both warm (rain) and cold (snow, sleet) precipitation exist (depending upon locality), and heat exchange occurs if there is a temperature differential between the precipitation and the surface.

Internal heat sources include geothermic heat from deep within the ground, latent heat attributed to phase changes within the soil moisture, and volumetric heat associated with the temperature of the system, in particular any gradient that exists between the soil temperature some distance from the surface and close to the surface.

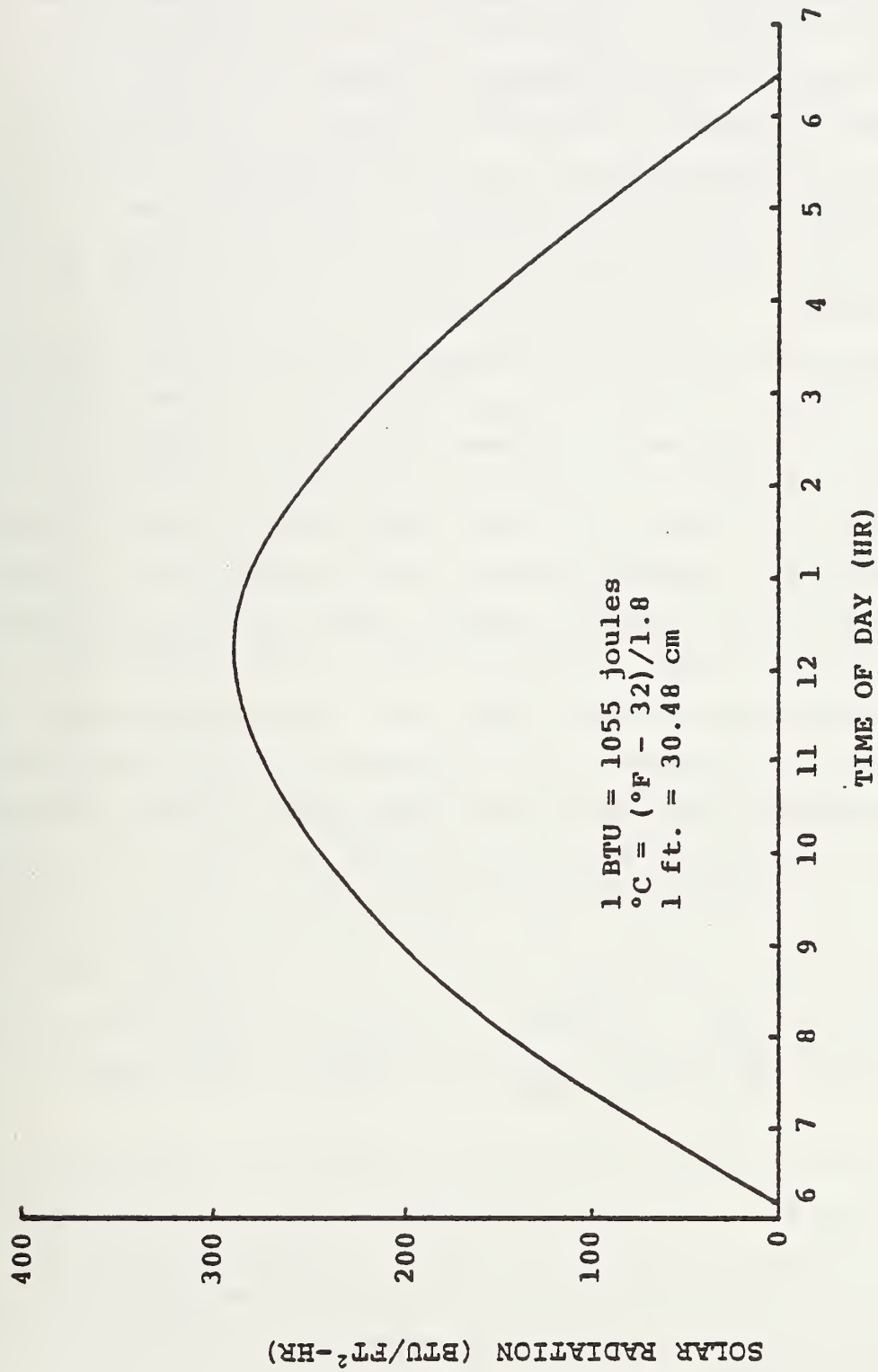


Figure 82. Variation of solar radiation intensity (Straub et al., 1968).

The surface heat balance is an equilibrium state; however, the quantities are seldom constant. Surface temperature is not constant either; it is closely linked to ambient air temperature and follows the same trends. As air temperature increases, surface temperature increases with very little, if any, phase difference or time lag. In winter in regions with frost conditions, there is very little difference between air and surface temperature (Figure 83); however, during summer there can be a substantial difference between surface and air temperature, often as much as 10 to 20°F (5 to 10°C), as indicated in Figure 84. (Surface temperature is greater during the day due to radiation effects).

Surface temperature of the pavement and natural ground depends on many factors, as indicated in the heat balance discussion. The temperature due to radiation is also color dependent; pavements with dark color absorb light energy and are therefore warmer. This condition is controlled by a property of the surface known as emissivity. Ground cover conditions can greatly influence surface temperatures. Vegetation creates a rough surface so that convection is different from that existing across a smooth pavement surface. Snow cover creates a reflective surface so that short-wave radiation is reflected.

The temperatures of lower layers within the system depend not only upon the heat balance at the surface, but also on heat flow to and from lower layers due to phase changes, conduction of heat through pore fluid and intergranular contacts, and any moisture migration along thermal gradients. Typical mean annual changes in temperatures at various depths are as follows: surface, about 50°F (28°C); at 12-in. (30.5 cm) depth, about 10°F (5°C); at 24-in. (61 cm) depth, about 2°F (1°C) (after Nordal, 1973). The soil profile at depth thus maintains a fairly constant temperature while surface layers, which are closer to the more widely variable ambient conditions, possess a higher degree of variability.

A typical recorded daily change of temperature in the desert is presented in Figure 85. The surface temperature varies to a large degree, being hottest during the day and coldest at night. Air temperature reflects this change, but is not as variable and does not reach the same magnitude of temperatures as the surface. Temperature at approximately a depth of 24 in. (61 cm) is more or less constant.

Based on several sets of similar temperature variations, summer and winter daily temperature histories were simulated by the models shown in

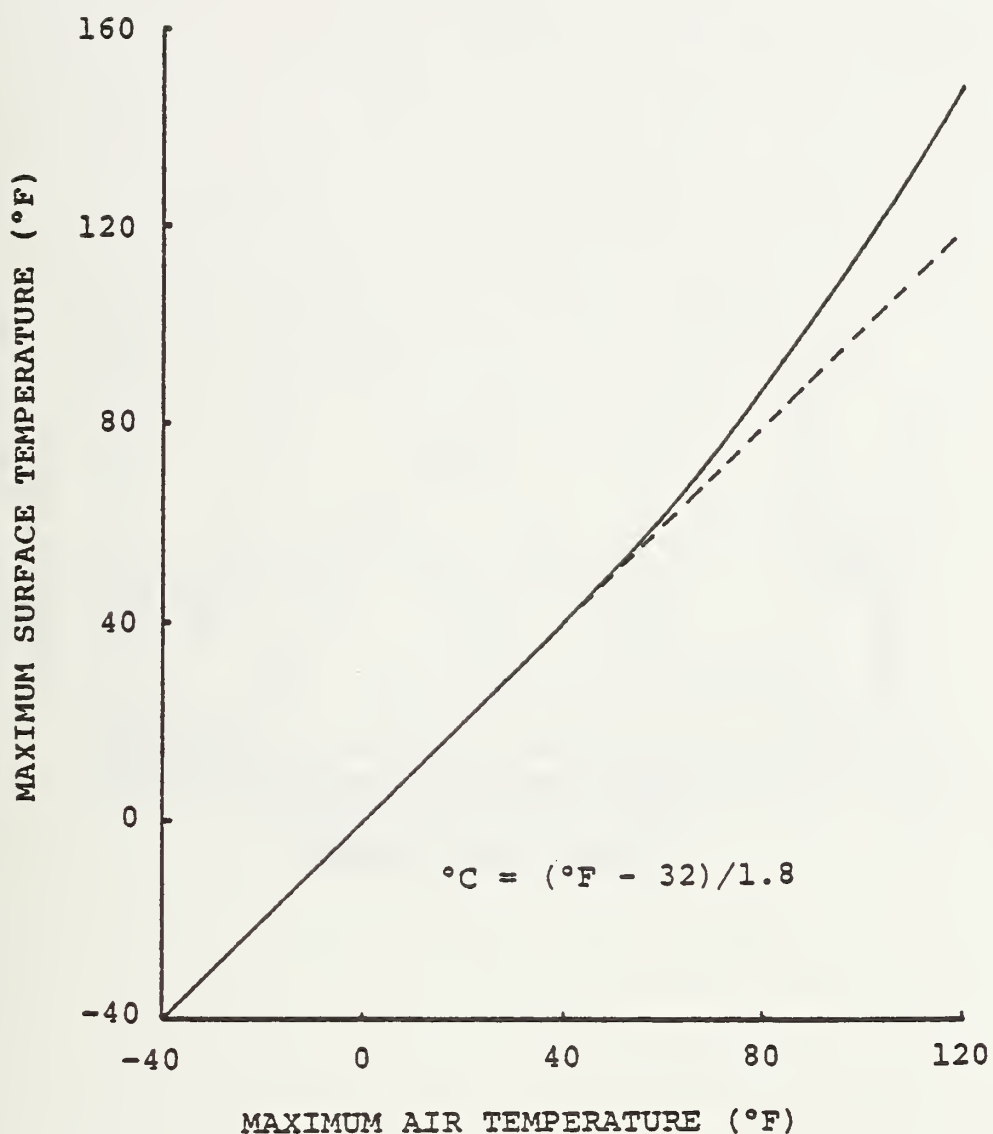


Figure 83. Correlation between surface and air temperatures (Venkatasubramanian, 1964).

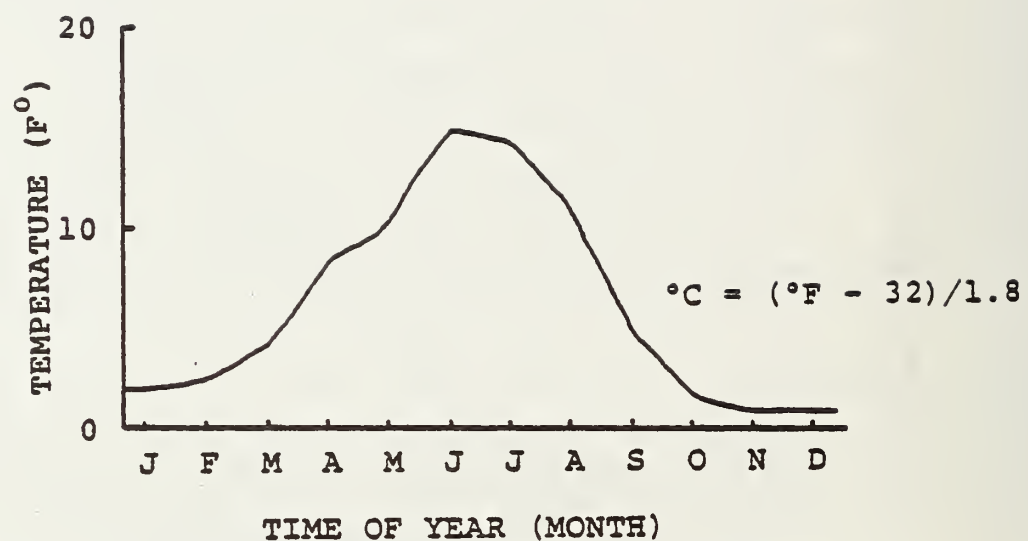


Figure 84. Temperature difference between pavement and air at various times of the year. (actual values vary for pavement colors, surface cover, etc. (Noss, 1973)).

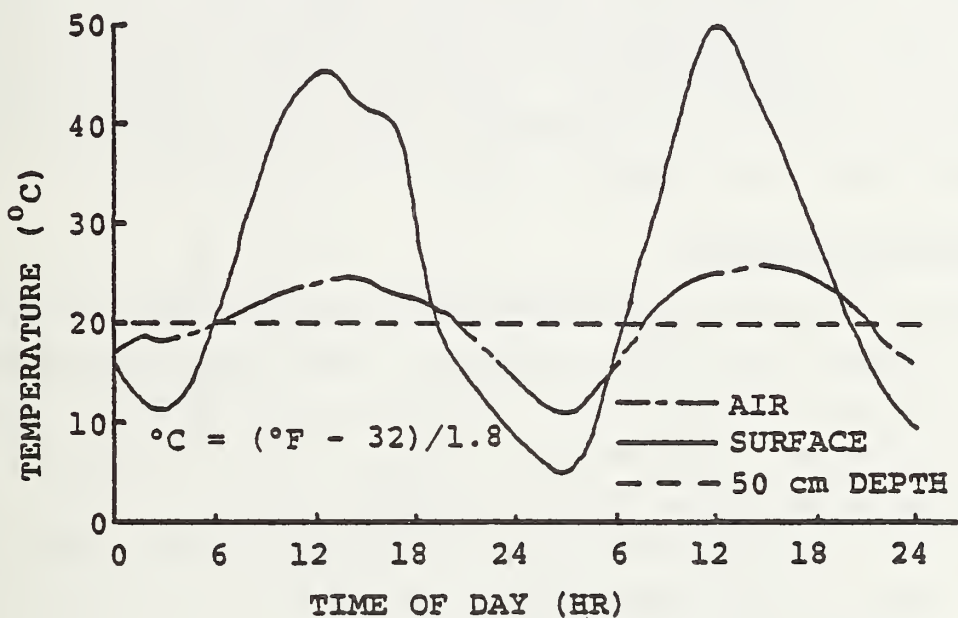


Figure 85. Typical diurnal variation of temperature in natural soil (Goetze and Mueller, 1969).

Figure 86 and Figure 87, respectively. The summer model is rather extreme (upper boundary), with a 60°F (33°C) differential between maximum and minimum surface temperatures. Soil surface temperature was modeled slightly lower than the pavement temperature, but this is not a general rule, only a particular example. Actual temperatures depend on ground cover. The summer condition was cycled for 2 days and rapidly approached a steady state condition (temperature distribution was nearly the same for corresponding times on different days).

The winter model attempts to generate a freeze/thaw cycle within the system. Most of the history is of subfreezing temperatures. This model was cycled for 6 days, but convergence to a steady state condition as defined above and a constant or progressing frost line is much slower, probably because of the problems associated with the phase change of water. This problem and a solution are discussed later in the report.

4.3.3 Description of Models

The first analysis performed was the two-dimensional heat transfer. Two modes of thermal loading were considered: simple input of surface temperature histories (Figure 88) and a surface convection analysis (Figure 89) in which temperatures were input indirectly through convection elements to simulate heating and cooling of the surface by an adjacent film of air. There was little difference in the resulting temperature distributions, and the latter model was abandoned. Because input temperatures are derived from actual measured surface temperatures, the first model seems justified.

The mesh used for this analysis is shown in Figure 90. Isoparametric elements are used to decrease the required fineness of the mesh (number of degrees of freedom) and still maintain accuracy. Each element contains a three-by-three Gaussian grid of integration points for the interpolation of temperatures (or stresses) within the element from the calculated nodal temperatures (forces). Each node has one degree of freedom (temperature) in the heat transfer analysis, and two degrees of freedom per node (translation in the plane) in the stress analysis. A detailed look at the slab-soil interface (Figure 91) reveals conduction elements (sliding interface elements in the stress analysis) to thermally link the slab and soil. To aid in the continuity of the slab and anchors, a temperature degree of freedom constraint is made to ensure that corresponding nodes have the same temperature. This modeling technique can also

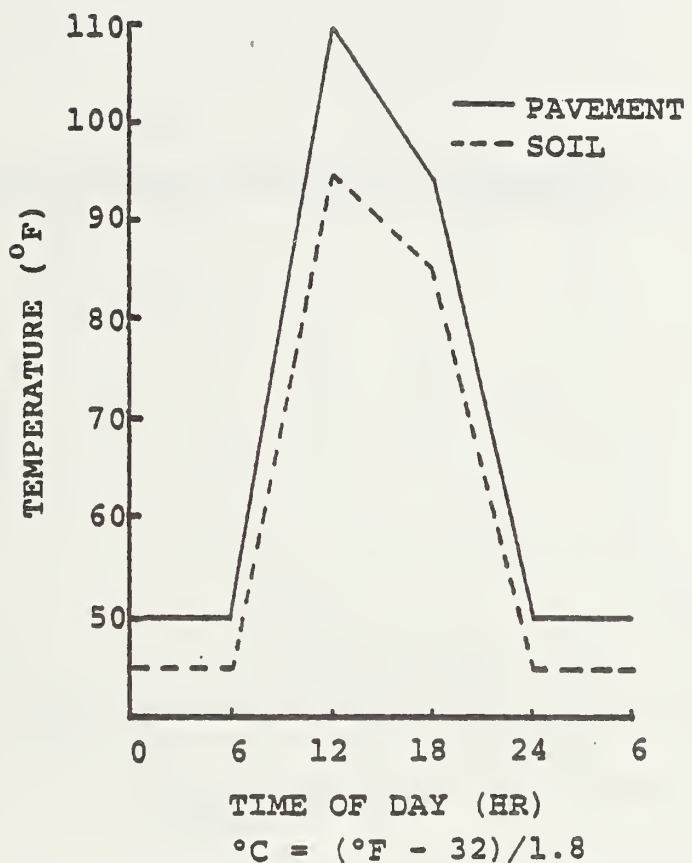


Figure 86. Surface temperature input for mathematical model (summer condition).

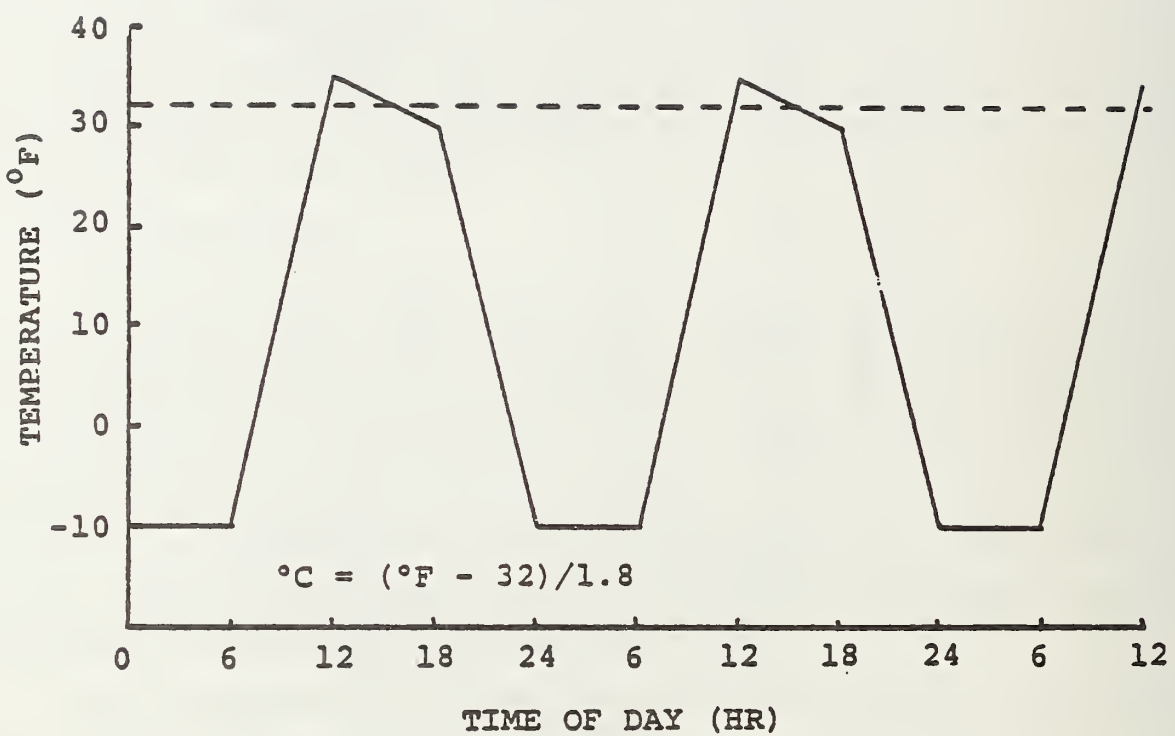


Figure 87. Surface temperature input for mathematical model (winter condition).

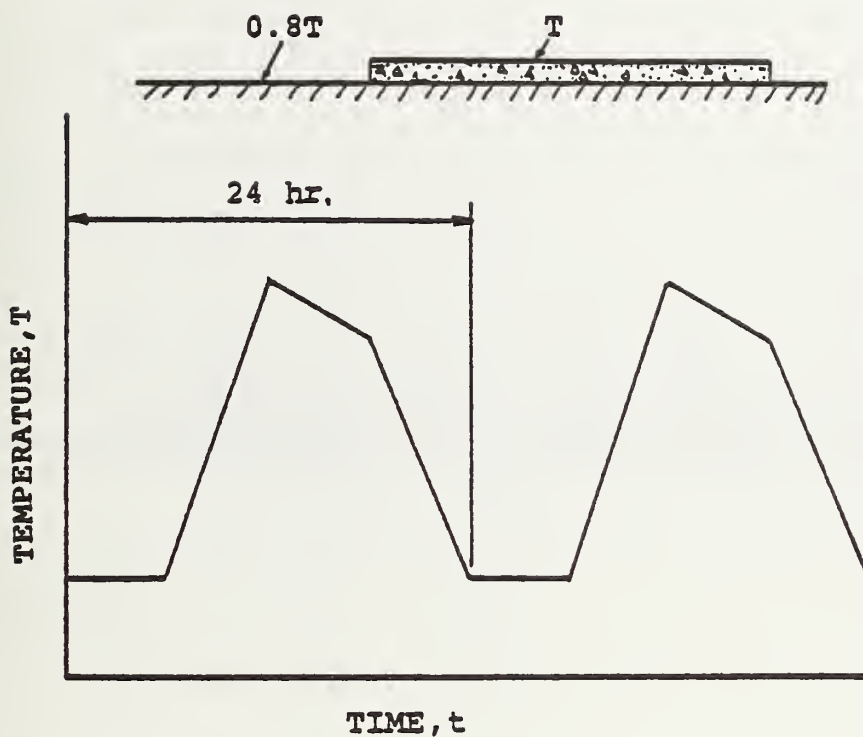


Figure 88. Model in which heat content of system is constant. Temperature content is controlled by surface temperature.

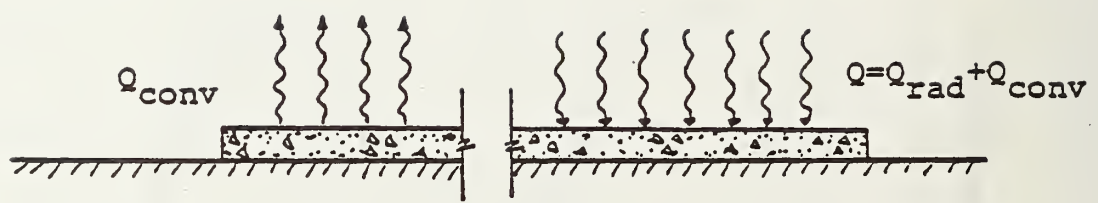


Figure 89. Model in which heat content of system is not constant because of added surface convection and radiation.

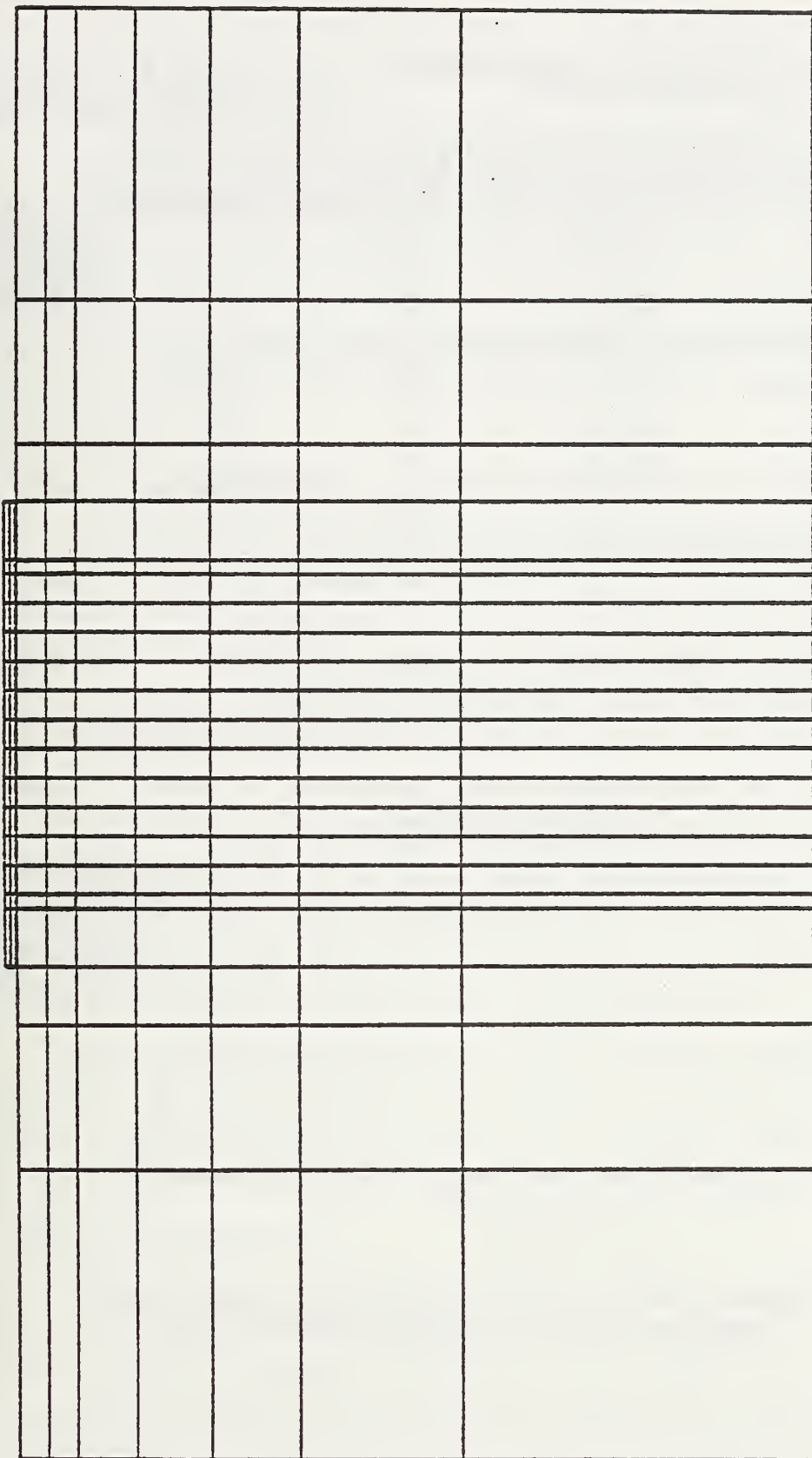
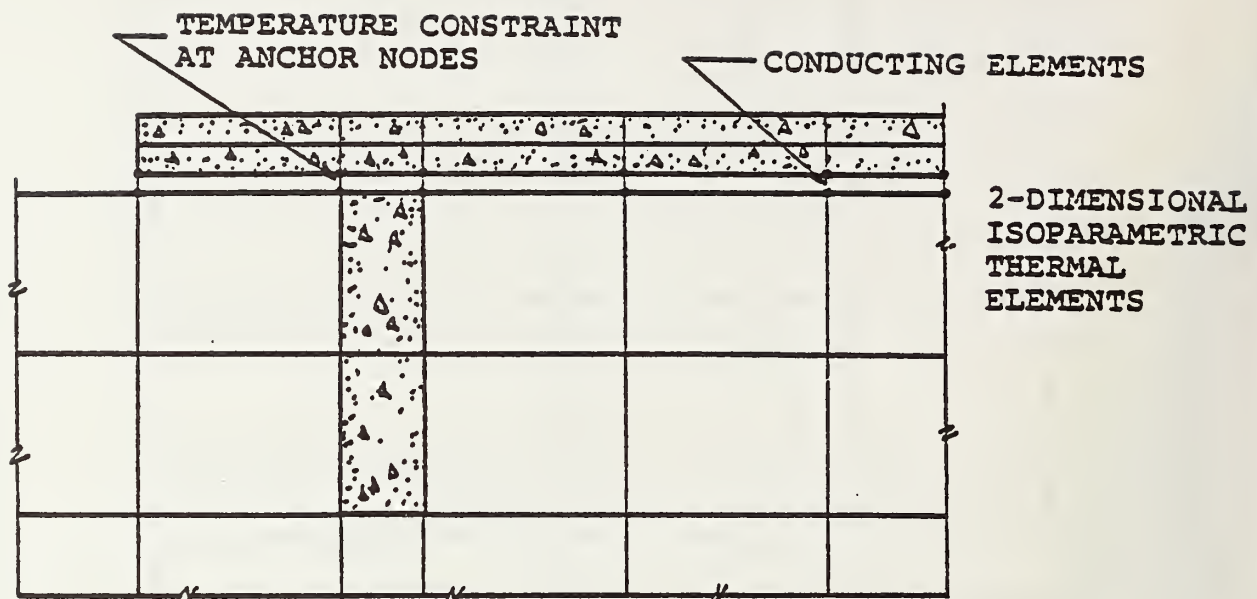
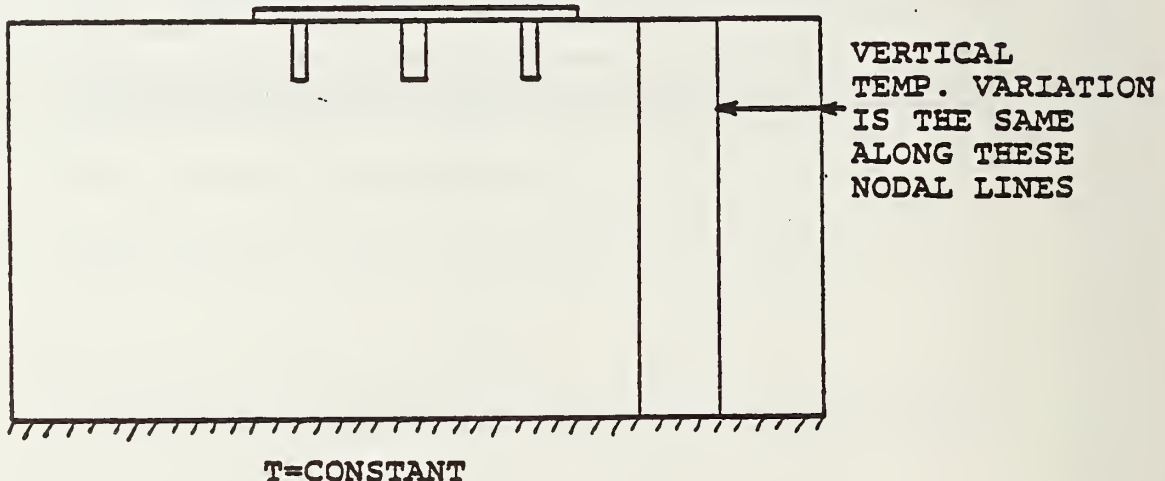


Figure 90. Two-dimensional mesh used in heat transfer and thermal stress analyses.



a) Detail of slab/soil interface modeling.



b) Boundary conditions for heat transfer model, both lower and lateral to simulate infinite extent.

Figure 91. Thermal modeling details.

simulate a link (dowels) between the slab and anchors, if the slab and anchors are poured separately.

Boundary conditions used in the model to simulate an infinite depth of the soil are as follows. In Figure 91 the lower boundary is fixed at a constant temperature (in summer 50°F (10°C) and in winter 45°F (7.2°C)). This boundary in this particular model is about 50 ft. (15.3 m) below the surface and should accurately simulate no heat flow. Lateral boundaries are simulated by constraining nodes along peripheral nodal lines so that the temperature variation with depth is the same.

4.3.4 Heat Transfer Analysis

The results of the heat transfer analysis used to generate temperature distributions within the pavement and soil for further stress analysis are presented in two forms: temperature profiles at various positions and times (tautochrones) and temperature contours. Typical summer and winter tautochrones for the anchored and conventional pavements are shown in Figures 92 and 93, respectively. Slight differences exist in the profiles under the anchors due to differences in conductivity and heat capacity between soil and concrete. The results correlate well with typical field data (Figure 94) in trends and relative magnitudes of temperatures. The lag in temperature peaks with increasing depth was accurately portrayed in the analysis by comparing the 1800-hr. and 2400-hr. tautochrones with the 1200-hr. profile; because of thermal damping, the higher temperature does not occur at lower depths until much later.

Typical temperature contours for both pavements (anchored and conventional) have been studied from analyses results, but they are not included in this report. The temperature gradients are not as steep in the anchors, due to differences in material properties between soil and concrete.

4.3.5 Thermal Stress Analysis

The temperatures generated in the heat transfer analysis were input in a stress model and the resulting stresses and strains computed. The stress model uses sliding interface elements that cannot sustain tensile loads and at a certain shear stress begin to slide with an irrecoverable displacement as shown in Figure 95. Actual values for μ , the coefficient of static sliding friction, and k , the modulus of subgrade reaction, were obtained from results of direct shear tests of concrete on soil reported in the literature. Relations such as

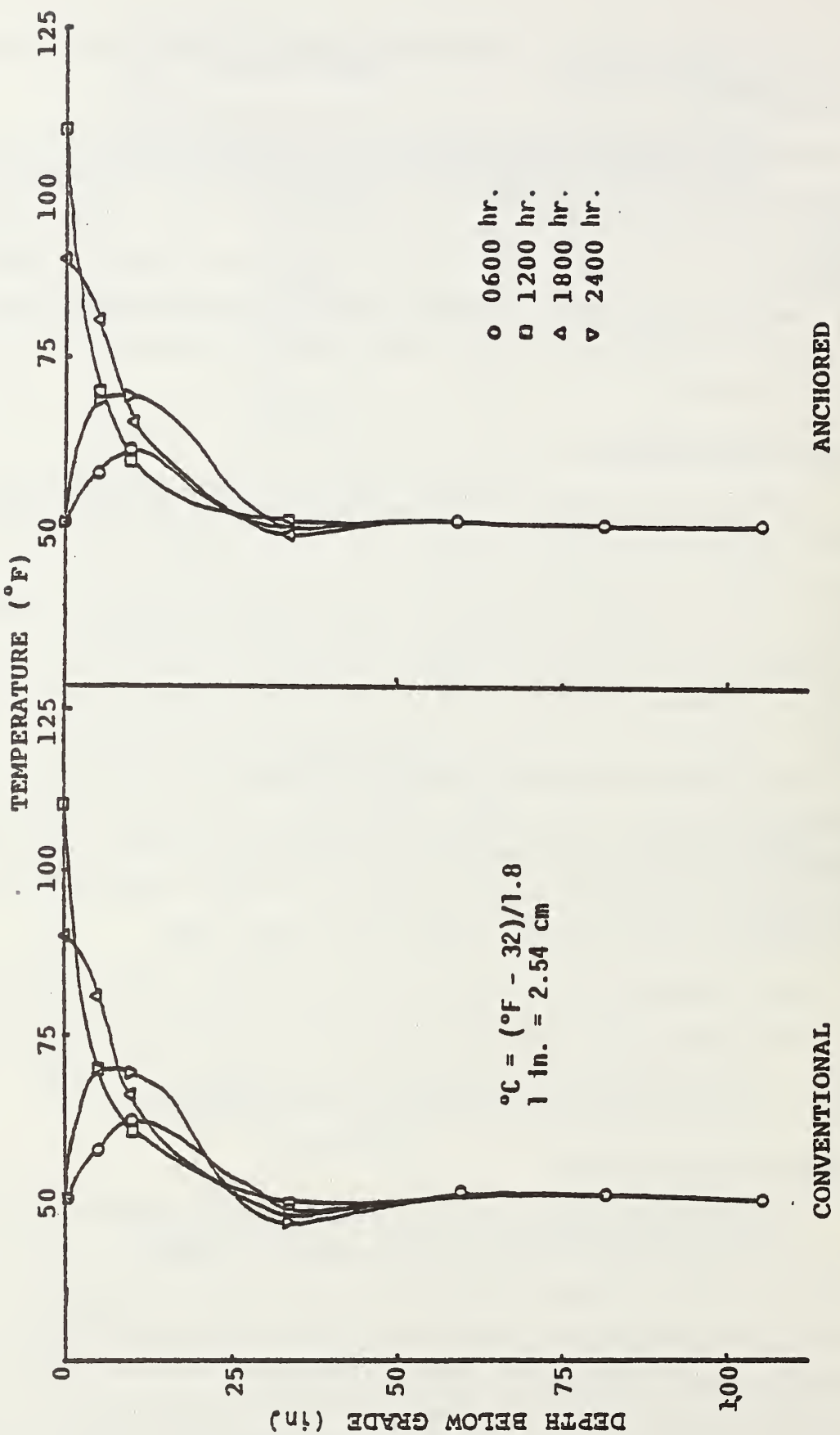


Figure 92. Summer tautochrones at pavement centerline.

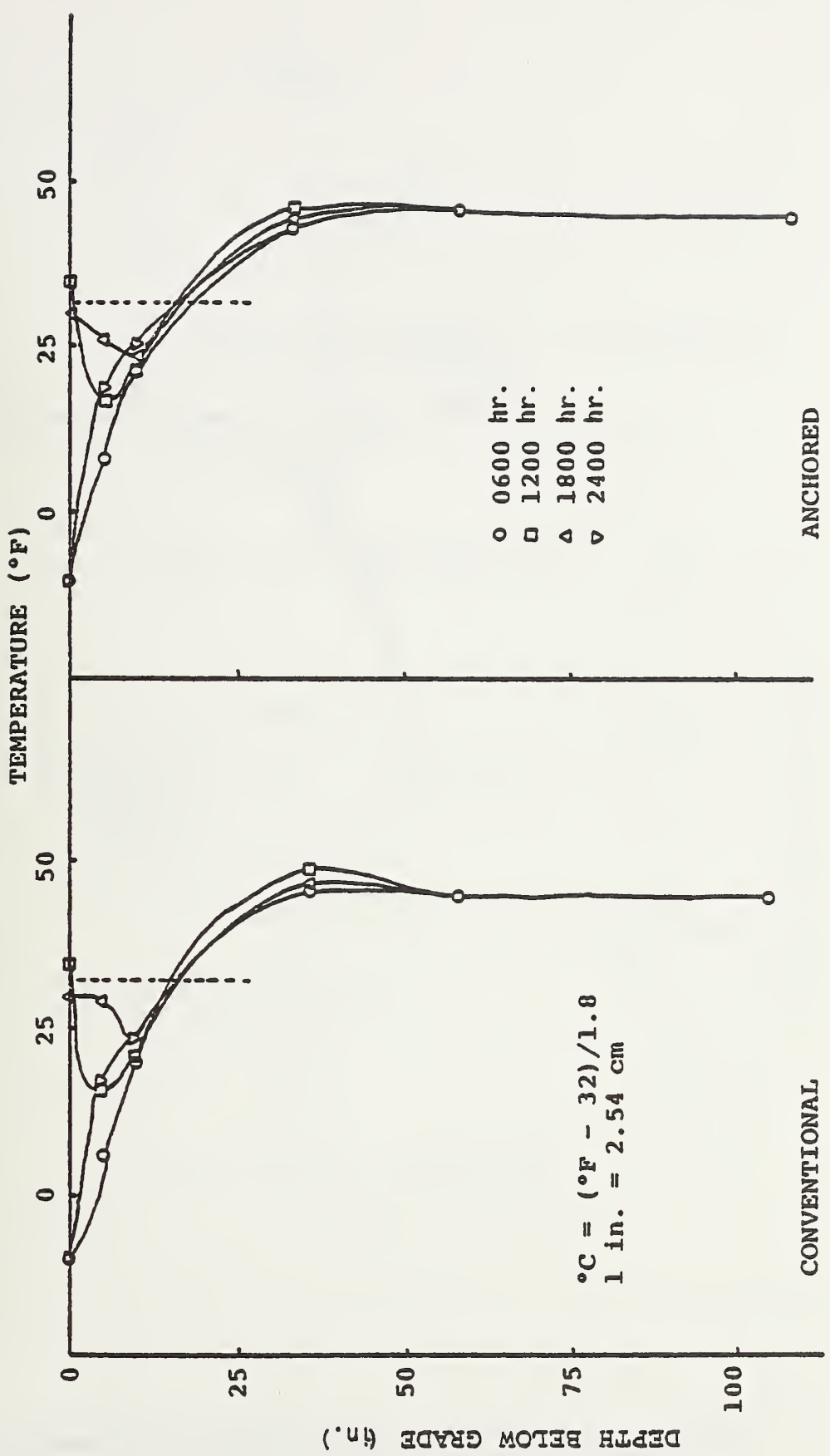


Figure 93. Winter tautochrones at pavement centerline.

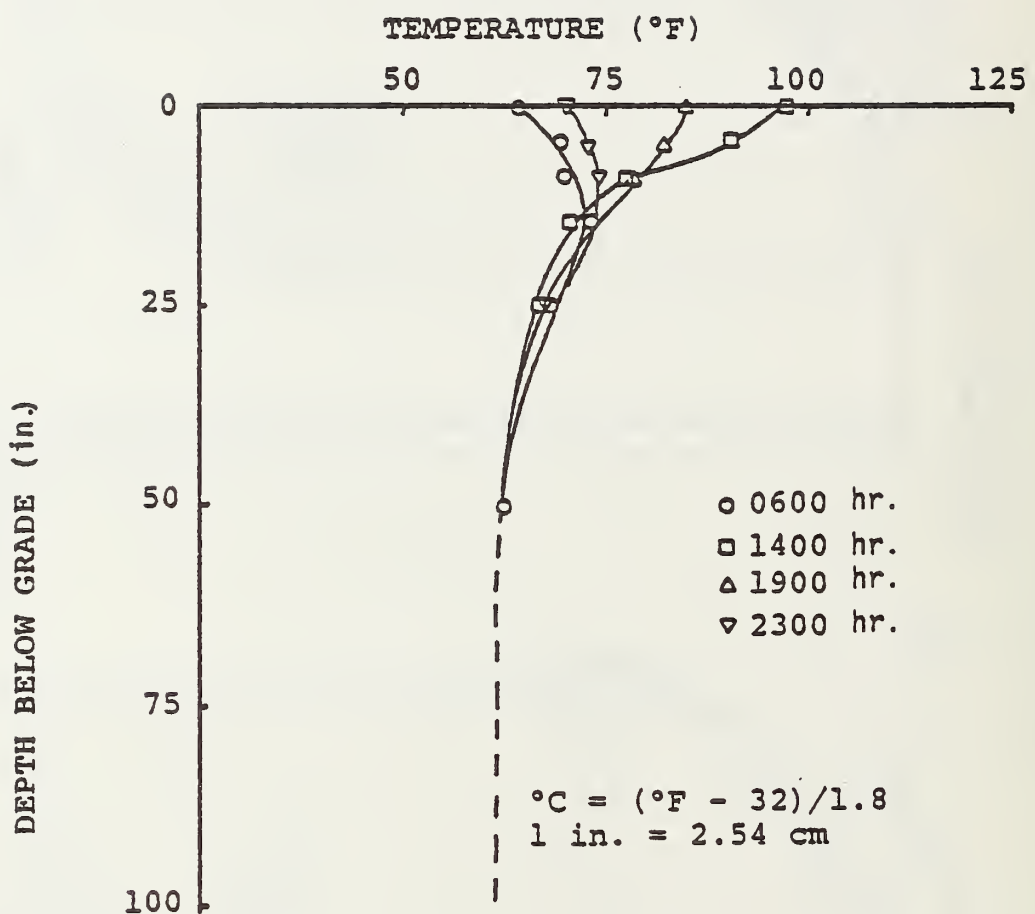
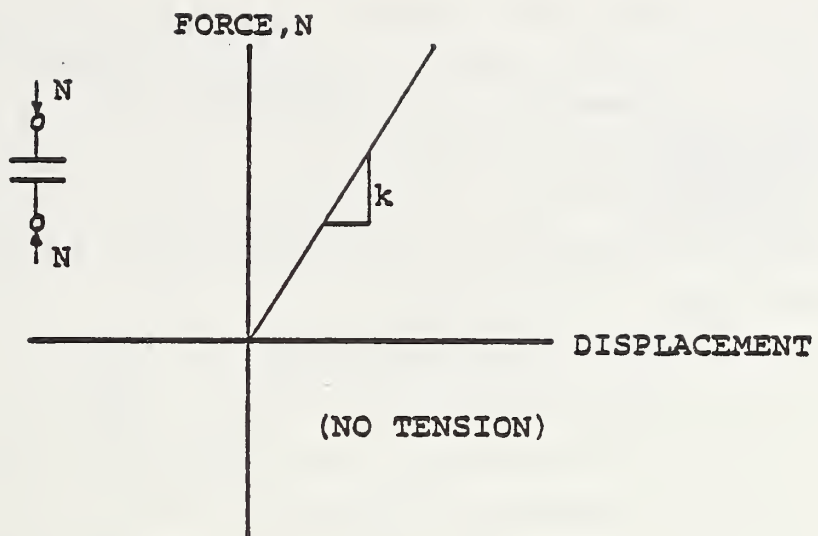
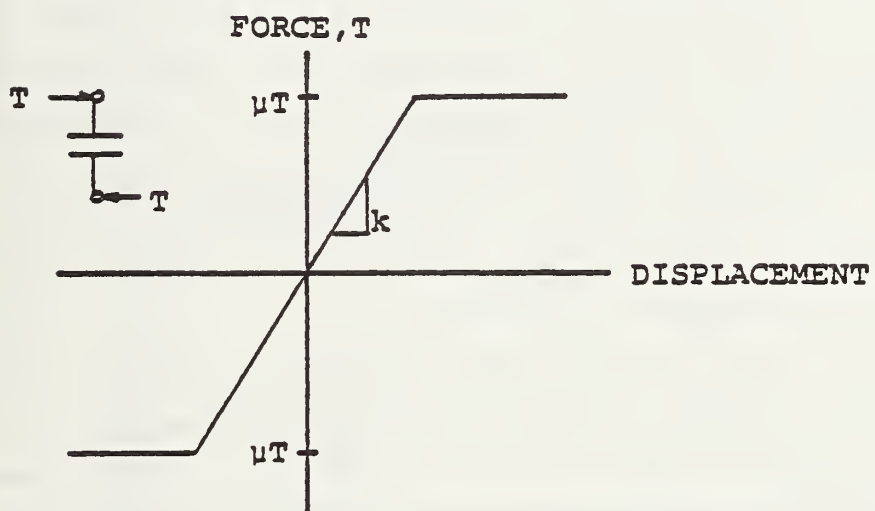


Figure 94. Tautochrones in natural slope on a summer day (Goetze and Muller, 1969).



a) Normal force/displacement model.



b) Shear force/displacement model.

Figure 95. Mathematical model used to simulate slab/soil interface behavior (DeSalvo and Swanson, 1975; Kohnke, 1977).

those found in Figure 96, Teller and Sutherland (1935), and Timms (1964) are typical. In most instances, k depends on confining pressure (Figure 97) or normal stress, σ , but lower bound values of 1000 lb./in. (178 kg/cm) for summer and 2000 lb./in. (356 kg/cm) in winter were used, more closely resembling clay behavior with increased adhesion. With the given density of nodes, this corresponds to a modulus of subgrade reaction of about 100 and 200 psi (2.7 and 5.4 kg/cm³), respectively.

With this type of interface behavior, it is possible to simulate curling of the slab with the associated loss of subgrade contact and also simulate penetration of the slab into the soil. If no penetration is desired, a constraint limiting the compressive deflection of the slab can be established by choosing a sufficiently large value for k . Surface deflections for summer curling conditions, day and night (Figure 98) and winter conditions (Figure 99) are presented. All thermal stress calculations are based on a zero stress reference temperature of 68°F (20°C), the assumed temperature of concrete when placed. Daytime deflections are concave down, due to the warmer surfaces; deflections during the night are concave up because of the cooler surface. Deflections are somewhat lower in winter than in the summer, because there is not as great a temperature differential between the slab top and bottom surfaces. The anchors reduced curling near the pavement edges with only slight curling of the shoulders. Stresses, however, are increased, and precautions must be made to increase the size of the slab-anchor joint by adding fillets to lower any stress concentrations that may occur.

From a study of various computer-generated contour plots of stress in the systems (not included in report) some observations pertaining to the nature of the state of stress within and the gross behavior of these pavements can be made. The transverse bending stress distribution at a distance from the shoulder is linear with depth, with a zero stress contour along the middle section. Nearer the shoulder, however, stresses tend to become uniform with thickness, primarily because the temperatures also tend to such a uniformity in distribution from increased heat dissipation at the shoulder edge. Because of the anchors in the anchored pavement, stresses are locally increased and contours are somewhat distorted near the anchors when compared with the corresponding conventional transverse bending stresses.

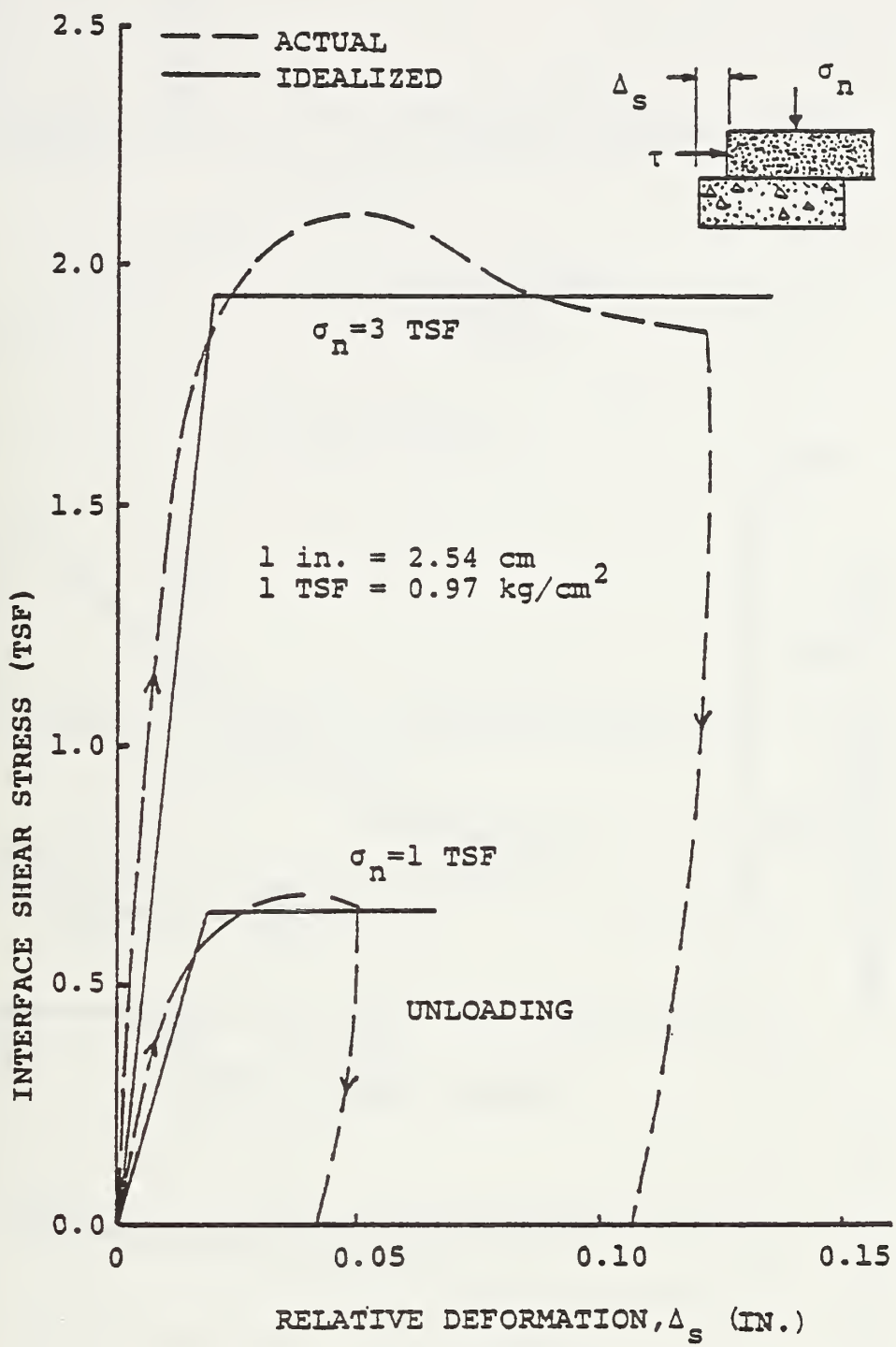


Figure 96. Interface behavior of sand on mortar for various contact pressures (Clough and Duncan, 1971).

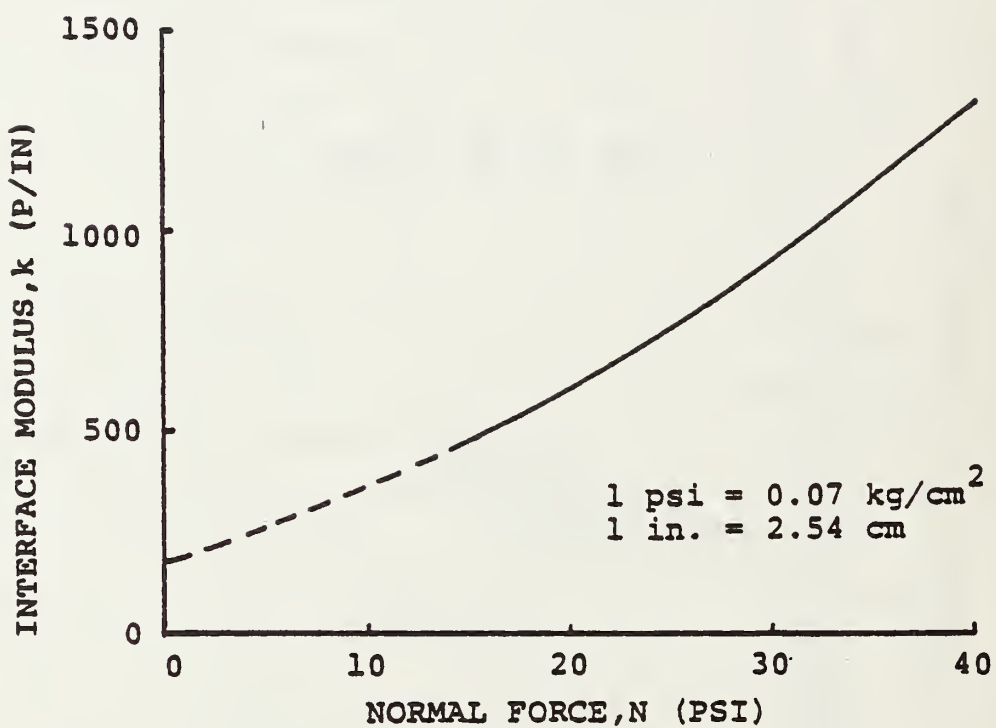
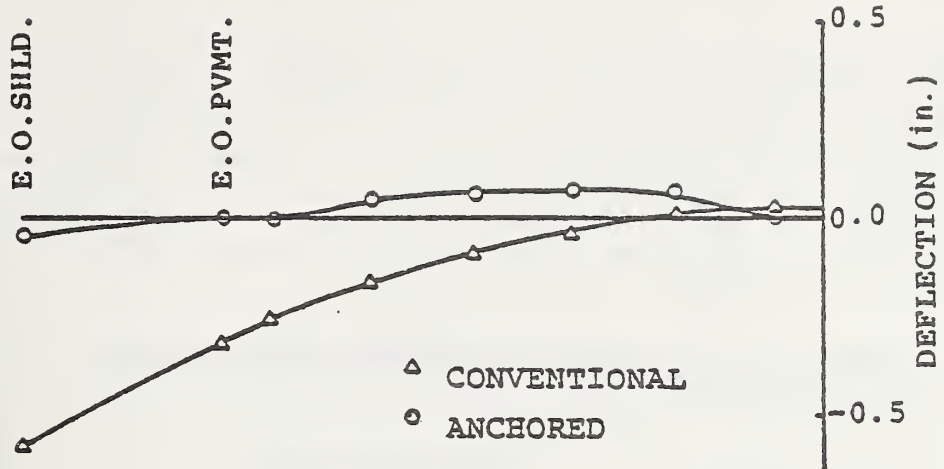
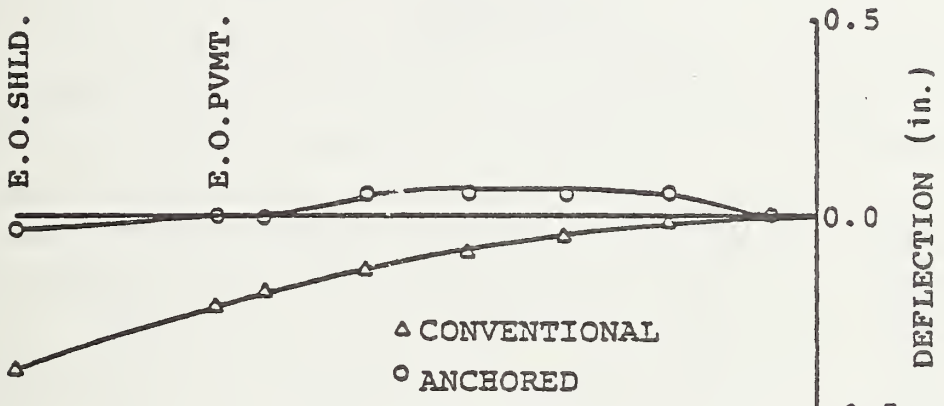


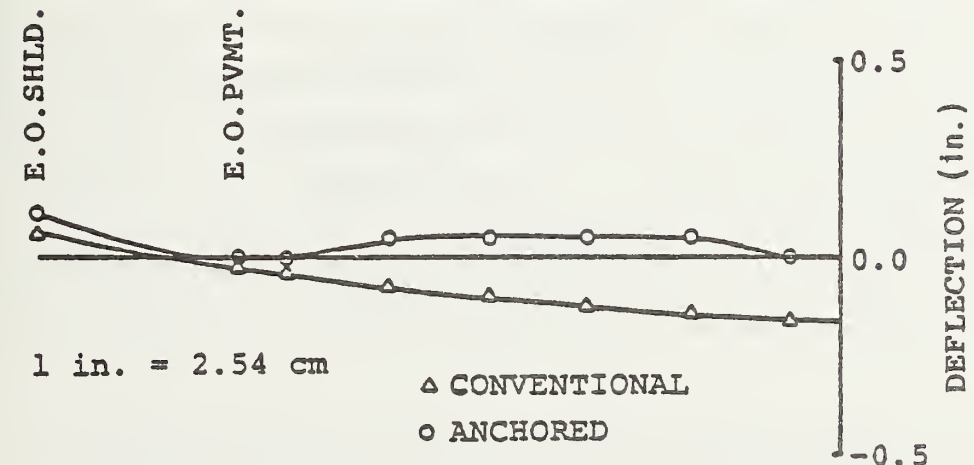
Figure 97. Variation of interface modulus with confining pressure (Clough and Duncan, 1971).



a) Early morning.

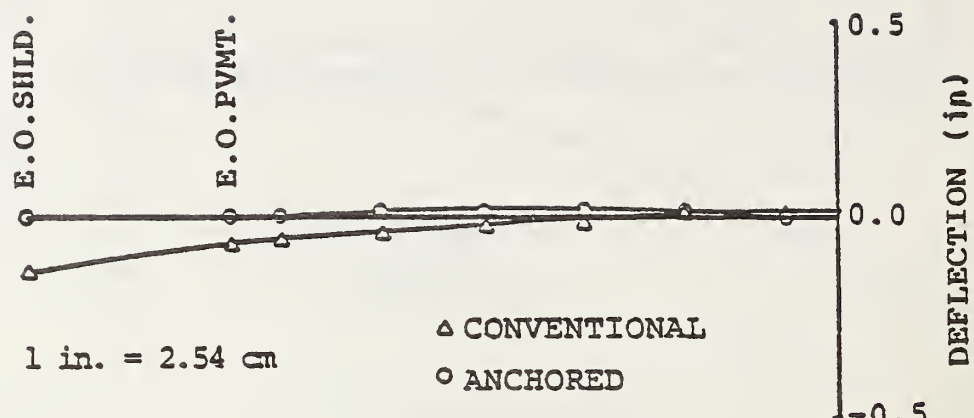


b) Mid-day.

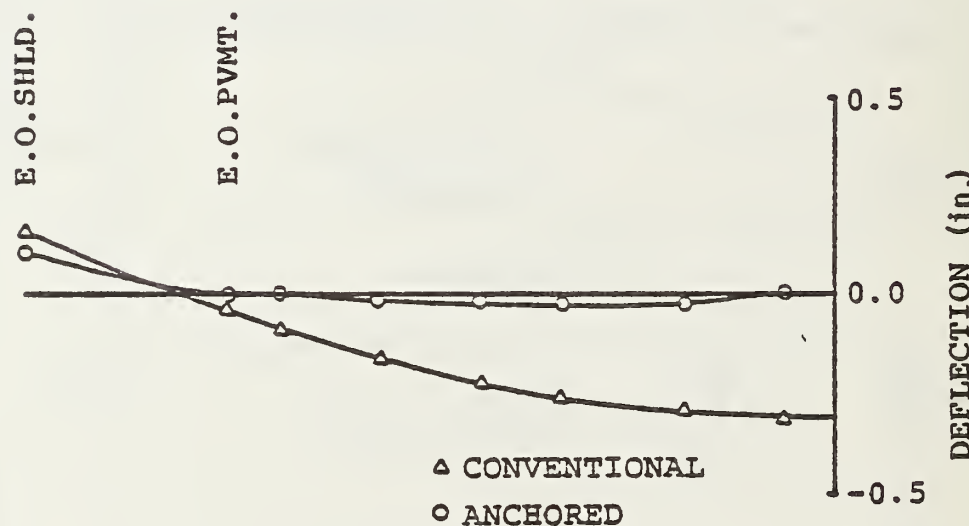


c) Night-time.

Figure 98. Surface deflections due to thermal strains, summer (early morning, mid-day, night-time).



a) Mid-day.



b) Night.

Figure 99. Surface deflections due to thermal strains, winter (mid-day, night).

Longitudinal stresses are quite different for the two pavements. The anchors are stressed within the soil and as a result tend to drag soil and thereby stress it (because of frictional adhesion at the slab/soil interface). The temperature difference between the anchors and the soil caused by the conduction of heat between the anchors and the slab make such longitudinal behavior possible.

Thermally induced shear stress contours in the conventional pavement are nearly vertical, reflecting the linear nature of the transverse bending stresses. Shear stress is nearly constant near the shoulder edge, especially at night. The anchored pavement shows rapid shear stress gradients near the anchors due to the restraint of curling deformation provided by the doweled connection between the anchors and the slab.

To find the effects of the third dimension on the analysis, a single slab was modeled (Figures 100 and 101) with identical cross sections as the corresponding two-dimensional models. The results for surface deflections of the anchored pavement indicate an increased shoulder (corner and edge) deflection (about double for this particular condition). The interior of the slab showed a decrease in the deflection due to the applied thermal loads as indicated in Figure 102. The reduction in these deflections is about 50%, compared with the two-dimensional results in Figure 98. Stress is expected to increase near the anchors, the reduced deflections again being attributed to the restrictive nature of these rigid anchors.

The accuracy of the analysis would not be credible unless the results could be checked against actual physical behavior of pavements in similar loading environments. There are numerous road test results published that support the results presented in this study. In general, the deflections obtained agree quite well for the simple slab, both qualitatively in general shape and quantitatively in magnitude. Differences can be found, but it must be remembered that for a true match, an identical physical or prototype system must be analysed.

The results from the analysis of the anchored pavement are obviously not as easy to corroborate since there are no prototype pavements of this configuration. Because the results obtained for the conventional pavement are reasonable and the primary purpose is to study and compare the two systems, the results seem acceptable.

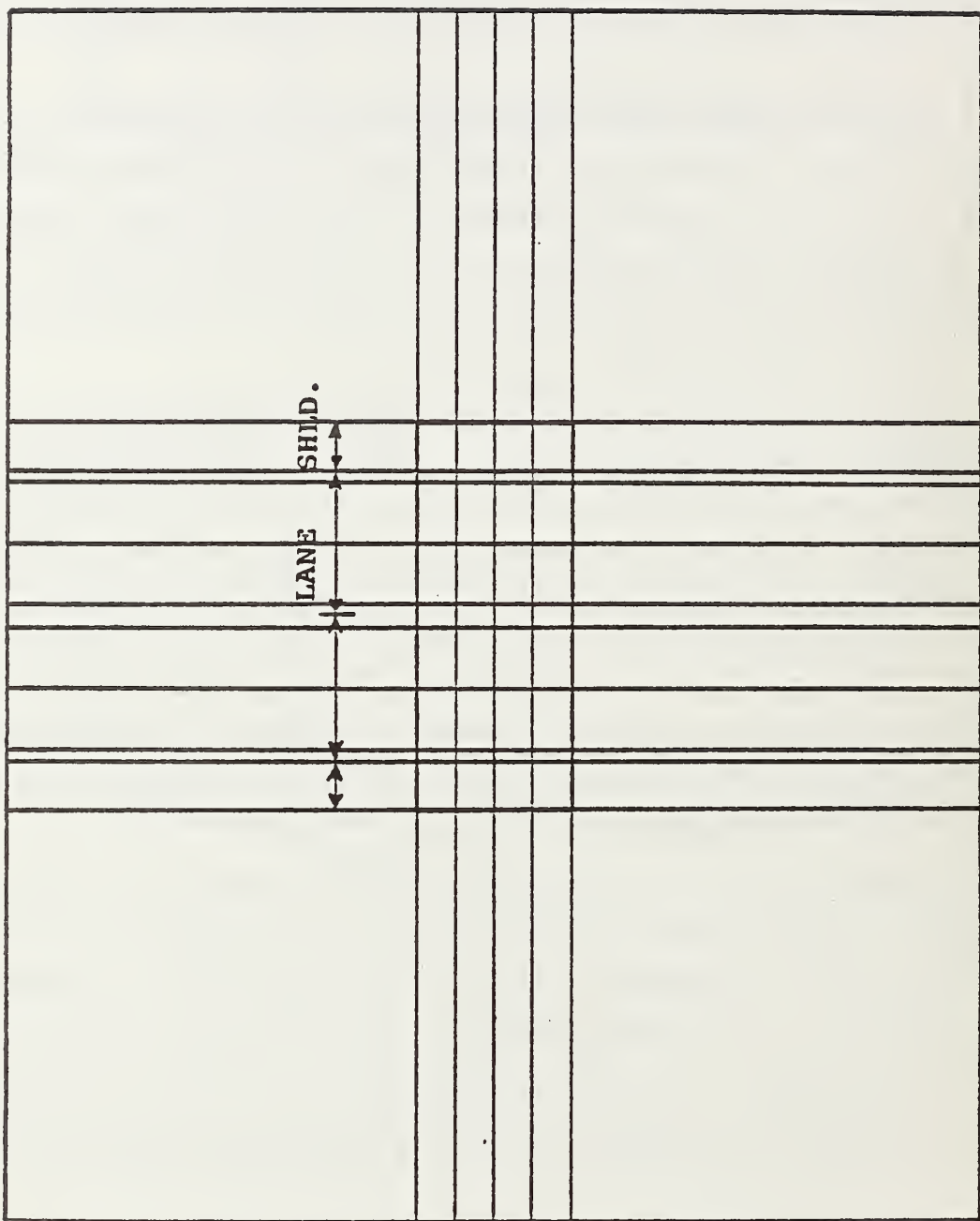


Figure 100. Plan view of three-dimensional mesh used for thermal stress analysis.

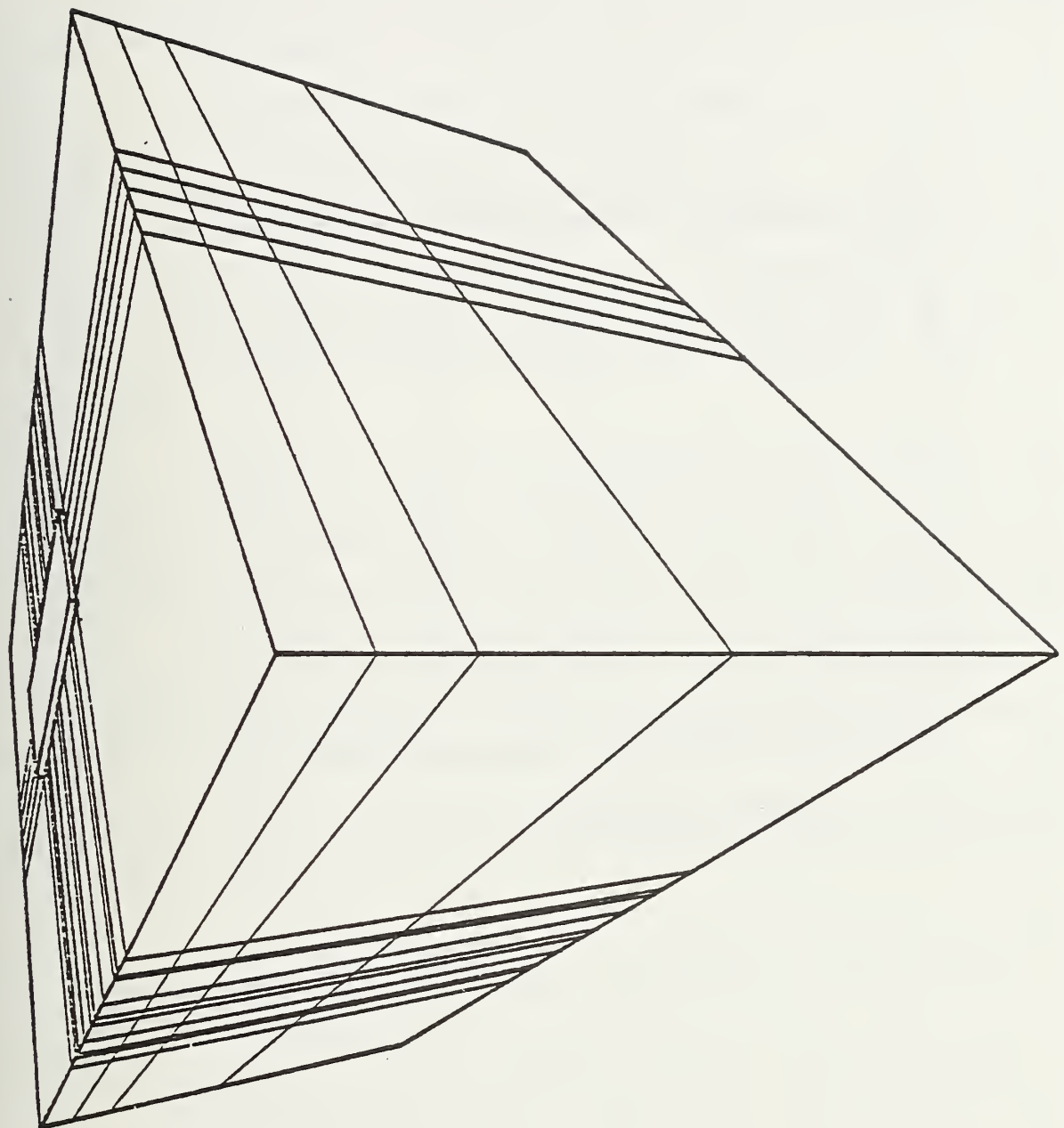


Figure 101. Perspective view of three-dimensional mesh used for thermal stress analysis.

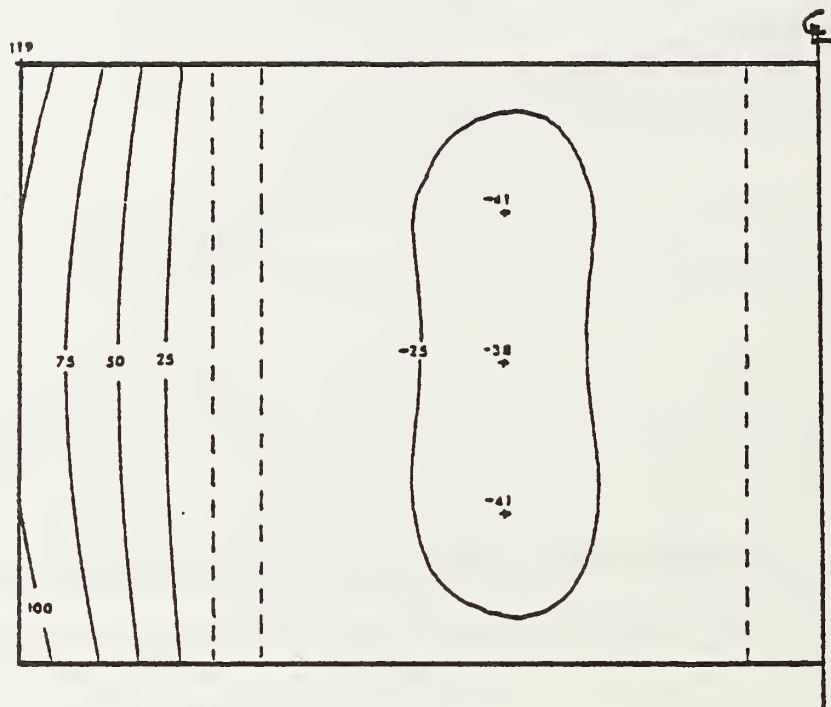


Figure 102. Deflection contours for three-dimensional anchored slab during summer day. (in mils, down is positive).

4.3.6 Moisture

The changing distribution of moisture within the load-bearing layers of pavement systems can often result in variable behavior of the system under applied loads. Mechanical and thermal properties of soil depend significantly upon moisture content.

Some sources of moisture and the impetus for movements are depicted in Figure 103. The more transient sources include forms of seepage that result when surface water percolates through the surface layers. Sources of surface water include precipitation and standing water. Fluctuations in groundwater table elevation can change moisture contents in soil, and water can reach upper layers above a water table by capillary action. Water vapor can also migrate through partially saturated pore structures and reach load-bearing layers in the subgrade.

There are some trends in the quantity of free moisture in any given soil. The amount of moisture varies between soils under similar conditions. Particle size and shape largely influence water content. As particle size decreases, water content generally increases due to the larger specific surface area. The thickness of film water depends on the mineral structure and ions in the film fluid. Particle surface charge can be an important factor. Pore structure is also important. Soils with fine pore structures are more prone to exhibit capillary action than poorly graded, more uniform soils. Other influencing factors include the Atterberg limits, viscosity of the permeating fluid, activity, relative humidity, vegetation, infiltration quantity, evaporation, and drainage conditions.

Angen (1973) has performed a regression analysis to determine factors influencing moisture content. For road surface materials, moisture content increases when density, the distance to the groundwater table, and the percentage of fines decrease. For soils, moisture content increases as density decreases and as precipitation, percentage of fines, and liquidity index increase.

The moisture content of a natural soil is altered when a pavement is constructed. Figure 104 shows the variation in water content of a soil subgrade before and after 80 days of traffic. The pounding of the pavement by the dynamic vehicle loads as well as the alteration in thermal behavior of the system create the increase in moisture content near the surface, in this case, within 3 ft. (0.9 m) of the surface.

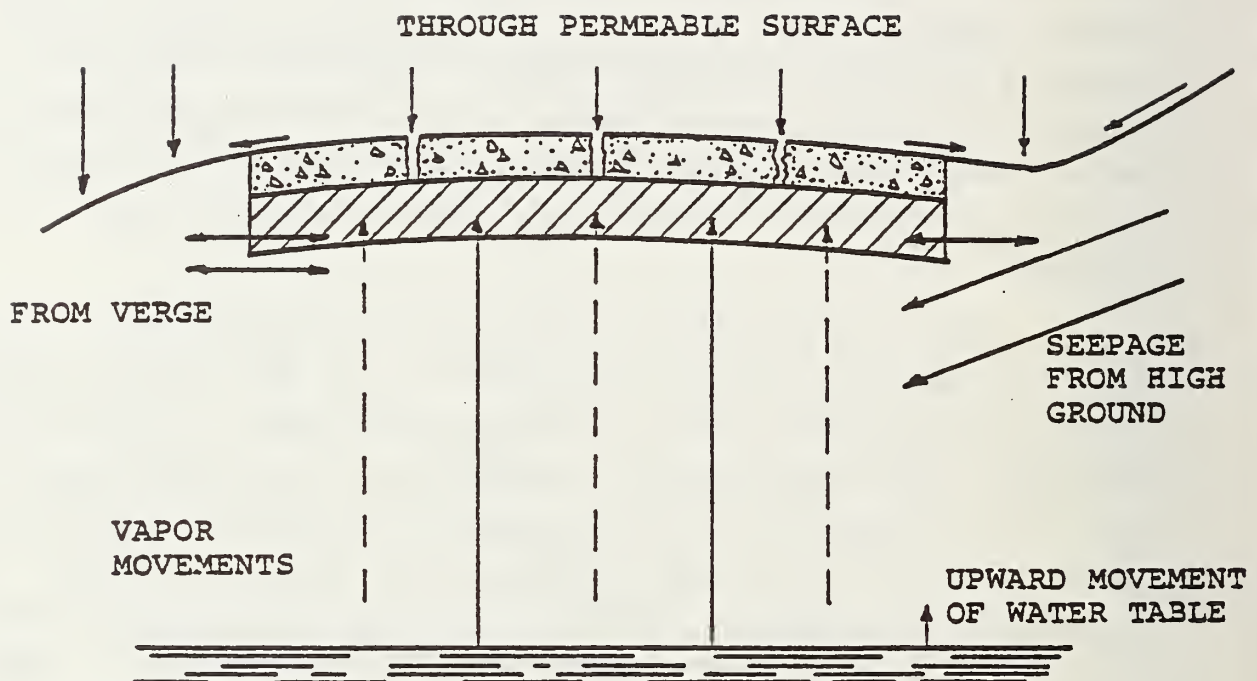


Figure 103. Sources of water and directions of flow in pavement systems (Low and Lovell, 1959).

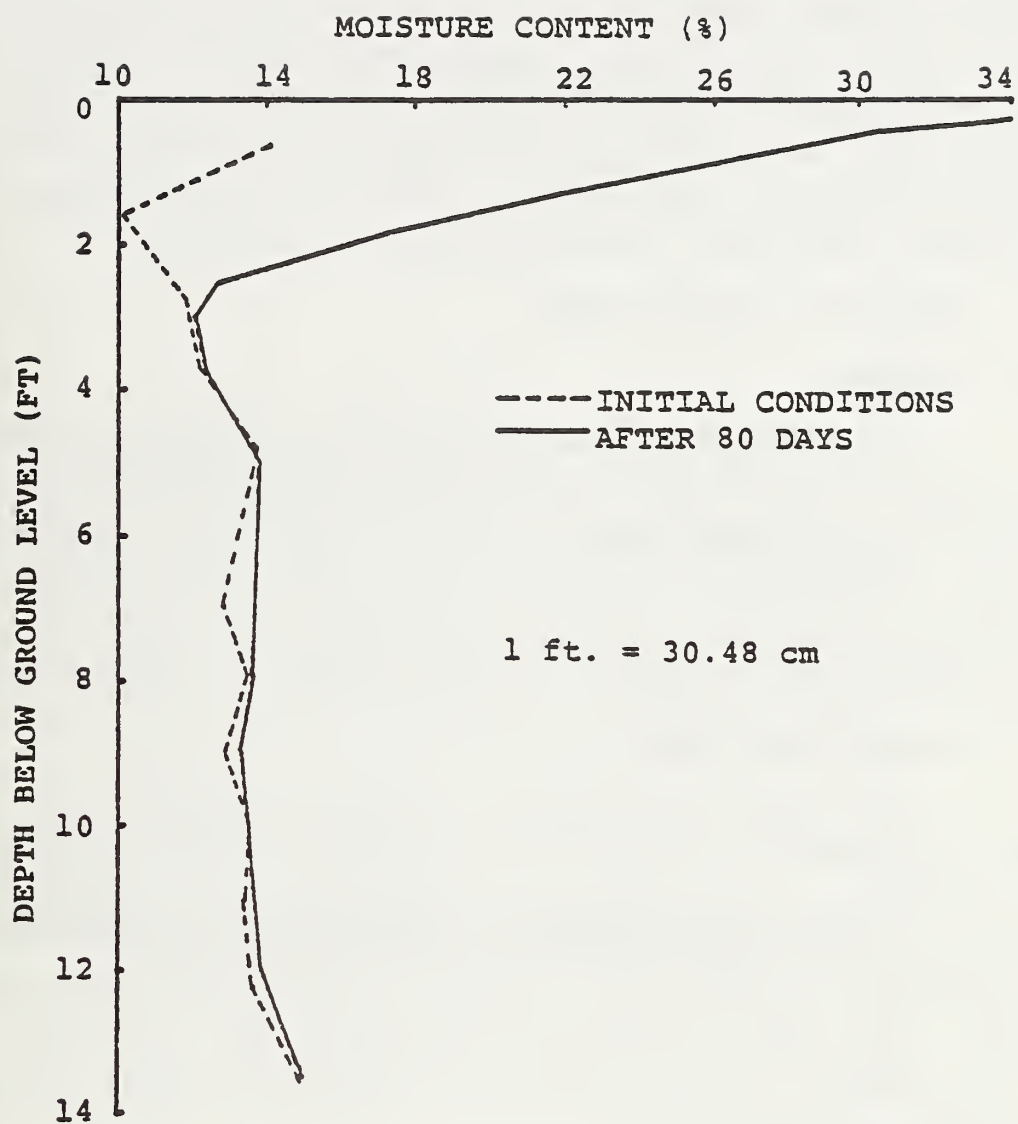


Figure 104. Effect of traffic on moisture content of subgrade soils (Lyton and Kher, 1970).

The behavior of soils and the pavement system in particular, depend on the water content of subgrade soil. Generally soils become weaker as water content increases, especially in more sensitive clays where small changes in water content can greatly alter strength characteristics. Because moisture content in freeze/thaw areas is greatest in the thaw period, the critical condition to study is the period of rapid strength loss in spring with the higher moisture content and lower strength. Modulus of the soil decreases under such conditions, and Poisson's ratio approaches a value of 0.5.

4.4 ANALYSIS OF MECHANICAL LOADS

4.4.1 General

The primary effort in analytical investigations of pavement behavior has been in the determination of the effects of vehicle (mechanical) loads. The deflections of the pavement surface are relatively easy to measure in the field. As techniques for measuring surface strains were developed, it became possible to determine the state of stress within the pavement, and verification of rapidly developing theories for stress analysis of slabs was possible.

4.4.2 Description of Models

All models used an identical 18 kip load (8100 kg) in a two-wheeled axle configuration. Each tire was simulated by a single concentrated load. It is realized that prototype loads are distributed over several square inches of area, but this poses a problem in three-dimensional analysis. A huge number of additional elements would be required, and the analysis would be extremely costly. The single concentrated load does represent a worst case, and stresses in the immediate vicinity of the load will tend to be higher than those from a distributed pressure load.

Each three-dimensional analysis uses the same layout of elements in a transverse section (Figure 105). An isometric view of a 100 ft. (30.5 m) slab (continuous) model is shown in Figure 106. The bottom surface is fixed against movement while vertical sides are on rollers such that no out-of-plane motion is allowed. These are standard boundary conditions used on all succeeding three-dimensional models. Both anchored and conventional pavements are analyzed in this configuration. Additionally, the anchored pavement has also been compared with conventional pavement having a) the same total cross sectional area as the anchored pavement, and b) the same rigidity as the anchored pavement

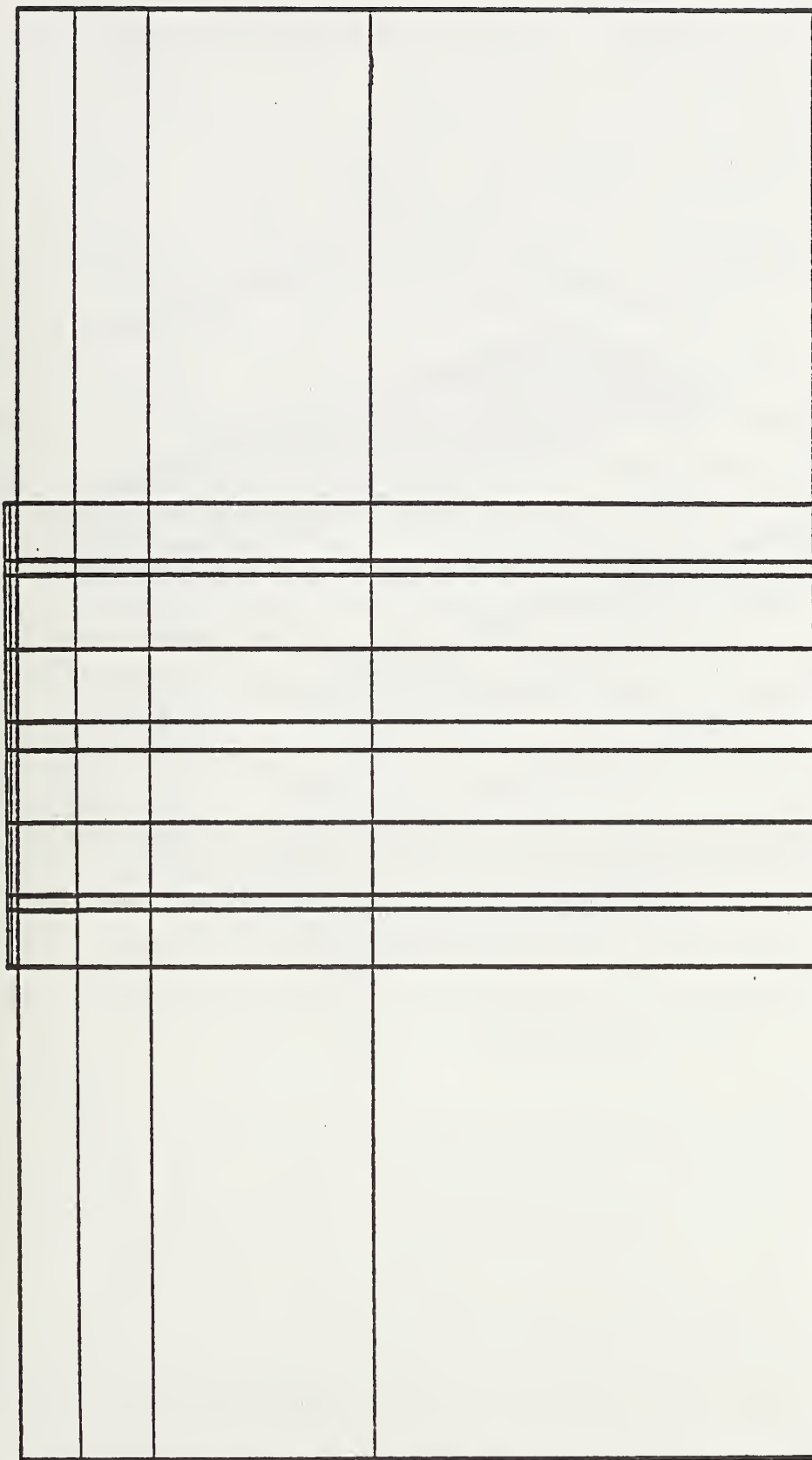


Figure 105. Transverse section of three-dimensional mesh used for thermal and mechanical stress analysis.

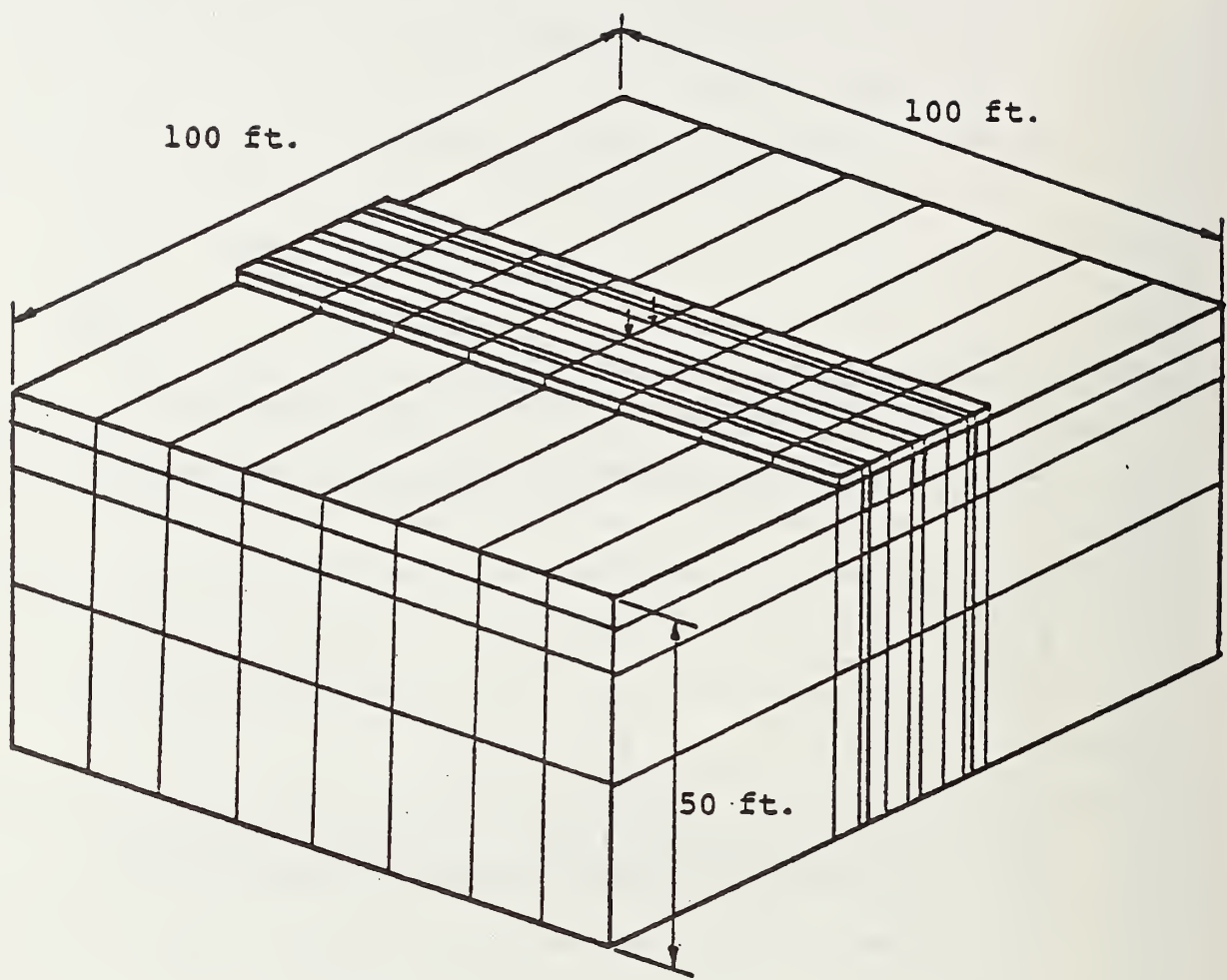


Figure 106. Three-dimensional continuous pavement model, anchored and conventional.

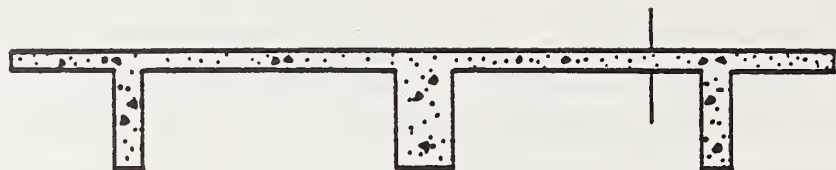
(Figure 107(a) through (e)). The effects of moisture variation are indirectly taken into account by the generally weakening of the top 4 ft. (122 m) of soil as indicated earlier and as shown in Figure 107(e). As a result, a two-layer elastic system is set up in the identical 100 ft. (30.5 m) slab configuration with the same load. The soil in this weakened zone is reduced to a value of 100 psi (7 kg/cm^2). With this radical alteration, the effects of subgrade weakening on pavement surface deflection response could be readily seen. It would also be possible to determine roughly the percentage of load transferred to the soil by the anchors.

Mechanically uncoupled jointed pavements are also considered. In this analysis the load positions are: an interior load and a joint load. In addition, slab size is considered with a single 12.5 ft. (3.8 m) slab and a 50 ft. (15.3 m) slab modeled. The single slab received interior and joint loads; the long slab (nearly continuous) received only joint loads, which are deemed more critical. The case of interior load has already been considered in the 100 ft. (30.5 m) slab analysis.

Sliding interface elements were again employed for modeling slab contact with soil and were used at every node on the subsurface of the slabs. The only possible joint load transfer was through movement of the subgrade soil. A jointed pavement with no load transfer across a joint that is loaded at the joint will exhibit somewhat different behavior near the joint, as depicted in Figure 108. The end surfaces will be unstressed and as a result will rotate as indicated. Continuous pavements have a continuity of the middle plane beneath the load, and since the rigidity is continuous in the longitudinal direction, will be stressed in a plane passing through the load.

4.4.3 Results

Surface deflections and stress distributions are presented for various conditions considered. Figures 109 and 110 present a comparison of transverse and longitudinal deflections of the anchored pavement with a conventional slab (10 in. (25.4 cm) thick, without anchors), a conventional slab with equivalent area ($1.33 \times 32 \text{ ft. (}0.4 \times 9.75 \text{ m}\text{)}$) and a conventional slab with equivalent stiffness ($3 \times 32 \text{ ft. (}0.9 \times 9.75 \text{ m}\text{)}$). The figures indicate the following magnitude of deflections under load:



a) Anchored pavement (for dimensions see figure 1).

1 in. = 2.54 cm



b) Conventional pavement 10 in. thick.



c) Conventional pavement 16 in. thick
(equivalent area to a).



d) Conventional pavement 36 in. thick
(equivalent rigidity to a).



$E_2 = 1000 \text{ psi.}$ $1 \text{ psi} = 7.03 \times 10^2 \text{ kg/cm}^2$

e) Anchored pavement on layered subsoil.

Figure 107. Pavement configurations.



a) Continuous.



b) Jointed.

Figure 108. Difference between deflection behavior with load at a joint in a jointed pavement and with load on a continuous pavement.

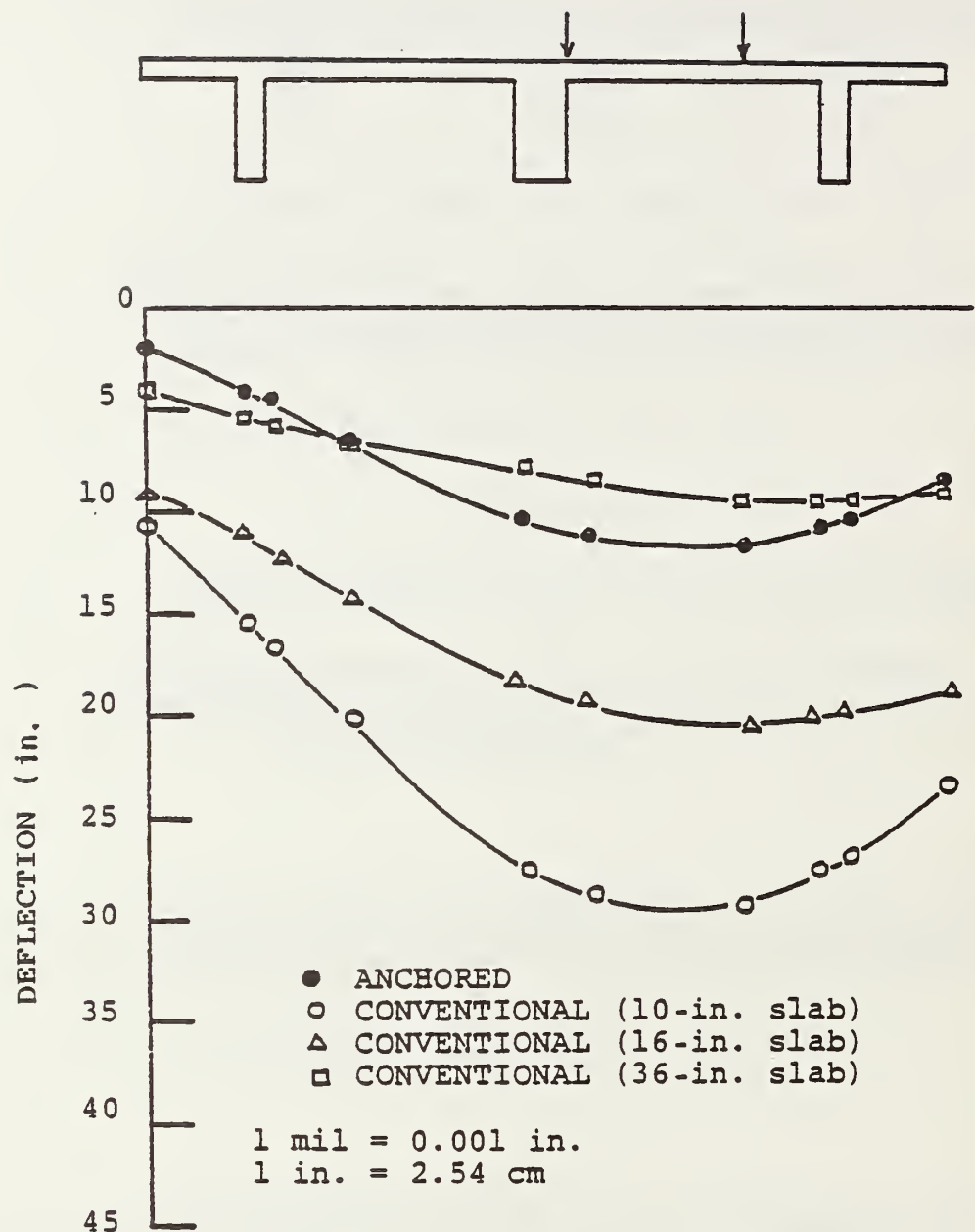


Figure 109. Transverse surface deflections at load in 100-ft. (30.5-m) models.

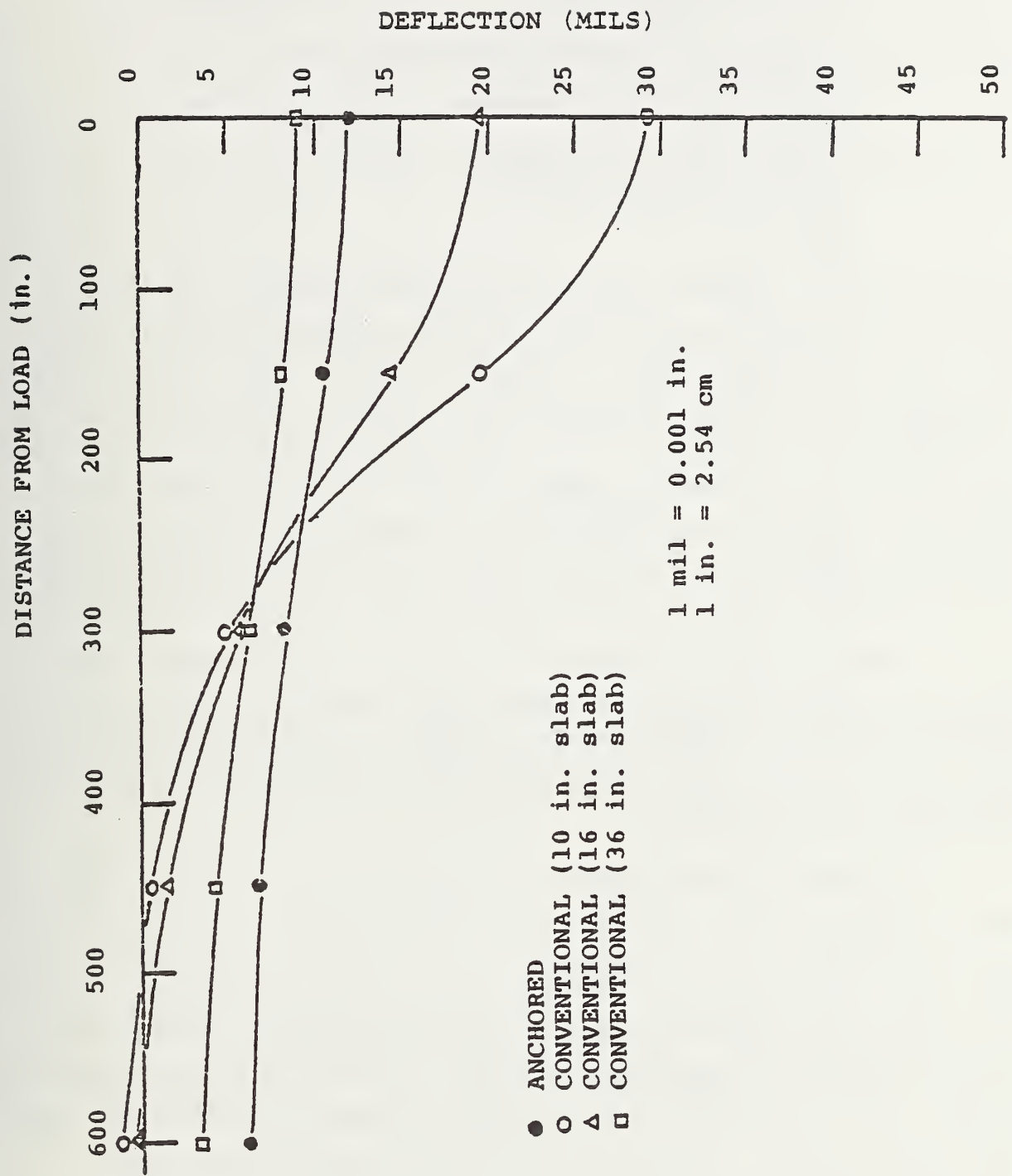


Figure 110. Longitudinal surface deflections in outer wheel path for 100-ft. (30.5-m) models.

a) anchored pavement	12 mils (1 mil = 2.54×10^{-3} cm)
b) conventional pavement (10 in. = 25.4 cm slab)	29 mils
c) conventional with equivalent area (16 in. = 40.64 cm slab)	20 mils
d) conventional with equivalent stiffness (36 in. = 91.4 cm slab)	9 mils

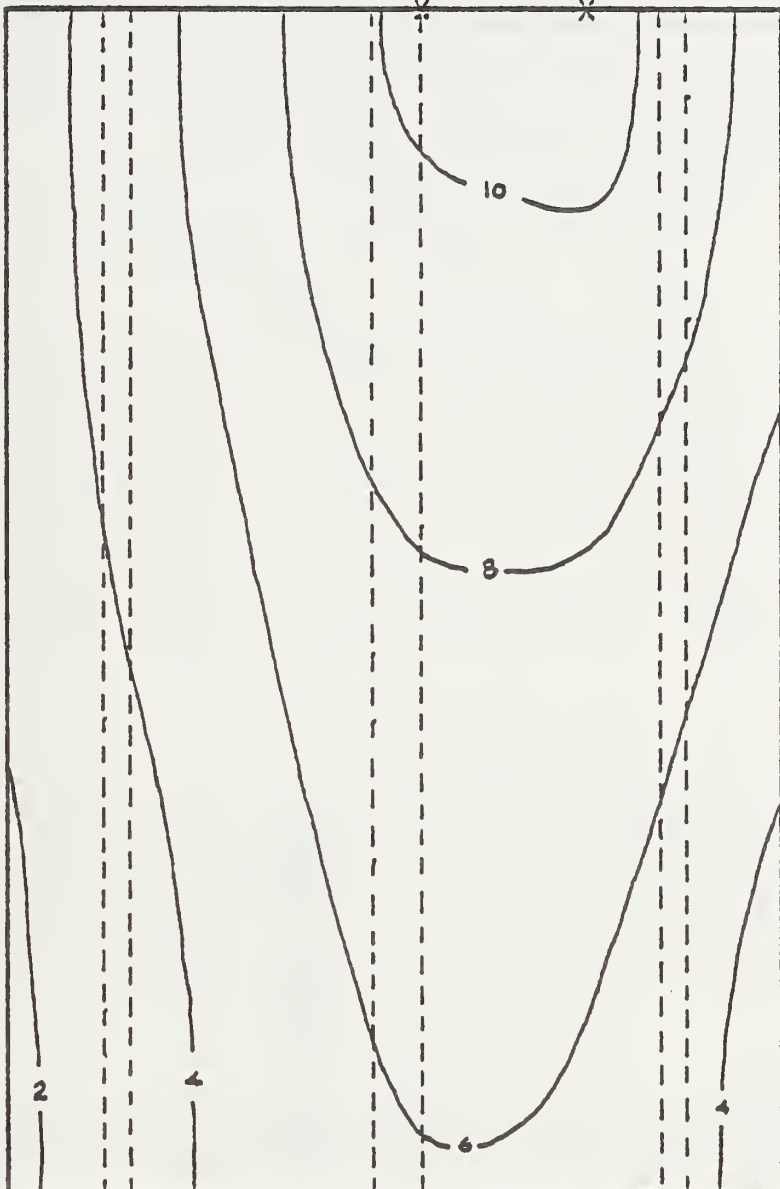
The cross sectional concrete area for the anchored pavement is 42.67 ft.² (3.96 m²) while that of the equivalent stiffness pavement is 96 ft.² (about 9 m²), which is more than double. Secondly, the 36-in. (91.4 cm) slab even if it is embedded 24 in. (61 cm) in subgrade will be heavily influenced by the freezing and thawing action of the soil. The investigators strongly believe that advantages offered by the anchored pavement in terms of transferring the load to below freeze/thaw depth by far excel the other configurations. In the following discussions, therefore, comparison has been made only of the anchored pavement with the conventional one without the anchors (i.e., 10 in. = 25.4 cm thick).

Deflection results agree quite favorably with prototypical behavior. Recalling the results presented by Moore et al. (1969) for a 100-lb. (484 kg) load and scaling for a 9000-lb. (4080 kg) wheel load, the deflection results are quite similar in magnitude. (Differences arise because the soil and structural properties are not the same.)

Surface deflection contours for the 100-ft. (30.5 m) slab models are shown in Figure 111. The conventional pavement exhibits the typical concentric contour deflection basin often reported in the literature. The anchored pavement, with its much higher longitudinal rigidity, tends to "barrel" and reveals more cylindrical rather than spherical deflection patterns. Deflections of the anchored pavement are approximately one-half of the values for the conventional pavement at the load points, but the anchored pavement deflections are somewhat larger near the end. Longitudinal deflection of the outer wheel path (Figure 112) reveals the shapes of the deflection basins in the 100-ft. (30.5 m) pavements. Since deflections at 50 ft. (15.2 m) from the load were quite small for the conventional pavement, it is felt that boundary conditions are satisfactory; deflections at the loads would still be slightly less for a truly

SYMMETRIC

LOAD LOCATIONS



1 mil = 0.001 in.
1 in. = 2.54 cm

Figure 111. Surface deflection contours (in MILS) for continuous anchored pavement (anchor locations are shown in dashed lines).

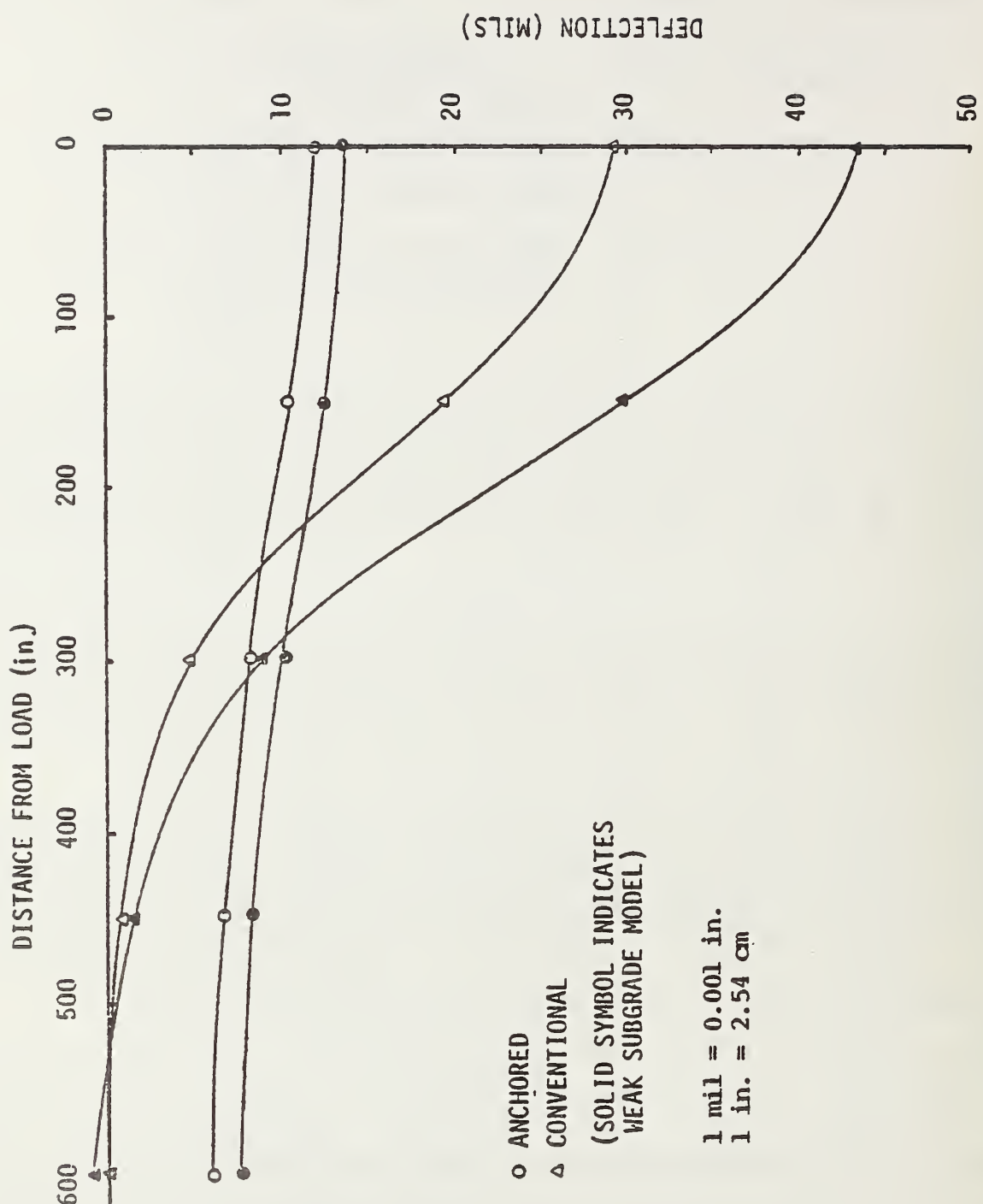


Figure 112. Longitudinal deflections in outer wheel path for 100-ft. (30-m) slab models.

infinite continuous slab. The anchored pavement, however, possesses a nearly uniform deflection basin. Also, while the maximum surface deflection of the anchored pavement with subgrade weakening increased by 15%, the maximum deflection of the conventional slab increased by 48%. Thus, in the transference of load to lower layers, anchors are extremely important, especially if they are found below the frost line and the zone of significant spring thaw weakening. Transverse deflections of the continuous anchored pavement indicate much smaller deflections that are more uniform along the transverse section (Figures 113 and 114). Farther from the load, conventional slab deflections are smaller, but shoulder edges tend to lose contact with the soil.

As expected, the deflections of the jointed pavements are substantially greater (as much as 50%) than the continuous pavement. Deflections are also larger at the joint for joint loads. The jointed pavement anchor lengths are the same as those for the continuous model and result in similar total stiffnesses. The anchors tend to spread load over a larger area and thus do not deflect as much as the conventional pavement. With an infinite (larger) length of anchors and subgrade extent, the edge-loaded anchored slab deflections should be somewhat smaller. The same holds true for the conventional slab with a larger subgrade extent: joint load deflections should be smaller at the joints with longer slabs. In Figure 115, the longitudinal deflections of the single slab are shown with both joint load and interior load. For comparison purposes, the 100 ft. (30.5 m) results are also included. Joint loads increase surface deflections in the conventional pavement significantly while they do not affect the anchored pavement nearly so much. The anchors in this case are continuous for 100 ft. (30.5 m), and the deflections are only increased in the wheel path, not directly over an anchor. Anchor deflections are similar for continuous or jointed slabs. Had the anchors also been discontinuous, much larger deflections would have occurred, but would be still less than the conventional slab deflections.

The longitudinal deflections of the longer (50 ft. (15.3 m)) pavements are shown in Figure 116. This analysis was performed with the weakened subgrade condition, and very large deflections at the joint in the conventional system were seen. The difference in the deflection of the loaded and unloaded slab is apparent, with load transfer taking place via subgrade movement. This amounts to about a 50% transference of deflection but not necessarily of load. There is, in essence, no direct load transfer. The anchored slab shows greater deflection,

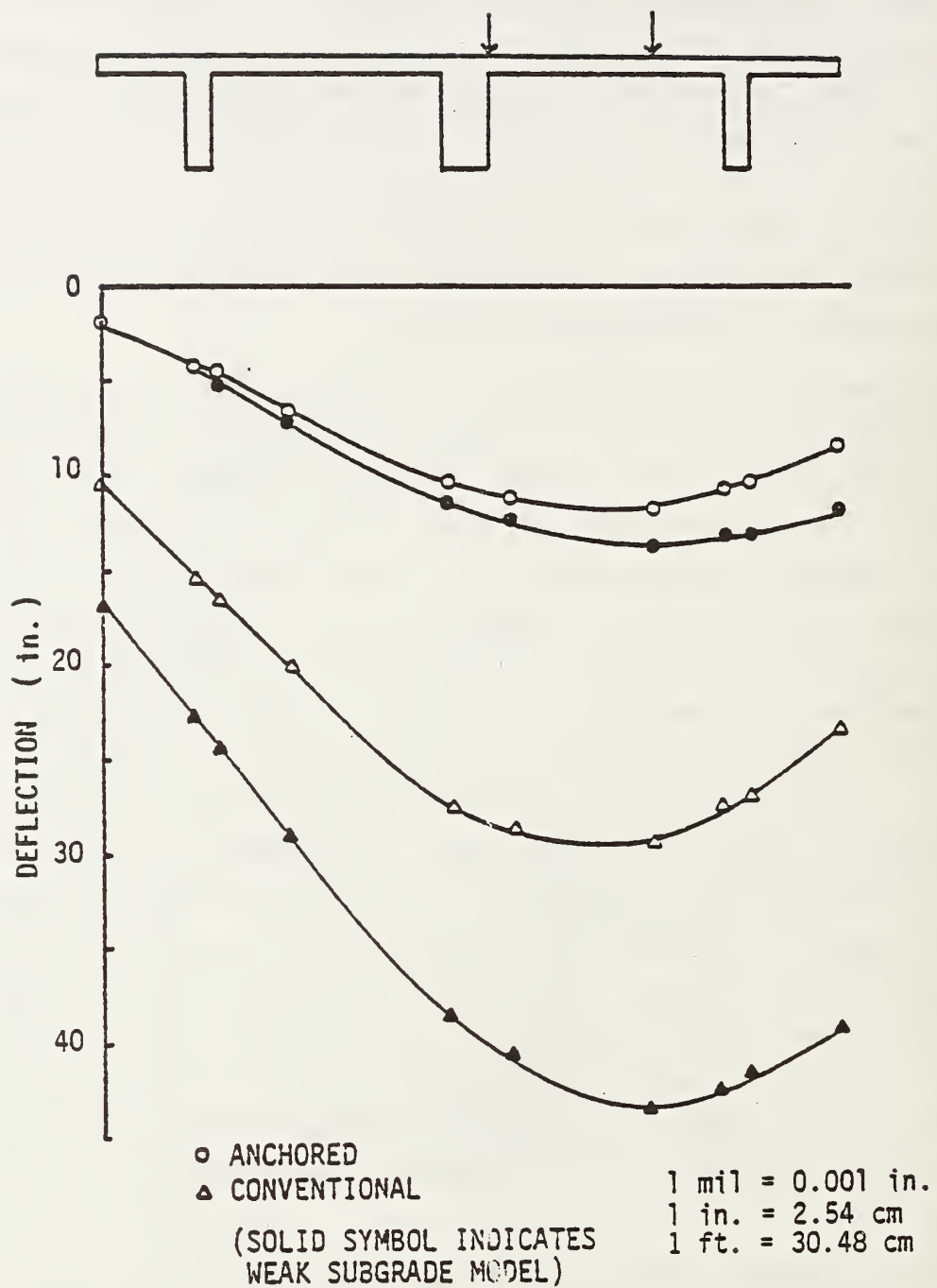


Figure 113. Transverse deflections at load in 100-ft. (30.5-m) models (weak upgrade).

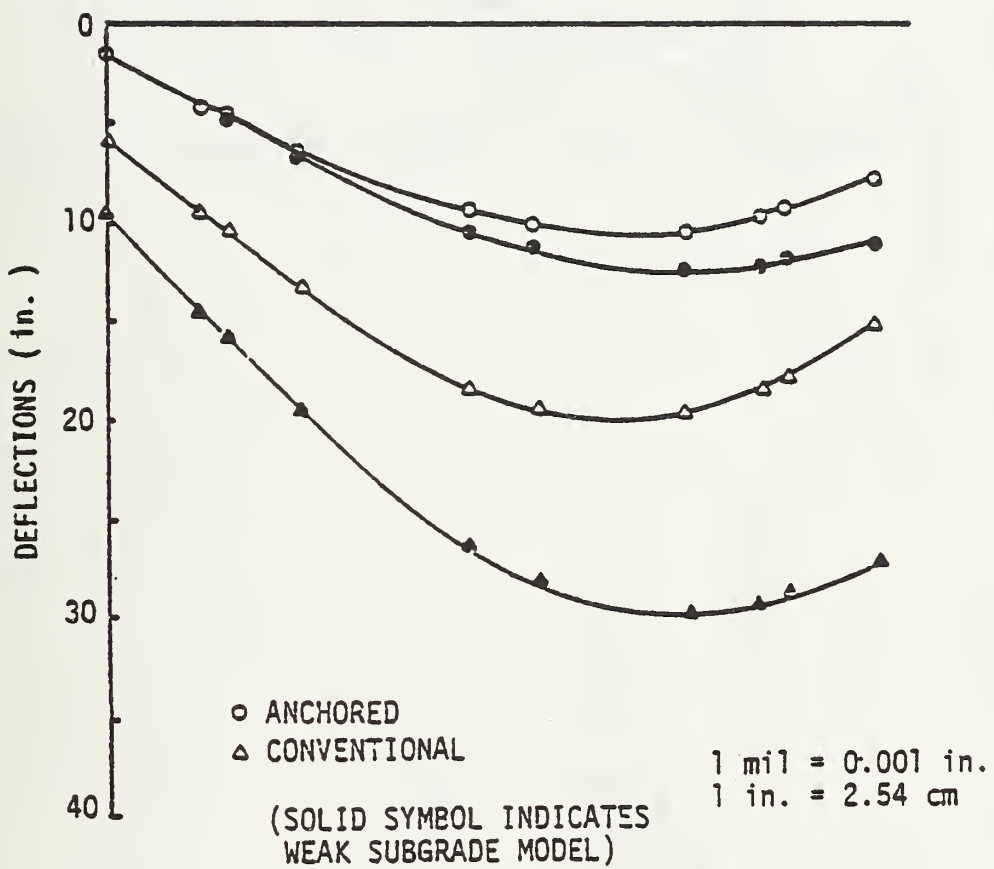


Figure 114. Transverse deflections 75 in. from load in 100-ft. (30.5-m) models.

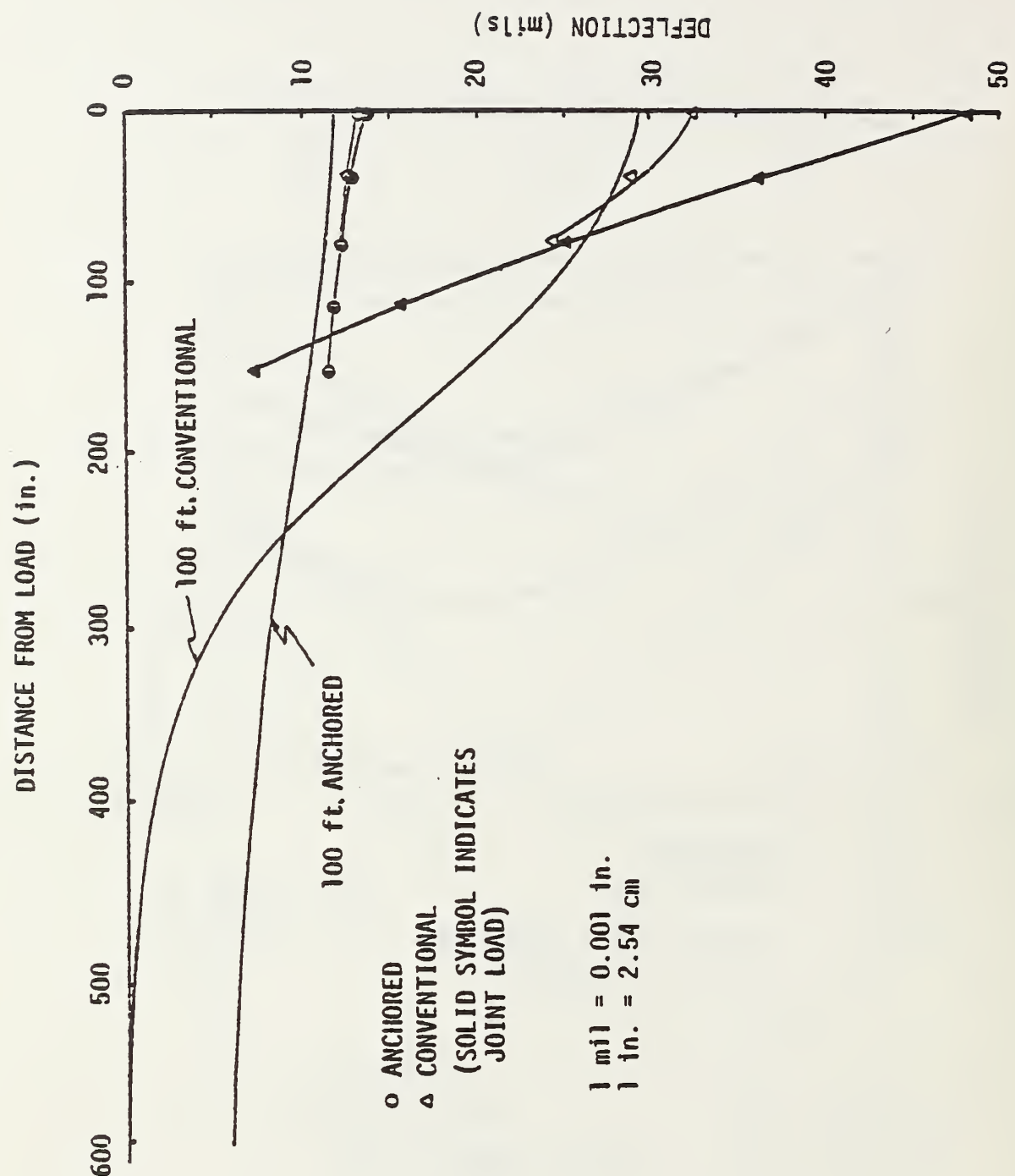


Figure 115. Longitudinal deflections in outer wheel path for single slab models.

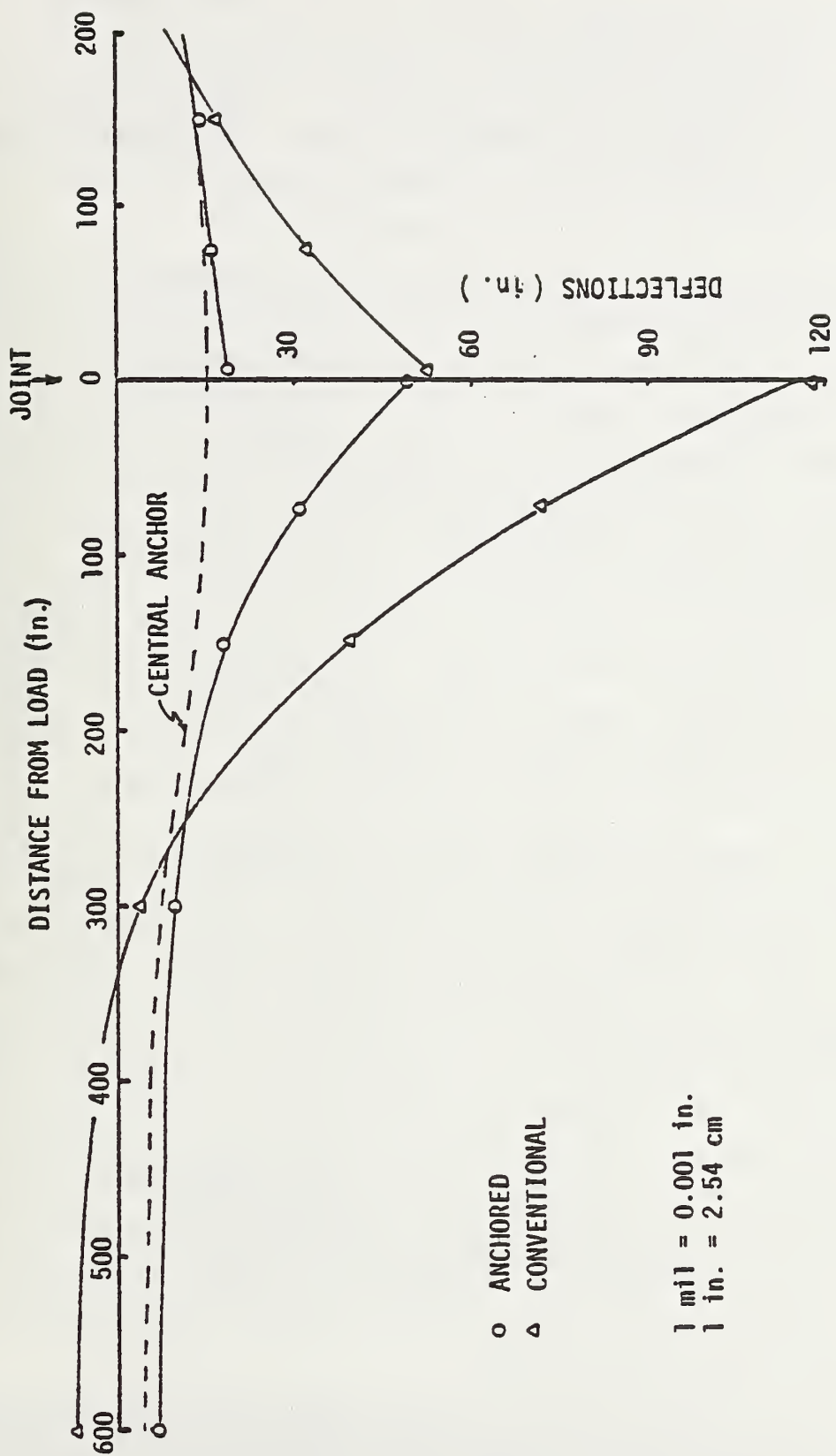


Figure 116. Longitudinal deflections for 50-ft, (15-in.) slab in weak subgrade with load at a 1 in. (2.5 cm) joint.

but the anchor deflection is again identical to that of the continuous 100-ft. (30.5 m) slab in the weakened soil.

Transverse surface deflections are shown in Figures 117 and 118 for conventional slab. Extreme deflections can be seen. The anchored pavement significantly decreases deflections and alters the nature of the slab deflections so that more uniform and controlled patterns arise.

Resulting stress contours for the various load conditions in the different models have been studied, and the results are presented in the following pages. Longitudinal bending stresses again show different behavior in anchored and conventional pavements. Because surface deflections are lower, the anchored pavement bending stresses are higher. The anchors also tend to pull soil at about the 2 to 4 ft. (0.6 to 1.2 m) level to contribute to this increased rigidity. The longitudinal surface stress contour patterns are also different in that the continuous anchored pavement has a stress reversal at about 20 ft. (6.5 m) from the load while conventional pavement longitudinal bending stresses tend to zero with distance from the load. Transverse surface bending stress distributions for the two concepts differ greatly. Conventional pavement stresses are more regular and appear as nearby concentric contour lines, because rigidity is similar in all directions far from the pavement edges.

The stresses introduced into the soil subgrade give further insight on the differences between the two pavement concepts. Vertical stresses for the conventional pavement appear as concentric rings at both the 24 and 48 in. (60 and 120 cm) levels. The anchored pavement, however, tends to distribute loads more uniformly. Localized vertical stress intensification at the 24 in. (60 cm) level results from increased stress in the anchors and the assumed compatibility between anchor and soil that also absorbs some vertical stress. In the continuous anchored pavement, the lower level stress directly beneath the anchors reveals a rather uniform longitudinal distribution, indicated by the contour lines that parallel the pavement length. The contours that cross the anchor lines (being spaced farther apart) indicate the more even distribution of load in the soil. Maximum vertical stress at 24 in. and 48 in. (60 cm and 120 cm) depth is also lower in the anchored system.

Jointed pavement behavior reflects some similar trends in the state of stress. The jointed anchored pavement tends to distribute loads deeper within the subgrade in a more uniform manner, more uniformly, in fact, than the con-

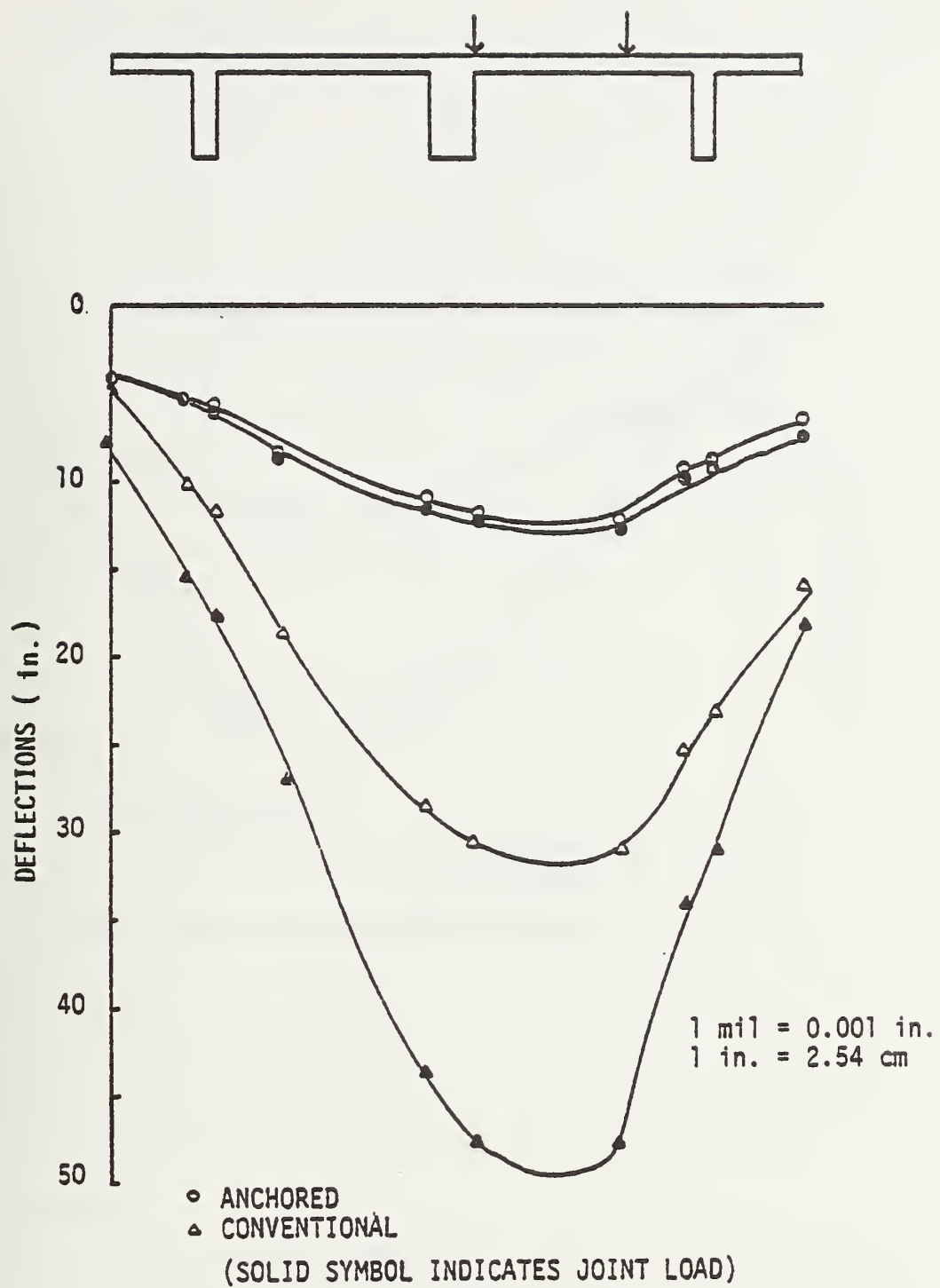


Figure 117. Transverse deflections at joint in 50-ft. (15-m) pavements in weak soil.

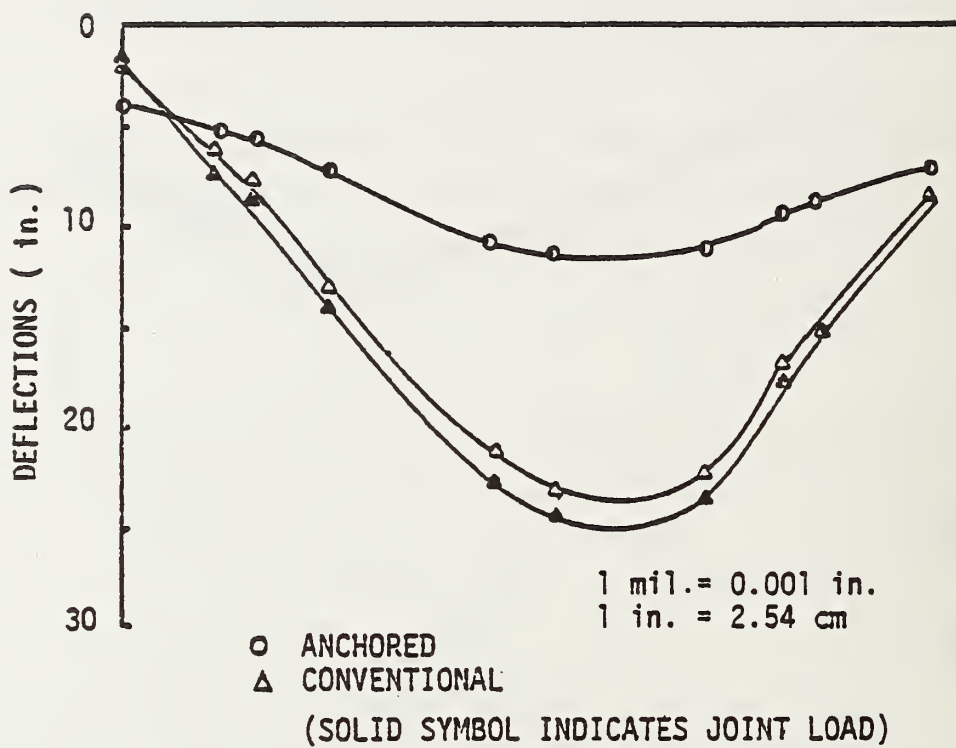


Figure 118. Transverse deflections 75 in. from load (joint) in 50-ft. (15 m) jointed pavements in weak soil.

tinuous anchored pavement, as little load is transmitted to adjoining slabs; most load is redistributed by the anchors. Stresses are generally increased in the anchored structural elements, but subgrade soil stresses are reduced. Because the load on the conventional slab is applied as traveling in the shorter direction, the longitudinal bending stress distribution is no longer a series of simple concentric rings. There are also more stress reversals in the jointed conventional slab than in the continuous conventional pavement.

Vertical stresses within the subgrade soils show similar trends. At the 24-in. (60 cm) level, conventional pavement stress contours are regular rings while the anchored slab pattern indicates stress pockets centered in the anchors that tend to pull the soil, spreading stress to the soil in this localized area. Below the anchors, however, conventional pavement stresses remain annular while anchored pavement stresses are nearly uniform in the longitudinal direction, regardless of where the load was applied (at a joint or within a slab).

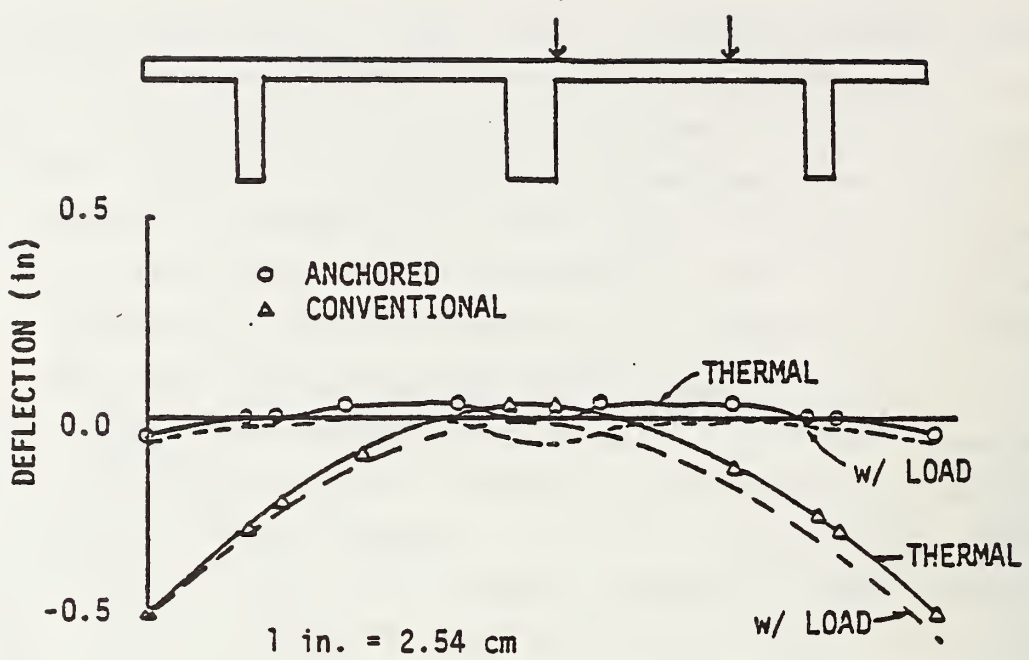
4.5 SUPERPOSITION OF ENVIRONMENTAL AND MECHANICAL LOADS

4.5.1 General

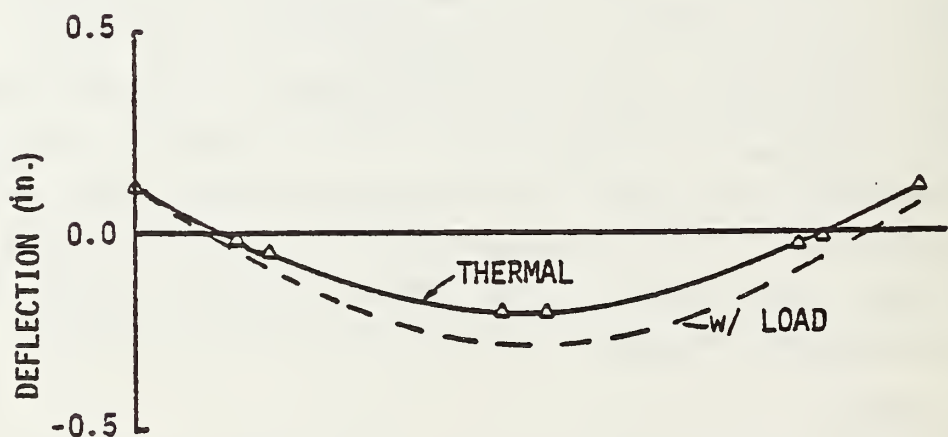
Analysis of the general response of pavements requires the superposition of effects caused by environmental loads on mechanical (vehicle) loads. A careful examination of the predicted magnitudes of the effects under each type of loading can provide a better understanding of the systems overall response and subsequent adequacy for designed use. Critical conditions and primary loads can be ascertained, and such contingencies can be managed. This section seeks to combine the effects of the previous analysis for a more complete description of each system's gross response to the types of loads and loading combinations that may be encountered throughout the design life of the structure.

4.5.2 Results

Of primary interest and by far the easiest quantities to superimpose are pavement surface deflections. Pavement analyses have historically begun with prediction and examination of deflections. The results of the superposition of some extreme conditions are shown in Figures 119 and 120. The results clearly show the significance of environmentally (thermally) induced deflections -- curling. Deflections from curling can be as much as one order of magnitude larger than vehicle-imposed deflections. These strains are usually applied over

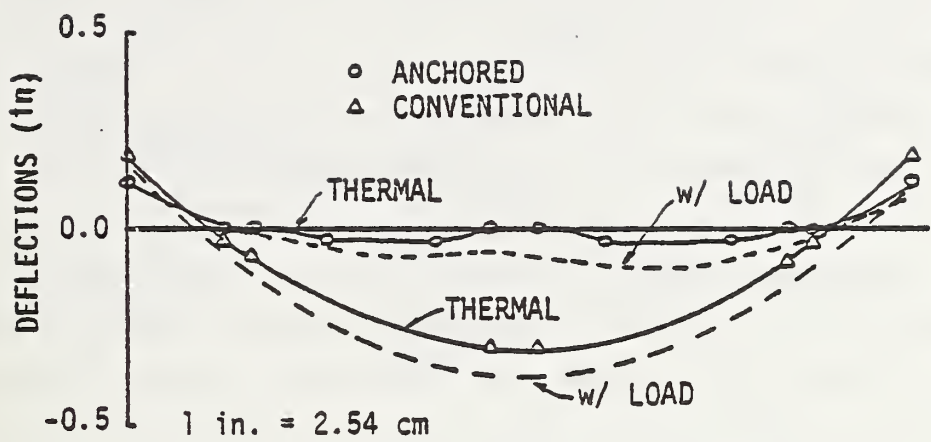


a) Extreme summer condition - daytime.



b) Extreme summer condition - nighttime.

Figure 119. Results of surface deflection load superposition (summer).



Extreme winter condition - night.

Figure 120. Results of surface deflection load superposition (winter).

longer periods (several hours), whereas vehicle loads are dynamic and nearly instantaneous. Dynamic loads are often smaller in magnitude than static loads but can cause reverses in deflection curves. These dynamic vehicle loads are dissipated quickly. Thermally induced strains, however, do not dissipate so quickly and can induce various creep and fatigue phenomena, which, coupled with constant vehicle load pounding, can accelerate the deterioration of the system.

Generally, the anchored pavement reduces deflections by as much as one order of magnitude. Especially affected are curling deflections which are nearly eliminated by the stiffening of the pavement edges. When deflection is reduced, however, stresses are increased near the anchors, because of the reaction restraint they impose on the slab. It may be necessary to include reinforcing rods as well as steel fibers to adequately provide for such stress increases.

4.6 ANALYSIS OF JOINTS

4.6.1 General

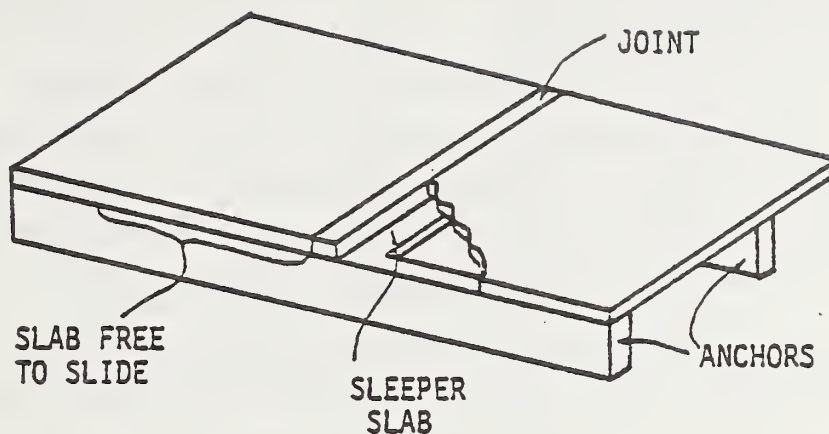
In areas prone to large diurnal or seasonal variations in temperature, pavement expansion and contraction become a problem. Joints must be included in the pavement system to adequately manage any movement in the system and still provide a relatively smooth surface.

The anchored pavement concept poses unique problems in joint design and construction. Theoretically, for a truly continuous pavement, separation of the slab and anchors to promote sliding may be necessary near expansion/contraction joints because of the difference in anchor and slab movements. However, an anchored pavement with a sleeper slab below the joint may not require such separation, because deflections from thermal strains are smaller for shorter slabs.

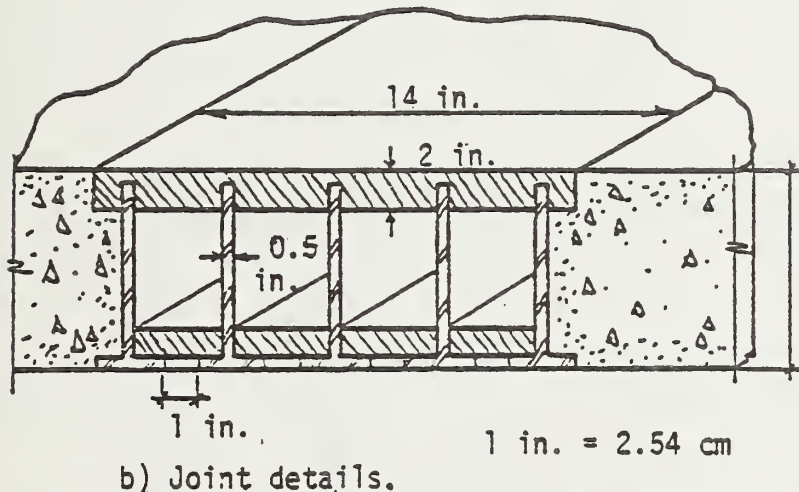
A prospective joint for the anchored pavement slab is presented in the following section. Analysis was undertaken to determine the behavior of the joint under compression and expansion loadings. Special construction details are also presented.

4.6.2 Description of Joint and Mathematical Model

The joint concept chosen is based on a system reported by Mogilevich *et al.* (1976). The joint consists of a set of parallel vertical plates (Figure 121) coupled at the tops and bottoms by an elastomeric material. This material was assumed to have a modulus of 500 psi (35 kg/cm^2) and a Poisson's ratio of 0.47, typical of many rubberlike materials. The material is rather weak to allow



a) Overall joint construction of prototype joint in anchored pavement.



b) Joint details.

Figure 121. Joint concept proposed for use in anchored pavement.

considerable flexibility, and because Poisson's ratio is taken near 0.5, deformations are at constant volume.

The joint is assumed to rest on a sleeper slab cast integrally with the anchors. This inhibits water infiltration and should eliminate problems, such as pumping, that may occur. The lower surface of the joint structure is frictionless and can slide freely on the sleeper slab. The elastomeric material is assumed to be bonded to the steel plates such that no gaps or peeling occur.

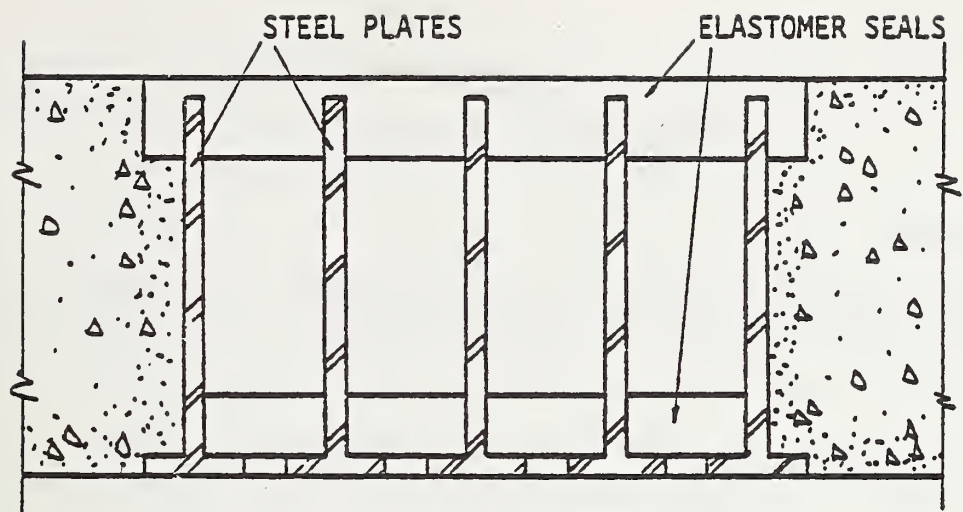
The system was given a 2-in. (5 cm) compression and extension from its initial unstressed state. This loading condition imposes a uniform deflection in the axial direction (no rotation or curling of the slab end) that can be controlled by the sleeper slab design.

4.6.3 Results

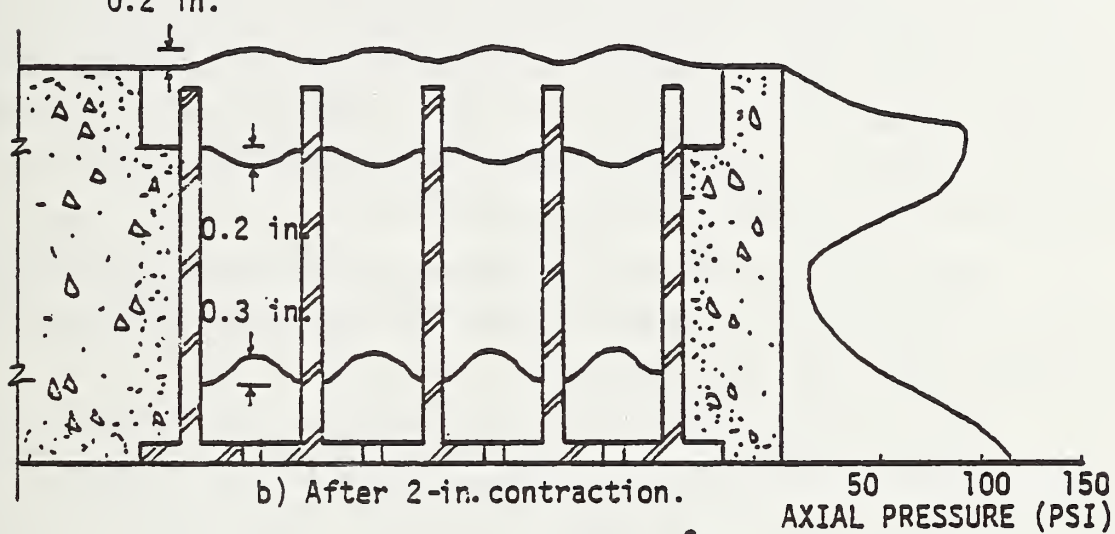
Deflections and stresses were determined for a plane strain longitudinal section of a typical transverse joint. Figure 122 presents deflections resulting from the expansion and contraction loadings. In this figure, vertical deflections are exaggerated by a factor of 2.5 to 1. The resulting deflections create small ridges approximately 0.2 in. (5 mm) high and depressions of about the same magnitude. This is consistent with values reported by Mogilevich (1976) for a 30% reduction in joint width, about 0.2 in. (4.8 mm) maximum.

Axial stresses in the concrete slab near the joint induced by the expansion and contraction of the joint are also shown in Figure 122. Maximum stresses of about 120 psi (8.4 kg/cm^2) in both tension and compression are manageable in steel fiber reinforced concrete (SFRC). Care must be taken to ensure proper anchoring of the joint to the slab by hooks or other conventional anchors. The pressure distribution shape is consistent with its loading geometry, as the low stress portion occurs in the void area that transfers only a small portion of the load through the end steel plates.

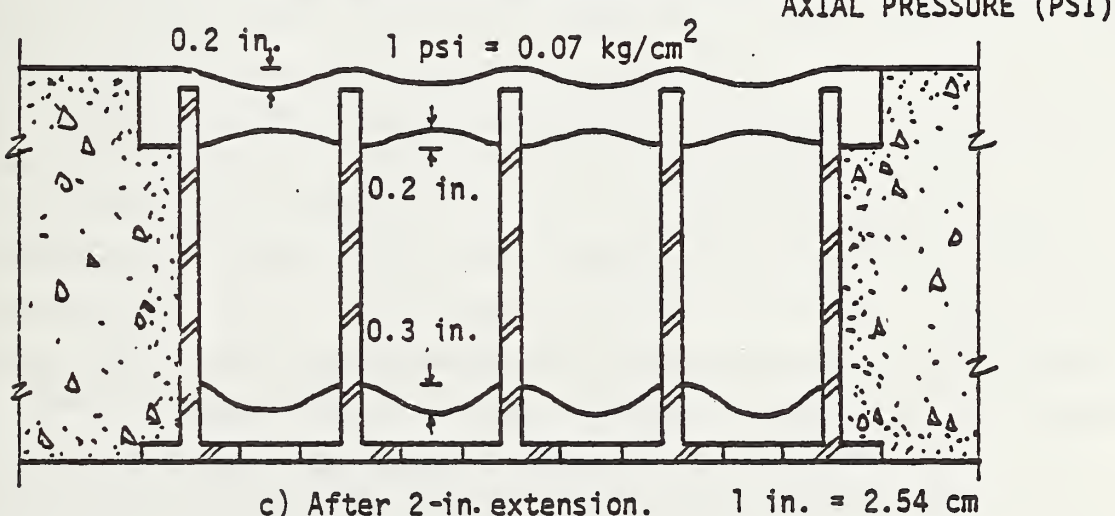
The results of this analysis indicate the feasibility of this joint-filling concept. Some physical details would need refining for field testing and evaluation.



a) Initial joint model.



b) After 2-in. contraction.



c) After 2-in. extension.

Figure 122. Results of joint response to slab movement analysis.

CHAPTER V

CONCLUSIONS AND RECOMMENDATIONS

5.1 CONCLUSIONS

This study has attempted to further advance the methodology for analysis and design of pavements. Of primary concern was the effect of environmental loads placed upon the system, in particular, cyclic temperature differentials. Relative magnitudes of the analytically obtained deflections compared favorably with field data collected from various road tests and reported in the literature. It is hoped that the use of three-dimensional finite element analysis will gain increasing acceptance as more efficient techniques are developed to handle the associated large system of equations, and also as faster and more powerful computers are utilized to cut analysis costs. Many problems in pavement system analysis, as well as in geotechnical engineering in general, can only be solved adequately by a full three-dimensional analysis.

The results of the analysis indicate the significance of environmentally induced stress. Pavement warping deflection can be greater than deflection due to applied wheel loads.

Various combinations of loading conditions that include as components the environmental and mechanical loads are possible. It is possible to choose a case that is sufficiently detrimental and occurs often enough to be considered a worst case. Usually such a condition involves high stress concentrations and numerous stress reversals. A conventional slab that warps down (during daylight hours) then is loaded mechanically will experience deflections similar to those in Figures 119 and 120, and reversals of transverse bending stresses will result in a "wrinkled" slab. The anchored pavement deflections are relatively uniform and smaller, thus, will be much more predictable; however, stresses near the anchors in the structural elements of the anchored pavement are increased. Precautions must be taken to ensure adequate reinforcement in these areas.

The anchored slab offers two distinct advantages over a conventional slab. First, deflections are lower and more uniform. Second, stresses in the soil are lower and distributed more widely by the rigid anchors. A significant portion of pavement distress mechanism arises from subgrade failure. If loads are transmitted deeper within the subgrade, to soil that is under greater confining stresses (and as a result is stronger) and where moisture and

temperature fluctuations are not acute, subgrade-related failure is less likely to occur.

As with any engineering solution, there are trade-offs. Generally soil behavior is much more random and uncontrollable; this should be a serious consideration. The actual structural elements can be strengthened in a controllable manner, and tolerance to increased stresses can be managed.

5.2 RECOMMENDATIONS

Finite element modeling techniques for the analytical determination of a pavement system response to various loading conditions have been presented. Full three-dimensional analysis of continuous and jointed pavements is relatively costly, but the analysis is much more sophisticated as complex loading and boundary conditions and system geometry are more accurately modeled. Plane strain analysis of longitudinal or transverse sections completely ignores out-of-plane rigidity of the structure, which is extremely important, especially in the anchored pavement. Loads are also input as line loads of infinite extent and do not accurately portray prototypical configurations. Techniques to extrapolate three-dimensional behavior from a two-dimensional model using prismatic solid finite elements (Cheung, 1976; Pichumani, 1973) have been developed. Continuous pavements with three-dimensional arbitrary loading patterns approximated by Fourier expansions in the longitudinal direction can be modeled; however, jointed or otherwise discontinuous (cracked) pavements have not been adequately simulated.

This study has considered fully continuous and discontinuous pavement slabs to simulate continuous rigidity and load transfer and finite rigidity and no load transfer, respectively. These represent the extremes in actual systems; the prototypes are actually categorized between continuous and discontinuous. It is possible to include the effects of partial load transfer by several methods. Perhaps the simplest method that does not add any elements to the system involves simulating load (force) transfer by constraining the movement of nodes along the joint of unloaded slabs adjacent to a loaded slab. It is possible to write an equation in the computer program utilized (ANSYS) to accomplish this:

$$c = \sum a_i u_i$$

where c is a constant, a_i is factors and u_i is displacements. For example, if a node 2 was allowed to move in the x direction only half as much as a node 1, the equation for this constraint would be:

$$x_1 - 2x_2 = 0$$

12

so that $a_1 = 1$, $a_2 = -2$, and $c = 0$. It is possible to simulate more complex phenomena such as limited rotational (moment) transfer by more complex equations.

Another method to simulate load transfer is to include dowel elements in the mesh, either in single or double layers. Care must be taken when using truss elements with pinned end conditions to model dowels embedded in concrete. A system of springs can be used to effectively fix the rotation of the bar with respect to the slab end.

Other techniques can involve the use of sufficiently weak joint filler material to transfer some load and absorb the rest as deformations, networks of springs to transfer load, or fractional loads on each side of the joint.

The heat transfer analysis performed for this study is a sufficiently accurate appraisal of conditions above freezing. However, there are problems associated with thermal properties of materials that phase (water in soil that freezes and thaws), in particular with the heat capacity. As stated earlier, as water freezes, latent heat is released, resulting in an abrupt discontinuity in the heat capacity - temperature relation, usually over a very small temperature range. Comini *et al.* (1974) present a method for resolving this problem when using the finite element method for nonlinear heat conduction problems. By redefining specific heat, c , as the derivative of enthalpy, H , such that:

$$c = \frac{dH}{dT}$$

13

and noting that the enthalpy-temperature relation in the interval of freezing and thawing temperatures is sufficiently smooth, heat capacity can be approximated by determining the gradient of enthalpy with respect to temperature. In this way any peaks in heat capacity relationship can be included.

It is also possible to model the complex phenomenon of ice lense formation, with specific attention focused upon the effects of such formations.

Figure 123 presents a conceptual finite element mesh to model isolated lenses in two or three dimensions. As water changes its phase from liquid to solid, its volume increases by about 9%. As a result, pressures develop that tend to push pavements upward. This movement can be simulated by opening a slit in the mesh with double nodes, then moving the nodes on either side, as shown. The amount of movement depends on the thickness of the ice lense, which, for any particular soil, can be determined experimentally or by field tests. For soils that exhibit rhythmic banding of ice in discrete layers, this is an approximate behavioral model. Figure 124 shows the deflection in a conventional slab at a joint. For the case of an anchored slab an analysis was performed (in 2 dimensions only) using the lense as shown in Figure 125, which also shows the resulting upward movement. The pavement will probably exhibit the same behavior if the total upward displacement of the soil surface is the same.

Finally, it is also possible to analyze the dynamic response of pavements due to moving load by the finite element method. Lewis and Harr (1969) studied moving loads on slabs within two dimensions with complex boundary conditions, such as slab warping, variable subgrade modulus, and slab discontinuities. The technique involves adding an acceleration term to the left side of the plate on the elastic foundation equation that has the following form:

$$\rho H \frac{\partial^2 w}{\partial t^2} \quad 14$$

where ρ and H are density and thickness of the slab, respectively, and w is vertical movement. A suitable finite difference formula is written, and the displacement or stress history of points within the slab is possible.

The finite element method can also be used for the transient dynamic analysis of the more complex anchored slab. Loads are applied at nodal points on the surface in ramplike fashion, as shown in Figure 126. With sufficient overlap of load and spacing in time governed by vehicle velocity, dynamic wheel loads can be simulated. A transient dynamic analysis similar to the transient heat transfer analysis is possible with ANSYS.

It has been reaffirmed that the finite element method, in either two or three dimensions, can be an extremely versatile and effective method of analysis for many phases of pavement design, especially for the critical environmental load regime. Its widespread use by state highway design departments is

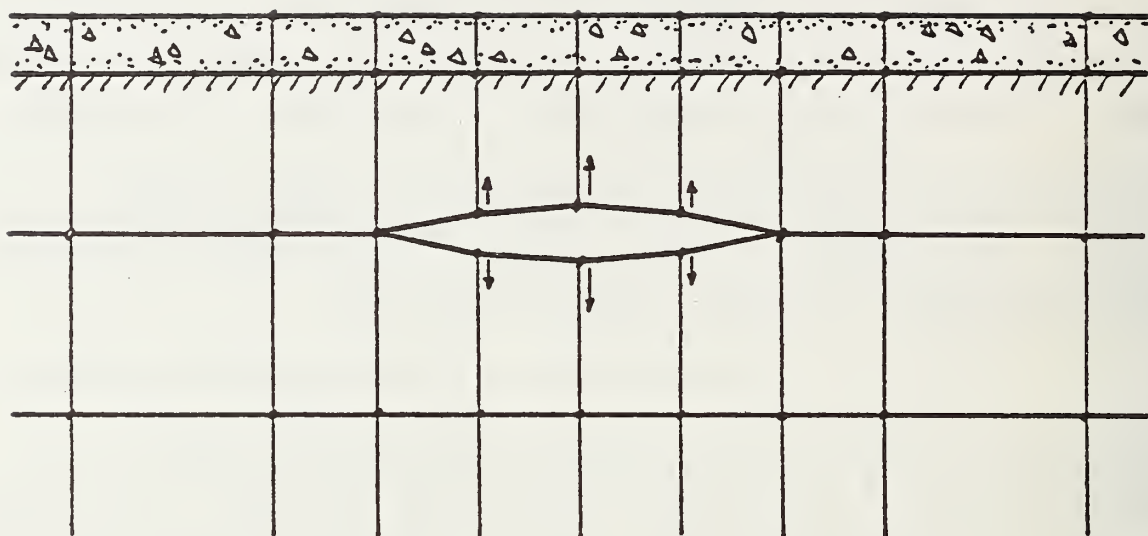


Figure 123. Possible technique for the analysis of the effects of isolated ice lenses in two and three dimensions by the finite element method.

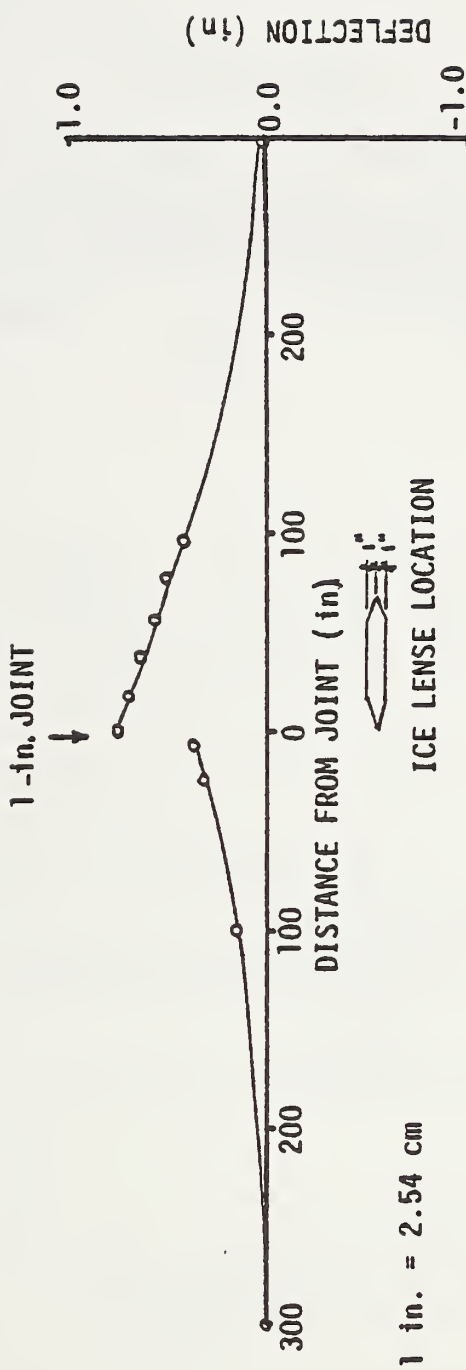


Figure 124. Deflections resulting from ice lens growth 24 in. (61 cm) beneath a conventional slab at joint.

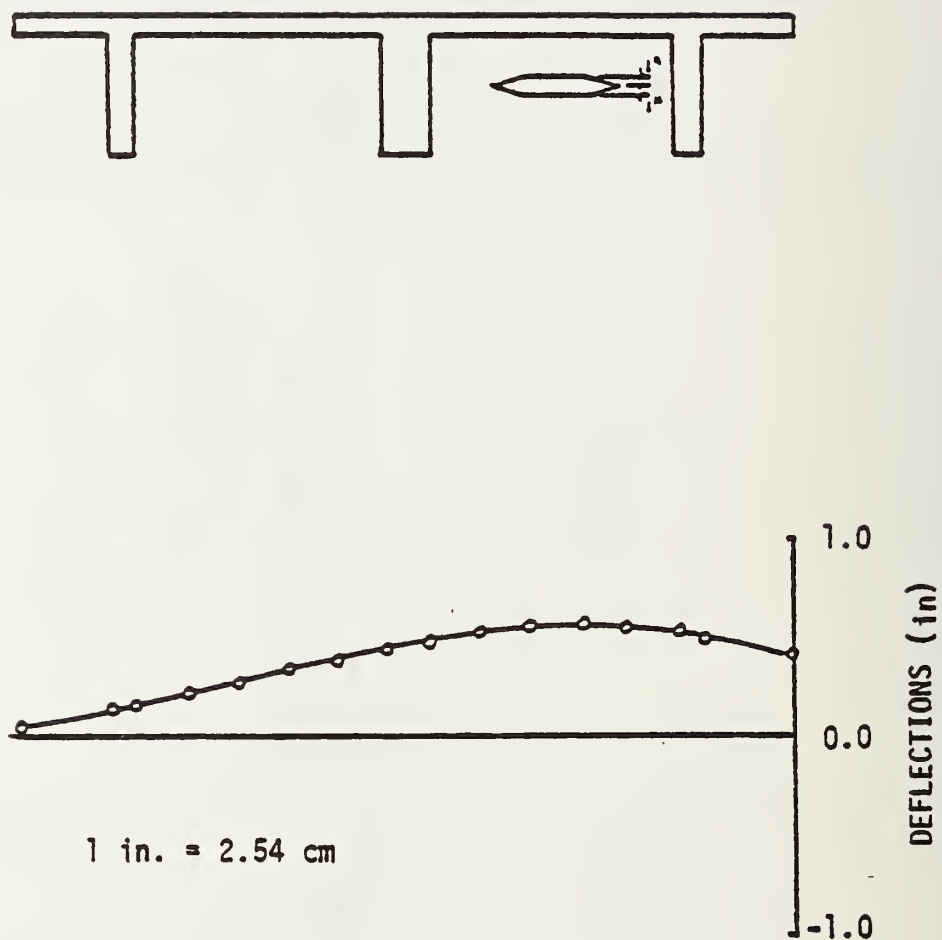


Figure 125. Results of ice lense growth 24 in. (61 cm) beneath pavement (anchored slab).

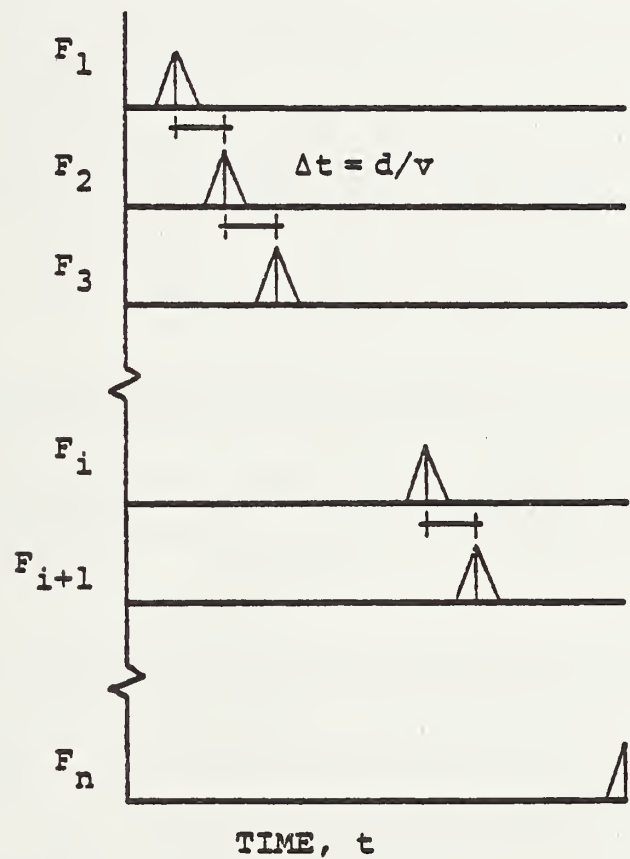
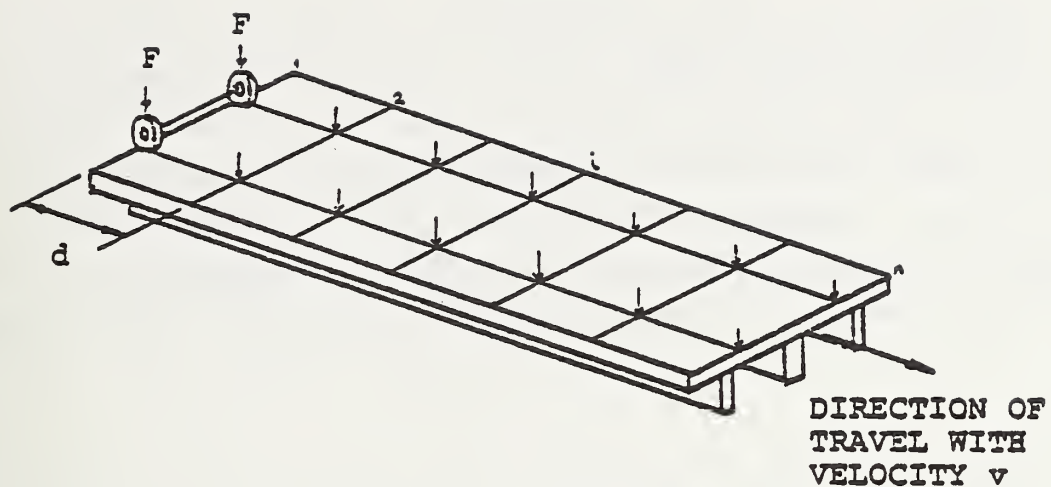


Figure 126. Scheme to study dynamic loads in pavement systems using transient dynamic finite element analysis.

anticipated as more advanced techniques are developed to analyze contingencies that have traditionally been overlooked, ignored, or confined to field or laboratory investigation. Versatile yet usable codes can be written with sophisticated data generation schemes, making model development much quicker and less costly. Comprehensive laboratory studies to determine realistic input material properties and geometric serviceability requirements coupled with engineering judgement will always be required to design or renovate pavements.

BIBLIOGRAPHY

Angen, E., 1973. Moisture in Road Surfaces, Symp. on Frost Action on Roads. Oslo, Norway.

Baladi, Y.J., Schoenhals, R.J. and Ayers, D.L., 1978. Transient Heat and Mass Transfer in Soils, ASME Paper 78-HT-31.

Bathe, K.J. and Wilson, E.L., 1976. Numerical Methods in Finite Element Analysis, Prentice-Hall, New Jersey.

Biot, M.A., 1941. General Theory of Three-dimensional Consolidation, J. of Applied Physics, v12, pp 155-164.

Bruch, J.C. and Zyroloski, G., 1974, Transient Two-dimensional Heat Conduction Problems Solved By the Finite Element Method, Int. J. for Numerical Methods in Engineering, v8, pp 481-494.

Burmister, D.M., 1943. The Theory of Stresses and Displacements in Layered Systems and Application to the Design of Airport Runways, Proc. of Highway Research Board, v23.

Carpenter, S.H., 1976. Thermal Susceptibility: A New Environmental Deterioration Mechanism for Pavements, Ph.D. Dissertation, Texas A&M University, August.

Chapman, A.J., 1974. Heat Transfer, Macmillan Publishing Co., Inc., New York, N.Y.

Cheung, Y.K., 1976. The Finite Strip Method in Structural Analysis, Pergamon Press, Oxford, U.K.

Comini, C., DelGuidice, S., Lewis, R.W., and Zienkiewicz, O.C., 1974. Finite Element Solution of Non-linear Heat Conduction Problem with Special Reference to Phase Change, Int'l. J. for Numerical Methods in Engineering, v8, pp 613-624.

Cumberledge, G., Hoffman, G.L., Bhajandas, A.C., and Cominsky, R.J., 1973. Moisture Variation in Highway Subgrades and the Associated Change in Surface Deflections, Penn. Dept. of Transportation.

Darcy, H., 1856. Les Fontaines publiques de la ville de Dijon, Paris.

Darter, M.I., 1976. Design of a Zero-Maintenance Plain Jointed Concrete Pavement, v1, Dept. of Civil Eng., Univ. of Illinois, Urbana, December.

Darter, M.I. and Barenberg, E.J., 1976. Zero-Maintenance Pavement: Results of Field Studies on the Performance Requirements and Capabilities of Conventional Pavement Systems, Interim Report of FHWA, USDOT, Univ. of Illinois, Urbana, April.

Dempsey, B.J., 1976. Climatic Effects on Airport Pavement Systems, State-of-the-Art, USDOT Report No. FAA-RD-75-196, Final Report, June.

Dempsey, B.J., 1978. A Mathematical Model for Predicting Coupled Heat and Water Movement in Unsaturated Soil, Int. J. for Numerical and Analytical Methods in Geomechanics, v2 n1, pp 19-34.

Desai, C.S. and Christian, J.T., 1977. Numerical Methods in Geotechnical Engineering, McGraw-Hill, New York, N.Y.

DeSalvo, G.J. and Swanson, J.A., 1975. ANSYS User's Manual, Swanson Analysis Systems, Inc., Elizabeth, Pa.

Duffie, J.A. and Beckman, W.A., 1974. Solar Energy Thermal Processes, John Wiley and Sons, Inc., New York, N.Y.

Fang, A.Y., 1969. Influence of Temperature and Other Climatic Factors on the Performance of Soil-Pavement Systems, Hwy. Res. Bd. Special Report 103, HRB.

Frivik, P.E., Thorbergsen, E., DelGuidice, S., and Comini, G., 1977. Thermal Design of Pavement Structures, J. of Heat Transfer, ASME, v99, November, pp 533-540.

Ghaboussi, J. and Wilson, E.L., 1973. Flow of Compressible Fluid in Porous Elastic Media, Int. J. for Numerical Methods in Engineering, v5 n3, pp 419-442.

Gilpin, R.R. and Wong, B.K., 1975. The Ground Temperature Regime and Its Relation to Soil Properties and Ground Surface Cover, ASME Paper No. 75-WA/HT-98.

Globus, A.M. and Mogilevsky, B.M., 1969. Thermal Transfer of Liquid in Porous Media, HRB Special Report 103, HRB.

Goetz, R. and Müller, S., 1969. Relationship Between the Daily Temperature Wave and the Development of the Natural Soil Profile, HRB Special Report 103, HRB.

Gurr, C.G., Marshall, T.J., and Hutton, J.T., 1952. Movement of Water in Soil Due to a Temperature Gradient, Soil Science, v74, pp 335-345.

Gurtin, M.E., 1964. Variational Principles for Linear Initial-value Problems, Quart. J. of Appl. Mathematics, v22, pp 252-256.

Harr, M.E., 1962. Groundwater and Seepage, McGraw-Hill, New York, N.Y.

Hetenyi, M., 1946. Beams on Elastic Foundation, University of Michigan Press, Ann Arbor.

Hoekstra, P., 1969. The Physical Chemistry of Frozen Soils, HRB Special Report 103, HRB.

Holl, A., 1969. Thermodynamics of Granular Systems, HRB Special Report 103, HRB.

Huang, Y.H. and Wang, S.T., 1973. Finite Element Analysis of Concrete Slabs and Its Implication of Rigid Pavement Design, Hwy. Res. Rec. No. 466, HRB, pp 55-69.

-----, 1974. Finite Element Analysis of Rigid Pavements with Partial Sub-grade Contact, Hwy. Res. Rec. No. 484, HRB, pp 39-54.

Hudson, W.R. and Matlock, H., 1966. Analysis of Discontinuous Orthotropic Placement Slabs Subjected to Combined Loads, Hwy. Res. Rec. No. 131, HRB.

Huebner, K.H., 1975. The Finite Element Method for Engineers, John Wiley and Sons, Inc., New York, N.Y.

Irons, B.M., 1970. A Frontal Solution Program for Finite Element Analysis, Int. J. for Numerical Methods in Engineering, v2, pp 5-23.

Jumikis, A.R., 1966. Thermal Soil Mechanics, Rutgers Univ. Press, New Brunswick, N.J.

Kersten, M.S., 1949. Thermal Properties of Soils, Bulletin No. 28, Univ. of Minnesota, Inst. of Tech.

Klute, A., 1952. A Numerical Method for Solving the Flow Equation for Water in Unsaturated Material, Soil Science, v73, pp 105-116.

Koehler, W. and Pittr, J., 1974. Calculation of Transient Temperature Fields with Finite Elements in Space and Time Dimensions, Int. J. for Numerical Methods in Engineering, v8, pp 625-631.

Kohnke, P.C., 1977. ANSYS Theoretical Manual Swanson Analysis Systems, Inc., Elizabeth, Pa.

Kreith, F., 1973. Principles of Heat Transfer, Intext Educational Publishers, New York, N.Y.

Laguros, J.G., 1969. Effect of Temperature on Some Engineering Properties of Clay Soils, HRB Special Report 103, HRB.

Langhame, Y. and Camarero, R., 1975. Unsteady Heat Conduction in Variable Conductivity Soils, ASME Paper 75-WA/HT-89.

Lewis, R.W. and Bass, B.R., 1976. The Determination of Stresses and Temperatures in Cooling Bodies by Finite Elements, J. of Heat Transfer, ASME, v98, August, pp 478-484.

Lewis, K.H. and Karr, M.E., 1969. Analysis of Concrete Slabs on Ground Subjected to Warping and Moving Loads, Hwy. Res. Rec. No. 291, HRB, pp 194-211.

Low, P.F. and Lovell, C.W., Jr., 1959. The Factor of Moisture in Frost Action, Bulletin 225, HRB, pp 23-44.

Lytton, R.L. and Kher, R.K., 1970. Prediction of Moisture Movement in Expansive Clays, Research Report 118-3, Center for Highway Research, Univ. of Texas at Austin, May.

McGraw, R., 1969. Heat Conductin in Saturated Granular Media, HRB Special Report 103, HRB.

Meyer, C., 1973. Solution of Linear Equations - State-of-the-Art, J. of the Structural Division, ASCE, v99 nST7, July, pp 1507-25.

Mitchell, J.K., 1969. Temperature Effects on the Engineering Properties and Behavior of Soils, HRB Special Report 103, HRB.

Moore, W.M., Scrivner, F.H., Poehl, R., and Phillips, M.B., 1969. Detecting Seasonal Changes in Load-Carrying Capabilities of Flexible Pavements, Texas Transportation Institute, Texas A&M Univ.

Myrayama, S., 1969. Effect of Temperature on Elasticity of Clays, HRB Special Report 103, HRB.

Nair, K. and Chang, C.Y., 1973. Flexible Pavement Design and Management - Material Characterization, NCHRP Report 140, HRB.

NCHRP., 1974. Road Design in Seasonal Frost Areas, NCHRP Synthesis of Highway Practice 26, Transportation Res. Board.

Neville, A.M., 1963. Properties of Concrete, John Wiley and Sons, Inc., New York, N.Y.

Nordal, R.S., 1973. The Thermal Regime of the Pavement and the Subgrade at the Vormsund Test Road, Symp. on Frost Action, Proc., Norwegian Road Res. Lab, Oslo, October.

Noss, P.M., 1973. The Relationship Between Meteorological Factors and Pavement Temperature, Proc., Symp. on Frost Action, Norwegian Road Res. Lab, Oslo, October.

Patten, H.E., 1909. Heat Transference in Soils, Bulletin No. 59, U.S. Dept. of Agriculture, Bur. of Soils, September.

Penman, H.L., 1940. Gas and Vapor Movement in Soil, J. of Agricultural Science, v30, pp 437-462.

Philip, J.R., 1953. Vapor Movement in a Soil Mass with Periodic Surface Temperature, Proc., Aust. Conf. in Soil Science, pp 4.4.1-7.

Philip, J.R. and deVries, D.A., 1959. Moisture Movement in Porous Material Under Temperature Gradients, Trans., Amer. Geophysical Union, v38 n2, April, pp 222-232.

Pichumani, R., 1973. Finite Element Analysis of Pavement Structures Using AFPAV Code, AFWL-TR-72-186, Kirtland Air Force Base, Kirtland, N.M., May.

Richards, B.G., 1969. Pavement Temperatures and Their Engineering Significance in Australia, HRB Special Report 103, HRB.

Roberts, C.C., 1973. Summer Microclimate at Death Valley 1969, Proc., Inst. of Environmental Sciences 19th Annual Technical Meeting, Anaheim, Calif., April 2-5.

Sandhu, R.S. and Wilson, E.L., 1969. Finite Element Analysis of Seepage in Elastic Media, J. of Engineering Mechanics, ASCE, v95 nEM3, June, pp 641-652.

Spangler, 1935. M.C., "Stresses in Concrete Pavement Slab," Proceedings HRB, v15, pp 122-146.

Spangler, M.G. and Lightburn, F.E., 1937. "Stresses in Concrete Pavement Slabs," Proceedings HRB, v17, pp 215-234.

Teller, L.W. and Sutherland, E.C., 1935, 1936, 1943. The Structural Design of Concrete Pavements, Public Roads, v16, Nos. 8, 9, and 10, pp 145-158, 169-197, 201, 221, v23, No. 8 pp 167-212.

Todhunter, I. and Pearson, K., 1960. A History of the Theory of Elasticity, v1 and 2, New York, N.Y.

Tsytovich, N.A., 1975. The Mechanics of Frozen Ground, McGraw-Hill, New York, N.Y.

Vander Veen, C., 1953. "Loading Tests on Concrete Slabs at Schiphol Airport," Proceedings of Third International Conference on Soil Mechanics and Foundation Engineering, Switzerland, pp 133-141.

Venkatasubramanian, V., 1964. Temperature Variations in a Cement Concrete Pavement and the Underlying Subgrade, Hwy. Res. Rec. No. 60. HRB, pp 15-27.

Vesic, A.S. and Saxena, S.K., 1970. Analysis of Structural Behavior of AASHO Road Test Rigid Pavements, NCHRP Rep. No. 97, HRB.

Westergaard, H.M., 1926. Stresses in Concrete Pavements Computed by Theoretical Analysis, Public Roads, v7 n2, April, pp 25-35.

-----, 1927. Analysis of Stresses in Concrete Roads Caused by Variations of Temperature, Public Roads, v8 n3, May, pp 54-60.

Williams, P.J., 1973. Determination of Heat Capacities of Freezing Soils, Proc. Symp. on Frost Action, Norwegian Road Res. Lab, Oslo, October.

Wilson, E.L and Nickell, R.E., 1966. Application of the Finite Element Method to Heat Conduction Analysis, Nuclear Engineering and Design, North Holland, Amsterdam, pp 276-286.

Wilson, E.L., Taylor, R.L., Doherty, W.P., and Ghaboussi, J., 1975. Incompatible Displacement Models, Numerical and Computer Methods in Structural Mechanics, (S.J. Fenves et al., editors), Academic Press, Inc., New York, N.Y.

Winkler, E., 1867. Die Lehre von der Elastizität und Festigkeit, Prague.

Winterkorn, H.F. and Fang, H.S., 1975. Foundation Engineering Handbook, Van Nostrand Reinhold, New York, N.Y.

Winters, R., 1974. Surface Icing of Insulated Pavements, NYSDOT Res. Rep. 24, New York State Dept. of Transp.

Wu, T.H., 1975. Retaining Walls, Foundation Engineering Handbook, Van Nostrand Reinhold, N.Y.

Xanthakos, P.P., 1974. Underground Construction in Fluid Trenches, National Educational Seminar, Univ. of Illinois, Chicago Circle, April.

Yoder, E.J. and Witczak, M.W., 1975. Principles of Pavement Design, 2nd Ed., John Wiley and Sons, New York, N.Y.

Yong, R.N., 1965. Soil Suction Effects on Partial Soil Freezing, Hwy. Res. Rec. No. 68, HRB, pp 31-42.

Zienkiewicz, O.C., 1971. The Finite Element Method in Engineering Science, McGraw-Hill, London.

Zienkiewicz, O.C. and Cheung, Y.K., 1965. Finite Elements in the Solution of Field Problems, The Engineer, v220, pp 507-510.

APPENDIX A: TABLES OF SURFACE STRAINS

Table 5 Surface strains (microin./in.) of AS62 for load position 1

Foil gage number	Load (lb.) (1 lb. = 0.45 kg)					
	250	500	750	1000	1250	1500
1	65	115	160	190	243	290
2	5	-36	-50	-68	-60	-50
3	30	57	40	46	50	56
4	-7	-14	-18	-23	-25	-35
5	-12	-22	-37	-45	-54	-58
6	14	20	27	33	38	45
7	11	21	28	42	49	45
8	-3	-4	6	11	13	12
9	4	-9	-18	-19	-24	-32
10	5	7	10	13	16	11

Table 6 Surface strains (microin./in.) of AS62 for load position 2.

Foil gage number	Load (lb.) (1 lb. = 0.45 kg)					
	250	500	750	1000	1250	1500
1	10	20	-32	-38	-20	15
2	10	18	78	92	100	126
3	-16	-18	36	45	68	66
4	-10	-13	-16	-19	-26	-24
5	-10	-18	-23	-25	-30	-34
6	-12	-17	-40	-36	-42	-33
7	-5	7	-12	-18	-31	-6
8	-9	-16	-14	-24	-20	-24
9	-7	-16	-21	-34	-38	-40
10	-6	-9	-14	-28	-24	-30

Table 7 Surface strains (microin./in.) of AS62 for load position 3.

Foil gage number	Load (lb.) 1 lb = 0.45 kg					
	250	500	750	1000	1250	1500
1	-12	-46	-68	-88	-80	-70
2	-48	-72	-84	-100	-140	-170
3	8	-30	-37	-46	-25	6
4	7	10	13	12	12	10
5	-4	-9	-15	-20	-16	-13
6	14	8	12	15	23	20
7	3	4	7	9	12	10
8	8	13	17	20	23	30
9	-13	-24	-36	-47	-55	-62
10	-22	-40	-64	-83	-100	-116

Table 8 Surface strains (microin./in.) of AS62 for load position 4.

Foil gage number	Load (lb.) 1 lb = 0.45 kg					
	250	500	750	1000	1250	1500
1	-230	-234	-166	-149	-125	-94
2	-227	-246	-254	-269	-257	-278
3	-260	-248	-246	-259	-259	-249
4	-53	-60	-61	-66	-72	-77
5	7	-38	-35	-23	-12	3
6	-2	-142	-138	-145	-154	-150
7	-8	-139	-145	-152	-167	-182
8	-2	-50	-54	-57	-60	-60
9	-1	-52	-51	-50	-49	-44
10	-2	-47	-46	-42	-40	-39

Table 9. Surface strains (microin./in.) of AS62 for load position 5.

Foil gage number	Load (lb.)					
	250	500	750	1000	1250	1500
1	-181	-178	-153	-127	-119	-100
2	-204	-190	-190	-168	-151	-135
3	-276	-274	-294	-288	-276	-280
4	-52	-56	-60	-64	-69	-72
5	-48	-42	-40	-35	-29	-22
6	-144	-148	-152	-154	-156	-149
7	-155	-164	-166	-169	-174	-178
8	-46	-48	-54	-56	-59	-62
9	-42	-34	-31	-27	-18	-5
10	-40	-42	-45	-48	-44	-43

Table 10. Surface strains (microin./in.) of AS62 for load position 6.

Foil gage number	Load (in.)					
	250	500	750	1000	1250	1500
1	-23	-49	-97	-112	-143	-158
2	-35	-30	-65	-68	-80	-96
3	-28	40	35	32	38	42
4	3	6	12	10	16	14
5	3	4	3	2	-4	-2
6	5	-17	-14	-16	-14	-16
7	-10	-13	-14	-17	-16	-18
8	8	6	8	10	14	17
9	2	-6	2	12	16	20
10	8	10	19	36	51	70

Table 11 Surface strains (microin./in.) of S62 for load position 1.

Foil gage number	Load (lb.)		
	250	500	750
1			
2	6	12	17
3	0	-1	-2
4	-4	-5	-6
5	-1	-2	-2
6	4	2	0
7	51	91	131
8	-10	-19	-29
9	0	2	2
10	2	4	6

Table 12 Surface strains (microin./in.) of S62 for load position 2.

Foil gage number	Load (lb.)		
	250	500	750
1			
2	-8	-13	-17
3	-15	-34	-53
4	-10	-17	-21
5	-8	-15	-21
6	8	10	10
7	-10	-14	-10
8	6	10	12
9	15	34	51
10	6	10	12

Table 13 Surface strains (microin./in.) of S62 for load position 3.

Foil gage number	Load (lb.)		
	250	500	750
1			
2	-8	-13	-14
3	16	26	35
4	-26	-41	-49
5	-80	-130	-150
6	2	8	8
7	-19	-27	-28
8	8	12	14
9	-16	-24	-32
10	21	34	39

Table 14 Surface strains (microin./in.) of S62 for load position 4.

Foil gage number	Load (lb.)		
	250	500	750
1			
2	28	41	58
3	-6	-8	-10
4	4	4	4
5	1	1	1
6	-6	-10	-17
7	45	78	116
8	-24	-36	-49
9	4	8	13
10	-4	-3	-1

Table 15 Surface strains (microin./in.) of S62 for load position 5.

Foil gage number	Load (1b.) 1 lb = 0.45 kg		
	250	500	750
1			
2	9	13	13
3	-19	-42	-72
4	9	19	25
5	-3	-5	-11
6	2	1	0
7	5	15	23
8	-9	-13	-19
9	17	40	64
10	-11	-19	-30

Table 16 Surface strains (microin./in.) of S62 for load position 6.

Foil gage number	Load (1b.) 1 lb = 0.45 kg		
	250	500	750
1			
2	-3	-9	-13
3	16	26	36
4	-11	-16	-21
5	-22	-28	-17
6	-1	1	5
7	-13	-19	-26
8	3	6	11
9	-15	-25	-34
10	-7	11	14

Table 17 Surface strains (microin./in.) of ASE62 for load position 1.

Foil gage number	Load (1b.)			1 lb = 0.45 kg
	100	200	300	
1	23	54	90	
2	-2	-2	2	
3	1	3	12	
4	-4	-8	-15	
5	-1	2	3	
6	-1	-1	-2	
7	-2	-2	-4	
8	-2	-2	-5	
9	0	1	1	
10	0	0	-1	

Table 18 Surface strains (microin./in.) of ASE62 for load position 2.

Foil gage number	Load (1b.)			1 lb = 0.45 kg
	100	200	300	
1	3	-2	5	
2	-2	8	17	
3	-1	-6	-2	
4	0	0	-2	
5	0	0	0	
6	2	0	1	
7	2	2	2	
8	0	-2	-4	
9	0	-2	0	
10	0	0	2	

Table 19 Surface strains (microin./in.) of ASE62 for load position 3.

Foil gage number	Load (1b.) 1 lb = 0.45 kg		
	100	200	300
1	-10	-21	-54
2	-3	-19	-30
3	-2	-4	-14
4	2	6	12
5	-2	0	1
6	0	2	4
7	-1	0	0
8	2	6	10
9	-2	-4	-4
10	-4	-6	-8

Table 20 Surface strains (microin./in.) of ASE62 for load position 4.

Foil gage number	Load (1b.) 1 lb = 0.45 kg		
	100	200	300
1	-15	-21	-13
2	0	3	6
3	2	8	15
4	-3	-6	-10
5	4	12	19
6	-1	-2	-4
7	-4	-10	-14
8	-2	-3	-6
9	2	6	6
10	0	2	0

Table 21 Surface strains (microin./in.) of ASE62 for load position 5.

Foil gage number	Load (lb.)			1 lb = 0.45 kg
	100	200	300	
1	-8	-10	-15	
2	4	8	15	
3	-2	-4	0	
4	-2	-4	-7	
5	2	5	9	
6	0	-2	-4	
7	-2	-6	-9	
8	-2	-4	-6	
9	4	6	11	
10	0	2	2	

Table 22 Surface strains (microin./in.) of ASE62 for load position 6.

Foil gage number	Load (lb.)			1 lb = 0.45 kg
	100	200	300	
1	-23	-41	-77	
2	-4	-10	-20	
3	0	6	1	
4	0	2	4	
5	0	2	2	
6	2	2	4	
7	0	-2	-4	
8	2	4	8	
9	4	9	14	
10	10	21	30	

APPENDIX B: GEOTECHNICAL PROPERTIES OF SUBGRADE

The properties of the subgrade used in experimental investigations were determined by a plate-bearing test, unconfined compression tests (UC), triaxial compression tests, consolidation tests, and soil classification and subgrade behavior.

PLATE-BEARING TEST

The soil subgrade was loaded by a round rigid plate. Observed settlement and consequent strains were plotted against theoretically computed stresses to estimate the modulus of elasticity of soil.

The sampling area, as shown in Figure 4 of the steel container, was used to perform the Plate Bearing Test.

The dimensions of the sampling area are 36.25 in. (92 cm) wide, 23.88 in. (61 cm) long, and 23.75 in. (60 cm) deep. Eleven layers of silty clay soil were placed and compacted in the same way and simultaneously with the testing area, so that similar properties can be expected of this subgrade. The height of soil subgrade was measured to be 22.75 in. (57.8 cm).

A pair of sensors (1-in. (2.54 cm) diameter) were placed in the soil at a depth of 1.63 in. (4.14 cm) in the center of the sampling area. The average distance between the two sensors was found to be about 0.75 in. (1.9 cm). Prior to the placement of the sensors, a standard calibration procedure was followed. A soil strain gage (Figures 127 and 128) and a calibration fixture for sensors were used.

Method of Calibration

One sensor was placed in the sliding rod and the other in the coarse adjustment of the calibration fixture as shown in Figure 129. They were connected in the signal input and in the oscillation output of the soil strain gage respectively. The calibration signal was set to 14, the coil separation to 1 diameter, and the sensitivity at low level (2 turns clockwise). The calibration was performed without balancing the phase.

The initial distance between the two sensors was measured and the corresponding amplitude was recorded. A change in the micrometer corresponded to an amplitude change which set the dial meter to zero. Figure 130 shows the relationship between the sensor spacing and the amplitude reading.

After the top soil surface was leveled, a rigid steel footing was placed in the center of the sampling area. The dimensions of the footing were 5.5-in. (14 cm) diameter and 2 in. (5 cm) thick. Three dial gages were attached from the sides of the container at 120 degree angles, and they were touching the footing to measure the surface deflections.

An average deflection was computed from the three measured deflections. A point load was applied at the center of the footing. The point load was connected to a manual jack through a load cell. The load cell was connected to a power supply and to a multimeter. The net point load applied on the footing is computed as follows:

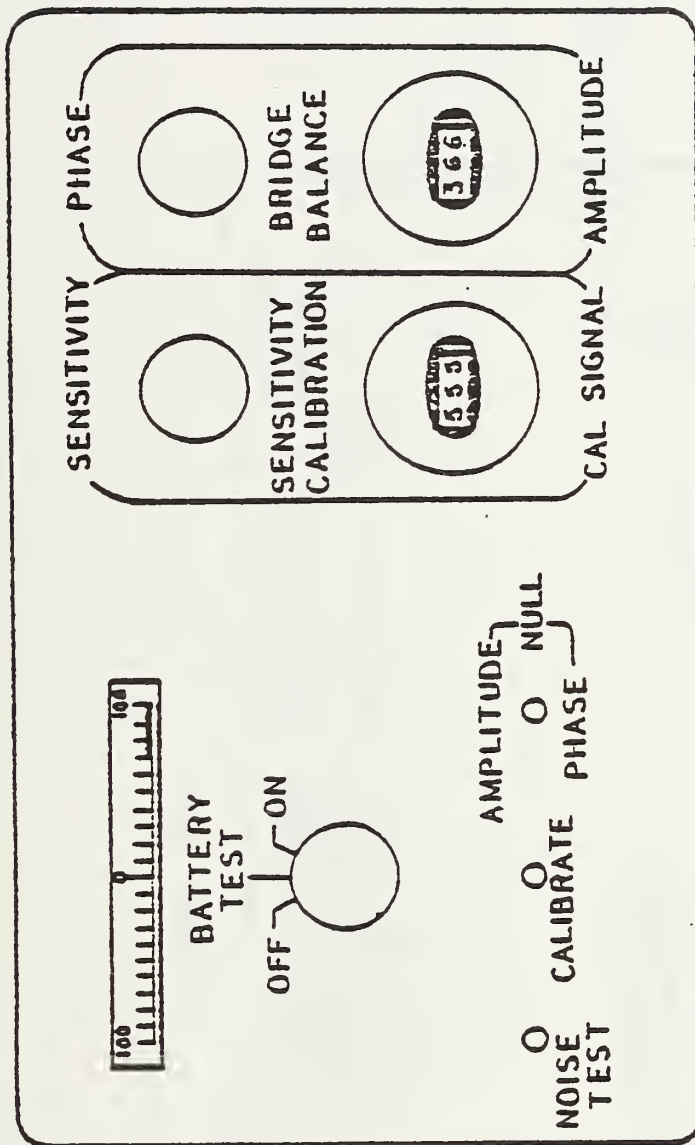


Figure 127. Front panel of soil strain gage.

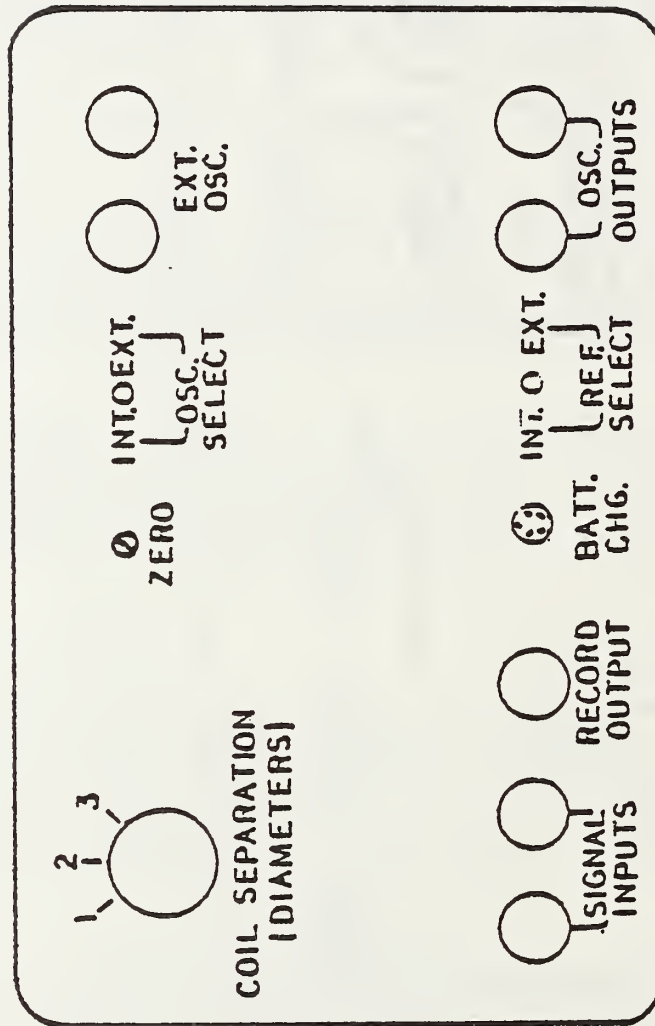


Figure 128. Rear panel of soil strain gage.

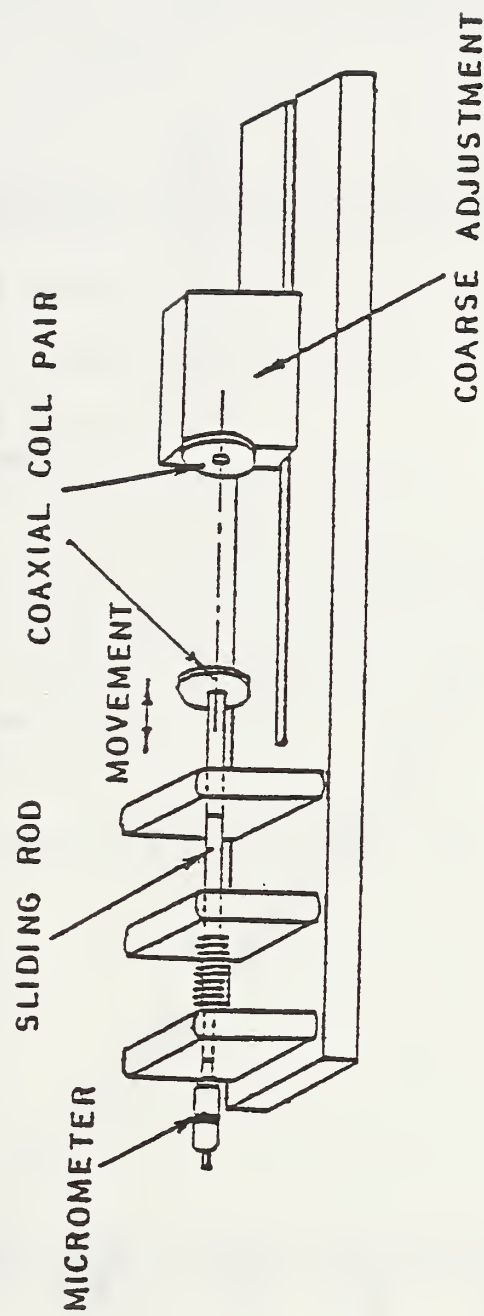


Figure 129. Calibration fixture for sensors.

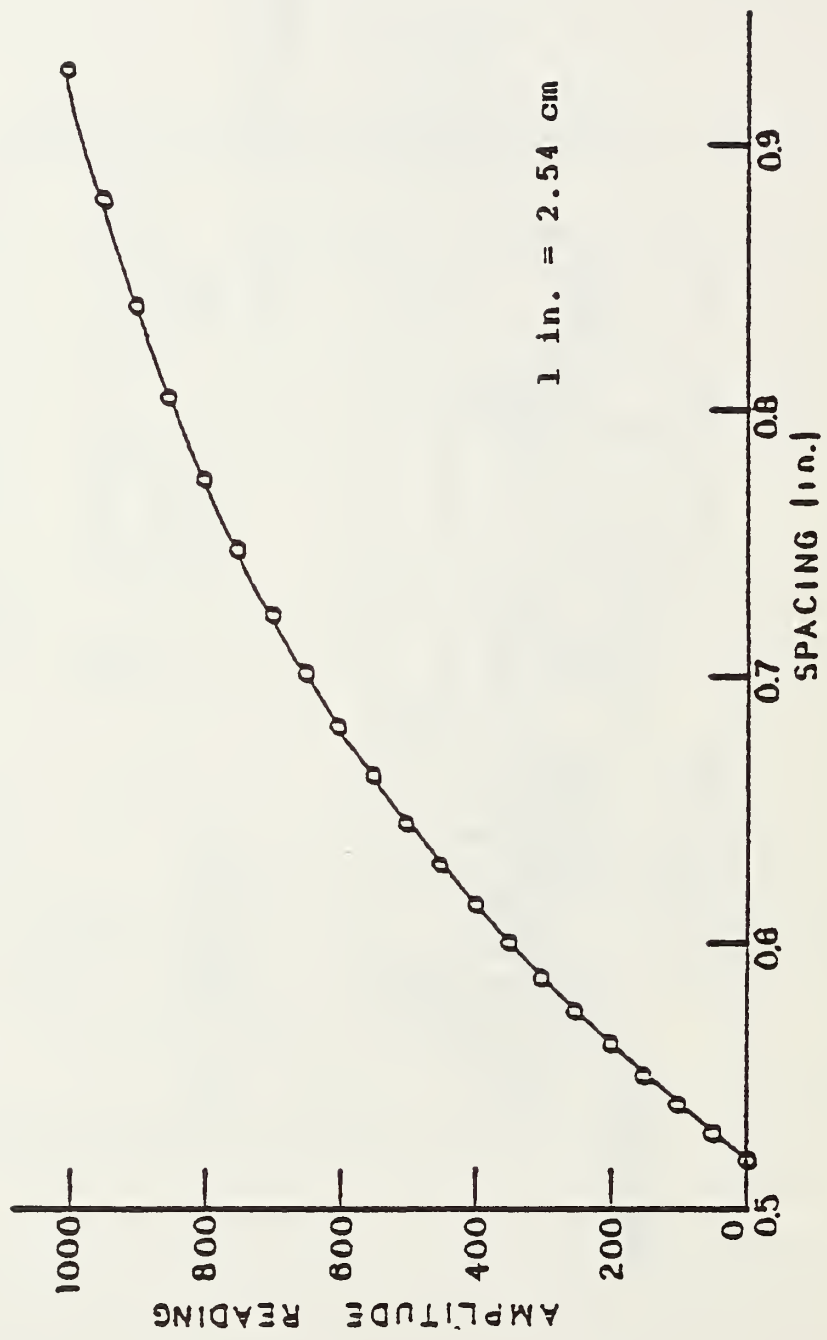


Figure 130. Sensor spacing calibration of amplitude dial (range = 1, calibration Signal = 14, sensitivity = 2 turns clockwise, phase unbalanced).

$$\text{Net load (lb.)} = \frac{\text{Multimeter reading (uV.)}}{15.33} + 15$$

B-1

To find the stresses in the soil at 1.63-in. (4.14 cm) depth underneath the load, the theory of circular load on semi-infinite mass was used. The following notations were considered:

- σ_z = vertical stress at 1.63 in. (4.14 cm) depth
- z = distance between top surface and point where vertical stress is to be computed = 1.63 in. (4.14 cm)
- a = radius of footing = 2.75 in. (7 cm)
- p_{av} = average applied pressure
- P = total load
- e = eccentricity and is zero in our case
- ρ_z = vertical surface displacement
- E = secant modulus of soil
- ν = Poisson's ratio of soil
- ζ = $\frac{z}{a} = 0.59$.

From Poulos and Davis (1974) and noting that $e = 0$ and $\zeta = 0.59$, we conclude that:

$$\frac{\sigma_z}{p_{av}} = 0.56 \quad \text{B-2}$$

Note that:

$$p_{av} = \frac{P}{\pi a^2} \quad \text{B-3}$$

From equations (B-2) and (B-3):

$$\sigma_z (\text{psi}) = 0.02357 P (\text{lb.}) \quad \text{B-4}$$

Equation (B-4) is a relationship between a point load P and the corresponding stress σ_z at 1.63-in. (4.14 cm) depth. The percentage strain at this depth was defined as the difference of the original sensor spacing with no load from the one at a given load, divided by the original one, and the result multiplied by 100.

Figure 131 shows a plot of applied load versus average surface deflection for ten load cycles.

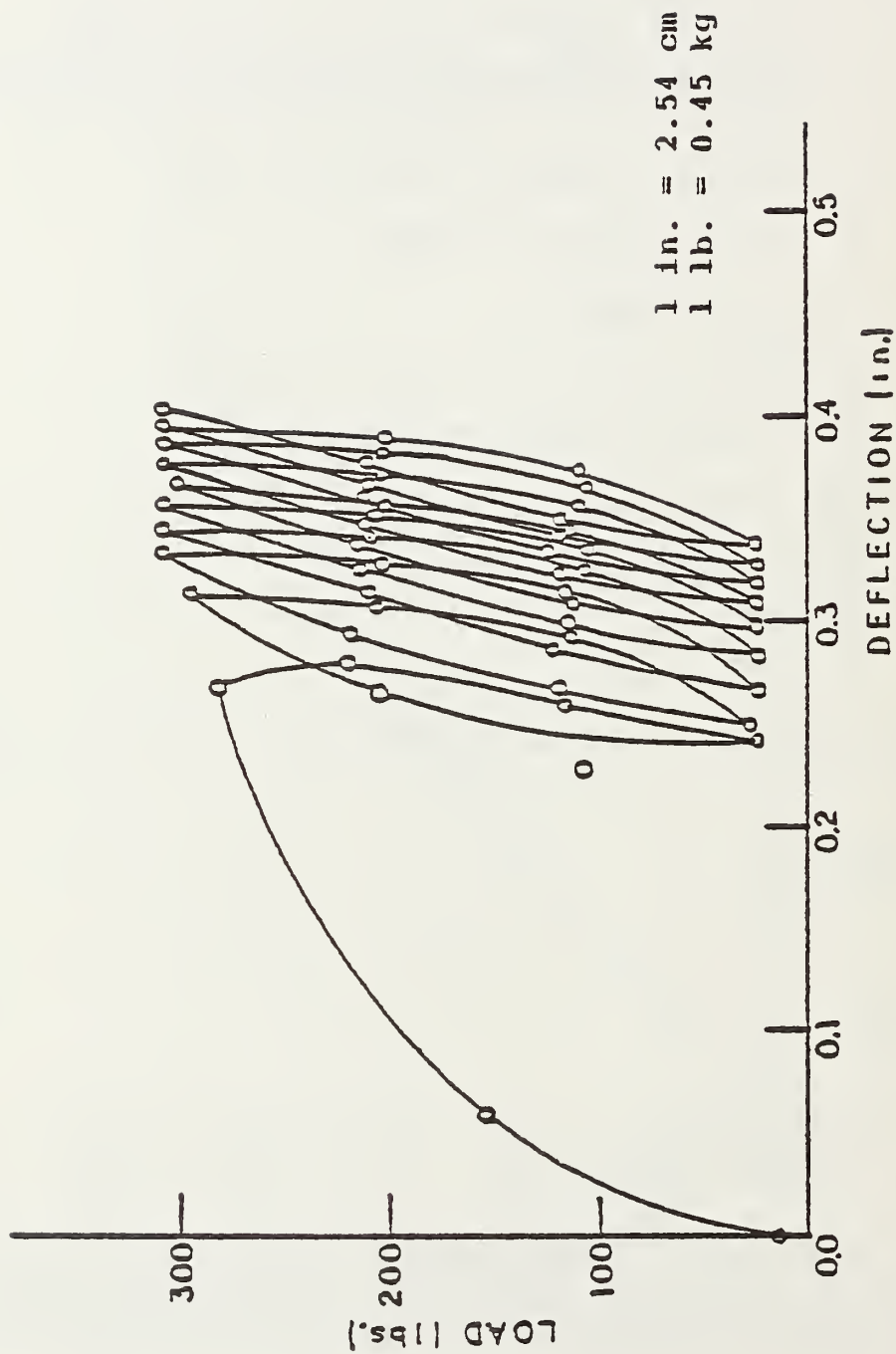


Figure 131. Applied load versus average surface deflection for rigid footing.

Figure 132 shows a plot of vertical stress versus average strain at 1.63 in. (4.14 cm) depth for 10 load cycles. After the tenth load cycle, the footing was loaded up to failure (Figure 133). The stress at failure was 20 psi (1.4 kg/cm²) and the corresponding strain was 18%. After unloading, the residual plastic deformation was observed as 0.1 in./in. (cm/cm).

Using the slope of the tenth cycle of the stress-strain curve, the secant modulus of the subgrade comes out to be around 850 psi (60 kg/cm²) (Figure 134). The relationship between the vertical surface deflection and the secant modulus of the soil is quoted as:

$$\rho_z = \frac{\pi}{2} (1 - v^2) \frac{p_{av} a}{E} \quad B-5$$

Equation (B-5) becomes:

$$\Delta\rho_z = \frac{\pi}{2} (1 - v^2) \frac{\Delta p_{av} a}{E} \quad B-6$$

Equation B-3 becomes:

$$\Delta p_{av} = \frac{\Delta p}{\pi a^2} \quad B-7$$

$\Delta\rho_z$ and Δp were found from the tenth load cycle in Figure 131 as:

$$\Delta\rho_z = 0.066 \text{ in. (0.17 cm)}$$

$$\Delta p = 284 \text{ lbs. (128 kg)}$$

Therefore, by combining equations B-6 and B-7, the result is:

$$E (\text{psi}) = 782.37 (1 - v^2) \quad B-8$$

Secant modulus is plotted against Poisson's ratio in Figure 135. It may be noted that for $v = 0.45$, the secant modulus is 623 psi (44 kg/cm²).

UNCONFINED COMPRESSION TEST (UC)

Five unconfined compression tests (ASTM-D2166) were completed to evaluate the compressive strength of soil. Many empirical relationships exist to relate E with undrained unconfined compressive strength.

The unconfined compression test is the simplest and quickest way to measure the unconfined compressive strength of a cylinder of soil. No lateral support is offered; therefore, it is used only for cohesive soils.

The failure surface tends to develop in the weakest portion of the sample. Internal soil conditions such as degree of saturation and pore water pressure, cannot be controlled. The sample is unprotected from moisture lost during testing. The sample was extruded from the sampling area by a modified Harvard compaction unit. The procedure followed the ASTM specifications. The samples had an initial diameter of 1.36 in. (3.45 cm) and an initial height of 2.75 in. (6.96 cm).

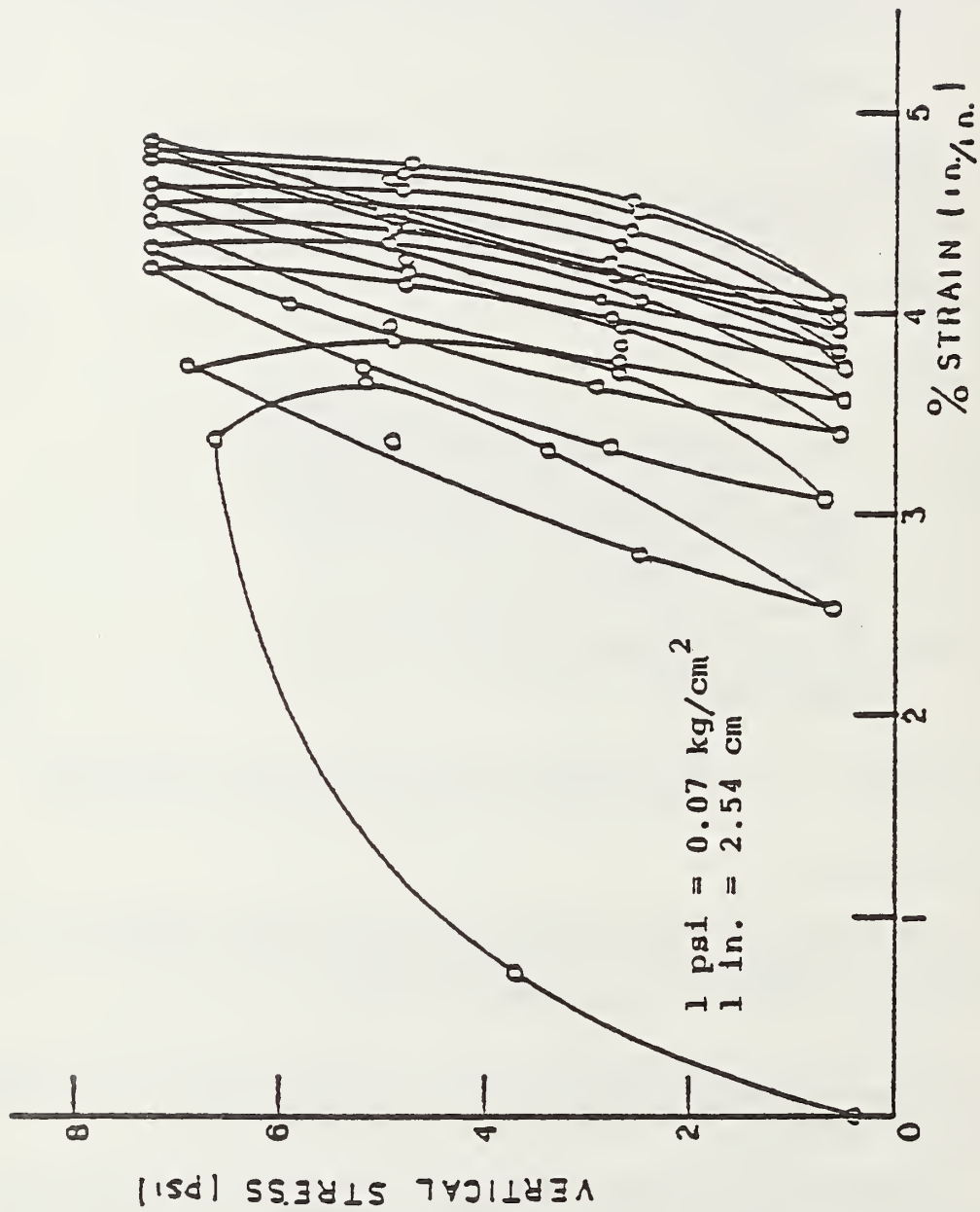


Figure 132. Vertical stress versus % average strain at 1.63 in. depth for footing.

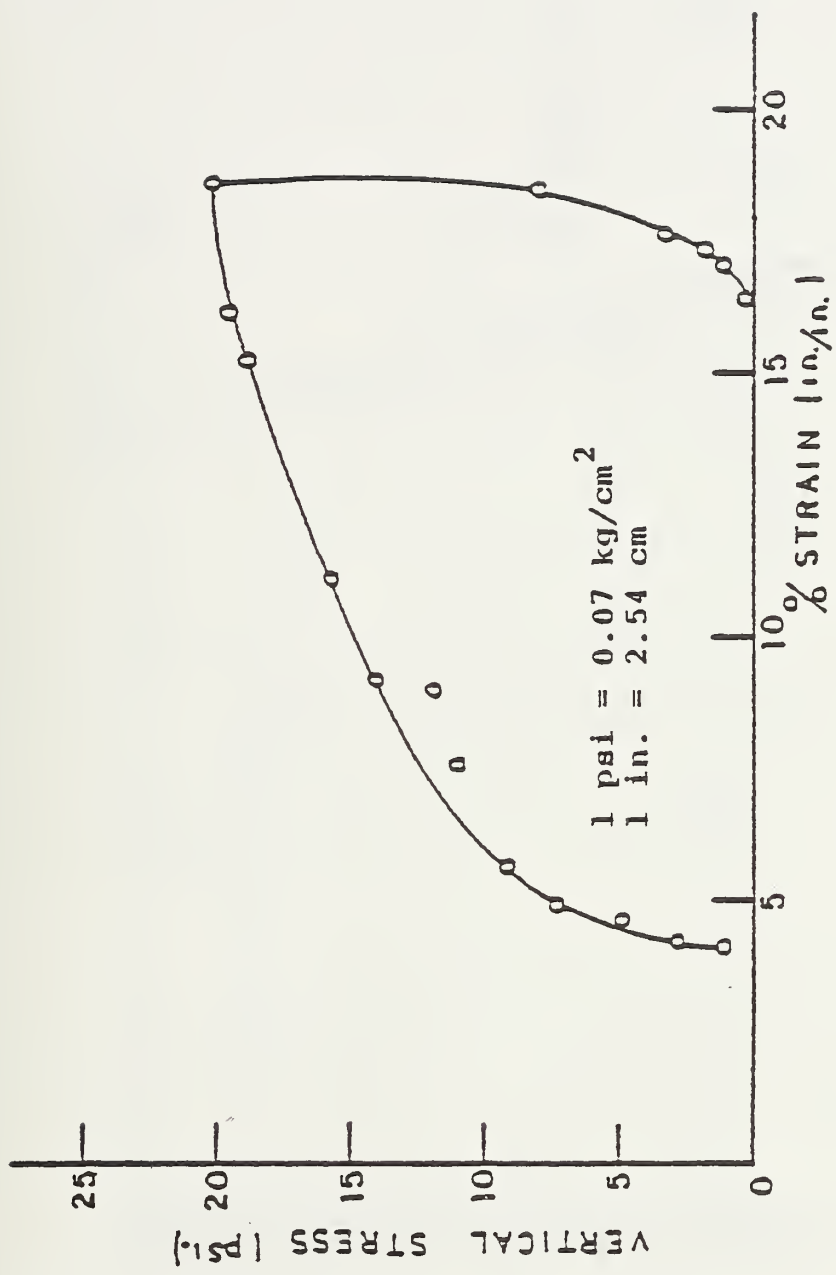


Figure 133. Vertical stress versus % average strain up to failure at 1.63 in. depth for rigid footing.

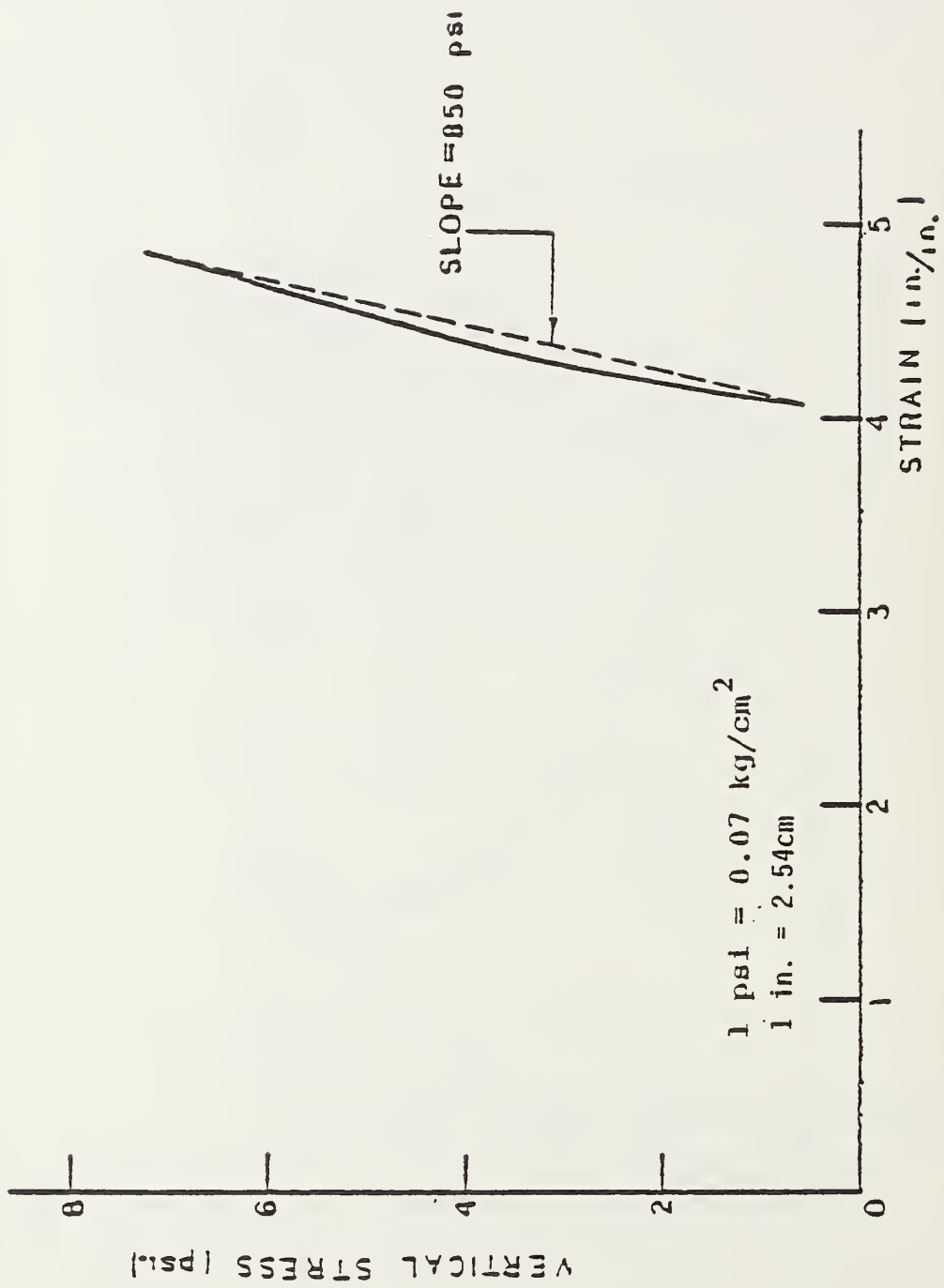


Figure 134. Secant modulus of subgrade using the slope of the stress vs. strain curve.

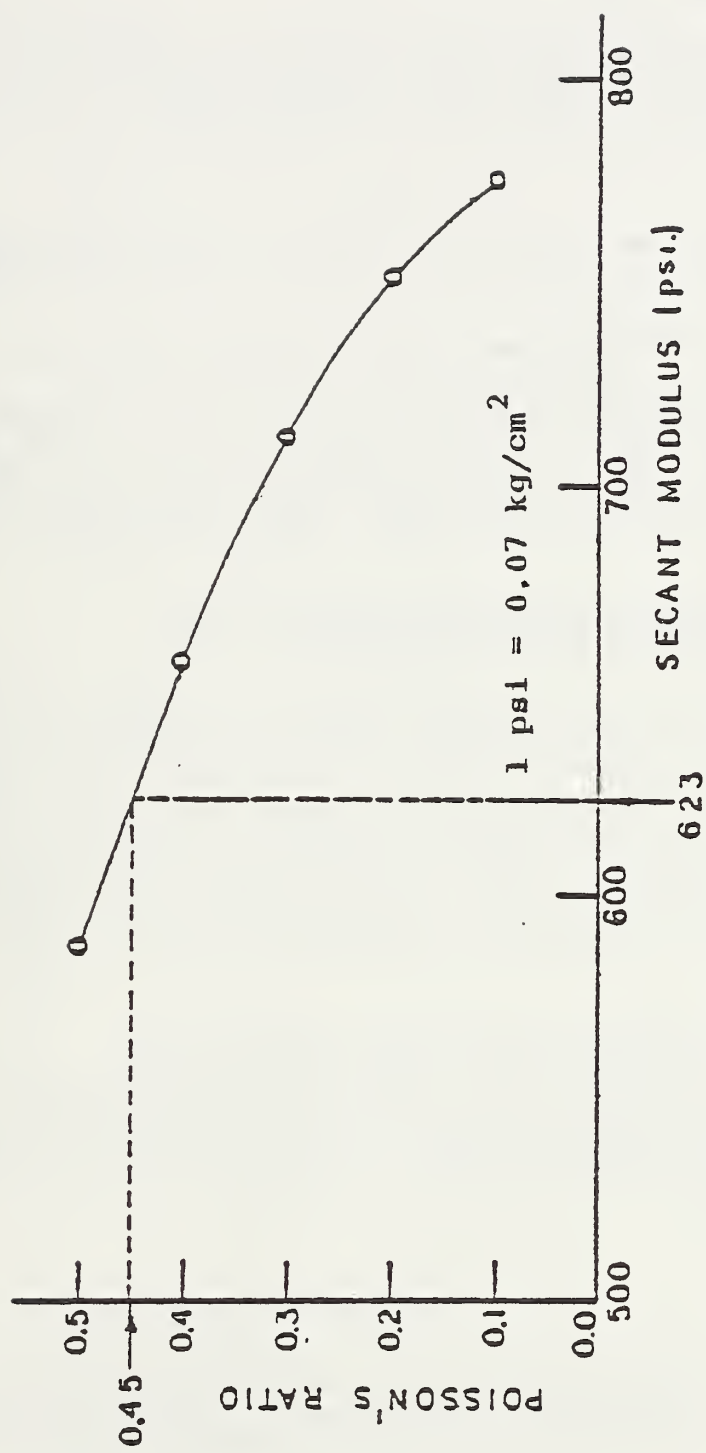


Figure 135. Secant modulus of subgrade versus Poisson's ratio.

A plot of the applied stress versus the percentage average strain is given in Figure 136. The secant modulus versus the percentage average strain was also plotted (Figure 137).

The maximum value of the secant modulus is observed to be 25 psi (18 kg/cm^2) at a strain of 0.0184 in./in. (cm/cm). At 0.1% strain, the corresponding secant modulus is about 155 psi (11 kg/cm^2).

TRIAXIAL TESTS (CU)

The tests that were done are called Q_c or consolidated-undrained or consolidated-quick.

The procedure followed was as per ASTM specifications.

The samples used were about 1.3 in. (3.3 cm) in diameter and 2.8 in. (7.1 cm) in height. The chamber pressures applied were 1, 5, 25, 50, 75, and 100 psi (1 psi = 0.07 kg/cm^2). Two sets of triaxial tests were performed, depending on the way the samples were taken. Both tests measured the compressive strength of a cylinder of soil at different lateral pressures.

CU Test on Samples Extended From the Sampling Area by a Modified Harvard Compaction Mould (Non-Standard)

. A plot of the deviator stress versus the percentage strain is given in Figure 138. Figure 139 shows the Mohr circles at failure. The angle of friction is 12° and the cohesion is 500 psf (0.24 kg/cm^2). The modulus of elasticity of the soil versus the chamber pressure is shown in Figure 140. The modulus of elasticity of 0 psi confining pressure is taken as the secant modulus from the UC test at 0.1% strain. The rest points were taken on the initial tangent values of stress-strain curve. At about 2 psi (0.14 kg/cm^2) confining pressure, the corresponding modulus of elasticity of the soil is 450 psi (31.5 kg/cm^2).

CU Test on Undisturbed Samples Taken From the Testing Area

A plot of the deviator stress versus percentage strain is given in Figure 141.. Figure 142 shows the Mohr circles at failure. The angle of friction is 18° and the cohesion is 200 psf (0.10 kg/cm^2). The secant modulus of the soil was defined as:

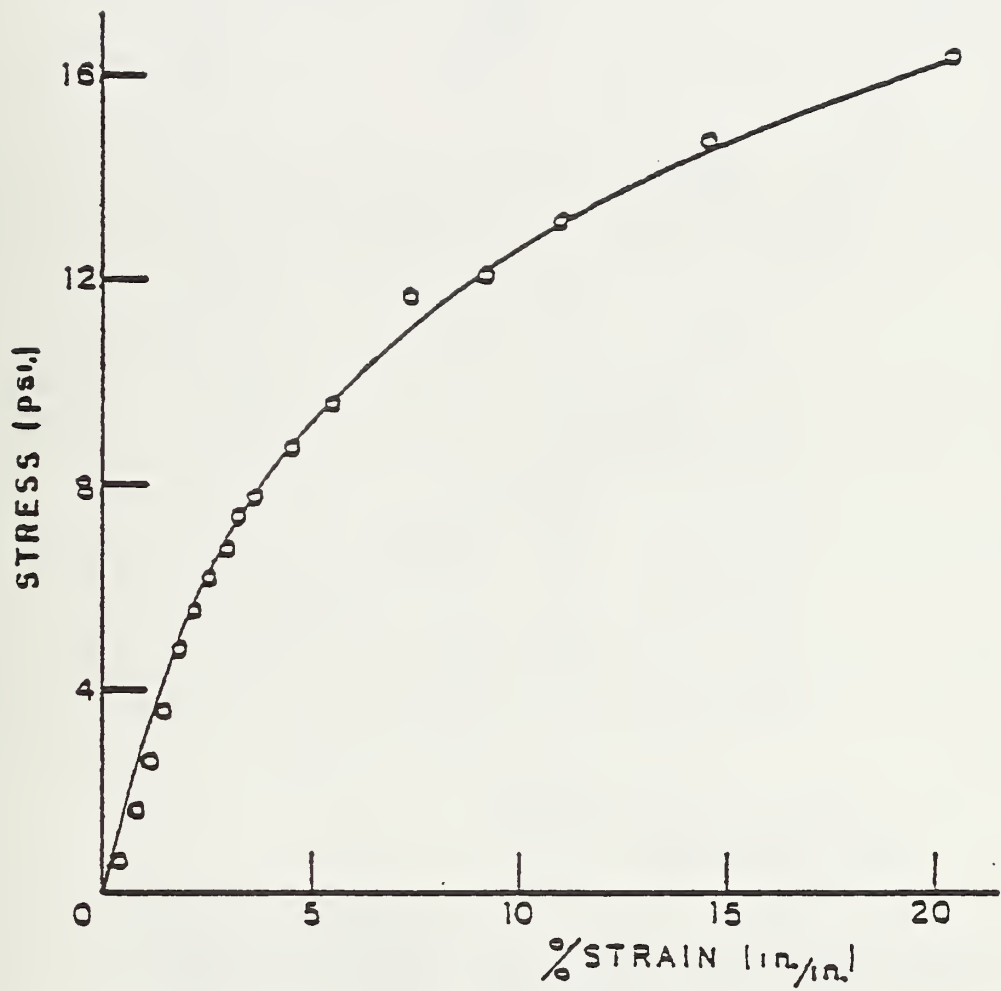
$$\epsilon = \frac{\sigma_d}{\epsilon}$$

B-9

The secant modulus verus percentage strain at different confining pressures is shown in Figure 143. Figure 144 shows the secant modulus at 0.1% strain versus the confining pressure. At 2 psi (0.14 kg/cm^2) pressure, the secant modulus is 600 psi (42 kg/cm^2).

CONSOLIDATION TESTS

The ASTM standard method (D2435-70) was followed. The data from the laboratory consolidation test make it possible to plot a stress-volume strain curve, which often gives useful information about the pressure history of the soil.



$$1 \text{ psi} = 0.07 \text{ kg/cm}^2$$
$$1 \text{ in.} = 2.54 \text{ cm}$$

Figure 136. Applied stress versus average % strain for unconfined compression test.

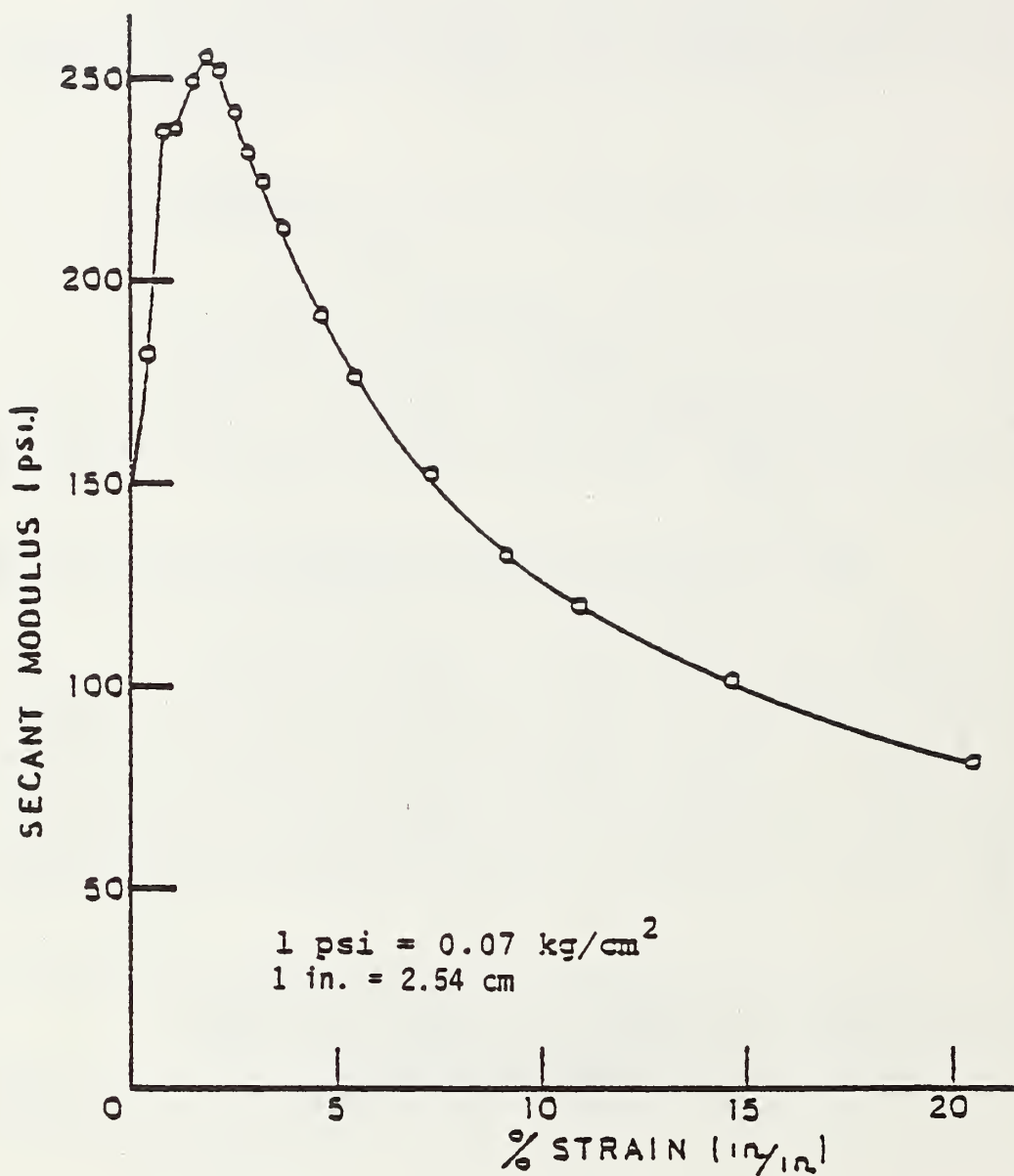


Figure 137. Secant modulus versus % strain for unconfined compression test.

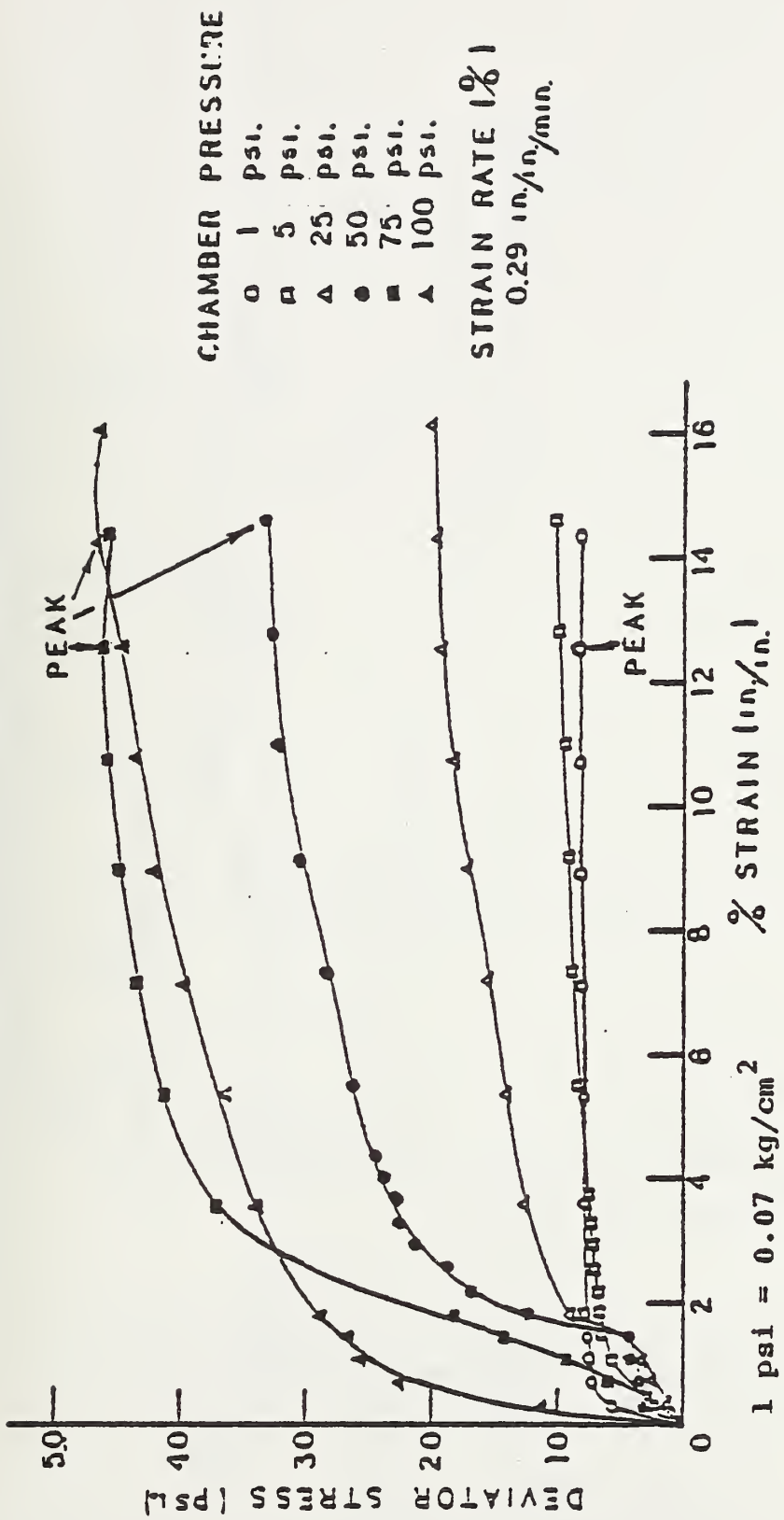


Figure 138. Deviator stress versus χ strain at different confining pressures for triaxial compression test.

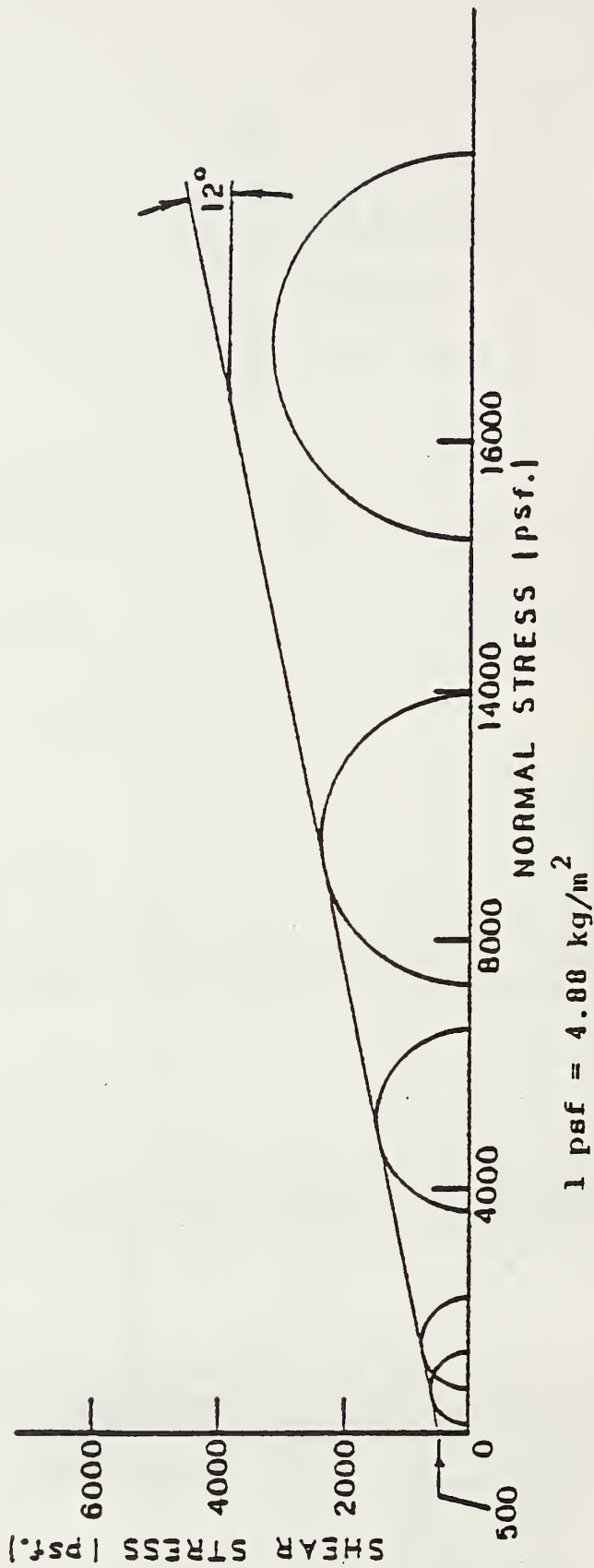


Figure 139. Mohr circles for triaxial compression test.

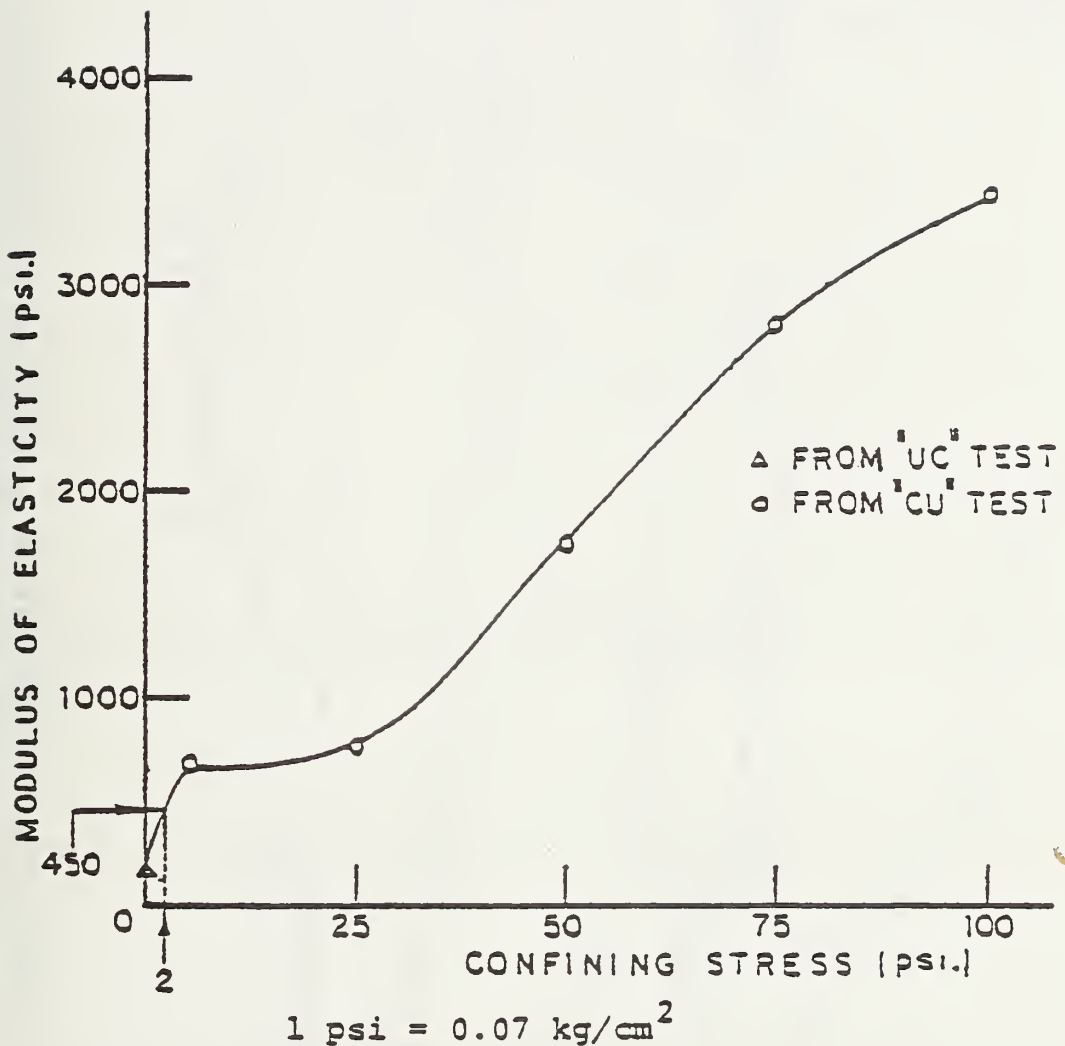


Figure 140. Modulus of elasticity versus confining stress from triaxial compression test.

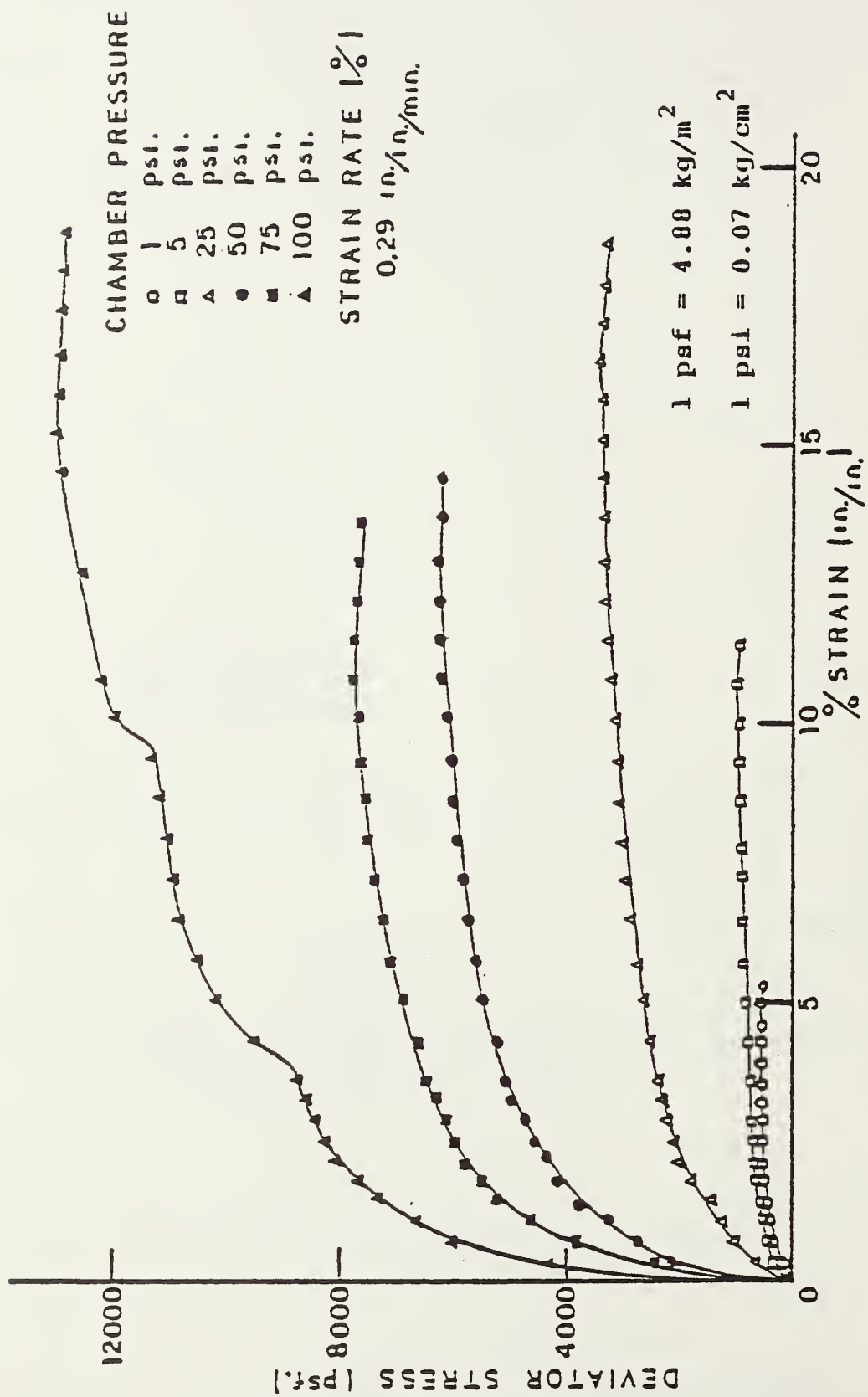


Figure 141. Deviator stress versus % strain at different confining pressures for triaxial compression test.

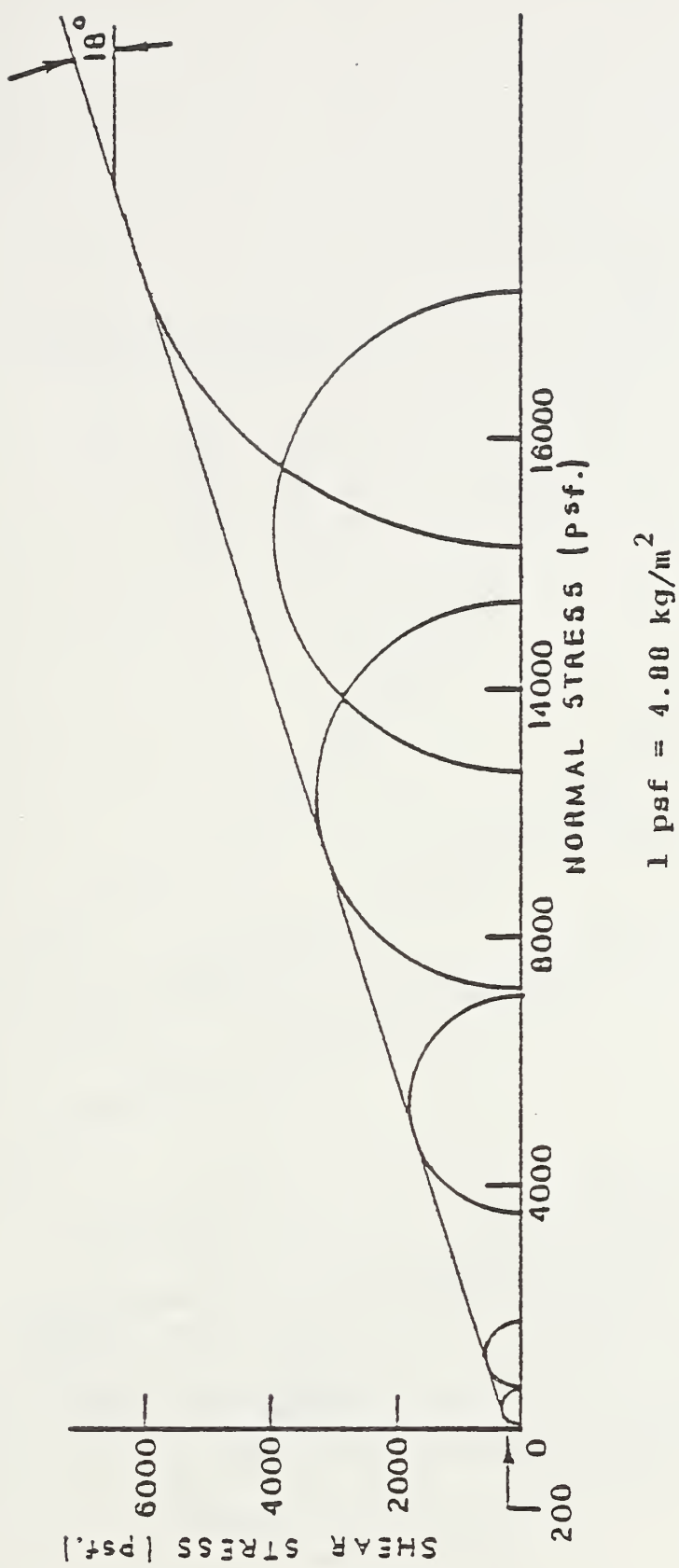
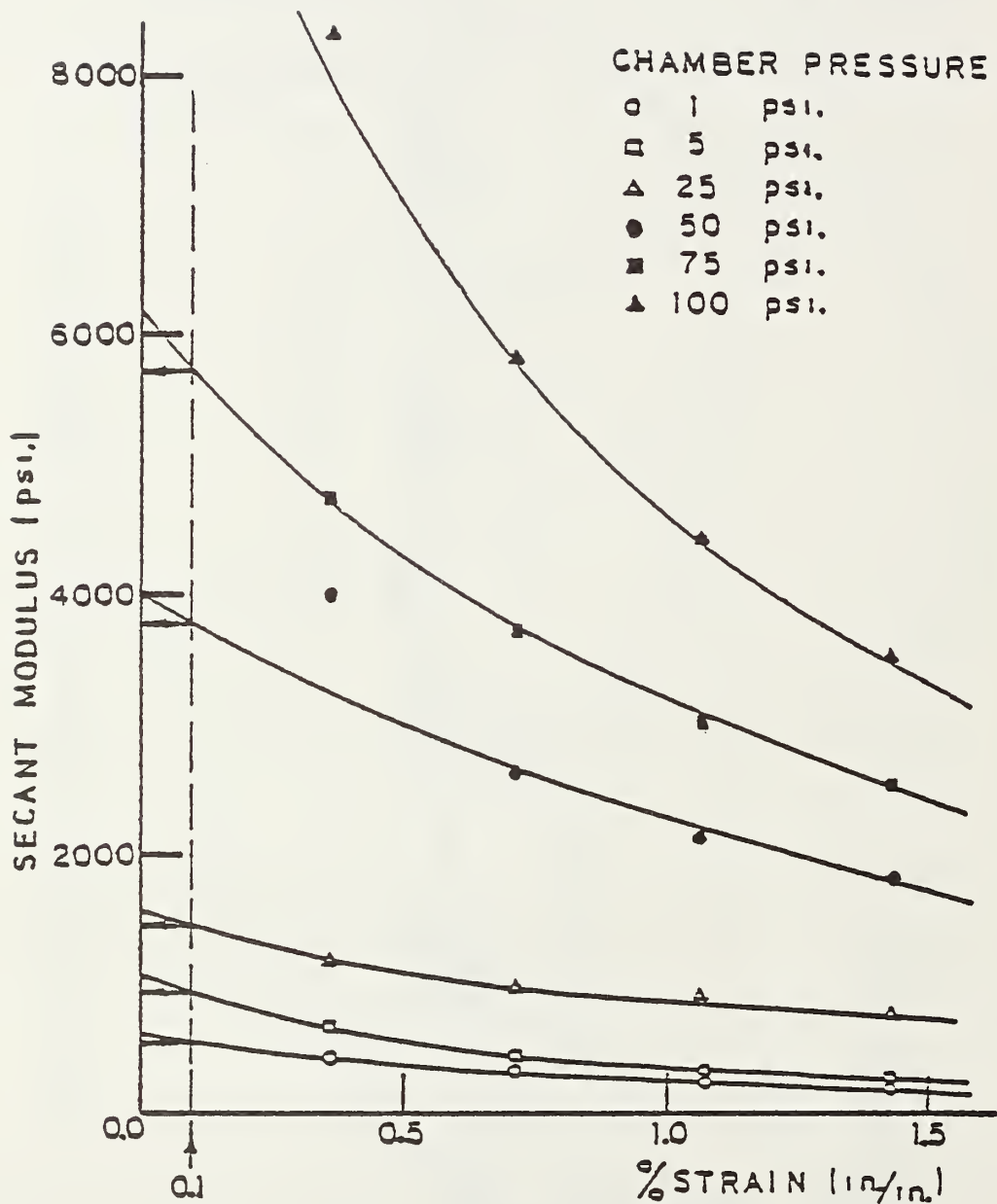


Figure 142. Mohr circles for triaxial compression test.



$$1 \text{ psi} = 0.07 \text{ kg/cm}^2$$

$$1 \text{ in} = 2.54 \text{ cm}$$

Figure 143. Secant modulus versus % strain at different confining pressures from triaxial compression test.

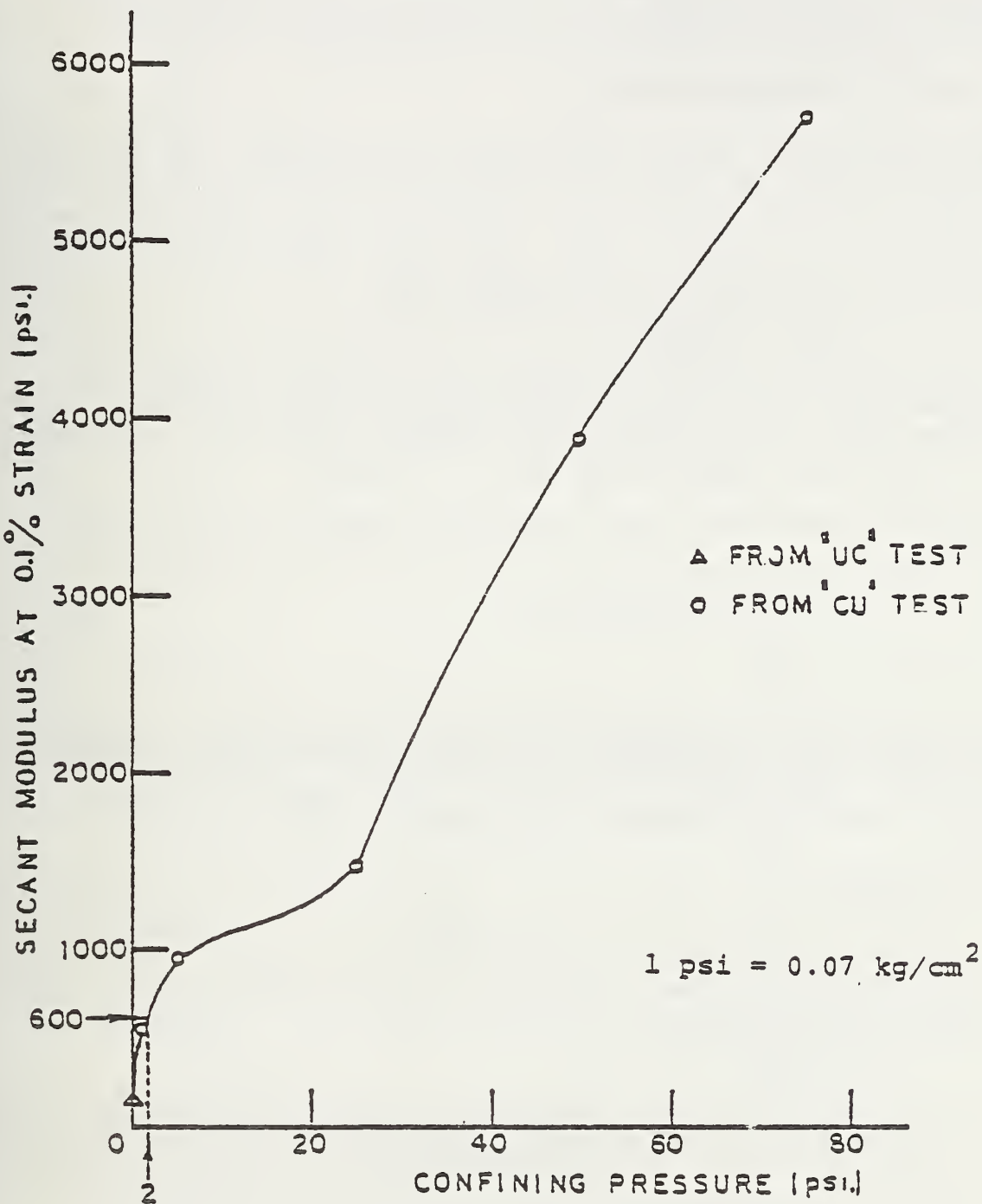


Figure 144.. Secant modulus at 0.1 % strain versus confining pressure from triaxial compression test.

Plots of coefficient of consolidation (C_v), primary compression ratio (τ), and void ratio (e) versus log of pressure are shown in Figure 145. Figure 146 shows a plot of applied pressure versus % strain. A plot of secant modulus at different percent strains is shown in Figure 147. The overconsolidation ratio (OCR) of this silty clay was established as 30, hence this soil was classified as an overconsolidated soil.

SOIL CLASSIFICATION AND SUBGRADE BEHAVIOR

The Atterberg limits and indices were found, and grain size analysis and hydrometer tests were performed (Lambe, 1951). Figures 148 and 149 show the grain size analysis and the flow curve respectively, the latter providing the Plasticity Index of 16 for the soil used. Figure 150 shows the dry density versus water content relationship - the optimum water content being 8%. The soil was mixed with an over-the-optimum water content (16%).

It is reasonable to assume that the plate load test will provide a better in situ value of the modulus of elasticity. The plate load test was conducted in the sampling area which did not undergo as many preloadings as the main experimental area. The preloadings will increase the modulus. The adopted modulus for an analytical comparison was 850 psi (60 kg/cm^2).

From the consolidation test, the overconsolidation ratio (OCR) was found to be 30.

From Figure 151, the following was obtained:

B-10

$$K_o = 2.6 \quad (K_o = \frac{\sigma_h}{\sigma_v})$$

The obtained value of K_o is in agreement with that in the published literature for overconsolidated clays and compacted clays (Wu, 1975). An unacceptable value of Poisson's ratio is obtained from the above K_o value, based on available relationship for isotropic, homogeneous and elastic material:

$$(K_o = \frac{v}{1-v})$$

B-11

Consequently in all analytical work a value of $v = 0.4$ was adopted. This value happens to agree with that obtained by using the formula $K_o = 1 - \sin\phi$, for normally consolidated material ($\phi = 18^\circ$).

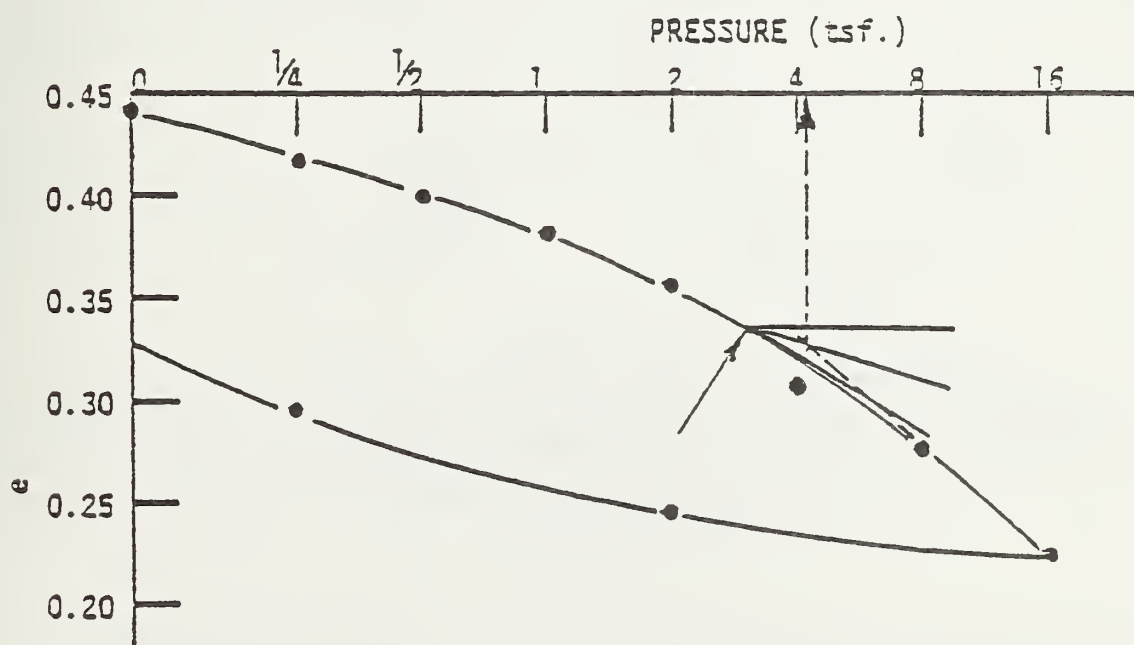
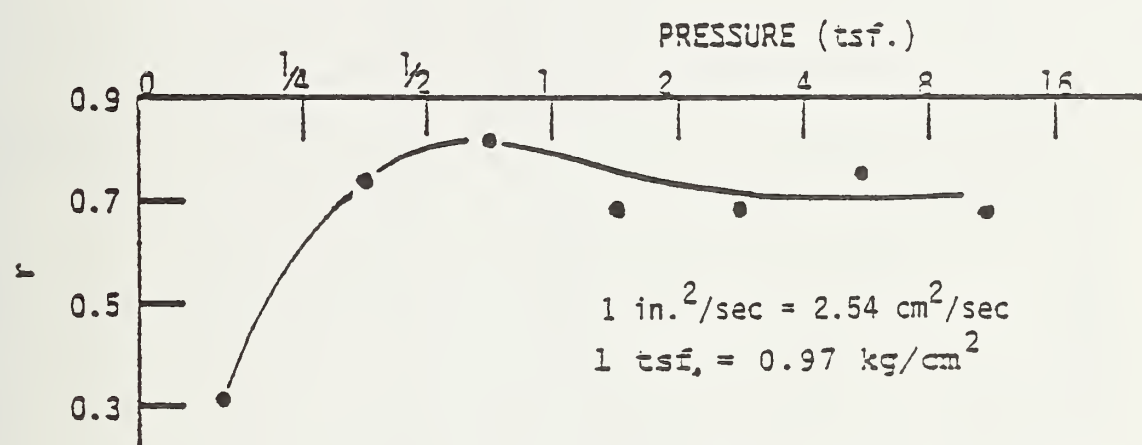
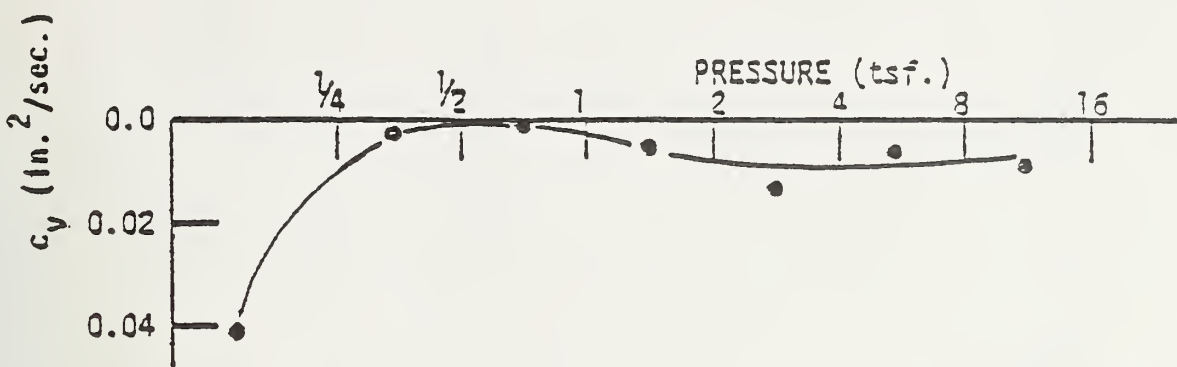


Figure 145. Coefficient of consolidation (top), primary compression ratio (middle), and void ratio (bottom) at different pressures using logarithmic fitting.

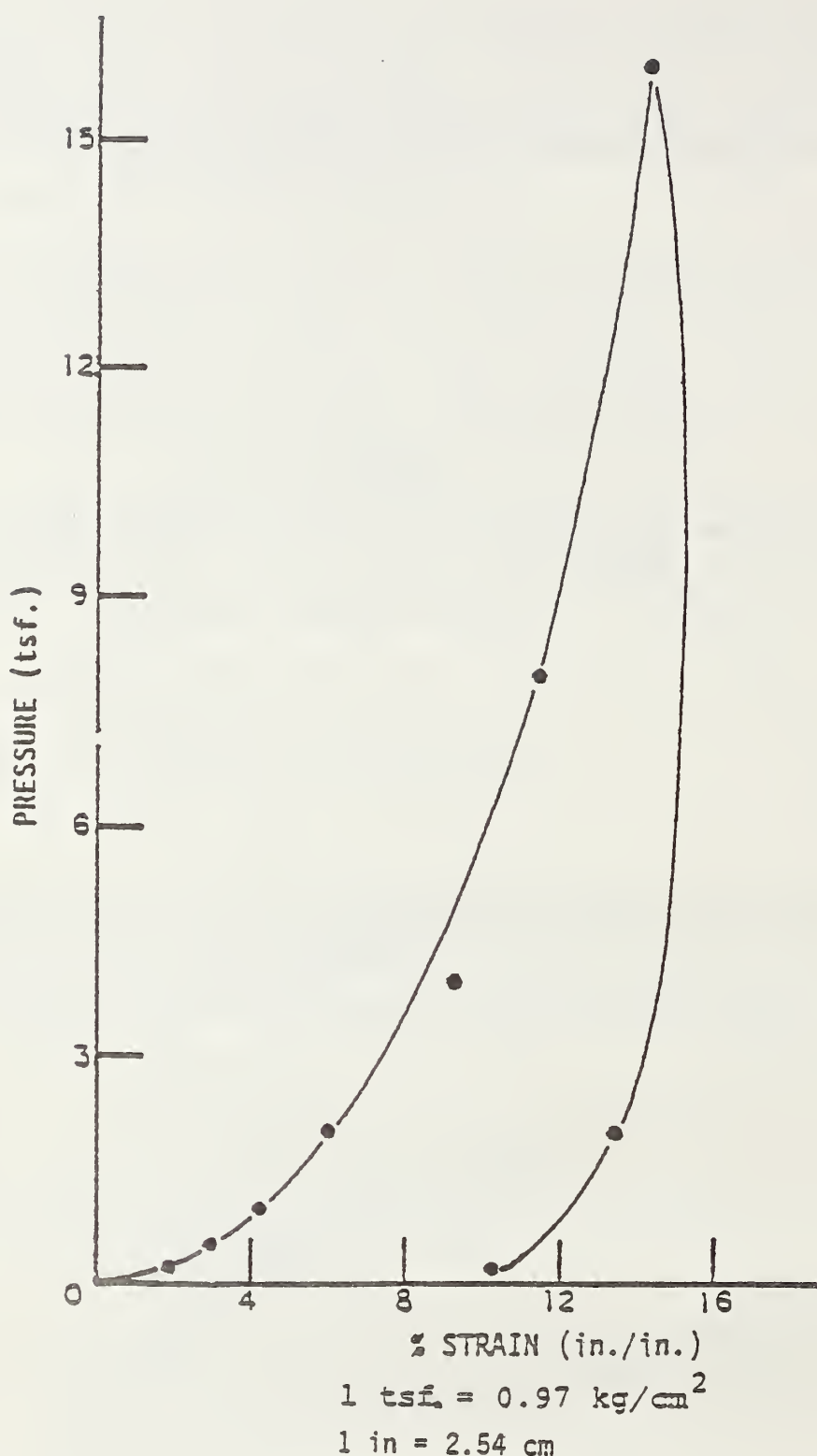


Figure 146. Applied pressure versus % strain.

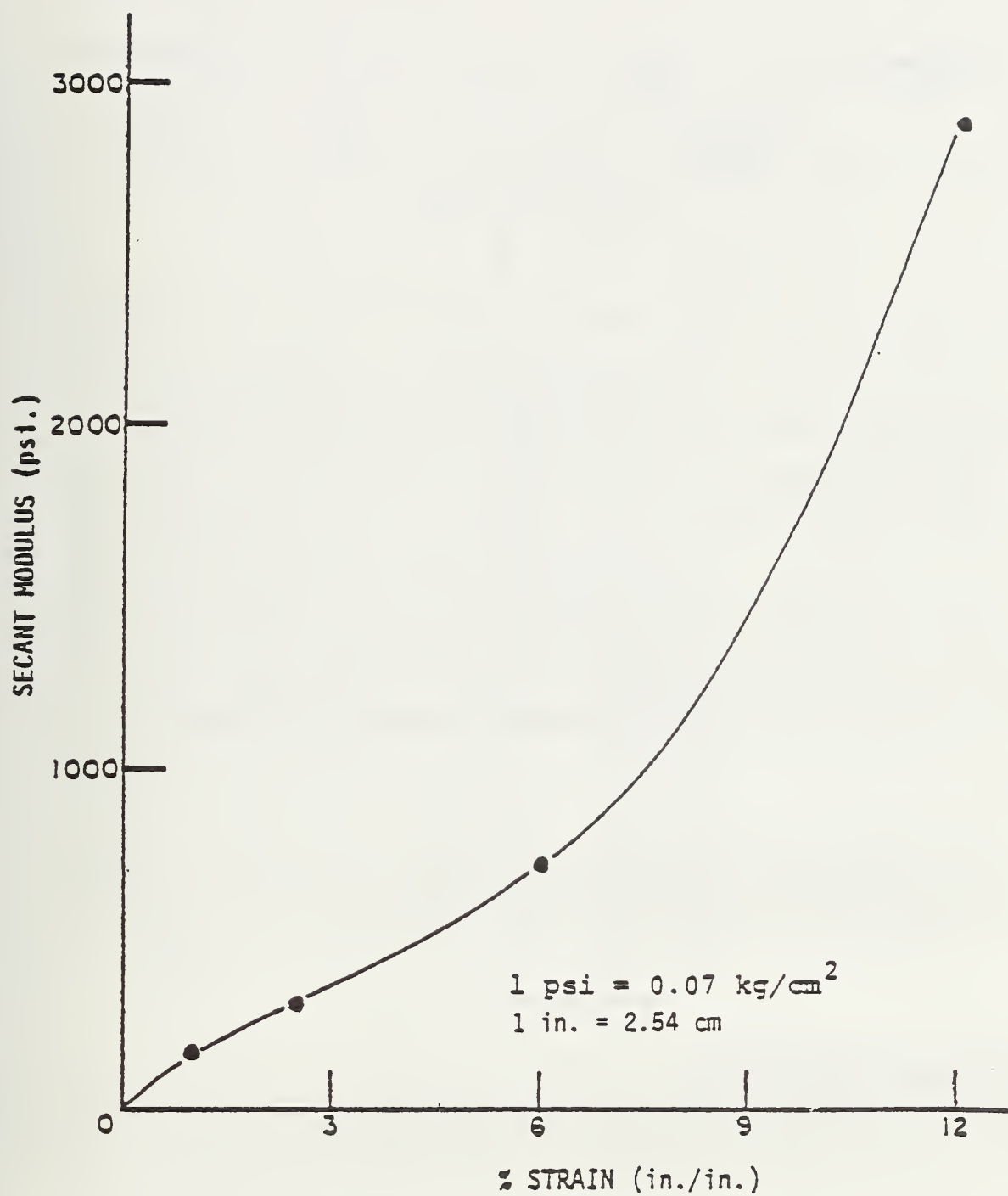


Figure 147. Secant modulus of soil at different % strains.

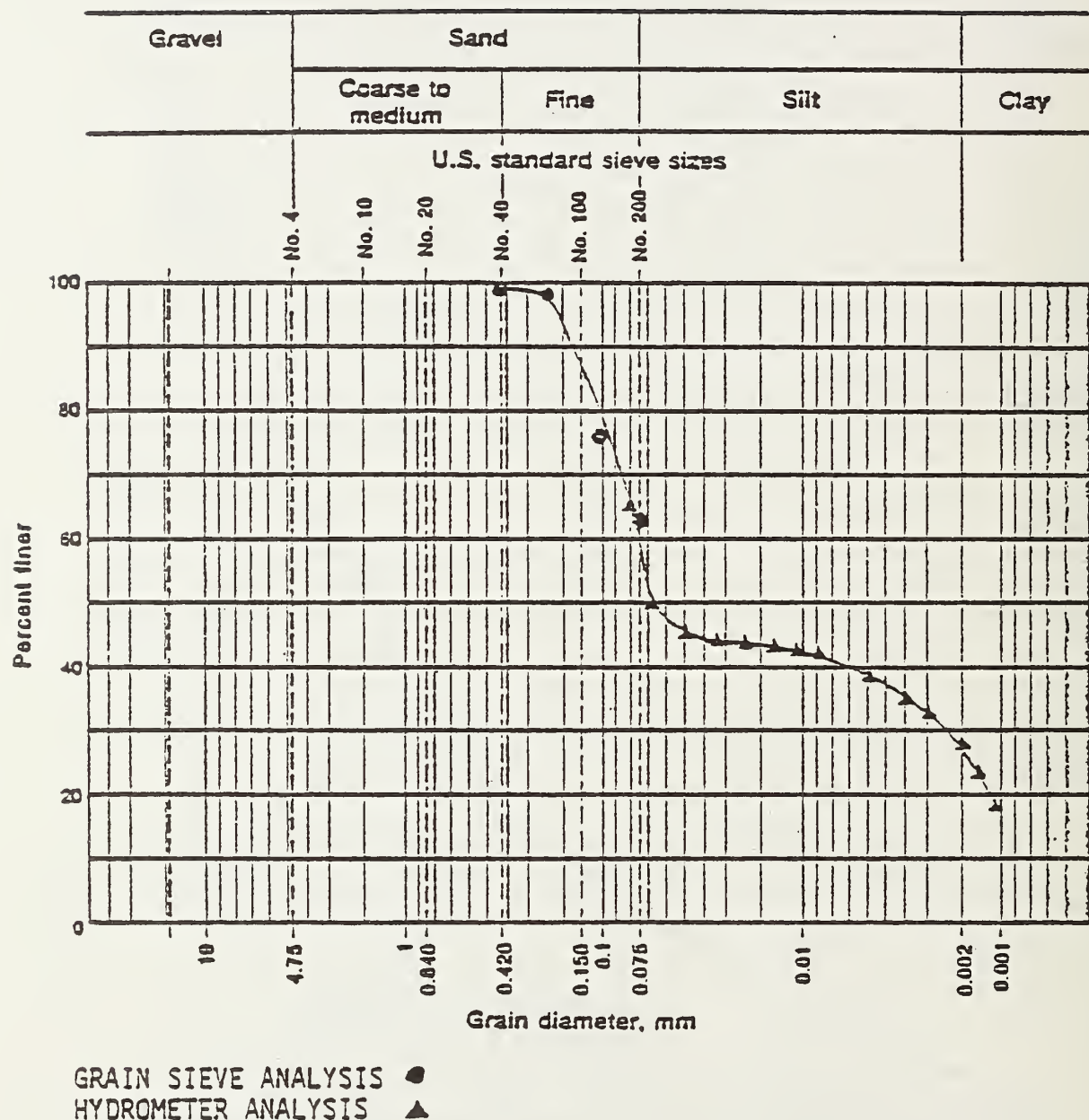


Figure 148. Grain size distribution.

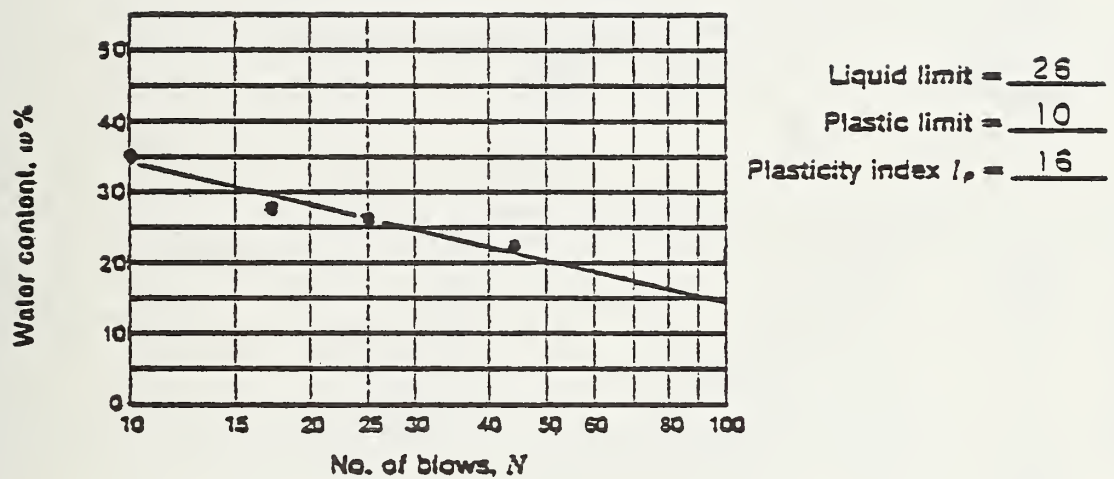


Figure 149. Flow curve and Atterberg limits.

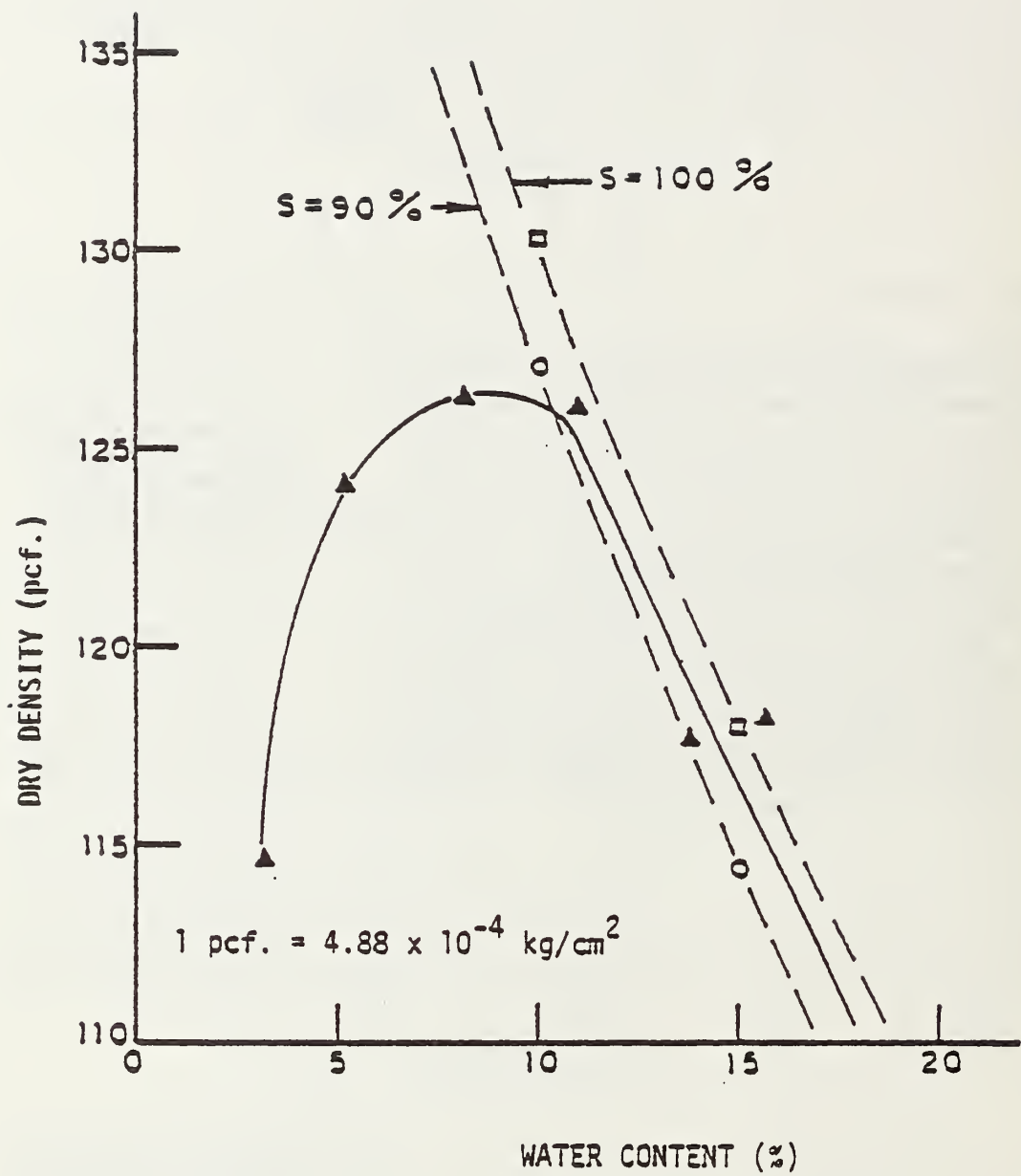
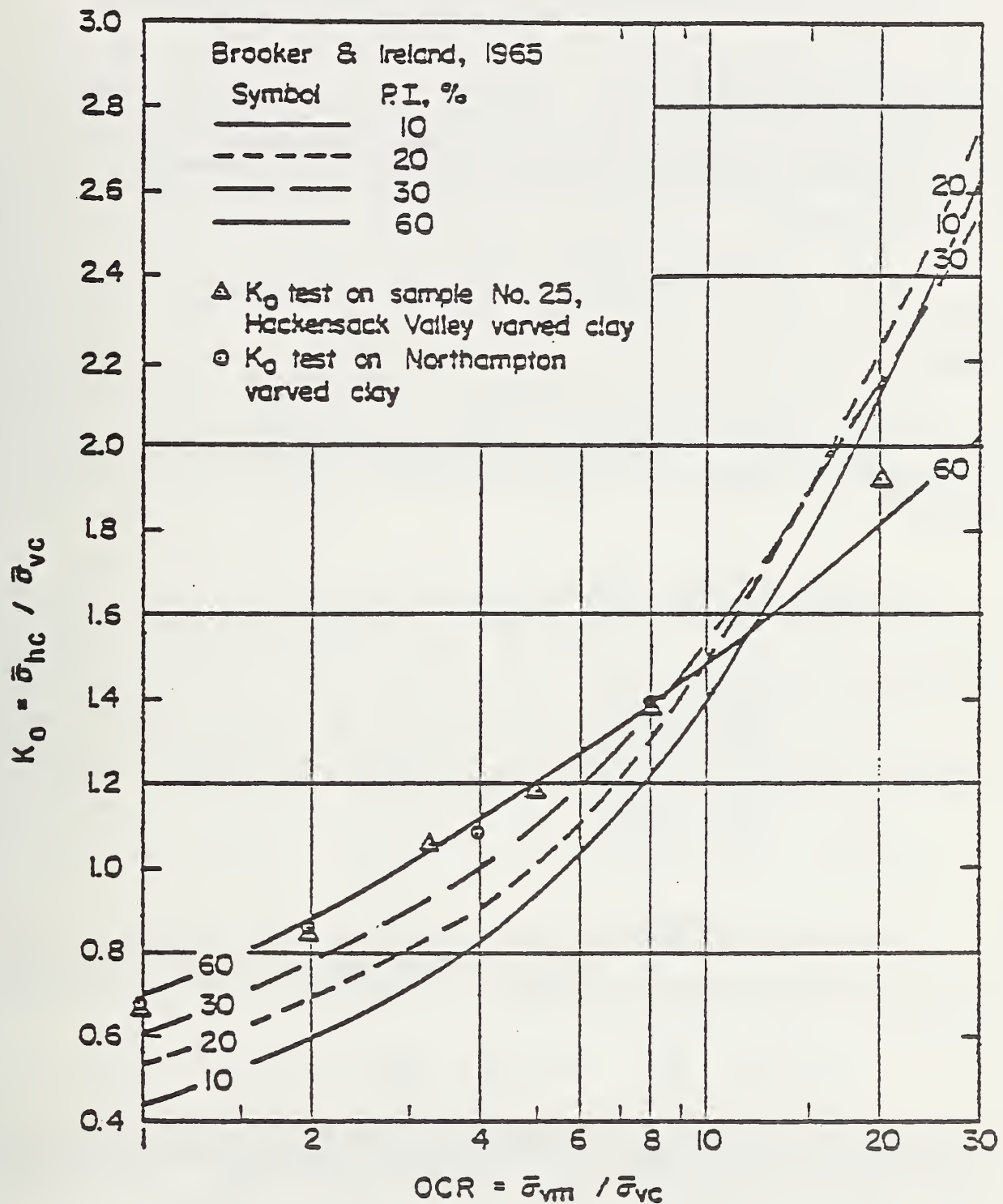


Figure 150. Dry density versus % water content.



Note: Brooker & Ireland data redrawn

Figure 151. K_0 versus OCR for soils of varying plasticity.

APPENDIX C: FINITE ELEMENT FORMULATION

This section presents a brief outline of the solution technique using the finite element method. Emphasis is placed on thermal stress analysis and transient heat flow analysis. Stiffness matrix derivations are given and a discussion of the methods used to solve the system of linear equations and the system of partial differential equations is also presented.

CLASSICAL METHODS

Most classical methods of plate analysis are derived from the equations of the theory of elasticity. Only a small portion of small deflection plate problems possess rigorous close-form solutions; as a result, numerical methods are usually applied.

The structures to be analyzed in this study are relatively complex. The anchored pavement consists of a slab with a non-uniform distribution of flexural rigidity. The problem can be modeled mathematically with the classic plate on elastic foundation formulation. From the plate bending equation

$$\frac{\partial^2 m_x}{\partial x^2} + 2 \frac{\partial^2 m_{xy}}{\partial x \partial y} + \frac{\partial^2 m_y}{\partial y^2} = p_z(x, y) - p^*(x, y) \quad C-1$$

where p_z is body forces, p^* is Winkler reactive forces, and m_x , m_y , and m_{xy} are internal moments such that

$$m_x = -D \left(\frac{\partial^2 w}{\partial x^2} + v \frac{\partial^2 w}{\partial y^2} \right) \quad C-2$$

$$m_y = -D \left(\frac{\partial^2 w}{\partial y^2} + v \frac{\partial^2 w}{\partial x^2} \right) \quad C-3$$

$$m_{xy} = -(1-v)D \frac{\partial^2 w}{\partial x \partial y} \quad C-4$$

where D is the slab flexural rigidity, v is Poisson's ratio, by substituting the internal moment expressions and keeping D variable, then

$$\frac{\partial^2}{\partial x^2} D \left(\frac{\partial^2 w}{\partial x^2} + v \frac{\partial^2 w}{\partial y^2} \right) + 2(1-v) \frac{\partial^2}{\partial x \partial y} D \frac{\partial^2 w}{\partial x \partial y} + \frac{\partial^2}{\partial y^2} D \left(\frac{\partial^2 w}{\partial y^2} + v \frac{\partial^2 w}{\partial x^2} \right) = p_z - p^* \quad C-5$$

This governing equation is not conveniently solved and may not possess a closed-form solution, except for simple boundary conditions and slab geometry. Because the small deflection theory of plates ignores second and higher order terms, numerical solutions may be prone to error. In addition, this classical plate equation with Winkler foundations considers only vertical reactive pressures that may not truly characterize the behavior of the system. The anchored pavement, in particular, utilizes vertical members which are restrained from rotation by passive earth pressure. This imposes a rotational constraint at the anchor locations. The anchors are expected to transfer a portion of the applied loads deeper into the subgrade where confining pressures are higher and as a result, modulus is greater. The problem becomes much more difficult with varying subgrade reaction and rotational constraints.

The finite element method can account for these conditions and also will readily determine stress distributions within the slab and the subgrade.

STATIC ANALYSIS

The finite element method involves the division of a continuum into an assemblage of discrete continua which are interconnected at nodal points such that the original character of the structure and its boundary conditions are maintained. The formulation of element stiffnesses that link applied nodal forces with nodal displacements through a relation of the form

$$\{F_e\} = K_e \{u_e\} \quad C-6$$

where $\{F_e\}$ is a vector of applied element forces, K_e is the element stiffness matrix, and $\{u_e\}$ is a vector of nodal displacements, begins with the choice of suitable functions that represent nodal displacements in terms of nodal coordinates. The displacement functions for the various elements used in this study are polynomials and listed in Table 23. The elements used are planar quadrilateral and hexahedral solid elements with translational and temperature degrees of freedom.

ANSYS uses a frontal solution for the system of simultaneous equations. The solution proceeds by advancing along increasing element numbers rather than nodes as in a conventional Gaussian scheme (Irons, 1970). An element with its associated nodal degrees of freedom is placed in core and the nodes comprising this element are scanned. If the degrees of freedom inherent to these nodes are no longer associated with any elements yet to be processed, then those degrees of freedom are condensed from the active equations in core by Gaussian elimination, and the wave front moves to subsequent elements. The solution proceeds until all elements have been considered. This technique can often be more efficient than a banded equation solver. ANSYS also has wave reordering capability that aids in the most efficient formulation of the structural stiffness matrix (least core space requirements) (Kohnke, 1977; Meyer, 1973).

The global formulation of the problem after the boundary conditions are applied on $\{u\}$ and $\{F\}$ is the partitioned form

$$\frac{K}{K_r^T} \frac{K_r}{K_{rr}} \frac{u}{u_r} = \frac{F}{F_r} \quad C-7$$

where the subscript r refers to the applied boundary conditions. The solution of the upper half of this equation results in an expression for the unknown displacements

$$\{u\} = -K^{-1} K_r \{u_r\} + K^{-1} F \quad C-8$$

while solution of the lower half yields reactive forces

$$\{F_r\} = K_r^T \{u\} + K_{rr} \{u_r\} \quad C-9$$

Strains are then calculated from derived strain-displacement relations, and stresses are determined from stress-strain relations.

TRANSIENT HEAT TRANSFER ANALYSIS

The solution to the Laplacian field equation

$$c^2 \nabla^2 u = \dot{u} \quad C-10$$

where ∇ is the Laplacian operator and the dot indicates a time derivative, by the finite element method, was first proposed by Zienkiewicz and Cheung (1965). The heat conduction form in three dimensions is the following quasi-linear parabolic equation:

$$\rho c \frac{\partial T}{\partial t} = \frac{\partial}{\partial x} (k \frac{\partial T}{\partial x}) + \frac{\partial}{\partial y} (k \frac{\partial T}{\partial y}) + \frac{\partial}{\partial z} (k \frac{\partial T}{\partial z}) \quad C-11$$

where ρ is density, c is specific heat, k is thermal conductivity, and T is temperature. The finite element method was then applied to heat conductivity (Wilson and Nickell, 1966).

The element level formulation proceeds with the statement of the principle of virtual work which is an energy balance relation equating a virtual change in internal strain energy with a virtual change in applied external work. Virtual internal work is

$$\delta U = \int_V \{\delta G\}^T \{Q_v\} dV \quad C-12$$

where

$$\{G\}^T = \left\{ \frac{\partial T}{\partial x} \frac{\partial T}{\partial y} \frac{\partial T}{\partial z} \right\} \quad C-13$$

a temperature gradient vector, and

$$\{Q_v\}^T = \{Q_x \ Q_y \ Q_z\} \quad C-14$$

is a vector of heat flow, Q_i is the heat flow in the i^{th} direction per unit area and T is temperature at a point in the element. Heat flows are related to temperature gradients through the conductivity matrix, D such that

$$\{Q_v\} = D \{G\} \quad C-15$$

Temperature gradients are related to nodal temperatures by

$$\{G\} = B \{T_e\} \quad C-16$$

where

$$\{T\} = N^T \{T_e\} \quad C-17$$

$$B^T = \left\{ \frac{\partial N}{\partial x} \right\}^T \left\{ \frac{\partial N}{\partial y} \right\}^T \left\{ \frac{\partial N}{\partial z} \right\}^T \quad C-18$$

Table 23 Displacement models for finite elements (Wilson et al., 1973; Kohnke, 1977).

ELEMENT	DEGREES OF FREEDOM PER NODE	DISPLACEMENT MODEL
2-D STRESS	u_x, u_y	$u_x = \sum_1^6 h_i u_{xi} + h_5 \alpha_1 + h_6 \alpha_2, \quad u_y = \sum_1^6 h_i u_{yi} + h_5 \alpha_3 + h_6 \alpha_4$ $T = \sum_1^6 h_i T_i + h_6 \alpha_1 + h_6 \alpha_2$ <p>where $h_1 = \frac{1}{4}(1-s)(1-t), \quad h_2 = \frac{1}{4}(1+s)(1-t)$ $h_3 = \frac{1}{4}(1+s)(1+t), \quad h_4 = \frac{1}{4}(1-s)(1+t)$ $h_5 = 1-s^2, \quad h_6 = 1-t^2$</p>
2-D TEMP	u_x, u_y	
3-D STRESS	u_x, u_y, u_z	$u_x = \sum_1^9 h_i u_{xi} + h_9 \alpha_{x1} + h_{10} \alpha_{x2} + h_{11} \alpha_{x3}, \quad \text{similar for } y \text{ and } z$ <p>where $h_1 = \frac{1}{6}(1+\xi)(1+\eta)(1+\zeta), \quad h_2 = \frac{1}{6}(1-\xi)(1+\eta)(1+\zeta)$ $h_3 = \frac{1}{6}(1-\xi)(1-\eta)(1+\zeta), \quad h_4 = \frac{1}{6}(1+\xi)(1-\eta)(1+\zeta)$ $h_5 = \frac{1}{6}(1+\xi)(1+\eta)(1-\zeta), \quad h_6 = \frac{1}{6}(1-\xi)(1+\eta)(1-\zeta)$ $h_7 = \frac{1}{6}(1-\xi)(1-\eta)(1-\zeta), \quad h_8 = \frac{1}{6}(1+\xi)(1-\eta)(1-\zeta)$ $h_9 = 1-\xi^2, \quad h_{10} = 1-\eta^2, \quad h_{11} = 1-\zeta^2$</p>

Table 23 (continued)

ELEMENT	DEGREES OF FREEDOM PER NODE	DISPLACEMENT MODEL
3-D CONVECTION LINK	q, heat flow	$q = h_f A E (T_i - T_j)$ <p>where h_f is film coefficient</p> <p>A is area</p> <p>E is a constant</p> <p>T_i, T_j are nodal temperatures</p>

and $\{T\}$ is a vector of temperatures within the element, $\{T_e\}$ is a nodal temperature vector, and N is a matrix of shape functions. Thus

$$\delta U = \int_V \{\delta T_e\}^T B^T D B \{T_e\} dV \quad C-19$$

The internal work associated with convection surfaces is

$$\delta U = \int_A \delta \Delta T Q_n dA \quad C-20$$

where

$$\Delta T = T|_s - T_B \quad C-21$$

with $T|_s$ being the temperature function evaluated at a point on the convection surface while T_B is the bulk temperature of the ambient material. For a constant T_B ,

$$\delta \Delta T = \delta T|_s \quad C-22$$

Defining heat flow over a unit area as

$$Q_n = h_f \Delta T \quad C-23$$

where h_f is the film coefficient of surface heat transfer, yields the resulting equation

$$\delta U = \int_A \{\delta T_e\}^T h_f \{N|_s\}^T \{T_e\} dA - \int_A \{\delta T_e\}^T h_f T_B \{N|_s\} dA \quad C-24$$

where $\{N|_s\}$ are the shape functions evaluated on the convection surface.

Internal heat generation rate has the associated virtual work

$$\delta U = \int_V \delta T q dV \quad C-25$$

or

$$\delta U = \int_V \{\delta T_e\}^T q \{N\} dV \quad C-26$$

The virtual work due to a change in stored energy is

$$\delta U = \int_V \delta T \gamma dV \quad C-27$$

where

$$\gamma = \rho c_p \frac{\partial T}{\partial t} \quad C-28$$

which is the total change in heat per unit volume per unit time. Specific heat is denoted by c_p and density by ρ . Thus

$$\delta U = \int_V \{\delta T_e\}^T c_p \{N\} \{N\}^T \{T_e\} dV \quad C-29$$

where $\{\dot{T}_e\}$ is time varying temperatures.

Consideration of nodal heat flows gives

$$\delta W = \{\delta T_e\}^T \{Q_e\} \quad C-30$$

where $\{Q_e\}$ is the nodal heat flow vector associated with the element.

Combining the internal work and equating this to external work results in the following:

$$(K_e + K_e^C) \{T_e\} + C_e \{\dot{T}_e\} = \{Q_e^C\} + \{Q_e^G\} + \{Q_e\} \quad C-31$$

where K_e is the conductivity matrix, K_e^C is conduction matrix associated with convection, C_e is the heat capacity or thermal damping matrix, $\{Q_e^G\}$ is internal heat generation, $\{Q_e^C\}$ is internal convection heat, and $\{Q_e\}$ is applied nodal heat flow.

The basic thermal diffusion equation

$$C \{\dot{T}\} + K \{T\} = \{Q\} \quad C-32$$

in global form is solved by a quadratic temporal integration scheme by the following substitutions:

$$\{\dot{T}\} = \frac{3T_{t+\Delta t} - 4T_t + T_{t-\Delta t}}{2\Delta t} \quad C-33$$

$$\{T\} = \{T_{t+\Delta t}\} \quad C-34$$

where $t+\Delta t$, t , and $t-\Delta t$ are current, past and second previous past times. The solution for temperature distributions at the current time is

$$.T_{t+\Delta t} = (K + \frac{3}{2\Delta t} C)^{-1} (\{Q\} + C \{\frac{4T_t - T_{t-\Delta t}}{2\Delta t}\}) \quad C-35$$

If K and C are temperature dependent, then each are evaluated at the current time based upon extrapolation from the previous time.

A current time solution requires information from two previous times, thus the solution procedure is not self starting. If the analysis starts at time $t = 0$, then a steady state analysis is performed. If, however, the first load step ends at time $t > 0$, then the initial two previous temperature distributions are set to a uniform temperature selected by the user and the solution proceeds from there.

TE 662-A3
026

Saxena, Sure

-

New structure
zero-maint

Form DOT F 172
FORMERLY FORM DC



FEDERALLY COORDINATED PROGRAM (FCP) OF HIGHWAY RESEARCH AND DEVELOPMENT

The Offices of Research and Development (R&D) of the Federal Highway Administration (FHWA) are responsible for a broad program of staff and contract research and development and a Federal-aid program, conducted by or through the State highway transportation agencies, that includes the Highway Planning and Research (HP&R) program and the National Cooperative Highway Research Program (NCHRP) managed by the Transportation Research Board. The FCP is a carefully selected group of projects that uses research and development resources to obtain timely solutions to urgent national highway engineering problems.*

The diagonal double stripe on the cover of this report represents a highway and is color-coded to identify the FCP category that the report falls under. A red stripe is used for category 1, dark blue for category 2, light blue for category 3, brown for category 4, gray for category 5, green for categories 6 and 7, and an orange stripe identifies category 0.

FCP Category Descriptions

1. Improved Highway Design and Operation for Safety

Safety R&D addresses problems associated with the responsibilities of the FHWA under the Highway Safety Act and includes investigation of appropriate design standards, roadside hardware, signing, and physical and scientific data for the formulation of improved safety regulations.

2. Reduction of Traffic Congestion, and Improved Operational Efficiency

Traffic R&D is concerned with increasing the operational efficiency of existing highways by advancing technology, by improving designs for existing as well as new facilities, and by balancing the demand-capacity relationship through traffic management techniques such as bus and carpool preferential treatment, motorist information, and rerouting of traffic.

3. Environmental Considerations in Highway Design, Location, Construction, and Operation

Environmental R&D is directed toward identifying and evaluating highway elements that affect

the quality of the human environment. The goals are reduction of adverse highway and traffic impacts, and protection and enhancement of the environment.

4. Improved Materials Utilization and Durability

Materials R&D is concerned with expanding the knowledge and technology of materials properties, using available natural materials, improving structural foundation materials, recycling highway materials, converting industrial wastes into useful highway products, developing extender or substitute materials for those in short supply, and developing more rapid and reliable testing procedures. The goals are lower highway construction costs and extended maintenance-free operation.

5. Improved Design to Reduce Costs, Extend Life Expectancy, and Insure Structural Safety

Structural R&D is concerned with furthering the latest technological advances in structural and hydraulic designs, fabrication processes, and construction techniques to provide safe, efficient highways at reasonable costs.

6. Improved Technology for Highway Construction

This category is concerned with the research, development, and implementation of highway construction technology to increase productivity, reduce energy consumption, conserve dwindling resources, and reduce costs while improving the quality and methods of construction.

7. Improved Technology for Highway Maintenance

This category addresses problems in preserving the Nation's highways and includes activities in physical maintenance, traffic services, management, and equipment. The goal is to maximize operational efficiency and safety to the traveling public while conserving resources.

8. Other New Studies

This category, not included in the seven-volume official statement of the FCP, is concerned with HP&R and NCHRP studies not specifically related to FCP projects. These studies involve R&D support of other FHWA program office research.

* The complete seven-volume official statement of the FCP is available from the National Technical Information Service, Springfield, Va. 22161. Single copies of the introductory volume are available without charge from Program Analysis (HRD-3), Offices of Research and Development, Federal Highway Administration, Washington, D.C. 20590.

DOT LIBRARY



00056776